Correlating misorientation, segregation and residual strains

Submitted in partial fulfillment of the requirements

of the degree of

Doctor of Philosophy

by

Namit Narasimhan Pai

Roll number: 204116001

Supervisor(s):

Prof. Anirban Patra

Prof. Indradev Samajdar

Metallurgical Engineering and Materials Science

Indian Institute of Technology Bombay

April 2025

Thesis Approval

This thesis entitled **"Correlating misorientation, segregation and residual strains"** by **"Namit Narasimhan Pai"** is approved for the degree of **Doctor of Philosophy**.

Examiners:

.....

.....

.....

Supervisor(s):

.....

.....

.....

Chairman:

.....

Date: .....

Place: .....

Declaration

I declare that this written submission represents my ideas in my own words and where others ideas or words have been included, I have adequately cited and referenced the original sources. I also declare that I have adhered to all principles of academic honesty and integrity and have not misrepresented or fabricated or falsified any idea/data/fact/source in my submission. I understand that any violation of the above will be cause for disciplinary action by the Institute and can also evoke penal action from the sources which have thus not been properly cited or from whom proper permission has not been taken when needed.

.....

(Signature)

.....

(Name of the student)

.....

(Roll No.)

Date: .....

Place: .....

Abstract

Plastic deformation in metals is inherently non-homogeneous and governed by the kinematics and kinetics of defect structures. These are manifested in the form of anisotropic mechanical properties and residual strains at the bulk scale, whereas by plastic strain gradients, complex dislocation patterns, particle deformed zones, etc. at the microstructural level. As with the case of structural metals and alloys, the intrinsic microstructural heterogeneity originating from modern manufacturing methods (for example, rapid solidification) and subsequent thermomechanical processing further complicates their behavior.

While a range of experimental characterization techniques are readily available to examine these, not much work has been carried out towards the development of relevant mesoscale models. This forms the motivation of the present study, to elucidate and predict the factors contributing to the heterogeneous plastic deformation in metals and alloys. This has been achieved with the broad objective of developing experimentally informed mesoscale plasticity frameworks to predict and correlate the inter-dependencies between the local substructure, compositional heterogeneity and residual strains in microstructures subjected to mechanical deformation. Towards these objectives, each Chapter of the thesis firstly introduces the novelties in the experimental/modeling approach, followed by its validation and subsequent application to a practical study.

Chapter 3 introduces a combined experimental and Taylor hardening based Strain Gradient Crystal Plasticity (SGCP) framework for studying the development of orientation and misorientation gradients at the grain boundaries during plastic deformation. The regions in the vicinity of prior-deformation grain boundaries experiencing localized plastic deformation are referred to as Near Boundary Gradient Zones (NBGZs). The substructure evolution within the NBGZs is quantified on grain pairs with different combinations of crystallographic orientations in a solid solution strengthened aluminum alloy. Realistic virtual microstructures are then simulated using the SGCP framework to study the evolution of local misorientations, stresses and strains and their correlation with the underlying substructure. Our combined study shows that the width (mean with deviation) of the distribution of the length of NBGZ, normalized by the grain size, scales with the grain-average Schmid factor.

Chapter 4 further extends these observations to a precipitation strengthened aluminum alloy. The key difference over here is in that the precipitates decorating the grain boundary play a dominating role over the crystallographic orientations, in governing the substructure evolution within the NBGZs, especially for the (plastically) intermediate (0.35<Schmid factor≤0.45) and hard (Schmid factor≤0.35) oriented grains. The softer (Schmid factor>0.45) grains on the other hand, still display an orientation dependence and a much wider NBGZ, as in Chapter 3. As with the grain boundaries showing solute segregation, the relationship between the NBGZ and Schmid factor observed in Chapter 3 is retained.

Further, we focus on capturing the thermal distortion induced substructure developments, specifically in terms of the rapidly solidified alloys. The adverse thermal gradients (and cooling rates) results in the development of significant microscale internal stresses, which are attributed to the printing induced dislocation substructures. The resulting backstress due to the Geometrically Necessary Dislocations (GNDs) is responsible for the observed Tension–Compression (TC) asymmetry. A combined Phase Field (PF)-Strain Gradient J_2 Plasticity (SGP) framework is developed to examine the TC asymmetry in such microstructures. The novelty of the modeling framework lies in its capabilities to account for the orientation-based anisotropy, multi-grain interaction, anisotropic elasticity, dislocation strengthening, solid solution strengthening along with GND-induced directional backstress. The results presented point to the microstructural factors, such as dislocation substructure and solute segregation, and mechanistic factors, such as backstress, which may contribute to the development of TC asymmetry in rapidly solidified microstructures.

We then focus on quantifying the residual strains (and corresponding strain gradients) using various experimental methodologies in Chapter 6. To begin with, a key challenge over here is in establishing the numerical convergence/scaling between various multi-scale residual strain measurement techniques, as these differ in scale and resolution while also yielding significantly different strain values. The High Resolution Electron Backscatter Diffraction (HR-EBSD) and Transmission Kikuchi Diffraction (HR-TKD) (sensitive to $\Delta\theta/\theta$), provides quantitatively higher residual strains than the micro-Laue X-Ray Diffraction (XRD) and Transmission Electron Microscope (TEM) based Precession Electron Diffraction (PED) (sensitive to $\Delta d/d$). Even after correcting the key known factors affecting the accuracy of HR-EBSD strains, a scaling factor of ~ 1.57 emerges. Simulated Kikuchi patterns obtained

from ideal lattices deformed by changing an interplanar angle or a lattice parameter also display a similar behavior. The differences in the strain measurements are further emphasized by mapping identical locations with HR-TKD and TEM-PED. These measurements exhibit different spatial resolution, but on scaling (with ~ 1.57) provide similar lattice distortions numerically.

Finally, Chapter 7 compares the $\Delta d/d$-sensitive XRD (bulk) and $\Delta\theta/\theta$-sensitive HR-EBSD (local) residual strains with their simulated counterparts in an austenitic stainless steel subjected to tensile and cyclic deformation. These are predicted using a dislocation density-based crystal plasticity model, with consideration for directional hardening due to the backstress evolution. The study emphasizes on bulk residual strain developments for four specific grain families: (111), (001), (101) and (311), specifically in terms of their correlation with the underlying microstructure, studied using crystallographic orientation, misorientation, dislocation density and backstress evolution. Further, the measured local residual strains, which are also qualitatively predicted by the crystal plasticity simulations, highlight the additional effect of spatial heterogeneity and neighboring grains on the development of residual strains. Finally, statistical analysis of the simulated predictions reveal the following hierarchy in the development of bulk residual strains for the different grain families: (001)>(311)>(111)>(101) for tensile deformation and (001)>(311)>(111)$\sim$(101) for cyclic deformation. The dominant factors contributing to the observed hierarchy are the elastic stiffness and the grain rotations (or lack thereof) for different grain families.

In summary, the thesis is directed towards the development of experimentally informed modeling frameworks to explore the process-structure-property relationship in structural metals and alloys.

Keywords: *Strain gradient, crystal plasticity, J_2 plasticity, phase field, backstress, EBSD, orientation gradients, residual strain*

Contents

List of Figures

List of Tables

Chapter 1

Introduction

1.1 Overview

Plastic deformation of structural metals and alloys is inherently heterogeneous and several factors may contribute to this. Prior processing may lead to a heterogeneity in the as-built microstructure, in the form of varied grain morphology and (mis)orientations, solute segregation, second phase precipitates and pre-existing residual stresses. These microstructural heterogeneities may in turn result in anisotropic plastic deformation, with effects including tension-compression asymmetry and orientation-dependent anisotropic residual strain developments during deformation. Further, loading conditions and constraints during service may lead to plastic strain gradients, which are accommodated by Geometrically Necessary Dislocations (GNDs), and may result in the development of opposing stress fields, commonly called backstress, that hinder the subsequent plastic deformation.

Generally speaking, the heterogeneities in the microstructure and plastic deformation are often inter-related. This is schematically shown in Figure 1.1. For example, GNDs may pile up at grain boundaries and interfaces with second phase precipitates, which are manifested in terms of misorientation developments. Residual strains (or stresses) may also develop at these heterogeneous interfaces during both processing and in-service deformation. Further, thermal gradients during processing may result in solute segregation, residual stresses and dislocation structures. Delineating and isolating their individual effects on plastic deformation is often challenging.

This serves as the main motivation for the present thesis, which attempts to quantify the inter-relationships between the microstructure and plastic deformation via combined modeling and experiments. The microstructural heterogeneities have been measured in terms of

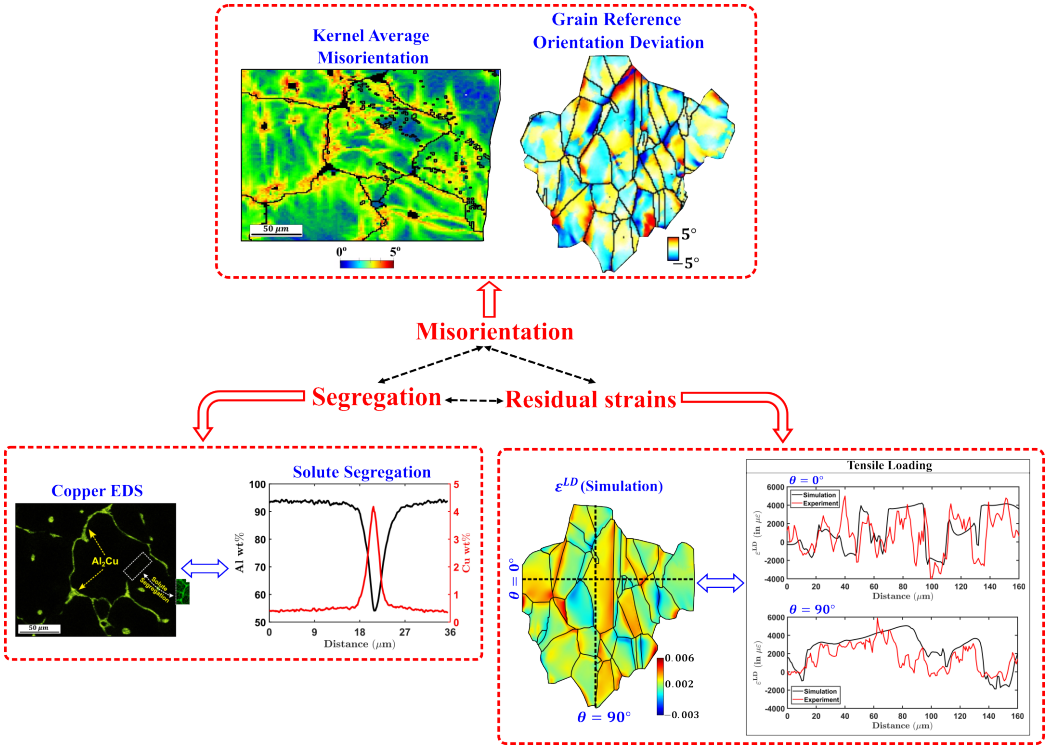

FIGURE 1.1: Schematic showing the inter-relationships between misorientation, solute segregation and residual strains, which influence heterogeneous plastic deformation in structural metals and alloys.

the misorientations, GND densities, solute segregation and residual strains. Novel modeling and experimental techniques have been developed and used to this end. Specifically, strain gradient crystal plasticity models have been developed to account for GNDs and their effect on deformation. Further, phase field models, coupled with strain gradient plasticity models, have been developed to simulate the microstructure evolution during solidification. The residual strains during processing and deformation have been predicted and compared with their experimental counterparts. Experimentally, the microstructures have been quantified using various diffraction-based techniques, such as High Resolution-Electron Backscattered Diffraction (HR-EBSD), High Resolution-Transmission Kikuchi Diffraction (HR-TKD), X-Ray Diffraction (XRD) and Precession Electron Diffraction (PED) within Transmission Electron Microscopy (TEM) to measure the misorientation and residual strain developments during processing and deformation. Further, solute segregation in the microstructure has been measured using Energy Dispersive X-ray Spectroscopy (EDS). Model predictions have been studied together with the experimental observations and measurements to identify the microstructural factors contributing to heterogeneous plastic deformation.

1.2 Thesis Outline

The following chapters of this thesis have studied these phenomena for different materials systems and applications. A literature review of the associated phenomena, as well as the modeling and experimental techniques used for quantifying them is first presented in Chapter 2. A summary of the gaps in the literature is presented, along with the objectives of the present thesis to address these gaps.

Following this, Chapter 3 deals with quantifying the plastic strain gradients developed in the vicinity of grain boundaries in deformed microstructures of a solid solution strengthened Aluminum-Magnesium (Al-Mg) alloy. These plastic strain gradients manifest in terms of the development of GNDs and misorientation gradients near grain boundaries, which are called as Near Boundary Gradient Zones (NBGZs). A Strain Gradient Crystal Plasticity (SGCP) framework has been developed to study the development of NBGZs. Model predictions have been compared with EBSD measurements of the Kernel Average Misorientation (KAM), with the objective of quantifying the length scale associated with the NBGZs.

Chapter 4 further extends these observations to study the NBGZ development in a precipitation strengthened Aluminum-Copper (Al-Cu) alloy. Since a majority of the aluminum alloys employed in the aerospace and automobile sectors manifest a significant volume fraction of precipitates embedded within the microstructure, it is crucial to quantify the heterogeneities developing in such alloys and subsequently reverse engineer appropriate heat treatments to avoid in-service failure of the components. In particular, this Chapter focuses on the role of local crystallographic orientation in influencing the orientation and misorientation gradients developing in the vicinity of precipitate and solute decorated grain boundaries and compares it to their (non-decorated) counterparts in Chapter 3.

Following this, Chapter 5 of the thesis examines the thermal distortion induced strain gradients and their subsequent effects on the underlying microstructure, mainly observed in rapidly solidified materials. Due to the enormous thermal gradients (and hence, cooling rates) imposed during rapid solidification, the GNDs entrapped within the chemical/dislocation cell walls and the inter-dendritic regions play a crucial role in maintaining the local lattice compatibility. The backstress arising as a result of these GNDs is primarily responsible for the ensuing anisotropy in the mechanical and microstructural properties. Chapter 5 proposes a combined Phase Field-Strain Gradient Plasticity (PF-SGP) framework, that not only allows us to predict in-hand the values of these microstructural parameters but also the governing physics occurring at these micro-scales, which are often neglected in the experiments. This framework is then employed to predict the dislocation substructure evolution and ensuing Tension-Compression (TC) asymmetry in a rapidly solidified Fe-Cr alloy.

To physically validate the residual strain predictions, it is essential to employ various experimental residual strain measurement techniques, ranging from the XRD-based single crystal micro-Laue to the newly developed TEM-PED technique. A key challenge to any such residual strain measurements is the variation in their relative magnitudes, since each method subtends a different interaction volume and relies on different algorithms. More importantly, they are sensitive to two different aspects of lattice distortion, $(\Delta\theta/\theta)$ for HR-EBSD and HR-TKD versus $(\Delta d/d)$ for micro-Laue and TEM-PED. Two questions naturally emerge: (i) are these strain measurements numerically similar and (ii) if not, is there a relationship between them. Addressing these and a general comparison of the techniques for an Interstitial Free (IF) steel were the motivations behind the Chapter 6 of the thesis.

Further, Chapter 7 studies the evolution of the anisotropic bulk lattice strains ($(\Delta d/d)$-sensitive) and the local residual strains ($(\Delta\theta/\theta)$-sensitive) using combined experimental and crystal plasticity approach, during tensile and cyclic deformation of an austenitic stainless steel. Here, the residual strain developments for various grain families have been explored, specifically in terms of their correlation with the underlying microstructure, studied using crystallographic orientation, misorientation, dislocation density and backstress evolution. Finally, the Chapter emphasizes on the factors contributing to the observed hierarchy in the bulk lattice strains for various grain families.

In summary, synergistic modeling and experiments have been used in this thesis to study the inter-relationships between the various internal and external factors contributing to the heterogeneities in the microstructure evolution across different length scales during plastic deformation. In order to highlight the effect of these factors, different material systems have been studied in different chapters, such that the contribution of one factor may dominate over the other for a given material system and application.

Chapter 2

Background

As discussed in Chapter 1, the primary objective of this thesis is to study the inter-relationships between misorientations, solute segregation and residual strains in deformed microstructures. In this regard, a detailed summary of the existing approaches, from an experimental as well as a modeling perspective, has been discussed in the present Chapter. In parallel, each Chapter of the thesis (Chapters 3-7) presents a thorough review of the literature on the topics of interest as well.

2.1 Crystallographic Orientation and Misorientation

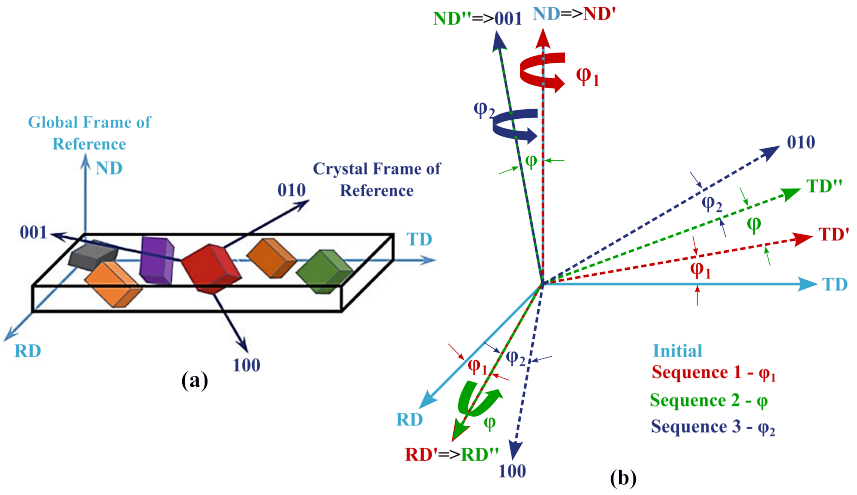

FIGURE 2.1: (a) Schematic denoting the global and crystal frame of reference. (b) Rotation operations involved while transforming the global reference to the crystal reference frame using Euler angles ϕ_1,ϕ,ϕ_2 (Bunge (2013) notation). Adapted from Rout et al. (2015).

The term crystallographic orientation refers to how a unit crystal is oriented with respect to a fixed global or laboratory frame of reference (Kocks et al., 1998; Randle and Engler, 2000). Generally speaking, the global frame of reference is represented in terms of the Rolling (RD), Transverse (TD) and Normal (ND) directions of the specimen, whereas the crystal reference frame is represented using the [100], [010] and [001] directions of a cubic unit cell (cf. Figure 2.1(a)). Mathematically, this can be quantified using the orientation tensor, $\boldsymbol{g}$, which constitutes of a series of rotation operations transforming the laboratory axes to the crystal axes. While a range of methodologies exists in the literature for defining $\boldsymbol{g}$ (Kocks et al., 1998; Randle and Engler, 2000; Verlinden et al., 2007; Bunge, 2013), the present study employs the Euler angle definition formulated by Bunge. This approach provides three rotation operations: ϕ_1 about the ND ($\boldsymbol{g_{\phi_1}}$), followed by ϕ about the new RD ($\boldsymbol{g_{\phi}}$), and a final rotation of ϕ_2 about the new ND ($\boldsymbol{g_{\phi_2}}$) (cf. Figure 2.1(b)). The resulting orientation tensor $\boldsymbol{g}$ can then be given by Randle and Engler (2000):

$$\boldsymbol{g} = \boldsymbol{g_{\phi_1}} \cdot \boldsymbol{g_{\phi}} \cdot \boldsymbol{g_{\phi_2}} \tag{2.1}$$

$$\boldsymbol{g} = \begin{bmatrix} \cos\phi_1 \cos\phi_2 - \sin\phi_1 \sin\phi_2 \cos\phi & \sin\phi_1 \cos\phi_2 + \cos\phi_1 \sin\phi_2 \cos\phi & \sin\phi_2 \sin\phi \\ -\cos\phi_1 \sin\phi_2 - \sin\phi_1 \cos\phi_2 \cos\phi & -\sin\phi_1 \sin\phi_2 + \cos\phi_1 \cos\phi_2 \cos\phi & \cos\phi_2 \sin\phi \\ \sin\phi_1 \sin\phi & -\cos\phi_1 \sin\phi & \cos\phi \end{bmatrix} \tag{2.2}$$

where ϕ_1, ϕ and ϕ_2 can be experimentally acquired using techniques such as Electron Backscatter Diffraction (EBSD) or Transmission Electron Microscopy based Precession Electron Diffraction (TEM-PED). Finally, based on the crystal symmetry, the Euler angles involved in the transformation from the global to the crystal frame of reference may not be unique and various combinations of Euler angles may be valid to achieve the same transformation.

By definition, all material points lying within a grain (crystal) should manifest the same orientation. However, the presence of local heterogeneities, dislocation substructures and anisotropic residual strains arising during solidification and subsequent thermomechanical processing result in perturbations/gradients in the orientation. Mathematically, these perturbations, often referred to as misorientation, between two material points A and B with orientation tensors $\boldsymbol{g_A}$ and $\boldsymbol{g_B}$ can be defined as:

$$\boldsymbol{\Delta g_{AB}} = \boldsymbol{g_B} \cdot \boldsymbol{g_A^{-1}} \tag{2.3}$$

The resulting misorientation angle can then be derived as: $\cos\Delta\theta = \frac{1}{2}\left(\Delta g_{AB}^{11} + \Delta g_{AB}^{22} + \Delta g_{AB}^{33} - 1\right)$ (Randle and Engler, 2000). For a uniformly spaced three-dimensional grid, the resulting misorientation vector at any material point can be given by $\boldsymbol{\Delta\theta} = [\Delta\theta_x \ \Delta\theta_y \ \Delta\theta_z]$, where $\Delta\theta_x$, $\Delta\theta_y$ and $\Delta\theta_z$ refer to the misorientation angles between its immediate neighbors along the x, y and z directions (Kocks et al., 1998; Wright et al., 2011). Generally speaking, a grain is considered to be constituted of all material points manifesting a misorientation $\leq 5°$ with their immediate neighbors (Thool et al., 2020). Note that the term 'misorientation' refers to the crystallographic mismatch between any two material points, whereas the term 'disorientation' denotes the minimum rotation angle (about an axis) required to align their crystal axes, while accounting for the symmetry of the crystal (Krakow et al., 2017).

As will be seen in the subsequent Chapters, various types of misorientation measures exist in the literature to quantify the orientation gradients developing in a material (Wright et al., 2011, 2016; Thool et al., 2020). Broadly, these are divided into two categories; the kernel based, which define the local pixel-by-pixel misorientation and the grain based, which quantify the average misorientation between all material points lying within the grain. The reader is referred to Chapter 3 for further detailed reading on this topic.

The subsequent sections focus on correlating the above-mentioned misorientation vector with various physical aspects of the deformed microstructure.

2.1.1 Geometrically Necessary Dislocations (GNDs)

According to Ashby (1970)'s classification, two types of dislocations exist in a material, namely, the Statistically Stored Dislocations (SSDs) and Geometrically Necessary Dislocations (GNDs). While the SSDs are generated to accommodate the plastic deformation processes via dislocation bowing, trapping and multiplication at junctions, the GNDs are essential to accommodate the lattice incompatibilities and strain gradients arising during heterogeneous deformation (Ashby, 1970; Arsenlis, 2001). Ashby (1970) suggested that both types of dislocations would act as forest obstacles during deformation, leading to enhanced strengthening in the material. Parallelly, some researchers have employed the analogy of charged particles, to signify that similar to repulsion between the like charges, a repulsive stress exists between the GNDs (Arsenlis, 2001; Evers et al., 2004a,b). This is primarily due to their identical Burgers vector and line tangent direction.

Based on Ashby (1970)'s theory, the GNDs are expected to form near regions of localized heterogeneous deformation. For example, regions in the vicinity of grain boundaries have to accommodate additional constraints imposed by their neighbors, thus impeding their free

deformation (Mishra et al., 2009; Tóth et al., 2010). The core-mantle analogy of a grain also points out that such regions develop large orientation or plastic strain gradients during mechanical deformation (Tóth et al., 2010). A significant work has thus been carried out, experimentally (Sun et al., 2000; Pantleon, 2008; Jiang et al., 2013a; Birosca et al., 2019; Hansen et al., 2020) along with the development of modeling frameworks (Evers et al., 2004b; Hansen et al., 2020; Zhang et al., 2023), to study the GND density accumulations in such regions. Further, Hansen et al. (2020) have also used the sign of the individual Nye tensor components, to examine the clustering of similarly-signed GNDs in these regions.

Another class of microstructures showing such deformation characteristics are those of rapidly solidified/Additively Manufactured (AM) materials. The large thermal gradients and cooling rates in AM necessitates the presence of GNDs to accommodate the thermal distortion induced lattice incompatibilities, especially in the vicinity of inter-dendritic boundaries and cell walls (Bertsch et al., 2020; Small et al., 2020; Small and Taheri, 2021; Voisin et al., 2021). The directional backstresses arising due to these GNDs have often been attributed to the anisotropy in their post-solidification mechanical properties (Chen et al., 2019; Liu et al., 2020a; Wang et al., 2023).

GNDs were first related to the presence of lattice curvatures in the material by Nye (1953). The lattice-geometric consequences due to a flux of GNDs results in a closure mismatch (B_i) in a Burgers circuit, and is given by (Nye, 1953):

$$B_i = \Lambda_{ij} l_j \tag{2.4}$$

where Λ_{ij} is the Nye tensor and l_j is the tangent line direction. Physically, Equation 2.4 provides an estimate of those dislocations whose geometric consequences were not annihilated by the remaining dislocations lying within the Burgers circuit. In other words, these dislocations are essential to accommodate the discontinuities in the crystalline lattice.

The Nye tensor can be related to the lattice curvature, $\boldsymbol{\kappa}$, as follows (Nye, 1953; Arsenlis, 2001),

$$\Lambda_{ij} = \kappa_{ji} - \delta_{ij}\kappa_{kk} \tag{2.5}$$

where, $\boldsymbol{\delta}$ is the second rank identity tensor. Note that the above formulation proposed by Nye (1953) does not account for the contribution of the elastic strain gradients. Further, the curvature tensor, which is defined as the gradient of the misorientation vector can be written as follows (Pantleon, 2008),

$$\kappa_{ik} = \frac{\Delta\theta_i}{\Delta x_k} \tag{2.6}$$

where, $\Delta\theta_i$ and Δx_k represent the misorientation (cf. Section 2.1) and spatial increment between the material points along directions $\boldsymbol{i}$ and $\boldsymbol{k}$, respectively (see Figure 2.2(a)). Thus, any technique that provides a spatially resolved grid of crystallographic orientations may be utilized to estimate the misorientation vector, $\boldsymbol{\Delta\theta}$, and hence lattice curvatures, $\boldsymbol{\kappa}$, and the Nye tensor, $\boldsymbol{\Lambda}$, for example, EBSD or TEM-PED.

Using the Nye tensor, the bulk GND density can hence be estimated as (Ruggles and Fullwood, 2013):

$$\rho_{GND} = \frac{1}{b} ||\boldsymbol{\Lambda}||_1 \tag{2.7}$$

where, $||\boldsymbol{\Lambda}||_1$ denotes the entrywise one norm of the Nye tensor (Ruggles and Fullwood, 2013). Note that other forms of equation 2.7, which employ the L_2 norm of $\boldsymbol{\Lambda}$, or scalar pre-factors may also be employed (Ruggles and Fullwood, 2013; Ruggles et al., 2016).

While Equation 2.7 provides an estimation of the bulk/total GND density, the slip system level GND densities can be determined based on the formulations provided by Nye (1953), Kröner (1962), Dai (1997), Arsenlis (2001) as follows,

$$\boldsymbol{\Lambda} = \sum_{\xi=1}^{18} \rho_{GND}^{\xi} b^{\xi} \boldsymbol{m_0^{\xi}} \otimes \boldsymbol{t_0^{\xi}} \tag{2.8}$$

where, b is the Burgers vector and $\boldsymbol{m_0}$ and $\boldsymbol{t_0}$ represent the unit vectors along the dislocation slip and line tangent direction, in the intermediate (or reference) configuration. The unit vector along the line tangent direction is given by $\boldsymbol{t_0} = \boldsymbol{n_0} \times \boldsymbol{m_0}$, where $\boldsymbol{n_0}$ represents the unit vector along the slip plane normal. ξ denotes the index (or type) of dislocation, the maximum value for which, in a Face Centered Cubic (FCC) crystal would be 18 (assuming 12 edge and 6 screw dislocations).

Based on the crystal structure and active GND configurations within a material, Equation 2.8 can be inverted to estimate the slip system level GND densities. However, the imposed plastic strain gradients can be accommodated by multiple varying GND configurations, especially in a crystal with high degrees of symmetry (for example, cubic systems). This leads to non-unique solutions (Arsenlis, 2001; Dunne et al., 2012) of Equation 2.8. As can be seen, the Nye tensor has nine independent components, whereas there are eighteen

distinct types of GND densities (cf. Equation 2.8). Hence additional constraints have to be imposed, in order to obtain the GND density, for example, minimizing the dislocation line length or minimizing the total energy due to the dislocations (Dunne et al., 2012). Additionally, different algorithms such as L_2 or L_1 optimization, least squares method, etc. can also be employed (Arsenlis, 2001; Kysar et al., 2007, 2010; Das et al., 2018). The choice of the algorithm has to be governed by the accuracy and the computation time required for an approach. One such algorithm routinely used for estimated GND densities is given by Arsenlis (2001), Das et al. (2018):

$$\boldsymbol{\rho}_{GND} = \left(\boldsymbol{A^T} \cdot \boldsymbol{A}\right)^{-1} \cdot \boldsymbol{A}^T \cdot \boldsymbol{\Lambda} \tag{2.9}$$

where, $\boldsymbol{A} = \sum b^{\xi} \boldsymbol{m_0^{\xi}} \otimes \boldsymbol{t_0^{\xi}}$ (cf. Equation 2.8). Equation 2.9 is known as the matrix inversion technique, which is derived by simple matrix manipulations (Arsenlis, 2001; Dunne et al., 2012; Das et al., 2018). We refer the reader to Chapter 3 for further details on alternate approaches such as the least squares, L_2 and L_1 optimization methods.

Experimentally, estimating the GND densities using Electron Backscatter Diffraction (EBSD) data has frequently been employed to study the local heterogeneities developing during deformation (Sun et al., 2000; Pantleon, 2008; Ruggles and Fullwood, 2013; Ruggles et al., 2016; Small et al., 2020), especially when the microstructure is subjected to cyclic loading (Jiang et al., 2015). However, an important drawback of this formulation is the absence of spatial derivatives along the z direction, since EBSD data is restricted to only two dimensions (plane stress approximation) (Fullwood et al., 2015; Pai et al., 2024a). Three dimensional EBSD data can be acquired by using the non-trivial serial sectioning technique (Saylor et al., 2004)/Focused Ion Beam (FIB) milling (Calcagnotto et al., 2010). However, such approaches are beyond the scope of the thesis. Owing to this drawback, only five out of the nine independent components of the Nye tensor can be obtained using EBSD. These are given by Pantleon (2008),

$$\Lambda_{12} = \kappa_{21};\ \Lambda_{13} = \kappa_{31};\ \Lambda_{21} = \kappa_{12};\ \Lambda_{23} = \kappa_{32};\ \Lambda_{33} = -\kappa_{11} - \kappa_{22} \tag{2.10}$$

The resulting bulk GND densities can be estimated using the formulation provided in Equation 2.8. Since a complete description of Nye tensor is absent in Equation 2.10, the resulting GND density magnitudes are referred to as lower bound estimates. Nevertheless, these lower bound ρ_{GND} can still reveal significant information about the GND density localizations near the grain and the phase boundaries (Kundu and Field, 2016, 2020; Hansen et al., 2020). As stated previously in Equation 2.9, to resolve the experimental GND densities onto the

individual slip systems, different optimization algorithms have been used in the literature (Kysar et al., 2007, 2010; Dunne et al., 2012). In either case, the obtained GND density will be a lower bound estimate of the actual GNDs present in the material.

Alternatively, some studies have proposed a rather simpler methodology to estimate the GND densities, using the pixel-by-pixel misorientation acquired from EBSD data (Calcagnotto et al., 2010). GND density in such formulations is given as: $\rho_{GND} = \frac{2\Delta\theta}{ub}$, where $\Delta\theta$ is the misorientation angle and u and b correspond to the unit length and the Burgers vector magnitude, respectively (Calcagnotto et al., 2010). Quantitatively, their estimates have proven to be nearly identical to those derived using Equations 2.7-2.9 (Calcagnotto et al., 2010).

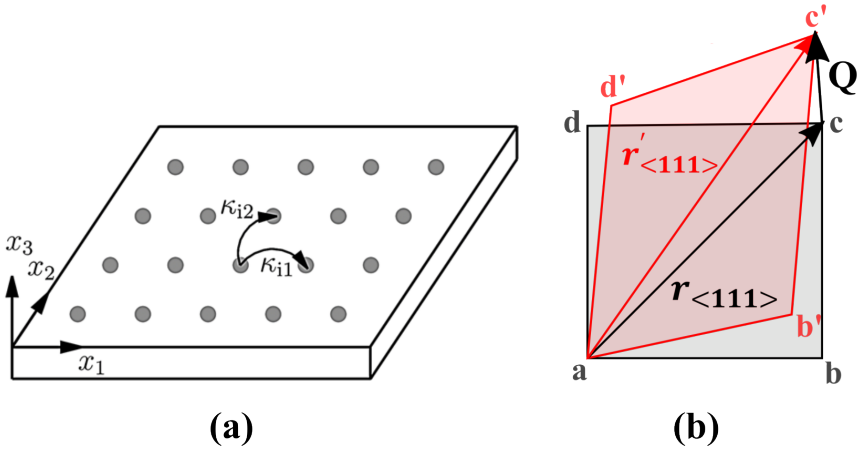

FIGURE 2.2: (a) Curvature κ calculation from EBSD data and (b) Shift in zone axes position due to lattice distortion and rigid body rotation. Adapted from Pantleon (2008) and Wilkinson et al. (2009)/Kumar et al. (2025).

The other approach for estimation of GND density is using the cross-correlation techniques (Wilkinson et al., 2006, 2009; Britton and Wilkinson, 2011; Ruggles and Fullwood, 2013; Fullwood et al., 2015; Ruggles et al., 2016). This formulation uses the shifts in the zone axes positions to get an estimate of the lattice distortion gradient tensor, which is used to obtain the elastic deformation gradient tensor and ultimately the Nye tensor for the GND density calculations. Consider an undistorted reference crystal in an initial strain free-sample, as shown in Figure 2.2(b), with a direction vector $\boldsymbol{r}$. On deforming the material, the crystal experiences a lattice distortion and rigid body rotation, modifying the direction vector $\boldsymbol{r}$ to $\boldsymbol{r'}$. Using the distortion gradient tensor $\boldsymbol{A}$, we can write,

$$\boldsymbol{r'} = \boldsymbol{A} \cdot \boldsymbol{r}; \boldsymbol{A} = \frac{\partial u_i}{\partial x_j} \tag{2.11}$$

The resulting displacement due to the strain and rigid body rotation $\boldsymbol{Q}$, can be related to $\boldsymbol{A}$ by:

$$\boldsymbol{Q} = \boldsymbol{r}' - \boldsymbol{r} = (\boldsymbol{A} - \boldsymbol{\delta}) \cdot \boldsymbol{r} \tag{2.12}$$

EBSD techniques only measure the distance $\boldsymbol{q}$, which is perpendicular to $\boldsymbol{r}$. Hence, using the reference of Figure 2.2(b) and basic vector calculus, we can write $\boldsymbol{q} = \boldsymbol{Q} - \lambda \boldsymbol{r}$, where λ is a scalar (Wilkinson et al., 2009). Further re-arranging the above equation:

$$\boldsymbol{q} = (\boldsymbol{A} - (\lambda + 1)\boldsymbol{\delta}) \cdot \boldsymbol{r} \tag{2.13}$$

The above expression results in 3 equations and 10 unknowns (nine components of the tensor $\boldsymbol{A}$ and λ). On elimination of the constant λ, we now have 2 equations and 8 unknowns, which can be written as (Wilkinson et al., 2009),

$$\begin{aligned} r_2 r_3 \left[\frac{\partial u_2}{\partial x_2} - \frac{\partial u_3}{\partial x_3}\right] + r_1 r_3 \left[\frac{\partial u_2}{\partial x_1}\right] + r_3^2 \left[\frac{\partial u_2}{\partial x_3}\right] - r_1 r_2 \left[\frac{\partial u_3}{\partial x_1}\right] - r_2^2 \left[\frac{\partial u_3}{\partial x_2}\right] = r_3 q_2 - r_2 q_3 \\ r_1 r_3 \left[\frac{\partial u_1}{\partial x_1} - \frac{\partial u_3}{\partial x_3}\right] + r_2 r_3 \left[\frac{\partial u_1}{\partial x_2}\right] + r_3^2 \left[\frac{\partial u_1}{\partial x_3}\right] - r_1^2 \left[\frac{\partial u_3}{\partial x_1}\right] - r_2 r_1 \left[\frac{\partial u_3}{\partial x_2}\right] = r_3 q_1 - r_1 q_3 \end{aligned} \tag{2.14}$$

Hence, to solve the above expression, $\boldsymbol{q}$ has to be measured at four widely spaced zone axes directions. However, additional measurements of $\boldsymbol{q}$ still cannot separate: $\frac{\partial u_1}{\partial x_1}$, $\frac{\partial u_2}{\partial x_2}$, $\frac{\partial u_3}{\partial x_3}$. To resolve these terms, which are related to the hydrostatic dilation, a plane stress assumption has to be employed (Wilkinson et al., 2009). Since the ESBD measurements come from a region $\leq 30\ nm$ from the sample surface, this assumption does hold to be valid. Combining the plane stress assumption with the Hooke's law, we can now separate the three terms, thus allowing us determination of the complete lattice distortion tensor (Fullwood, 2020). This is then used to calculate the elastic deformation gradient tensor ($\boldsymbol{F}^e$), and finally the Nye tensor using:

$$\boldsymbol{\Lambda} = (\boldsymbol{\nabla} \times \boldsymbol{F}^e) \tag{2.15}$$

The resulting GND density (bulk as well as slip system level) can be estimated using Equations 2.7-2.9, respectively.

These formulations, along with Equations 2.11-2.15, shall again be revisited in Chapter 6. Note that variations in the EBSD-based data acquisition parameters (for example, detector

binning and step size) can alter the estimated GND density magnitudes (Jiang et al., 2013b; Ruggles et al., 2016). These parameters should hence be optimized before-hand, in order to derive reliable GND density estimates. In addition, this formulation (Equation 2.11-2.14) can also be employed to determine the residual strains in the material (see Small et al. (2020); Small and Taheri (2021); Manda et al. (2024) and Chapter 6). Finally, we do note that more sophisticated techniques for quantifying the GND densities, such as the Integrated-DIC (I-DIC) EBSD exist (Zhong et al., 2024). However, they are beyond the scope of the present study.

From a mesoscale modeling perspective, the GND densities can be quantified using the Strain Gradient Crystal Plasticity (SGCP) type of formulations (Arsenlis, 2001; Evers et al., 2004a; Bayley et al., 2006; Geers et al., 2006a). These are often referred to as non-local frameworks, since they account for the deformation behavior of neighboring material points within their constitutive equations. The mathematical formulations employed in SGCP to quantify ρ_{GND} are identical to those described previously in Equations 2.7-2.9, the only key difference being that the Nye tensor is now derived using a much more precise/complete formulation based on the curvature of the plastic deformation gradient tensor as follows (Dai, 1997; Arsenlis, 2001):

$$\Lambda_{ij} = -\left(\boldsymbol{\nabla} \times \boldsymbol{F}^{pT}\right)^{T} = -e_{jlk} F^{p}_{ik,l} \tag{2.16}$$

where, F^{p}_{ik} and e_{jlk} denote the plastic deformation gradient tensor and the permutation tensor. The reader is further referred to Chapter 3 (Section 3.2.3) for a detailed mathematical description of the SGCP formulation used in the thesis.

2.1.2 Backstresses

As discussed previously in Section 2.1.1, GNDs constitute of like-signed dislocations that accommodate the discontinuities in the crystalline lattice (Arsenlis, 2001). These are typically observed near regions manifesting localized heterogeneous deformation, for example, grain boundaries, second-phase precipitates, etc. A pile-up of GNDs hence results in a long-range repulsive stress, also referred to as backstress, which resists the applied deformation, thereby raising the strength of the material. Some physical evidences of such a phenomenon are the Hall-Petch effect (Hall, 1951), bending of beams (Stölken and Evans, 1998) and torsion of thin wires (Fleck et al., 1994; Gan et al., 2014).

In terms of constitutive models for plastic deformation, these backstresses result in kinematic hardening, i.e., a translation of the yield surface in the stress space without altering its

size/shape during the operation (Khan and Huang, 1995). Mathematically, this can be written as:

$$f(\boldsymbol{\sigma} - \boldsymbol{\chi}) - s_a = 0 \tag{2.17}$$

where, $\boldsymbol{\chi}$ and s_a account for the kinematic and isotropic hardening of the yield surface $f(\boldsymbol{\sigma})$. Various empirical, phenomenological and physically-based formulations have been described in the literature to accurately predict the directional backstresses developing in a material. Note that while the GND density predictions are limited to non-local formulations which account for gradients in the plastic strains (Arsenlis, 2001), kinematic hardening has been implemented within local (empirical and phenomenologically-based laws) as well as non-local (physically-based laws) plasticity frameworks.

To begin with, Prager (1955) proposed a linear empirical relationship between the backstress ($\boldsymbol{\chi}$) and plastic strain increment given by:

$$d\boldsymbol{\chi} = C d\boldsymbol{\varepsilon^p} \tag{2.18}$$

where C is a material constant. In order to mitigate the drawbacks associated with this formulation (i.e., transverse softening during tensile loading (Khan and Huang, 1995)), Ziegler (1959) proposed the following formulation: $d\boldsymbol{\chi} = (\boldsymbol{\sigma} - \boldsymbol{\chi})d\mu$, where $d\mu$ represents the scalar proportionality constant. Further, Armstrong et al. (1966) proposed a non-linear (single component) phenomenologically-based backstress formulation, given by:

$$d\boldsymbol{\chi} = C d\boldsymbol{\varepsilon^p} - \gamma \boldsymbol{\chi} \left| d\boldsymbol{\varepsilon^p} \right| \tag{2.19}$$

where, $d\boldsymbol{\varepsilon^p}$ denotes plastic strain increment and C and γ are material parameters obtained by calibrating the experimental mechanical response with simulated predictions. As can be seen, the first term on the RHS accounts for the initial linear increment in $\boldsymbol{\chi}$, while the second term captures the non-linear saturation behavior (Armstrong et al., 1966).

An important extension to this formulation was proposed by Chaboche and Nouailhas (1989), to account for multiple backstress components, thus improving the model predictions of (anisotropic) cyclic plasticity and multiaxial loading. They (Chaboche and Nouailhas, 1989) represented the backstress as a superposition of multiple backstress components, i.e.,

$$d\boldsymbol{\chi} = \sum_{i=1}^{n} d\boldsymbol{\chi}_i \tag{2.20}$$

where, n represents the total number of backstress components, with each component denoted by the index i. The definition of each of the components, $d\boldsymbol{\chi}_i$, is given by Equation 2.19. Various other formulations for incorporating kinematic hardening within plasticity frameworks have been proposed in the literature, for example, the Ohno and Wang (1993) model or the Burlet-Cailletaud (Burlet and Cailletaud, 1987; Taleb et al., 2006) model.

While Equations 2.17-2.20 described the backstress developments using a continuum tensor representation, these can also be employed to predict the slip system level backstresses, i.e., these formulations can be implemented within a macro-plasticity or a crystal plasticity framework, with the only difference being that the latter predicts the backstress increments at a slip system level, thus accounting for orientation-based anisotropy, whereas the former would estimate an effective backstress. Further, many recent studies have employed non-local crystal plasticity formulations to predict the slip system level plastic strain gradients and GND densities, followed by using physically-based scalar backstress formulations to examine the local heterogeneities developing during deformation (Evers et al., 2004a,b; Bayley et al., 2006; Geers et al., 2006a). A key advantage of these models is that they explicitly account for the underlying substructure, for example, ρ_{GND}, $\boldsymbol{\kappa}$, while estimating the backstress evolution. These formulations are broadly classified into two categories. The lower order models, where non-locality is accounted for using constitutive equations such as the Taylor hardening-based formulations (Kapoor et al., 2018), exhibit a direct relationship between the χ and the ρ_{GND}. For a given slip system α, these kinematic hardening models can be written as: $\chi^{\alpha} \propto Gb^{\alpha}\sqrt{\rho^{\alpha}_{GND}}$, where G and b denote the shear modulus and the Burgers vector, respectively.

On the other hand, the higher order models formulate the χ as a function of the spatial gradient of ρ_{GND}, i.e., $\chi \propto f\left(\boldsymbol{\nabla}\rho_{GND}\right) \propto f\left(\nabla^2\varepsilon^p\right)$. These models imply that any spatial reordering of GNDs into special (low energy) configurations, for example, polygonization during recovery, should not lead to a backstress field. Mathematically, this class of physically-based kinematic hardening models can be given by:

$$\chi^{\alpha} \propto \frac{Gb^{\alpha}R^2}{2\pi(1-v)}\left(\boldsymbol{\nabla}\rho^{\alpha}_{GND}\cdot\boldsymbol{m}^{\alpha}_0\right) \tag{2.21}$$

where, ν denotes the Poisson's ratio. This formulation incorporates the long-range internal stresses due to GND distribution within a domain of interest of radius R. Since these models

depend upon higher order gradients of plastic strain, these are computationally expensive over other lower-order formulations. As with other kinematic hardening models, these can be implemented within a macro as well as a crystal plasticity framework.

Note that Equation 2.21 assumes the backstress due to dislocation fields on a slip system α will only affect the shearing rate on that specific slip system, referred to as self-backstress by Bayley et al. (2006). Further modifications to Equation 2.21 have also been proposed, for example, the full internal stress model proposed by Bayley et al. (2006), which accounts for the drawbacks associated with self-backstress based models. We also refer the reader to Brahme et al. (2011); Zecevic and Knezevic (2015); Castelluccio and McDowell (2017); Zirkle et al. (2021); Agius et al. (2022); Zhang et al. (2023) for further reading on the various physically-based backstress formulations implemented within the plasticity frameworks.

Finally, the ρ_{GND}, the plastic strain gradients and the lattice curvatures are a direct outcome of the local heterogeneities developing in a crystalline lattice, whereas the backstress is derived using various (proposed) mathematical formulations within the plasticity frameworks. Hence, backstresses cannot be measured explicitly from any experimental characterization techniques, although, their effects can be quantified to a sufficient extent from the anisotropy in the material behavior (for example, from the hysteresis loop during cyclic loading).

2.2 Residual Strains and their Quantification

The GND densities, essential to accommodate the local heterogeneities, result in localized stress fields in a material which may not get fully relaxed upon unloading (Erinosho and Dunne, 2016). The resulting self-equilibrating (elastic) strains retained in a material after the removal of external loads are termed as residual strains (Verlinden et al., 2007; Noyan and Cohen, 2013). These are often a byproduct of the non-uniform elastic-plastic strain gradients developing in a material during deformation (Manda et al., 2024). At an atomic level, residual strains denote the distortion of the crystalline lattice, whose non-equilibrium structure is retained by the defects (Verlinden et al., 2007). Similar to GNDs, the residual strains are indicative of incompatible deformation arising due to external (deformation) or internal (thermal strains) causes and serve as potential indicators of damage nucleation (Sudhalkar et al., 2024). These are particularly important in rapidly solidified/AM microstructures which often manifest dislocation substructures primarily composed of GNDs (Bertsch et al., 2020; Voisin et al., 2021). The resulting "unrelaxed residual stresses" have been attributed as a root cause for their anisotropic post-solidification mechanical properties (Chen et al., 2019).

More recently, the use of in-situ deformation setups have provided significant information on the heterogeneous distribution of stresses and strains during loading (Neil et al., 2010; Kanjarla et al., 2012; Upadhyay et al., 2019). Examining the evolution of residual strains in such setups have allowed for a detailed understanding on the role of thermal, elastic and plastic anisotropy during thermomechanical processing (Verlinden et al., 2007; Brown et al., 2017; Pokharel et al., 2019). Finally, these have also been correlated with the evolution of local substructure and specimen failure (Wang et al., 2003; Zheng et al., 2013). It is therefore crucial to quantify and examine the development of residual strains in a material.

2.2.1 Classification of Residual Strains

Based on the length scales over which residual strains/stresses self-equilibrate, they are divided into three distinct categories (Verlinden et al., 2007; Lodh et al., 2017, 2018; Zhang et al., 2022) (see Figure 2.3).

- Bulk or macroscopic (type-I): These stresses often equilibrate over the scale of the entire component.
- Intergranular (type-II): These equilibrate over the scale of a few grains.
- Local or intragranular (type-III): These stresses are primarily due to the individual stress fields of local defect structures, such as dislocations and point defects.

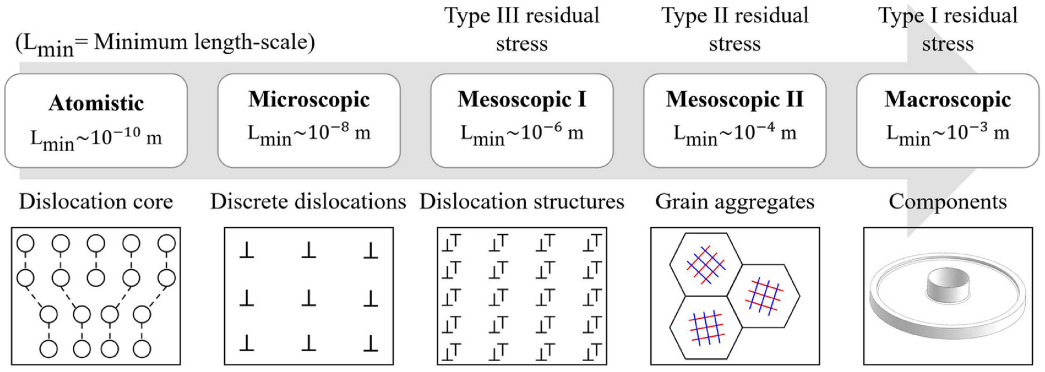

FIGURE 2.3: Classification of residual stresses based on the length scales at which they self-equilibrate. Adapted from Bandyopadhyay et al. (2024).

The subsequent sections discuss various residual strain measurement techniques, followed by a brief discussion on predicting their simulated counterparts.

2.2.2 Experimental Residual Strain Measurements

A range of experimental techniques, destructive and non-destructive, exist to measure the bulk residual strains. The hole drilling method is one such semi-destructive technique, which quantifies the near-surface (bulk) residual stresses in a material by employing strain gauges to analyze the strain relief in the vicinity of a drilled hole (Valentini et al., 2019; Olson et al., 2021). These are often used to provide estimates up to depths of a few millimeters. More recently, the non-destructive ultrasonic methods, which measure changes in the ultrasonic wave velocity and compare it to those for a stress-free material have been employed to measure the bulk residual stresses in the aerospace and automotive sector (Acevedo et al., 2020; Liu et al., 2021). Of interest to the present study are the non-destructive techniques of X-ray/neutron diffraction, which have frequently been used to characterize the bulk residual strain evolution during thermomechanical processing of metallic materials (Cullity, 1956; Withers and Bhadeshia, 2001; Verlinden et al., 2007; Noyan and Cohen, 2013). The large penetration depth subtended by these techniques ensures an aggregate data over numerous grains in the material (Randle and Engler, 2000; Verlinden et al., 2007). In particular, the (hkl)-specific residual strains, or lattice strains, provide an understanding of the load bearing capacities and the deformation mechanisms active within various grain families, along with their influence on the local as well as aggregate properties during deformation (Korsunsky et al., 2002; Wang et al., 2003; Zheng et al., 2013).

The (hkl)-specific bulk residual strains (ε_{hkl}) using neutron diffraction are obtained by tracking the shift in peak positions for a given (hkl) family compared to its undeformed strain-free counterpart. Mathematically, this can be written as (Neil et al., 2010):

$$\varepsilon_{hkl} = \frac{d}{d_0} - 1 \tag{2.22}$$

where, d and d_0 denote the interplanar spacing (for a given (hkl) family) in the deformed and undeformed/strain-free specimens, respectively. The ε_{hkl} values parallel to the loading direction are termed as longitudinal lattice strains, whereas those perpendicular to the loading direction (in-plane) are termed as transverse lattice strains.

On the other hand, the (hkl)-specific bulk (biaxial) residual strains from X-ray Diffraction (XRD) are commonly quantified using the d-$sin^2\psi$ technique, the formulations for which have been provided below (Cullity, 1956; Verlinden et al., 2007; Lodh et al., 2022). To begin with, the reader should note that the angles ϕ and ψ refer to the in-plane rotation and out-of-plane tilt angles of the Eulerian cradle, respectively. Additionally, the subscripts 1, 2 and 3 denote the rolling/loading, transverse and surface normal directions, respectively. This technique measures the interplanar spacing $d_{\phi\psi}$ for multiple (ϕ, ψ) combinations. With

increasing ψ tilts, the corresponding shift obtained in the XRD peaks is directly proportional to the accumulated residual strains for a particular grain family (Cullity, 1956). The residual strains can be then be determined from the slope of the best-fit line (typically using least squares regression) between $d_{\phi\psi}$ versus $\sin^2\psi$ using the following formulation:

$$\begin{aligned}\frac{d_{\phi\psi}-d_0}{d_0} =& \frac{1+v}{\mathrm{E}}\left\{\sigma_{11}\cos^2\phi+\sigma_{12}\sin 2\phi+\sigma_{22}\sin^2\phi-\sigma_{33}\right\}\sin^2\psi+\frac{1+v}{\mathrm{E}}\sigma_{33} \\ &-\frac{v}{\mathrm{E}}\left(\sigma_{11}+\sigma_{22}+\sigma_{33}\right)+\frac{1+v}{\mathrm{E}}\left\{\sigma_{13}\cos\phi-\sigma_{23}\sin\phi\right\}\sin 2\psi\end{aligned} \tag{2.23}$$

Note that the residual stresses in Equation 2.23 can be interchanged with residual strains and vice-versa by using appropriate anisotropic X-ray Elastic Constants (XECs), i.e., the (directional) elastic modulus, E and the Poisson's ratio, ν (Van Houtte and De Buyser, 1993; Lodh et al., 2022). Further, the undeformed strain-free interplanar spacing d_0 can be approximated to be equivalent to $d_{\phi 0}$, since the (directional) elastic modulus, $E >> \sigma_{11}+\sigma_{22}$ (error$\leq 0.1\%$) (Prevéy, 1986). In cases where the out-of-plane shear stresses are zero, i.e., $\sigma_{13},\ \sigma_{23}=0$, the above equation would result in a straight line between $d_{\phi\psi}$ and $\sin^2\psi$. Non-zero magnitudes of $\sigma_{13},\ \sigma_{23}$ would otherwise result in ψ-splitting, as shown in Lodh et al. (2022). Assumption of biaxial plane stress condition further simplifies the Equation 2.23. In summary, Equation 2.23 determines the longitudinal and transverse components of ε_{hkl} by measuring the interplanar spacing $d_{\phi\psi}$ across multiple combinations of (ϕ,ψ). The conventions for longitudinal as well as transverse lattice strains are identical to those described for the neutron diffraction.

Further, differentiating the Bragg's law provides us with the following relationship: $-\Delta d/d_0 = \Delta\theta\cot\theta$, which indicates that a minor variation in the interplanar spacing (Δd) should result in a pronounced peak shift ($\Delta\theta$) at larger 2θ angles. Hence, the resolution of strains measured using the d-$sin^2\psi$ technique gets significantly improved at larger 2θ angles (Prevéy, 1986; Verlinden et al., 2007).

From an application standpoint, multiple studies have captured the elastic anisotropy, elastic-plastic transition, neighborhood interactions and subsequent load transfers/relaxations in the bulk lattice strains (Neil et al., 2010; Wang et al., 2013; Brown et al., 2017; Upadhyay et al., 2019) under varying imposed loading conditions. For example, Brown et al. (2017) noted a marked difference in the lattice strain developments, and hence load bearing capabilities, of the (200) family of grains during tensile and compressive loading of an Additively Manufactured (AM) SS 304L specimens. Further, Upadhyay et al. (2019) used in-situ neutron diffraction to understand the lattice strain evolution during biaxial load path change (LPC) experiments on SS 316L cruciform specimens. Neil et al. (2010), in their in situ neutron diffraction experiments on copper and stainless steel noted that the

transverse lattice strains (perpendicular to the loading direction) exhibited a large grain to grain scatter, as compared to the axial lattice strains due to a significant dispersion of the transverse scattering vector.

While the above studies focused on measuring the in-plane residual strains/stresses, out-of-plane residual stresses have also been estimated and correlated with the deformation behavior of materials (Kumar et al., 2016; Neog et al., 2024). For example, Neog et al. (2024) showed that the magnitude of out-of-plane normal stresses largely governed the fracture behavior of their as-deposited Thermal Barrier Coatings (TBCs). In summary, the determination of bulk residual strains, or (hkl)-specific residual strains have routinely been explored and correlated with various aspects of material deformation (Clausen et al., 1999; Wang et al., 2003; Kanjarla et al., 2012; Wang et al., 2013; Zheng et al., 2013; Thool et al., 2020; Manda et al., 2024).

Owing to their large interaction volumes, the X-ray/neutron based in situ diffraction experiments can measure the bulk residual strains (Verlinden et al., 2007). To further examine the microstructure evolution at a finer length-scale, alternative residual strain measurement techniques such as the High Energy X-ray Diffraction Microscopy (HEDM) (Kapoor and Sangid, 2018; Tayon et al., 2024), single crystal micro-Laue X-ray Diffraction (XRD) (Manda et al., 2024) and High Resolution Electron Backscattered Diffraction (HR-EBSD) (Wilkinson et al., 2006, 2009; Fullwood et al., 2015) have been designed. We refer the reader to Chapter 6 for a detailed mathematical description of the formulations involved in estimating the micro-Laue based (Section 6.3.1) and HR-EBSD based (Section 6.3.2) residual strains, which are of interest to the present study. For brevity, those formulations have not been placed here.

These techniques focus on measuring the spatially resolved intergranular, or type-II (HEDM, micro-Laue XRD) and intragranular, or type-III (HR-EBSD) residual strains in a material. For example, Tayon et al. (2024) incorporated the far field-HEDM measured type-II residual strains into their crystal plasticity simulations and noted a significant influence of the former on sample lifing during high cycle fatigue. Wilkinson and co-workers have frequently employed cross-correlation based HR-EBSD (Wilkinson et al., 2006, 2009) to study the substructure evolution (for example, intragranular stresses, Geometrically Necessary Dislocation (GND) density) under different loading scenarios (Kartal et al., 2012; Jiang et al., 2015; Guo et al., 2017). These techniques have also been used to spatially map the thermal-mismatch based GNDs, along with residual stresses in the vicinity of a non-metallic inclusion (Zhang et al., 2014). A recent study on AM Inconel 625 (Small et al., 2020) used HR-EBSD estimated residual strains and GND densities and observed lower elastic strains in regions manifesting subgrains and vice-versa. This hence led to the conclusion that the dislocation

substructures, in particular the subgrain formation during AM, was governed by elastic strain energy minimization (Small et al., 2020). A similar observation on the correlation between elastic strains and GND densities was also reported by Manda et al. (2024), albeit on IF steel specimen subjected to uniaxial tensile deformation.

The recently introduced Precession Electron Diffraction (PED) technique within the TEM, which measures the shift in the diffraction vector $\boldsymbol{g}$ with respect to a strain free reference, have enabled mapping residual strains at the submicron level as well ($\leq 10^{-8}\ m$) (Ghamarian et al., 2014; Ghamarian, 2017). The reader is referred to Chapter 6 for a detailed description on the mathematical formulation used in TEM-PED. Their application however, has mostly been limited to measuring the residual strains in Silicon and Germanium micro discs, typically used in the semiconductor industries (Bashir et al., 2019).

In summary, the methodologies to experimentally quantify the residual strains across multiple length scales have been established and have been routinely employed to study the deformation behavior of metallic materials (Verlinden et al., 2007).

2.2.3 Simulated Predictions of Residual Strains

A detailed review on the simulated predictions of residual strains, bulk as well as local, along with their successes and shortcomings have been presented in Section 7.1 of Chapter 7. For brevity, we only summarize a few of those studies in the present context.

From a modeling perspective, approaches to predict the bulk residual strain evolution mainly involve the use of polycrystal plasticity models to project the elastic strain tensor along specific $< hkl >$ directions, or (hkl) poles. Two class of crystal plasticity models are commonly employed for this purpose: the full-field approach and the homogenization or mean-field approach. The former involves solving the constitutive equations over each material point in a spatially discretized field (for example, finite element method) (Kanjarla et al., 2012). This enables the prediction of local heterogeneities and stress distributions, within the grains and also in the vicinity of grain boundaries (Kanjarla et al., 2012; Zheng et al., 2013; Thool et al., 2020; Sedaghat and Abdolvand, 2021). The latter assumes each grain as an ellipsoidal inclusion surrounded by a Homogeneous Effective Media (HEM) and iteratively solves the interaction equation linking the microscopic (grain-level) scale to the macroscopic scale (HEM) (Lorentzen et al., 2002; Neil et al., 2010; Wang et al., 2013; Tome and Lebensohn, 2023; Patra and Tomé, 2024). Since the mean-field approach estimates the aggregate response over a polycrystal (Tome and Lebensohn, 2023), these models are computationally cheaper in comparison to their full-field counterparts and hence, routinely employed to

predict the developments of bulk lattice strains. Advances in computing power have also permitted the use of full-field models (Dawson et al., 2001; Kanjarla et al., 2012; Zheng et al., 2013; Aburakhia et al., 2022) to accurately predict the bulk lattice strains during tensile deformation.

Similar to their experimental counterparts, the existing frameworks have accurately captured the bulk lattice strain developments under various types of loading conditions: namely the tensile/compressive (Clausen et al., 1999; Dawson et al., 2001; Neil et al., 2010; Kanjarla et al., 2012; Chen et al., 2019; Aburakhia et al., 2022), cyclic (Lorentzen et al., 2002; Wang et al., 2003; Saleh et al., 2013) and biaxial Load Path Change (LPC) experiments (Upadhyay et al., 2019). Incorporating the initial/undeformed residual strains based on experimentally-informed methods suggested by Musinski and McDowell (2015) or Kapoor and Sangid (2018) have further allowed to account for the realistic initial conditions of the as-received specimen. On the other hand, the local elastic (residual) strains, lattice rotations and substructure developments are generally predicted by the full-field crystal plasticity simulations and then compared with their counterparts from HEDM and HR-EBSD based experiments (Dunne et al., 2012; Zhang et al., 2014; Abdolvand et al., 2018; Kapoor and Sangid, 2018).

2.3 Solute Segregation in Metallic Systems

The presence of solute atoms in the crystalline lattice adds up to the frictional resistance for dislocation glide (Labusch, 1972; Nabarro, 1977). Further, solute segregation at the cell walls and low angle grain boundaries, generally observed in rapidly solidified/AM (Wang et al., 2018; Bertsch et al., 2020; Voisin et al., 2021) or (certain) thermomechanically treated materials (Sauvage et al., 2014; Xiao et al., 2020), leads to dislocation tangling, which further trap or retard the movement of mobile dislocations (see Figure 2.4(a,b)). In addition to chemical micro-segregation, these dislocation substructures also host a network of fine precipitates typically composed of metallic carbides, nitrides and oxides (Saeidi et al., 2015; Voisin et al., 2021) (cf. Figure 2.4(b)).

For example, Figure 2.4(a) shows the STEM-HAADF (Scanning Transmission Electron Microscopy-High Angle Annular Dark Field) image and the corresponding elemental composition map in an Al-Mg alloy subjected to High Pressure Torsion (HPT) at 200° C (Sauvage et al., 2014). Regardless of the noise, they qualitatively provide evidence of Mg segregation along the grain boundaries (Sauvage et al., 2014). Further, Figure 2.4(b) presents the HAADF image, along with the line profiles (see yellow marker across the cell walls in Figure

2.4(b)) and elemental composition maps (for Iron (Fe), Chromium (Cr) and Molybdenum (Mo)) for an austenitic stainless steel manufactured using the Laser Powder Bed Fusion (LPBF) technique (Voisin et al., 2021). These results clearly display higher Cr and Mo concentrations across the cell walls, from the line profile analyses as well as the composition maps. In addition, the HAADF images show a network of fine precipitates distributed along the cell walls. Such non-equilibrium microstructures necessitate the presence of GNDs to accommodate the interface incoherency and local lattice discontinuities. These dislocation substructures have also been linked to elastic strain minimizations by Small et al. (2020), in their AM Inconel 625. Finally, many studies (Liu et al., 2018a; Shamsujjoha et al., 2018; Wang et al., 2018) have attributed such solute/precipitate decorated dislocation substructures to be the key factor responsible for high strength and ductility in AM alloys.

Though Bertsch et al. (2020) attributed the formation of dislocation cell structures to the large magnitude of thermal distortion induced lattice incompatibilities, they did note that the organization of dislocation substructures is significantly influenced by the chemical micro-segregation and second-phase precipitation. In addition, the local stress fields arising due to the accumulation of GNDs around these chemical cell walls and inter-dendritic regions often remains unequilibrated, and is an important factor contributing towards the development of large local residual strains in AM materials (Chen et al., 2019; Small et al., 2020; Small and Taheri, 2021). Finally, these factors are responsible for their anisotropic mechanical properties (Chen et al., 2019; Jeon et al., 2019) (see Figure 2.4(c)).

These observations highlight the existence of a correlation between the solute segregation, GND densities and residual strains, especially in rapidly solidified or thermomechanically treated microstructures. It is hence crucial to quantify the local elemental composition, in particular the micro-segregation and the distribution of second-phase particles in these microstructures, to elucidate their role in developing the local heterogeneities during deformation. While the previous Sections focused on the latter aspects (cf. Section 2.1, 2.2), the subsequent paragraphs introduce methodologies to quantify the former, mainly from an experimental and a mesoscale modeling perspective.

2.3.1 Experimental Determination of Solute Segregation

The local chemical composition at the mesoscale can be readily quantified using an Energy Dispersive X-ray Spectroscopy (EDS) setup (Bell and Garratt-Reed, 2003; Newbury and Ritchie, 2013), typically mounted within a Scanning Electron Microscope (SEM). While the SEM can provide a detailed understanding of the surface properties, the local elemental composition can be quantified using EDS, up to a spatial resolution of few hundred

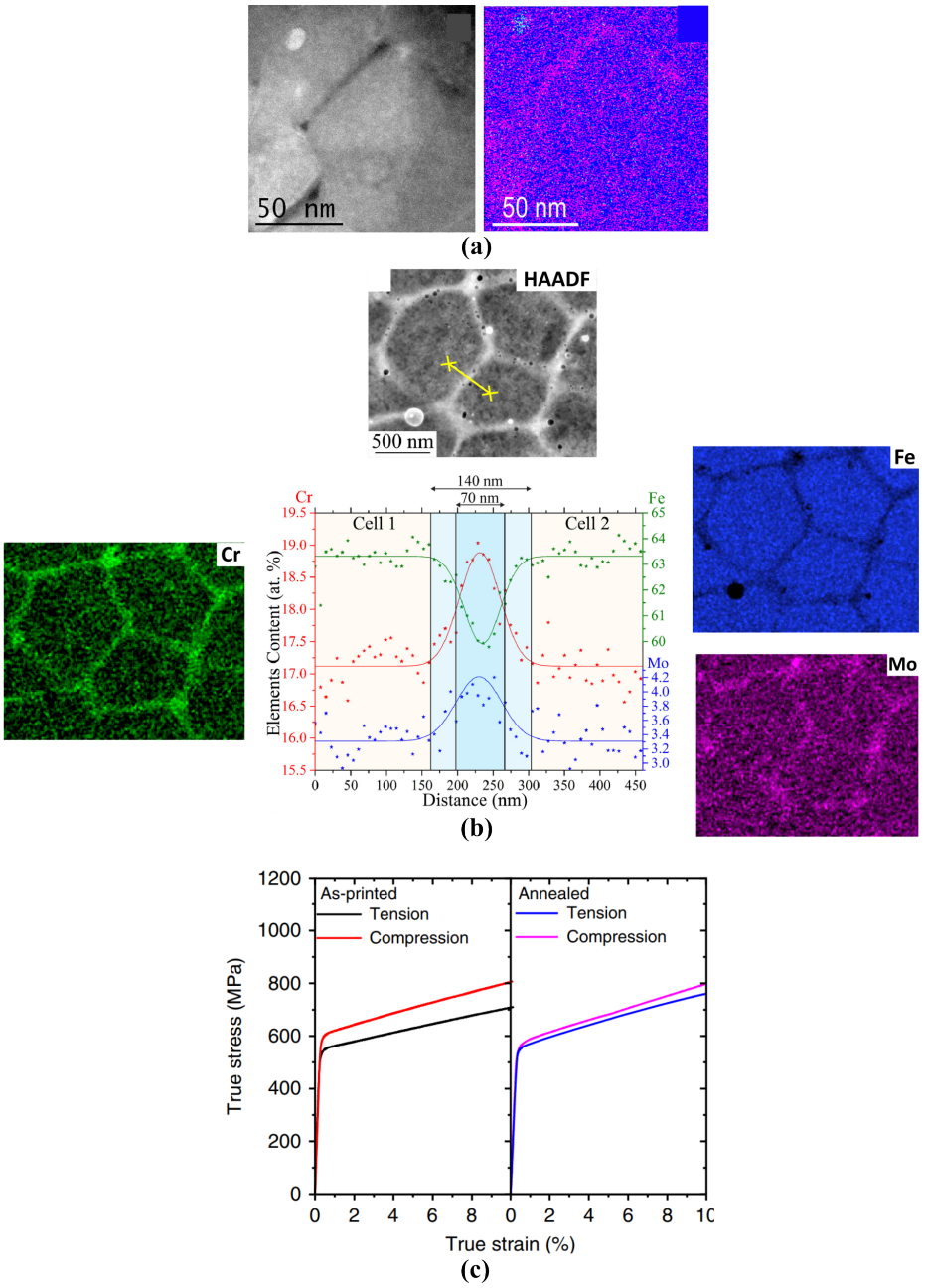

FIGURE 2.4: (a) STEM-HAADF (Scanning Transmission Electron Microscopy-High Angle Annular Dark Field) image along with the Energy Dispersive Spectroscopy (EDS) based composition map for an Al-Mg alloy subjected to High Pressure Torsion (HPT) at 200° C (Al(Kα)-blue, Mg(Kα)-red). (b) HAADF image, along with the line profiles (see yellow marker across the cell walls) and elemental composition maps (for Iron (Fe), Chromium (Cr) and Molybdenum (Mo)) for an austenitic stainless steel manufactured using the Laser Powder Bed Fusion (LPBF) technique. (c) Comparison of the anisotropic mechanical response of as-printed stainless steels with their annealed counterparts. Adapted from Sauvage et al. (2014), Voisin et al. (2021) and Chen et al. (2019).

nanometers ($\sim 120\ eV$) (Verlinden et al., 2007), thus making it an essential tool to map the solute segregation and precipitate distribution (Prakash et al., 2019). When the incoming electron beam strikes the sample, it removes an inner-shell electron from the atom. This, in turn results in an electron from a higher energy orbital filling the vacancy, and thus, in that process, emitting energy in the form of X-ray photons. The intensity as well as the energy of the emitted X-rays is a unique characteristic of each element. The EDS detectors (for example, Silicon Drift Detectors (SDD) (Newbury and Ritchie, 2013)) hence produce an energy spectrum, where the peaks can be uniquely correlated to the corresponding elements on the periodic table.

An important disadvantage of the SEM-EDS technique is in that the reliability of the quantified composition reduces drastically for elements lighter than Boron. Moreover, the surface preparation, dwell time and step size also effect the reliability of the quantified chemical composition. The overlap of peaks in the energy spectrum too introduces significant errors during the quantification. This has resulted in the development of an alternate SEM-based technique, commonly referred to as Wavelength Dispersive X-ray Spectroscopy (WDS), which quantifies the wavelength of the emitted X-rays from the specimen (Prakash et al., 2019). Though time consuming, this provides a much better resolution over the EDS and is useful in separating the overlapping peaks in the energy spectrum. Alternatively, application of the ChemiSTEM^{TM} technique (or TEM-EDS) on very thin foils can quantify the local elemental composition up to atomic level resolution (Sarkar et al., 2022). Though based on a similar principle, its primary advantage over SEM-EDS lies in its low electron-atom interaction volume, which provides a significant improvement in the spatial resolution for elemental analysis.

Lastly, the Atom Probe Tomography (APT) is a recently developed analytical technique that quantifies elemental composition at a sub-nanometer resolution (Gault et al., 2021). In addition, this technique also allows for a complete reconstruction of the 3D atomic structure of the specimen, including the grain boundaries, phase boundaries and precipitates (Sauvage et al., 2014; Devaraj et al., 2019; Gault et al., 2021). Note that the present study used SEM-EDS to quantify the local elemental composition and SEM-EBSD to identify/index the Al_2Cu precipitates observed in Chapter 4.

2.3.2 Modeling Effects of Solute Segregation on Strengthening

From a modeling perspective, the effect of local elemental composition and precipitate distribution can be introduced using field variables in crystal plasticity modeling framework to alter the thermal vibrations or short-range (Labusch, 1972; Nabarro, 1977; Sieurin et al.,

2006; Zander et al., 2007) and the athermal or long-range slip resistances (Shenoy et al., 2008; Li et al., 2020b).

Models accounting for the solid solution strengthening in binary alloys were first proposed by Labusch (1972) and Nabarro (1977). The strain field associated with a homogeneous solute distribution can be described using the misfit parameters, ε_b and ε_G, as follows (Fleischer, 1963; Sieurin et al., 2006):

$$\varepsilon_b = \frac{1}{b}\frac{db}{dc}; \varepsilon_G = \frac{1}{G}\frac{dG}{dc} \tag{2.24}$$

where, b is the Burgers vector, G is the shear modulus and c denotes the solute concentration in terms of atomic fraction. Physically, Equation 2.24 accounts for perturbations in the size (ε_b) and shear modulus (ε_G) associated with addition of solute atoms in the solvent matrix.

As proposed by Fleischer (1963); Sieurin et al. (2006), the resultant solute strengthening can be described using an interaction of these two parameters as follows:

$$\varepsilon_L = \sqrt{\left(\frac{\varepsilon_G}{1 + 0.5\,|\varepsilon_G|}\right)^2 + (\alpha\varepsilon_b)^2} \tag{2.25}$$

where, α typically lies in the range $9 - 16$ (Sieurin et al., 2006). The maximum force of interaction, f_m, between the dislocations and the added solute atoms is given by (Butt and Feltham, 1993; Sieurin et al., 2006):

$$f_m = \frac{Gb^2}{120}\varepsilon_L \tag{2.26}$$

Based on the works of Labusch (1972) and Nabarro (1977), this interaction results in a significant hindrance to the dislocation glide, thus resulting in a strengthening (τ_{ss}) within the range (of f_m), w. This can be mathematically written as follows:

$$\tau_{SS} = \frac{\left(2wf_m^4c^2\right)^{\frac{1}{3}}}{2b^{\frac{7}{3}}\left(Gb^2\right)^{\frac{1}{3}}} \tag{2.27}$$

Equation 2.27 suggests that the solid solution strengthening, τ_{ss}, varies as a function of the solute concentration, c, and ε_L as a function of $\tau_{ss} \propto c^{2/3}\varepsilon_L^{4/3}$. The constants associated with this expression can be determined using ab-initio calculations or by statistical analysis of experimental datasets (Sieurin et al., 2006; Zander et al., 2007). For a system composed

of N alloying elements, τ_{ss} can be written as a superposition of the hardening contributions of each of the solute species:

$$\tau_{ss} = K_1 \sum_{i=1}^{N} c_i^{\frac{2}{3}} \varepsilon_{L_i}^{\frac{4}{3}} \tag{2.28}$$

where K_1 is a constant (cf. Equation 2.27) and i denotes the solute species in consideration. These formulations have been employed to predict strengthening in Aluminum (Zander et al., 2007), Steel (Sieurin et al., 2006), Copper (Butt and Feltham, 1993) and Nickel (Chaudhary et al., 2023) alloys. Finally, recent studies have also shown that a linearized form of Equation 2.27, given by $\tau_{ss} \propto c\, \varepsilon_L^{4/3}$, sufficiently predicts the solid solution strengthening (Zander et al., 2007). A detailed review on the implementation and applicability of the above model (cf. Equation 2.28) within a Strain Gradient Crystal Plasticity (SGCP) framework (for an Aluminum-Copper alloy) and a Strain Gradient Plasticity (SGP) framework (for a Iron-Chromium binary alloy) has been presented in Chapters 4 and 5 of the thesis.

Models accounting for the precipitate strengthening contributions typically vary based on the size of precipitates under consideration, i.e., precipitate shearing due to weakly coupled dislocation pairs dominates for the finer precipitates, whereas, Orowan looping dominates for the large precipitates (Shenoy et al., 2008; Kozar et al., 2009; Collins and Stone, 2014; Chaudhary et al., 2023). The critical shearable to non-shearable transition radius may also differ based on the alloy grades under consideration (Li et al., 2020b). In addition, these models also have to account for geometrical factors owing to the varying shape of precipitates based on the thermomechanical treatment employed (Esmaeili et al., 2003; Li et al., 2020b). Since the alloys used in the thesis do not manifest such a phenomenon, we have not further deliberated on this topic.

The spatially resolved solute concentrations, on the other hand, can either be obtained from experimental measurements using SEM/TEM based EDS, or from phase field based process simulations of the evolution of solute concentrations during solidification, for example, see Pinomaa et al. (2020a,b); Lindroos et al. (2022). While a detailed discussion on the former was presented earlier in Section 2.3.1, the latter has been described in Section 5.2.1 of Chapter 5.

2.4 Scope of the Present Research: Correlating Misorientation, Solute Segregation and Residual Strains

While Section 2.1, 2.2 and 2.3 focused on individually addressing the aspects related to GNDs/backstress, residual strains and solute segregation/precipitates, the deformation behavior of commercial alloys and structural materials often displays a combined interaction between these three (Fribourg et al., 2011; Guo and Wu, 2018; Bhattacharyya et al., 2019). For example, two of the key strengthening mechanisms in commercial alloys are the solid solution strengthening and the precipitate strengthening (Dieter and Bacon, 1976). Starting from the works of Labusch (1972) and Nabarro (1977), to the more advanced empirical formulations proposed by Sieurin et al. (2006) and Zander et al. (2007), the former assumes that substitutional solute atoms enhance the obstruction to free dislocation glide. On the other hand, the latter considers the presence of randomly distributed second-phase particles, spontaneously nucleated during heat treatments, to locally enhance the stresses required for continuing plastic flow/dislocation glide by mechanisms such as Orowan bowing or precipitate shearing (Dieter and Bacon, 1976; Bhattacharyya et al., 2019).

Generally speaking, either or both of these act as sites for the development of local heterogeneities during deformation, thus resulting in the generation of GNDs to maintain the ensuing lattice compatibility. The resulting backstresses and unrelaxed elasto-plastic strain gradients would govern the failure mechanisms in such alloys. The materials manufactured through rapid solidification/AM form the other set of microstructures, were such a combined interplay between the three aspects is commonly observed (Yoo et al., 2018; Bertsch et al., 2020; Voisin et al., 2021). As noted in Section 2.3, the dislocation substructures, which are mainly composed of GNDs are largely influenced by the micro-segregated solutes as well as precipitates, which in turn influence the bulk as well as local residual strains, and ultimately the failure behavior of these materials.

In summary, GNDs are essential to accommodate the local lattice discontinuities. These discontinuities may arise due to various imperfections such as the grain/phase boundaries, second-phase particles, solute-enriched cell walls, etc. The backstresses associated with the GNDs have been attributed to significantly alter the macroscopic mechanical behavior. For example, the long range backstresses arising due to the GND pileups at grain boundaries during deformation have been attributed to the well-known Hall-Petch effect (Hall, 1951). Similarly, the printing induced dislocation structures, for example, those arising due to adverse thermal gradients/cooling rates, chemical micro-segregation and second-phase precipitation, typical in rapidly solidified microstructures have been attributed to the development of significant microscale internal stresses and multiscale residual stresses in the

microstructure (Bertsch et al., 2020; Voisin et al., 2021). During deformation, these dislocation networks resist subsequent dislocation motion, which in turn are responsible for the increase in strength of rapidly solidified microstructures. An in-depth analysis and quantification of GNDs in the vicinity of these imperfections in various structural materials has been carried out in the subsequent Chapters.

While a range of studies exist in the literature to quantify and independently examine the role played by each of these three aspects (see Section 2.1, 2.2 and 2.3), a combined experimentally informed modeling approach that simultaneously accounts for all three has not yet been looked upon. Such a unified modeling framework holds significant practical importance, as majority of the materials employed today in aerospace, automobile as well as communication sectors are either additively manufactured or are subjected to complex heat treatment procedures, in order to tailor the microstructure to achieve the desired mechanical properties (Sharma, 2003; Kaufman and Rooy, 2004; Schmitt et al., 2021). From a modeling perspective, this is partly because accounting for GND densities and backstress necessitates the development of a strain gradient plasticity framework which often introduces additional degrees of freedom in the system, thus making it computationally expensive (Evers et al., 2004a,b). In addition, though solute behavior as well as the role of precipitates can be accounted for by existing empirical relationships (Labusch, 1972; Nabarro, 1977; Sieurin et al., 2006; Zander et al., 2007), predicting micro-segregation and solute partitioning under realistic temporal profiles invites the use of phase field frameworks (Moelans et al., 2008; Plapp, 2011). Further, coupling these with mechanistic models is essential to capture the local heterogeneities and residual strains arising during manufacturing and thermomechanical treatments, which later lead to anisotropy in their mechanical behavior (Liu et al., 2020a; Lindroos et al., 2022; Pinomaa et al., 2022; Hu et al., 2023). Addressing these gaps in the literature, and exploring their inter-dependencies by developing a unified mesoscale plasticity framework, which derives its inputs from experimental observations forms the key motivation for Chapters 3-5 in the thesis.

Similarly, from an experimental standpoint, a key deterrent to any such combined examination is the variation in the relative magnitudes between the predictions of various residual strain measurement techniques, namely the $(\Delta d/d)$-sensitive (for example, X-ray/Neutron Diffraction, TEM-PED) and the $(\Delta\theta/\theta)$-sensitive (for example, HR-EBSD and HR-TKD). While much of the literature has focused upon quantifying the GND densities, solute segregation and even residual strains (though individually, the $(\Delta d/d)$ or $(\Delta\theta/\theta)$-sensitive), not much attention has been paid towards a direct comparison of the evolution of $(\Delta d/d)$-sensitive and $(\Delta\theta/\theta)$-sensitive residual strains, especially with progressive deformation. As

can be seen, such an experiment, though complex, would provide a significant understanding on the strengths and shortcomings of the methodologies associated with each of the residual strain measurement techniques. In addition, deriving a scaling factor between these techniques would also enable in achieving numerical convergence, though artificially, in their magnitudes. Addressing this issue, followed by further employing it to examine the bulk and local residual residual strain evolution during progressive deformation forms the motivation for Chapters 6 and 7 in the thesis.

Finally, employing the mesoscale plasticity frameworks provides significant information on the local substructure as well as micro-texture evolution. Understanding the role played by various substructure governing variables in influencing the bulk as well as local residual strains derived above can aid researchers in designing microstructures exhibiting improved mechanical properties/failure behavior. This forms the motivation for Chapters 6 and 7 in the thesis.

2.4.1 Thesis Objectives

To address the gaps summarized in the preceding section, the following are the primary objectives of the present thesis:

- Development of a Taylor hardening based Strain Gradient Crystal Plasticity framework (SGCP), which can accurately predict the GND density, backstress and other substructural features evolving during deformation.
- Experimental evaluation of the predicted Near Boundary Gradient Zones (NBGZs) in an Al-Mg alloy subjected to interrupted tensile deformation.
- Combined experimental and SGCP study to examine the role of grain boundary solute segregation and precipitates on the orientation dependence of NBGZs in an Al-Cu alloy subjected to compressive loading.
- Development of a coupled Phase Field (PF)-Strain Gradient Plasticity (SGP) framework to predict the underlying microstructural features developing during rapid solidification of a Fe-Cr alloy, followed by SGP simulations to study the evolution of mechanical and microstructural properties during (post-solidification) deformation.
- Exploring the relative magnitudes of residual strains predicted by $(\Delta d/d)$-sensitive and $(\Delta\theta/\theta)$-sensitive measurement techniques.

- Development of a combined experimental and crystal plasticity framework to predict the factors influencing the evolution of orientation dependent bulk and local residual strains during tensile and cyclic deformation of an austenitic stainless steel (SS 316L).

These objectives have been addressed in the following Chapters of the thesis. The choice of the material systems in different Chapters has been made in order to highlight the different factors affecting correlated mechanical property and microstructure evolution. In brief, Chapters 3 and 4 focus on the Aluminum-based alloy systems, while Chapters 5, 6 and 7 use Iron-based alloy systems. The appropriate material systems are decided based upon the microstructural and mechanical properties dominant during the chosen thermomechanical treatment regime.

Chapter 3

Study of Grain Boundary Orientation Gradients

3.1 Introduction

Plastic deformation in polycrystals is inherently heterogeneous, with differential hardening and deformation in the individual grains. This may be attributed to various factors such as orientation-dependent micro-yielding, incompatibility with neighboring grains, proximity to regions of stress concentrations (geometrical and microstructural), and the imposed state of deformation. Generally speaking, the crystal lattice undergoes significant rotation during deformation; the grain rotates towards the neighboring (grain) orientation with which it shares the minimum misorientation (Nagarajan et al., 2021; Chen et al., 2022b). Further, the lattice planes in the grain interior are able to rotate with relative ease during deformation, whereas rotation of the lattice planes in the vicinity of the grain boundaries is restricted, due to the additional constraints imposed by neighboring grains (Randle et al., 1996; Nave and Barnett, 2004; Tóth et al., 2010). The grain boundaries should not only ensure the lattice continuity across the interface, but they should also try to maintain mechanical compatibility and force equilibrium (Taylor, 1938; Jiang et al., 2013a). During straining, differential rotation within the grain contributes to the division of grain into two zones: an exterior grain mantle, where lattice rotation is more constrained, resulting in a curvature in lattice planes, and an interior grain core, which can rotate with relative ease (Drury and Humphreys, 1986; Tóth et al., 2010). The lattice curvatures and strain gradients in these regions are accommodated by Geometrically Necessary Dislocations (GNDs) (Nye, 1953;

[1] Significant parts of this Chapter have been published in Pai et al. (2022).

Ashby, 1970; Arsenlis and Parks, 1999; Tóth et al., 2010). GNDs consist of identical Burgers vector and line tangent direction; a pile-up of GND density hence results in a repulsive stress opposing the applied deformation (Li et al., 2020a; Zhao et al., 2021). Further, the grain mantle developing such a localized misorientation gradient, is generally known as the Near Boundary Gradient Zone (NBGZ) (Mishra et al., 2009; Raveendra et al., 2011; Keskar et al., 2014; Singh et al., 2015, 2017).

Based on experimental characterization of a large number of grain pairs in an aluminum alloy, Mishra et al. (2009) proposed an empirical relationship, relating the length of NBGZs of two neighboring grains to their crystallographic orientations of the form: $L_i/L_j = (M_j/M_i)^{2.5}$, where L_i and M_i are the NBGZ length and the Taylor factor, respectively, and i, j denote the grain indices. Such a correlation stems from the fact that neighboring grains with a large difference in Taylor factors (a measure of the proclivity for deformation) may be expected to have higher orientation gradients, with the softer grain developing a wider NBGZ. The NBGZs have been studied in terms of sensitization to corrosion (Srinivasan et al., 2015), effect on grain fragmentation (Keskar et al., 2014) and their effect on deformation twinning during plane strain compression of Zr alloys (Singh et al., 2015). In related studies, Sun et al. (2000) observed the development of orientation gradients in channel die compressed aluminum bicrystals and correlated this with a pile-up of GND density at the bicrystal interfaces. Liang and Dunne (2009) developed an explicitly coupled length scale dependent 3D crystal plasticity model, to simulate these bicrystal deformation experiments, and predicted GND densities identical to the experimental counterparts (Sun et al., 2000). It should be noted that GND pile-up in the vicinity of grain boundaries were also simulated by Evers et al. (2004b), although not directly compared with experiments.

Experimental characterization of local misorientations and substructural properties are generally performed using measures such as Kernel Average Misorientation (KAM) and GND density. Allain-Bonasso et al. (2012) observed the build-up of misorientation at grain boundaries in deformed interstitial-free steel specimens and correlated this with the corresponding GND densities. Ohashi et al. (2009) estimated the GND density during tensile loading of a Ni bicrystal specimen. This combined experimental and modeling study showed that based on the grain orientation, GNDs may pile-up at the grain boundaries, or may accumulate over a narrow band in the grain interior (Ohashi et al., 2009). Pokharel et al. (2015) studied the misorientation development near grain boundaries during tensile deformation of polycrystalline copper and observed that larger grains exhibit a much smoother buildup of misorientation as compared to the fine grains. GNDs are also essential for accommodating the lattice mismatch at phase boundaries. To this end, Kundu and Field (2016) observed that the rate of increase of GND density reduced with increasing strain in a Dual Phase

(DP) steel. They attributed this to the lowering of compatibility requirements between the neighboring ferrite and martensite grains.

Microstructural evolution in the NBGZs can perhaps be better predicted by non-local models for plastic deformation, due to their inherent ability to account for the strain gradients and the development of GNDs near incompatible interfaces. Strain Gradient Crystal Plasticity (SGCP) models are one such class of non-local formulations, which consider the effect of plastic strain gradients on the hardening response due to GNDs. The contribution of GNDs to hardening has been modeled in several different constitutive forms in crystal plasticity frameworks. GNDs have been considered as forest obstacles, thus contributing to enhanced strengthening by (Ashby, 1970; Dai, 1997; Dunne et al., 2012). Others have considered the GND contribution to act as a repulsive backstress, that opposes dislocation glide (Evers et al., 2004a,b; Bayley et al., 2006; Geers et al., 2006b; Kapoor et al., 2018; Bandyopadhyay et al., 2021). The frameworks considering backstress evolution can be further classified into: *lower order models*, where non-locality is incorporated via constitutive equations (Kapoor et al., 2018; Bandyopadhyay et al., 2021), *work conjugate higher order models*, where additional terms in the virtual work relation are considered to account for the presence of higher order stresses, work conjugate to the gradients of plastic strain (Gurtin, 2002), and *non-work conjugate high order models*, where backstress explicitly influences the crystallographic slip rates (Kuroda and Tvergaard, 2006, 2008). The reader is referred to a comprehensive review of the related modeling and experimental studies by Mayeur and McDowell (2014) and Voyiadjis and Song (2019).

Studies linking the length of NBGZs to the crystallographic orientation of the grains, followed by subsequent comparison between simulations and experiments have largely been restricted to bicrystals (Liang and Dunne, 2009; Ohashi et al., 2009). A detailed quantitative assessment of NBGZs, combined with a study of the underlying microstructure evolution is generally missing. Specifically, there is a lack of insight on how various substructural and local mechanical properties evolve within the NBGZ, and how they get affected by the orientation of the neighboring grains. Further, the length scale dependence of the NBGZs has not been studied systematically. Although, experiments (Subedi et al., 2015; Kundu and Field, 2016) as well as simulations (Evers et al., 2004b; Geers et al., 2006b; Kysar et al., 2007; Dunne et al., 2012) have shown that regions close to the grain boundaries and stress concentrations deform heterogeneously, however, their dependence on microstructural parameters, such as the grain size, has not been established explicitly. Addressing these gaps in the literature form the main objectives of the present work.

Although previous works have focused on studying the NBGZs experimentally, we believe that it is essential to develop a modeling framework that can provide insights into the

development of local microstructure-mechanical property correlations within the NBGZs. Towards this end, the present work studies the formation of NBGZs in a polycrystalline aluminum-magnesium (Al – 6wt.% Mg) alloy using combined experiments and modeling. Interrupted tensile testing is performed and the microstructures are characterized using Electron Backscattered Diffraction (EBSD) to obtain the local orientation, misorientation and GND density as a function of distance from the grain boundaries. We also simulate deformation in realistic microstructures using a non-local SGCP framework. The SGCP model uses a Taylor hardening based backstress model to capture the length scale effects. The model is first qualitatively validated by demonstrating grain size dependent strengthening and then used to simulate deformation in idealized microstructures. The combined experimental and modeling methodology is then used to correlate the various microstructural and substructural properties such as the KAM, GND density, SSD density, and effective plastic strain within the NBGZs. Finally, we also establish statistical correlations of the length of NBGZs with the underlying microstructural features such as the initial grain average Schmid factor and the grain size.

The study of deformation in these NBGZs is important because the Hall-Petch type grain boundary strengthening is primarily owed to the development of strain gradients and GNDs in the NBGZs. While much focus has been placed on understanding the mechanistic origins of these grain size effects, the underlying microstructural evolution has not been studied systematically. Grain fragmentation is also another consequence of the development of NBGZs. The broad objectives of this research are to understand the microstructural factors contributing to development of misorientation gradients at grain boundaries, towards engineering grain boundaries with enhanced mechanical properties.

3.2 Materials and Methods

3.2.1 Material

The material used in the present work is an Aluminum-Magnesium (Al – 6wt.% Mg) alloy. This is a solute solution strengthened alloy, with higher strength (relative to pure Al) and enhanced strain hardening capability (Driver and Papazian, 1985; Hughes, 1993; Sauvage et al., 2014). The composition of the alloy is given in Table 3.1. The material was annealed in a laboratory vacuum furnace ($\sim 10^{-6}$ torr) at 500° C for 6 hours, followed by water quenching, to homogenize the texture and provide residual strain relief, if any. Equiaxed grains, with near random crystallographic texture (Texture Index: 1.14) were obtained with a mean grain size of $\sim 92 \pm 22\ \mu m$.

TABLE 3.1: Composition of Al – 6wt.% Mg alloy.

	Al	Mg	Mn	Si	Cr	Cu	Fe
Comp.(wt%)	92.4	6.55	0.66	0.16	0.008	0.01	0.14

3.2.2 Experimental Methodology

Micro-tensile specimens were machined out of the material with dimensions: 16 mm (total length), 5 mm (gauge length), 2 mm (gauge width) and 1.5 mm (thickness), respectively. Uninterrupted tensile deformation was carried out on micro-tensile specimens in a screw-driven Instron^{TM} 3345 Universal Testing Machine (UTM), with a 5 kN load cell, at nominal strain rates of 10^{-3} s^{-1} and 10^{-4} s^{-1}. The deformation was performed up to an applied strain of 10%. Subsequent microstructural characterization using EBSD and the tensile stress-strain response indicated that the effect of essentially quasi-static strain rates on the mechanical behavior as well as the microstructure evolution was negligible and there was no appreciable difference between the materials deformed at the two different strain rates (the data has not been presented here for brevity). Following this, interrupted tensile tests were then performed on the micro-tensile specimens in a DEBEN^{TM} micro tensile stage at a nominal strain rate of 10^{-3} s^{-1}. Data from the uninterrupted tensile tests at $\dot{\varepsilon} = 10^{-3}$ s^{-1} were used to calibrate the SGCP model, while the data from interrupted tensile tests were used for microstructural characterization and comparison with SGCP model predictions.

Microstructural characterization was performed for samples deformed to 0%, 2.5%, 5%, 7.5%, 10% nominal strain. Traditional metallography, followed by electropolishing the specimens in an electrolyte of 80 : 20 ratio of methanol and perchloric acid, was used for preparing the samples for microstructural characterization. The electropolishing was carried out in a Stuers^{TM} Lectropol-5 equipment at 273K and 12V. A FEI^{TM} Quanta 3D-FEG (Field Emission Gun) scanning electron microscope, equipped with TSL-EDX^{TM} EBSD system, was used for microtextural characterization. A Confidence Index (CI) cutoff of 0.1, which signifies $\sim$ 95% accuracy in indexing, was used during data analysis. The step size (0.5 μm) and beam conditions of the EBSD scans were identical at all stages. Although the dimensions of the gauge region were 5 $mm \times 2$ $mm \times 1.5$ mm, we restricted the region of interest for our microstructural characterization to 1200 $\mu m \times 1200$ μm near the center to avoid boundary effects, if any. Impressions from micro-hardness indents were utilized for identification of the region of interest during interrupted EBSD measurements.

The present work utilizes Kernel Average Misorientation (KAM) and GND density to study NBGZs. KAM is a point-to-point misorientation measure calculated using the orientation data obtained from the EBSD maps and is given by: $\frac{1}{n}\sum \Delta g_{ij}(g_i, g_j)$, where $\Delta g_{ij}(g_i, g_j)$

is the misorientation between the pixel, i, and its neighboring pixel, j (Kocks et al., 1998; Wright et al., 2011, 2016). The number of neighbors is indicated by n (4 for the square grid considered in the present work). Further, the maximum intragranular misorientation allowed is 5° (Thool et al., 2020).

GND density calculated from the EBSD orientation data (Sun et al., 2000; Field et al., 2005; Pantleon, 2008; Ruggles and Fullwood, 2013) has been used to study the orientation gradients near grain boundaries (Liang and Dunne, 2009; Allain-Bonasso et al., 2012). The bulk GND density can also be estimated using the entry-wise one-norm of the Nye tensor as (Ruggles and Fullwood, 2013; Ruggles et al., 2016):

$$\rho_{GND} = \frac{3}{2b} \sum_{i} \sum_{j} \Lambda_{ij} \tag{3.1}$$

where, $\mathbf{\Lambda}$ denotes the Nye tensor and b is the magnitude of the Burgers vector. The Nye tensor can be derived from the curvature of the crystal lattice using the following relationship in index notation (Pantleon, 2008):

$$\Lambda_{ik} = \kappa_{ki} - \delta_{ki}\kappa_{mm} \tag{3.2}$$

where, $\boldsymbol{\kappa}$ is the curvature tensor. Further, the curvature tensor is related to the misorientation vector by $\kappa_{kl} = \Delta\theta_k/\Delta x_l$, where $\Delta\theta_k = -\epsilon_{kij}\Delta g_{ij}(\Delta\theta/2sin(\Delta\theta))$ (Pantleon, 2008). Only 6 components of the lattice curvature tensor can be derived using this method, as derivatives along the third direction (normal to the surface) cannot be accessed.

We have used the OIM-based method available in the open-source OpenXY software (Fullwood, 2020) for calculating the GND density. OpenXY permits GND calculation using three different algorithms, $\mathbf{\Lambda_3}$, $\mathbf{\Lambda_5}$ and $\mathbf{\Lambda_9}$, where the subscript denotes the number of terms in the Nye tensor used for GND estimation. We have used the nine-term approximation for the present work. Although this technique estimates the bulk GND density from an incomplete Nye tensor, it can still reveal valuable information regarding the GND pile-up near grain boundaries (Ruggles and Fullwood, 2013).

3.2.3 Strain Gradient Crystal Plasticity (SGCP) Framework

3.2.3.1 Finite Deformation Kinematics and Kinetics

The finite deformation framework utilizes the multiplicative decomposition of the deformation gradient tensor, $\boldsymbol{F}$, into the elastic and plastic parts (Asaro and Rice, 1977), i.e.,

$$\boldsymbol{F} = \boldsymbol{F^e} \cdot \boldsymbol{F^p} \tag{3.3}$$

where, $\boldsymbol{F^p}$ accounts for the effect of plastic deformation on the initial, strain-free lattice, transforming it from the reference to the isoclinic, intermediate configuration. The transformation from intermediate to the current configuration is represented by $\boldsymbol{F^e}$, which accounts for the lattice distortion due to elastic deformation and the rigid body rotation. Further, $\boldsymbol{F^p}$ is related to the plastic spatial velocity gradient, $\boldsymbol{L^p}$, as $\dot{\boldsymbol{F}}^{\boldsymbol{p}} = \boldsymbol{L^p} \cdot \boldsymbol{F^p}$ where, $\boldsymbol{L^p}$ is the tensorial sum of crystallographic shearing rates over all the slip systems and is given by:

$$\boldsymbol{L^p} = \sum_{\alpha=1}^{N} \dot{\gamma}^{\alpha} \boldsymbol{m_0^{\alpha}} \otimes \boldsymbol{n_0^{\alpha}} \tag{3.4}$$

Here, $\dot{\gamma}^{\alpha}$ represents the crystallographic shearing rate on slip system α, $\boldsymbol{m_0^{\alpha}}$ and $\boldsymbol{n_0^{\alpha}}$ represent the unit vectors along slip and slip plane normal directions, respectively, and N represents the total number of slip systems. The crystallographic shearing rate, $\dot{\gamma}^{\alpha}$, is a function of the resolved shear stress, τ^{α}, slip system level backstress, τ_b^{α}, and the SSD density, ρ_{SSD}^{α}, on slip system α. Further, the backstress, τ_b^{α}, is assumed to evolve primarily a function of the GND density, ρ_{GND}^{α}.

The elastic Green strain tensor in the intermediate configuration is given by:

$$\boldsymbol{E^e} = \frac{1}{2}(\boldsymbol{F^{eT}} \cdot \boldsymbol{F^e} - \boldsymbol{\delta}) \tag{3.5}$$

The second Piola-Kirchhoff stress tensor is obtained using $\boldsymbol{S} = \boldsymbol{C_0} : \boldsymbol{E^e}$, where $\boldsymbol{C_0}$ is the fourth rank elasticity tensor in the intermediate configuration. The Cauchy stress tensor is derived from the second Piola-Kirchhoff stress using the relationship: $\boldsymbol{S} = J^e \boldsymbol{F^{e-1}} \cdot \boldsymbol{\sigma} \cdot \boldsymbol{F^e}$, where $J^e = det(\boldsymbol{F^e})$ denotes the Jacobian of the elastic deformation gradient. Finally, the resolved shear stress acting on the slip system α, is given by the Schmid law as,

$$\tau^{\alpha} = \boldsymbol{m^{\alpha}} \cdot \boldsymbol{\sigma} \cdot \boldsymbol{n^{\alpha}} = \frac{1}{J^e} \boldsymbol{m^{\alpha}} \cdot \boldsymbol{S} \cdot \boldsymbol{n^{\alpha}} \tag{3.6}$$

where, $\boldsymbol{m^{\alpha}}$ and $\boldsymbol{n^{\alpha}}$ denote the slip and slip plane normal directions in the deformed configuration, and can be related to the reference configuration using, $\boldsymbol{m^{\alpha}} = \boldsymbol{F^{e}} \cdot \boldsymbol{m_{0}^{\alpha}}$ and $\boldsymbol{n^{\alpha}} = \boldsymbol{F^{e}} \cdot \boldsymbol{n_{0}^{\alpha}}$.

The shearing rate due to dislocation glide has been modeled using a Kocks-type thermally activated flow rule (Kocks et al., 1975), i.e.,

$$\dot{\gamma}^{\alpha} = \dot{\gamma}_{0} \exp\left\{\frac{-\Delta F}{kT}\left(1 - \left(\frac{|\tau^{\alpha} - \tau_{b}^{\alpha}| - s_{a}^{\alpha}}{s_{t}^{\alpha}}\right)^{p}\right)^{q}\right\} \operatorname{sgn}\left(\tau^{\alpha} - \tau_{b}^{\alpha}\right); |\tau^{\alpha} - \tau_{b}^{\alpha}| > s_{a}^{\alpha} \tag{3.7}$$

where, $\dot{\gamma}_{0}$ is the reference shear rate, ΔF is the activation energy for dislocation glide in the absence of applied stress, k is the Boltzmann constant and T is the absolute temperature. p and q are parameters that govern the shape of the activation enthalpy curve. s_{t}^{α} accounts for the thermal slip resistance due to short range barriers, while the athermal slip resistance, s_{a}^{α}, accounts for the slip resistance due to long range stress fields of dislocation junctions. The thermally activated flow rule can be used to model temperature and strain rate effects using a more physically based model (Kothari and Anand, 1998), as compared to the simple power law flow rule. While these effects have not been studied in the present work, the model implementation allows us to explore such aspects in the future.

The athermal slip resistance is modeled using a Taylor type hardening model,

$$s_{a}^{\alpha} = \tau_{0} + k_{ih} G b \sqrt{\sum_{\xi=1}^{Ns} A^{\alpha\xi} \rho_{SSD}^{\xi}} \tag{3.8}$$

where, τ_{0} represents the threshold lattice resistance of an annealed crystal, k_{ih} is the hardening coefficient associated with isotropic hardening due to SSDs and $A^{\alpha\xi}$ is the interaction matrix for dislocation junctions formed between dislocations on slip systems α and ξ (α,ξ = 1,2,...,12 for FCC metals) (Evers et al., 2004b).

We use a Kocks-Mecking type model for substructure evolution, which has been modified to account for the GND density, and is given by (Estrin, 1996; Kocks and Mecking, 2003; Evers et al., 2004a,b; Li et al., 2020b):

$$\dot{\rho}_{SSD}^{\alpha} = \frac{k_{mul}}{b} \sqrt{\rho_{SSD}^{\alpha} + \rho_{GND}^{\alpha}} \, |\dot{\gamma}^{\alpha}| - k_{dyn} \rho_{SSD}^{\alpha} \, |\dot{\gamma}^{\alpha}| \tag{3.9}$$

The first term on the right-hand side of Equation (3.9) accounts for dislocation multiplication at pre-existing junctions, while the second term accounts for dislocation annihilation due to dynamic recovery. The parameters k_{mul} and k_{dyn} can be obtained by fitting the model to the experimental response.

3.2.3.2 GND Density and Backstress

Based on prior works (Nye, 1953; Dai, 1997; Arsenlis and Parks, 1999; Arsenlis et al., 2004), the Nye tensor may be written as a function of the plastic deformation gradient as follows:

$$\boldsymbol{\Lambda} = -\left(\boldsymbol{\nabla} \times \boldsymbol{F}^{pT}\right)^{T} = \sum_{\xi=1}^{18} \rho_{GND}^{\xi} b^{\xi} \boldsymbol{m}_{0}^{\xi} \otimes \boldsymbol{t}_{0}^{\xi} \tag{3.10}$$

where, b^{ξ} is the Burgers vector magnitude and $\boldsymbol{m}_{\boldsymbol{0}}^{\boldsymbol{\xi}}$ and $\boldsymbol{t}_{\boldsymbol{0}}^{\boldsymbol{\xi}}$ represent the unit vectors for the dislocation slip direction and line tangent direction in the intermediate (or reference) configuration. The unit vector along the line tangent direction can be given by $\boldsymbol{t}_{\boldsymbol{0}}^{\boldsymbol{\xi}} = \boldsymbol{n}_{\boldsymbol{0}}^{\boldsymbol{\xi}} \times \boldsymbol{m}_{\boldsymbol{0}}^{\boldsymbol{\xi}}$. ξ denotes the index (or type) of dislocation, the maximum value for which in a FCC crystal would be 18 (12 edge, 6 screw) (Evers et al., 2004a). The present work utilizes a rate form of Equation (3.10), and is given by:

$$\dot{\boldsymbol{\Lambda}} = -\left(\boldsymbol{\nabla} \times \dot{\boldsymbol{F}}^{pT}\right)^{T} = \sum_{\xi=1}^{18} \dot{\rho}_{GND}^{\xi} b^{\xi} \boldsymbol{m}_{0}^{\xi} \otimes \boldsymbol{t}_{0}^{\xi} \tag{3.11}$$

The rate form of Nye tensor ensures that any remnant incompatibility in the lattice is taken into account, even after the reversal of loading direction. The material considered in the present work has an fcc crystal structure, with 12 slip systems. Following previous works (Evers et al., 2004a,b; Geers et al., 2006b), SSD densities are assumed to be of edge type only (12 distinct types), whereas both screw and edge type GNDs (18 distinct types) are considered in the model. The dislocation configurations considered in the present work are given in Table 3.2. The procedure for estimating GND densities from the Nye tensor is given below.

We adopt the method for estimating GND densities from the Nye tensor as given in Das et al. (2018). The 2^{nd} order Nye tensor can be reshaped as a 9×1 column vector. The GND density can also be represented as a $\xi \times 1$ column vector, $\boldsymbol{\rho}$. Here, we define a tensor, $\boldsymbol{A}$, which is a $9 \times \xi$ tensor, where ξ is the total number of GND configurations. Thus, Equation (3.11) is rewritten as (Arsenlis and Parks, 1999; Das et al., 2018):

$$\boldsymbol{A} \cdot \boldsymbol{\rho} = \boldsymbol{\Lambda} \tag{3.12}$$

By comparing Equation (3.11) and (3.12), it can be seen that each column in $\boldsymbol{A}$ comprises of a dyadic product between the Burgers vector and line tangent direction for a dislocation of type ξ. Note that $\boldsymbol{\rho}$ and $\boldsymbol{\Lambda}$ are represented here as column vectors.

Since $\xi > 9$, the number of slip systems on which the GND density has to be resolved for a FCC crystal is higher than the individual components of the Nye tensor, there is no unique solution for the GND density. The imposed plastic strain gradients may be accommodated by multiple dislocation configurations, especially in a crystal with high degrees of symmetry. Mathematically, this may lead to non-unique solutions for the GND density (Arsenlis and Parks, 1999). Hence, we aim to obtain a lower bound on the GND density, which can accommodate the lattice incompatibility (Kysar et al., 2010). This issue has been addressed previously by imposing additional constraints in order to obtain the GND density, for example, minimizing the dislocation line length or minimizing the total energy due to dislocations. The minimization schemes can be broadly classified into L_1 and L_2 norms, which are given by (Arsenlis and Parks, 1999; Kysar et al., 2010; Dunne et al., 2012):

$$L_1 = \sum_{\alpha=1}^{N} |w^\alpha \rho_{GND}^\alpha| \text{ and } L_2 = \sqrt{\sum_{\alpha=1}^{N} \left[w^\alpha \rho_{GND}^\alpha\right]^2} \tag{3.13}$$

where, w^α are the weight factors and α is the slip system with GND density, ρ_{GND}^α, respectively. Various weighting factors, such as $w^\alpha = b^\alpha$, $w^\alpha = (b^\alpha)^2$ (minimizing the total strain energy), $w^\alpha = 1$ (minimizing total GND density over all slip systems), etc. can be used. Unlike the L_1 norm, L_2 minimization scheme is a purely mathematical construct and it does not have any physical interpretation (Kysar et al., 2010). Here, we employ the L_2 minimization scheme with $w^\alpha = 1$, which is also referred to as the least squares technique (Dunne et al., 2012).

Followed by simple matrix manipulations, the expression for rate of change of GND density can be rewritten as (Arsenlis and Parks, 1999; Kysar et al., 2007, 2010; Das et al., 2018):

$$\dot{\rho}_{GND}^{\xi} = \left(\boldsymbol{A}^T \cdot \boldsymbol{A}\right)^{-1} \cdot \boldsymbol{A}^T \cdot \dot{\Lambda} \tag{3.14}$$

This slip system level rate of change of GND density is computed from the current value of $\boldsymbol{F}^p$, which in turn is computed using a finite difference approximation, i.e.,

$$\dot{\boldsymbol{F}}^p = \frac{\boldsymbol{F}_t^p - \boldsymbol{F}_{t-\Delta t}^p}{\Delta t} \tag{3.15}$$

where, t denotes the current time step, and Δt is the time step increment. The rate of change of Nye tensor is calculated from the spatial gradient of $\dot{\boldsymbol{F}}^p$ calculated above. Subsequent to this, the rate of change of slip system level GND density is calculated using Equation 3.14.

Finally, the slip system GND density at the current time step is calculated as:

$$\rho^{\xi}_{GND}\Big|_{t} = \rho^{\xi}_{GND}\Big|_{t-\Delta t} + \dot{\rho}^{\xi}_{GND}\Delta t \tag{3.16}$$

We also refer the reader to Patra et al. (2023b), where the detailed numerical algorithm for the implicit time step integration for a similar, albeit J_2 plasticity formulation, has been provided.

Note that both screw and edge type GNDs are considered in the framework, leading to 18 distinct types of GNDs (12 edge and 6 screw GNDs), i.e., $\xi = 18$. The GND configurations considered in the present work have been represented in Table 3.2.

TABLE 3.2: GND configurations considered for fcc crystals in the present work. $\boldsymbol{m_0^\alpha}$ represents the slip direction and $\boldsymbol{n_0^\alpha}$ represents the direction of slip plane normal (Evers et al., 2004b).

Dislocation density index	Dislocation density type	$\boldsymbol{m_0^\alpha}$	$\boldsymbol{n_0^\alpha}$
1	Edge	$\frac{1}{\sqrt{2}}[1\bar{1}0]$	$\frac{1}{\sqrt{3}}[111]$
2	Edge	$\frac{1}{\sqrt{2}}[10\bar{1}]$	$\frac{1}{\sqrt{3}}[111]$
3	Edge	$\frac{1}{\sqrt{2}}[01\bar{1}]$	$\frac{1}{\sqrt{3}}[111]$
4	Edge	$\frac{1}{\sqrt{2}}[\bar{1}\bar{1}0]$	$\frac{1}{\sqrt{3}}[1\bar{1}\bar{1}]$
5	Edge	$\frac{1}{\sqrt{2}}[101]$	$\frac{1}{\sqrt{3}}[1\bar{1}\bar{1}]$
6	Edge	$\frac{1}{\sqrt{2}}[01\bar{1}]$	$\frac{1}{\sqrt{3}}[1\bar{1}\bar{1}]$
7	Edge	$\frac{1}{\sqrt{2}}[110]$	$\frac{1}{\sqrt{3}}[\bar{1}1\bar{1}]$
8	Edge	$\frac{1}{\sqrt{2}}[\bar{1}01]$	$\frac{1}{\sqrt{3}}[\bar{1}1\bar{1}]$
9	Edge	$\frac{1}{\sqrt{2}}[0\bar{1}\bar{1}]$	$\frac{1}{\sqrt{3}}[\bar{1}1\bar{1}]$
10	Edge	$\frac{1}{\sqrt{2}}[1\bar{1}0]$	$\frac{1}{\sqrt{3}}[\bar{1}\bar{1}1]$
11	Edge	$\frac{1}{\sqrt{2}}[\bar{1}0\bar{1}]$	$\frac{1}{\sqrt{3}}[\bar{1}\bar{1}1]$
12	Edge	$\frac{1}{\sqrt{2}}[011]$	$\frac{1}{\sqrt{3}}[\bar{1}\bar{1}1]$
13	Screw	$\frac{1}{\sqrt{2}}[110]$	$\frac{1}{\sqrt{3}}[1\bar{1}\bar{1}]$ or $\frac{1}{\sqrt{3}}[\bar{1}1\bar{1}]$
14	Screw	$\frac{1}{\sqrt{2}}[101]$	$\frac{1}{\sqrt{3}}[1\bar{1}\bar{1}]$ or $\frac{1}{\sqrt{3}}[\bar{1}\bar{1}1]$
15	Screw	$\frac{1}{\sqrt{2}}[011]$	$\frac{1}{\sqrt{3}}[\bar{1}1\bar{1}]$ or $\frac{1}{\sqrt{3}}[\bar{1}\bar{1}1]$
16	Screw	$\frac{1}{\sqrt{2}}[\bar{1}10]$	$\frac{1}{\sqrt{3}}[111]$ or $\frac{1}{\sqrt{3}}[\bar{1}\bar{1}1]$
17	Screw	$\frac{1}{\sqrt{2}}[10\bar{1}]$	$\frac{1}{\sqrt{3}}[111]$ or $\frac{1}{\sqrt{3}}[\bar{1}1\bar{1}]$
18	Screw	$\frac{1}{\sqrt{2}}[0\bar{1}1]$	$\frac{1}{\sqrt{3}}[111]$ or $\frac{1}{\sqrt{3}}[1\bar{1}\bar{1}]$

Various models have been proposed in literature to account for the contribution of GND density to kinematic hardening in SGCP frameworks. Geers and co-authors have proposed the backstress as a function of spatial distribution of GND density ($\tau_b^\alpha \propto (\partial\rho^\alpha_{GND}/\partial x^\alpha_j)m^\alpha_j$) (Evers et al., 2004a,b; Bayley et al., 2006) to account for the "long-range" stress fields due to GNDs. Gerken and Dawson (2008) proposed a higher order continuum framework in which

the backstress opposing the applied deformation is derived using the Volterra dislocation theory. Work conjugate formulations were also proposed by Gurtin (2002). More recently, Sangid and co-authors have considered a Taylor hardening type of formulation for backstress $\left(\tau_b \propto Gb\sqrt{\rho_{GND}}\right)$ (Kapoor et al., 2018; Bandyopadhyay et al., 2021). Additionally, there have been various local phenomenological and micromechanical models that account for the effect of physically observed substructure evolution mechanisms on the backstress (Armstrong et al., 1966; Chaboche and Nouailhas, 1989; Ohno and Wang, 1993; Zirkle et al., 2021).

In the present work, we adopt the model proposed by Kapoor et al. (2018), where the backstress is modeled using a Taylor hardening type of formulation. Accordingly, the slip system-level backstress is given as a function of the square root of the GND density, i.e.,

$$\tau_b^\alpha = k_{kh} Gb \sqrt{\left|\rho_{GND}^\alpha\right|}\, \mathrm{sgn}\left(\rho_{GND}^\alpha\right) \tag{3.17}$$

where, k_{kh} is the hardening coefficient associated with kinematic hardening due to GNDs. In the above equation, the signum function has been added to account for the directionality of the signed GND density, which in turn influences the slip system-level backstress (Mayeur, 2011). Arsenlis (2001) have shown that GND density can be negative, depending on the discrete basis chosen as reference. This is also important for cyclic deformations, where load reversals can result in a significant variation in dislocation configurations (Laird et al., 1986). The backstress on a slip system may be positive or negative, depending these dislocation configurations. Further, we have implemented the backstress model in the rate form, i.e.,

$$\dot{\tau}_b^\alpha = k_{kh} \frac{Gb}{2\sqrt{\left|\rho_{GND}^\alpha\right|}} \dot{\rho}_{GND}^\alpha \tag{3.18}$$

Physically, Equation (3.18) signifies that an accumulation of GND density on a slip system α leads to development of a backstress τ_b^α, which resists the dislocation glide on that slip system. The rate form ensures that on changing the loading direction the contribution of remnant backstress from the previous loading cycle is not diminished (cf. Patra et al. (2023b)).

These constitutive equations have been implemented and integrated with the open-source finite element library, Multiphysics Object Oriented Simulation Environment (MOOSE) (Permann et al., 2020). For a given Gauss point, the deformation gradient tensor for the current as well as previous timestep is provided to the material model by MOOSE. The material model implicitly updates the stress, the tangent stiffness tensor and the internal state variables, which are then passed back to MOOSE, for checking the global convergence.

Only the displacement variables are considered as degrees of freedom for each of the Gauss points. The spatial gradient terms (cf. Equation (3.11)), which take into account the deformation behavior of neighboring Gauss points, are implemented using the auxiliary variable interface in MOOSE. Finite element shape functions of appropriate order are assigned to these auxiliary variables for computation of the spatial gradients. The auxiliary variable interface in MOOSE facilitates the decoupling of a system of equations. It acts as an in-situ post processing unit and enables the parallel calculation of spatially varying terms and then feeds them back into the material model (Permann et al., 2020). Calculations involving the auxiliary variables do not affect the computation of global Jacobian, thus leading to a significant reduction in the computation costs.

3.2.3.3 SGCP Model Calibration

The SGCP model was calibrated to predict the stress-strain curve as obtained from the uninterrupted tensile tests for Al – 6wt.% Mg alloy.

The experimental EBSD texture for the undeformed material (cf. Figure 3.5) is plotted in the pole figure in Figure 3.1(a). The reduced texture shown in Figure 3.1(a), comprising of 64 randomly selected orientation points from the original texture, was used for the calibration simulations. A cube shaped simulation domain, comprising of 64 cubic grains, with a grain size of 100 μm, and 8 elements per grain, was deformed in uniaxial tension at a nominal strain rate of $10^{-4}\ s^{-1}$.

The elastic constants $(C_{11}, C_{12}, C_{44}, G)$ for Al were used from literature (Alankar et al., 2009). The parameters governing the shape of the enthalpy curve (p and q) should lie in the regime $0 < p < 1$ and $1 < q < 2$ (Patra and McDowell, 2012). Accordingly, we have chosen an estimate that best fits the simulated curve to the experimental response. Since the material under consideration is annealed, a low initial value of SSD density ($1 \times 10^5\ mm^{-2}$) was assumed in our simulations. Further, the isotropic hardening coefficient due to SSDs and the dislocation evolution parameters were calibrated based on fit to the experimental stress-strain response. The most important model parameter governing the strength contribution of GNDs is the kinematic hardening parameter, k_{kh}. We have used a value of $k_{kh} = 0.87$ for all our simulations. The rationale for the choice of this parameter value is given by the demonstration of grain size effects in Section 3.2.3.4. Further, specimen size effects on beam bending are demonstrated in the Section 3.2.3.5. Comparison of the model predictions with the experimental stress-strain response is shown in Figure 3.1(b). As can be seen, a reasonable fit is obtained. Further, the deformed texture predicted by the model is also in

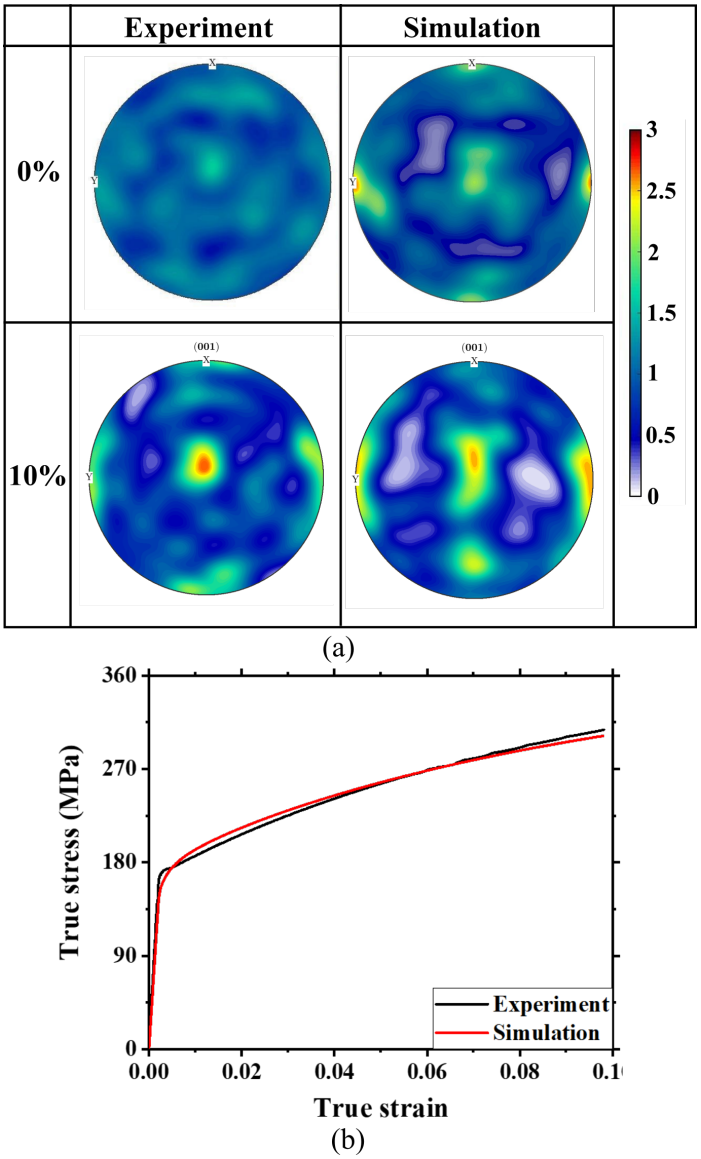

FIGURE 3.1: (a) Experimental and simulated texture, at 0% and 10% applied strain, shown in terms of the (001) pole figure. Orientation data has been obtained from the EBSD maps shown in Figure 3.5. (b) Comparison of the SGCP predicted stress-strain response with the experimental response.

qualitative agreement with the experiments. The calibrated model parameters are given in Table 3.3.

3.2.3.4 Model Prediction of Grain Size Effects

We have performed simulations of polycrystalline ensembles to verify the Hall-Petch effect. Virtual microstructures with four different mean grain sizes ($6\ \mu m, 22\ \mu m, 36\ \mu m, 60\ \mu m$) were tessellated and meshed in a simulation domain of $150 \times 150\ \mu m$ using the open-source

TABLE 3.3: Model parameters calibrated to the experimental stress-strain response.

Parameter	Value	Meaning
C_{11}	108 GPa	
C_{12}	61.3 GPa	Elastic constants
C_{44}	28.5 GPa	
G	25 GPa	Shear modulus
b	2.86 Å	Burger's vector magnitude
$\dot{\gamma}_0^\alpha$	$4 \times 10^2\ s^{-1}$	Reference shear strain rate
ΔF	$0.45Gb^3$	Activation energy barrier
p	0.233	Shape parameter
q	2	Shape parameter
τ_0	58.5 MPa	Threshold slip resistance
$A^{\alpha\xi}$	0.055 if $\alpha \neq \xi$, else 1	Interaction matrix
s_t^α	130 MPa	Thermal slip resistance
k_{mul}	0.2	Dislocation multiplication constant
k_{dyn}	32	Dynamic recovery constant
k_{ih}	0.4355	Isotropic hardening parameter due to SSDs
k_{kh}	0.87	Kinematic hardening parameter due to GNDs
ρ_{SSD}^0	$1 \times 10^5\ mm^{-2}$	Initial SSD density
ρ_{GND}^0	0	Initial GND density

Voronoi tessellation software Neper (Quey et al., 2011). The 2D microstructure was meshed using triangular elements, with quadratic interpolation and a mesh size of $\sim 3\ \mu m$. Further, a generalized plane strain assumption was used. Displacement controlled tensile loading was applied on the top face of the simulation domain at a nominal strain rate of $10^{-4}\ s^{-1}$, up to an effective strain, $\bar{\varepsilon} = 0.015$, while the side faces are traction free. The resulting stress-strain response for the different grain sizes is shown in Figure 3.3(a). The corresponding evolution of total GND density and the effective backstress, $\bar{\tau}_b$, are shown in Figure 3.3(b) and 3.3(c), respectively. It can be seen that the strength of the material increases as the grain size decreases.

It is noted here that the macroscopic stress-strain curves in Figure 3.3(a) do not show appreciable grain size effect, with respect to the initial yield stress (or 0.2% proof stress), while it becomes much more pronounced at higher strains. This is primarily because the strength contribution due to GNDs arises only after the commencement of plastic deformation ($\boldsymbol{\Lambda} = 0$ for $\boldsymbol{F^p} = \boldsymbol{\delta}$ (cf. Equation 3.10)). We note that there are other higher order SGCP frameworks and Discrete Dislocation Dynamics informed crystal plasticity frameworks which are able to predict such phenomena (Ohashi et al., 2007; Ohno and Okumura, 2007). While this is a shortcoming of our model, it is not expected to influence the prediction of misorientations at larger strains. As will be seen later, both our simulations and

experiments predict appreciable misorientations near the grain boundaries only at applied strains $> 5\%$.

As seen in Figure 3.3(b), higher GND density is predicted in the fine-grained microstructures as compared to its coarse-grained counterparts. As the grain size decreases, regions with incompatible deformation and strain gradients (in the vicinity of grain boundaries) increase, which are accommodated by the GNDs. Trends similar to GNDs are observed for the (effective) back stress profiles in Figure 3.3(c). Deformation contours for these simulations are shown below.

Figure 3.2 shows the deformation contours for polycrystalline ensembles in terms of their effective plastic strain, total GND density and the effective backstress contours at 1.5% applied strain. These correspond to the aggregate properties presented in Figure 3.3. Note that these simulations are different from the idealized simulation setups shown later for the prediction of NBGZs, where only two grains were assigned different orientations. The polycrystalline ensembles comprised of several grains with random initial crystallographic orientations, resulting in a weak initial texture. The same can be observed in the IPF maps in Figure 3.2. The effective plastic strain, $\bar{\varepsilon}^p$, contours indicate some sharp localizations in the vicinity of the grain boundaries. Accumulation of GND density is severe in the fine-grained microstructure ($\bar{D} = 6\ \mu m$); its intensity gradually diminishes at higher grain sizes. Similar trends are observed in the contours of effective backstress in Figure 3.2. Further, it can be seen that there is generally a high GND density at the grain boundary triple points and quadruple points. For larger grain sizes ($\bar{D} = 36,\ 60\ \mu m$), the GND density and backstress localizations are restricted to a region close to the grain boundary, whereas finer grain sizes exhibit significant localizations even in the grain interior.

We next present an analysis showing that the model is indeed able to present the Hall-Petch effect (Hall, 1951) using the chosen value of k_{kh}. We only present a brief description here and the reader is referred to Patra et al. (2023b) for a detailed discussion on this topic. As described in Equation 3.17, GNDs contribute to the strengthening through the backstress term, τ_b^α. It has been shown in Patra et al. (2023b) that for small strains and uniaxial loading, a 1D approximation can be used for estimating the size-dependent strength contribution due to GNDs, i.e.,

$$\sigma_{\text{size-dependent}} = k_{kh} G b \sqrt{\rho_{GND}} \approx \bar{\tau}_b \approx \frac{k_{HP}}{\sqrt{\bar{D}}} \tag{3.19}$$

where, ρ_{GND} is the total GND density across all slip systems, $\bar{\tau}_b$ is the effective backstress predicted by the model, k_{HP} is the Hall-Petch coefficient and $\bar{D}$ is the mean grain size. This has been verified from our simulation data in Table 3.4 at 1.5% applied strain.

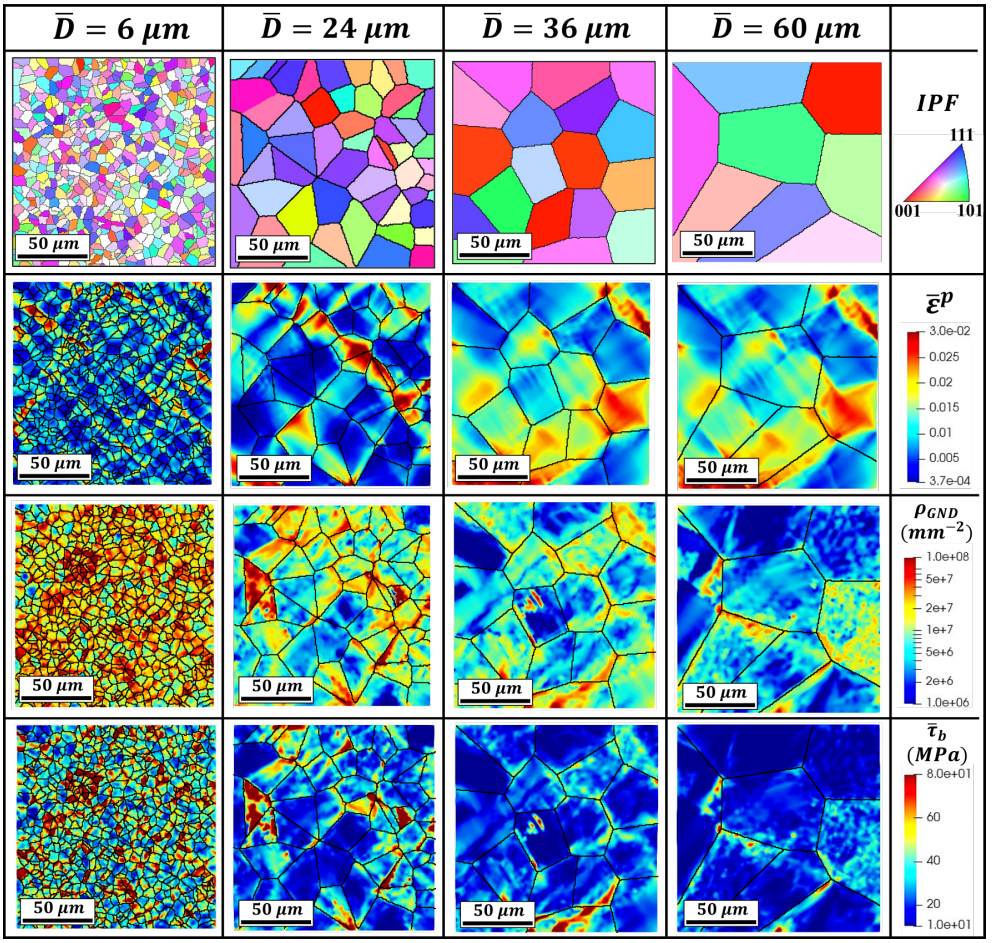

FIGURE 3.2: Deformation contours shown in terms of the effective plastic strain, total GND density and effective back stress at 1.5% applied strain for four different grain sizes. GND density localizations are significantly higher in lower grain size microstructures ($\bar{D} = 6,\ 22\mu m$ as compared to its coarse-grained counterparts ($\bar{D} = 36,\ 60\mu m$)

Based on the total GND density predicted from our simulations, we have first verified that $\sigma_{size-dependent} \approx \bar{\tau}_b$. Small deviations between $\sigma_{size-dependent}$ (estimated directly from the total GND density) and $\bar{\tau}_b$ are due to the fact that 1D approximation may not hold in all cases.

TABLE 3.4: Comparison of $\sigma_{size-dependent}$ with simulated values of $\bar{\tau}_b$ at 1.5% applied strain for simulations with different mean grain sizes.

$\bar{D}(\mu m)$	$\rho_{GND}(mm^{-2})$	$\sigma_{size-dependent}(MPa)$	$\bar{\tau}_b(MPa)$
6	$45.2 \times 10^6\ mm^{-2}$	43.82	45.04
22	$26.2 \times 10^6\ mm^{-2}$	31.26	30.33
36	$11.5 \times 10^6\ mm^{-2}$	22.95	26.29
60	$0.82 \times 10^6\ mm^{-2}$	19.27	18.42

Using the above datapoints, we now estimate the grain size-dependent scaling relations. On

fitting the effective back stress, $\bar{\tau}_b$, to the mean grain size, $\bar{D}$, using Equation (3.19), we obtained a k_{HP} ranging from $56-112 MPa\sqrt{\mu m}$, at different applied strains (from 0.5% to 1.5%). This is also graphically shown in Figure 3.3(d). These values of model predicted Hall-Petch coefficients are within the range of experimentally measured Hall-Petch coefficients ($60-110 MPa\sqrt{\mu m}$), commonly observed in literature for Al alloys (Armstrong et al., 1962; Cordero et al., 2016; Hansen, 1977). Further, as shown in Patra et al. (2023b), the Hall-Petch coefficient may be expected to evolve with applied strain (Ashby, 1970; Cordero et al., 2016). Effect of the variation of k_{kh} has also been discussed in Patra et al. (2023b). An estimate of $k_{kh} = 0.87$ is thus justified and used for all simulations discussed in the present manuscript. Note that, at present, we do not have the experimental data for our material to directly compare the model predicted grain size effects with the experimental counterparts. Finally, we also note that grain size effects have recently been simulated using FFT-based crystal plasticity models by (Berbenni et al., 2020; Haouala et al., 2020) as well.

3.2.3.5 Cantilever Beam Bending Simulations

Size effect during micro beam bending was initially observed by Stölken and Evans (1998). They attributed this phenomenon to the development of sharper strain gradients in smaller beams, which led to higher GND density accumulation and backstress. Such benchmark tests have also been carried out by Arsenlis (2001) and Mayeur and McDowell (2011) in order to investigate the effects of GND density on mechanical properties. We have performed the same here.

The simulation setup and boundary conditions used for the present work are shown in Figure 3.4(a). The simulation domain was discretized using 8 noded brick elements of size 3 μm each. Simulations were performed for different specimen size, while keeping a constant value of L/H = 3. Here, L represents the micro-beam length, and H represents the height and width of the micro-beam. The single crystal micro-beam was of the $< 100 >$ orientation (along the z-axis), and the simulation was performed at 298 K. Three micro-beams of varying thickness (9 μm, 18 μm , 27 μm) were considered for our SGCP simulations. The boundary conditions used for the simulations are schematically shown in Figure 3.4(a) and are described below.

The bottom edge of the left face (nodes ranging from $z = 0|_{x,y=0}$ to $z = 0|_{x,y=0}$) was restricted to move only in the Z direction. The left face of the micro beam is kept vertical at all instants, but allowed to contract freely to accommodate the Poisson effect. The node at $x,\ y = 0$ and $z = H/2$ (edge center) has been pinned, for preventing any rigid body translation. The right face of the micro beam, is subjected to a deformation along the

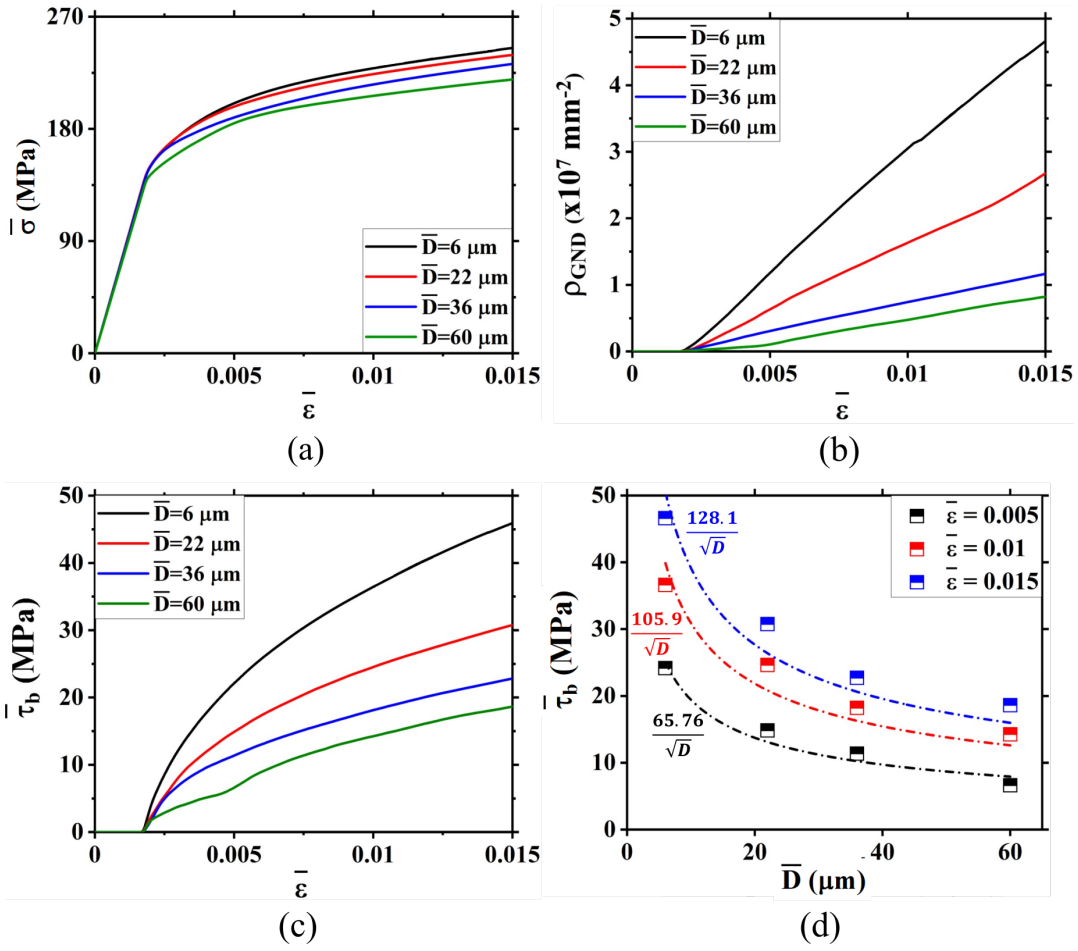

FIGURE 3.3: (a) Tensile stress-strain response predicted by the SGCP model for simulations with different mean grain sizes. Evolution of (b) total GND density, and (c) effective back stress, $\bar{\tau}_b$, with applied strain for the different grain sizes. (d) $\bar{\tau}_b$ plotted as a function of the mean grain size, $\bar{D}$, at different applied strains. The legend in (d) is representative of the best fit parameters to the Hall-Petch equation for each dataset.

negative Y direction, with an additional requirement being that all nodes should be collinear at all instances. The remaining faces of the micro-beam are traction free. A constant strain rate of $\dot{\varepsilon} = 0.0001\ s^{-1}$ has been applied for all the simulations irrespective of its size, up to an effective strain of $\bar{\varepsilon} = 2\%$. The constitutive model parameters used for the material model are specified in Table 3.3.

The bending moment can be given by (Mayeur, 2011):

$$M = \int_0^{\frac{H}{2}} \sigma_{xx}(L, y) y dy \tag{3.20}$$

where, the basis x, y and z have been shown in Figure 3.4 and L and H indicate the length and height of the microbeam, respectively. Since the microbeam length varies significantly, it is essential to quantify the deformation in terms of an independent variable, M_{ref} (reference

bending moment), given by (Mayeur, 2011):

$$M_{ref} = \frac{2}{3}\bar{\tau}_{\text{nuc}}\left(\frac{H}{2}\right)^2 \tag{3.21}$$

where $\bar{\tau}_{nuc}$ is the critical stress for dislocation nucleation (Mayeur, 2011). $\bar{\tau}_{nuc}$ may be written in terms of Schmid factor (m) and yield stress ($\bar{\sigma}_y$) as $\bar{\tau}_{nuc} = \bar{\sigma}_y$. From the tensile stress-strain curves shown in Figure 3.3(a), $\bar{\sigma}_y$ can be seen to be $\sim 140\ MPa$, which gives $\bar{\tau}_{nuc} = 57\ MPa$.

Figure 3.4(b) shows the evolution of the normalized bending moment with the imposed rotation angle (Θ). It can be observed that the bending moment increases on decreasing the beam width from $H = 27\ \mu m$ to $H = 9\ \mu m$. Higher bending moment is observed for the smaller microbeams. Further, the inset in Figure 3.4(b) shows the normalized bending moment at $\Theta = 0.15$ plotted as a function of $H^{-0.5}$. As proposed by Arsenlis (2001), this highlights a nearly linear relationship between the normalized bending moment and $H^{-0.5}$, akin to a Hall-Petch type size dependence (Hall, 1951). Further, the total GND density and effective backstress were also found to increase with decreasing specimen size (see figure 3.4(c,d)). Simulating these effects is generally not possible by using a local crystal plasticity finite element formulation. Our results provide qualitative validation of the model's ability to predict specimen size effects.

3.3 Results and Discussion

3.3.1 Microstructure Evolution During Interrupted Tensile Test

Figure 3.5 shows the microstructure evolution during progressive deformation in terms of the Inverse Pole Figure (IPF), KAM and GND density maps. There is not much change in the IPF maps, indicating the absence of grain fragmentation or significant deformation texture evolution, although the KAM and GND density increase with progressive deformation. However, not all the grains have deformed similarly. Certain grains exhibit higher values of KAM and GND density, as compared to the others. This is possibly due to the orientation-dependent deformation and spatial location of grains with respect to their neighbors; grains which are oriented favorably undergo higher deformation than their counterparts. Further, majority of the grains show higher KAM/GND pile-up in the vicinity of grain boundaries. KAM has generally been found to correlate with the accumulation of GNDs (Calcagnotto et al., 2010; Kundu and Field, 2016) and may be indicative of the development of orientation and strain gradients. Thus, our results are indicative of heterogeneous deformation at the

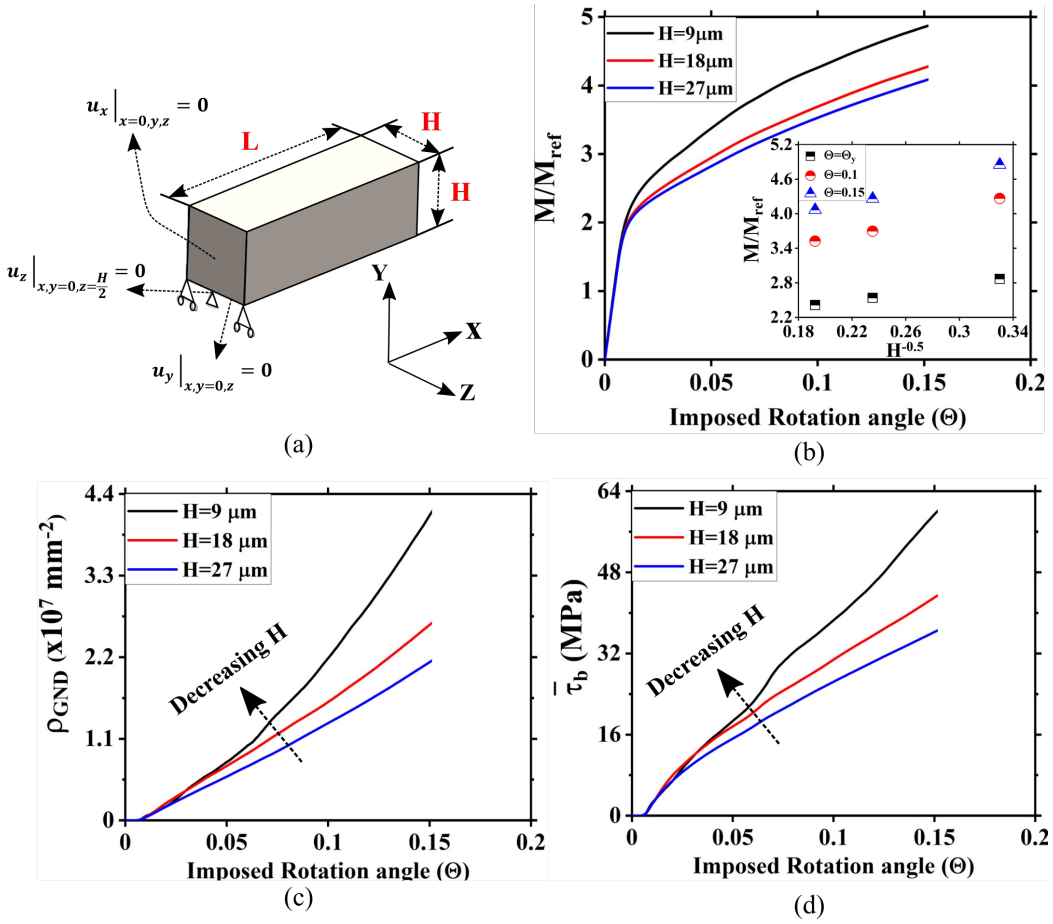

FIGURE 3.4: (a) Simulation setup and boundary conditions for the cantilever beam bending simulations and (b) Normalized bending moment versus imposed rotation angle for beams of different thicknesses. The inset represents the normalized bending moment at $\Theta = 0.15$ plotted as a function of $H^{-0.5}$. Evolution of (c) total GND density and (d) effective backstress, $\bar{\tau}_b$, with increasing beam rotation.

grain boundaries. Further, it is also observed that the severity of these accumulations increases with increasing strain, especially at 7.5% and 10% applied strain.

Various grain clusters were then extracted from such microstructures (see Figure 3.6) to study the characteristics of localized deformation near the grain boundaries. Each grain cluster comprised of two neighboring grains with distinct orientations ($\Delta\theta > 5°$). Further, multiple experiments were carried out in order to accumulate data for statistically significant number of grains.

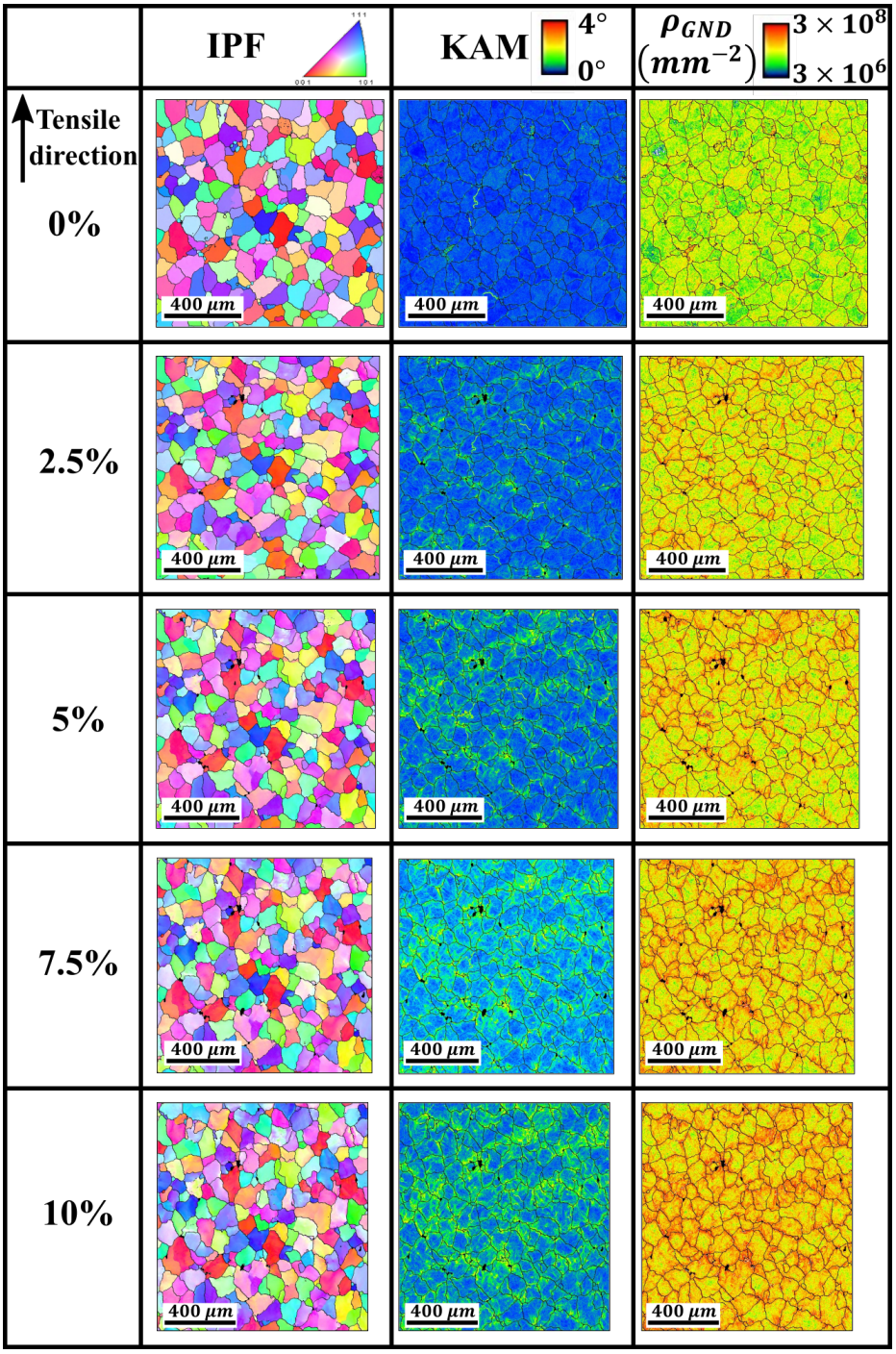

FIGURE 3.5: Inverse Pole Figure (IPF) maps, Kernel Average Misorientation (KAM) maps and GND density maps measured at different stages of progressive tensile deformation.

3.3.2 Estimating the Length of Near Boundary Gradient Zones (NBGZs) from Misorientation Data

For a polycrystalline material, with insignificant crystallographic texture, the microstructure evolution and mechanical properties are expected to be relatively isotropic under uniaxial deformation. However, these properties demonstrate orientation dependence at the grain and sub-grain level, thus leading to a heterogeneous local deformation (Dai, 1997). Multiple slip systems may be activated in the vicinity of a grain boundary, in order to accommodate the constraints posed by the neighboring grains (Mishra et al., 2009; Rollett et al., 2012). Further, GNDs are generated in order to accommodate the local lattice curvature resulting from differential rotation (Tóth et al., 2010). These regions in the vicinity of grain boundaries, with higher localized deformation as compared to the grain interior, are the Near Boundary Gradient Zones (NBGZs) and may be characterized in terms of their length, L_{NBGZ}. In the present work, we study the development of NBGZs primarily in terms of the crystallographic orientation of the grain and its neighbor with which it shares the grain boundary, and also its grain size. However, before moving further, we first describe the method for estimating L_{NBGZ}.

Consider a grain boundary between two grains, with different crystallographic orientations, as shown in Figure 3.6(a). While localized deformation is observed near the grain boundaries after 10% strain, the width of the localized region on either side of the grain boundary is not identical (Figure 3.6(b, d)). Further, heterogeneity in deformation is visible even along length of the grain boundary. Hence, in order to quantitatively measure L_{NBGZ}, it is essential to evaluate the localizations developed along the entire length of the grain boundary. This is accomplished using the procedure described below:

1. KAM values were extracted along sections perpendicular to the grain boundary at regular intervals of 10 μm (Figure 3.6(a)). These extracted KAM values were averaged over the entire length of the grain boundary. Further, they were normalized with respect to the maximum KAM values, generally observed at the grain boundary for the respective experiment or simulation, for 10% applied strain. This normalization has also been performed since the same exact grain pairs were not used in the experiments and simulations. The resulting mean KAM profile is calculated from these measurements and is shown in Figure 3.6(c).

2. We denote L_{NBGZ} as the normal distance from the grain boundary to the point where the mean KAM profile approaches the average KAM value at the grain center (KAM^{avg}_{center}). This procedure was repeated for several grains extracted from the EBSD scans and crystal plasticity simulations (described later).

3. The mean GND density profiles were estimated in a similar fashion as shown in Figure 3.6(d, e), although they were not used to estimate L_{NBGZ}. This is because there is significantly more noise in the GND data as compared to the KAM data.

The GND noise floor, ρ_{nf}, is given as the mean GND density of the undeformed specimen. As described in Genée et al. (2021), the uncertainty, δ, in orientation measurements can be derived from the GND noise floor by $\delta = \rho_{nf} b \Delta x$, where b is the Burgers vector magnitude and Δx is the measurement step size. For the present work, $\rho_{nf} \sim 9.26 \times 10^6\ mm^{-2}$ and $\delta \sim 0.076°$; these values are in range with those in the literature (Genée et al., 2021). At 10% applied strain, the fraction of pixels with GND density below the noise floor, $\rho_{GND} < \rho_{nf}$ was found to be 5.2% and the fraction of pixels with KAM values below the uncertainty, δ, was found to be 0.92% ($KAM_{nf} \sim 0.21°$). Hence, it is perhaps better to compare the NBGZs in terms of the average KAM profiles, instead of the GND densities. Moreover, most of these pixels are expected to lie in the grain interior, rather than at the grain boundary, and are not expected to influence the analysis of the results presented in the following sections. Finally, it should also be noted that EBSD step size may also contribute to the noise/fluctuations in the GND density measurements (Jiang et al., 2013b).

It should be noted here that any further reference to the term "KAM profile" or "GND density profile" refers to the mean KAM or GND density profiles, i.e., the values averaged over the entire length of the grain boundary. Further, since grain sizes vary between different grains, we have plotted L_{NBGZ} as a normalized value with respect to the grain size, D.

In order to study the effect of grain orientation on L_{NBGZ}, it is important to understand the deformation characteristics between different pairs of grains. Hence, we have classified the grain orientations shown in the EBSD microstructure (Figure 3.5) into three regions based on their initial grain-averaged Schmid factor, m. The reason for the choice of this as a classification parameter is because we have verified that the grain averaged Schmid factor does not vary significantly in the deformation range of interest (results are not presented here for brevity). The three regions can be briefly summarized as follows:

1. Region A, with $m < 0.35$, comprises of hard grains unfavorably oriented for deformation.

2. Region B, with $0.35 < m < 0.45$, represents grains with intermediate Schmid factors, comprises of grains which are neither hard nor soft.

3. Region C, with $m > 0.45$, represents the soft grains that are favorably oriented for deformation.

Using the above classification, numerous grain clusters were considered, where a grain boundary was shared between grains lying in either of the three distinct regions. Finally, it was also ensured that the length of the grain boundary is sufficiently large ($> 50\ \mu m$) to minimize the effect of triple and quadruple junctions, if any. Note that all further references to the term "Schmid factor" indicate the "initial grain average Schmid factor", and not the local instantaneous Schmid factor.

Further, the use of local micromechanical Schmid factors is avoided due to the use of virtual microstructures over their experimental counterparts for our Strain Gradient Crystal Plasticity (SGCP) simulations. In the undeformed condition (at $\varepsilon = 0$), our simulation cell, though realistic does not account for the orientation gradients/residual strains in the as-received material, thus leading to differences in the local Schmid factor values between experiments and simulations. In order to mitigate such differences and have an identical baseline, we have used grain-average Schmid factors for our analysis.

Finally, the Schmid factor is used over the Taylor factor, because the latter is generally used to characterize ensemble averaged properties, while we are interested in the local properties.

3.3.3 SGCP Simulations of Polycrystalline Ensembles

Figure 3.7 shows the simulation setup used in the crystal plasticity simulations. This comprises of three domains with different crystallographic orientations. The two domains in the interior are representative of a cluster of two grains with different orientations and sharing a grain boundary where NBGZs are expected to develop. This grain cluster is embedded in a domain which has a crystallographic orientation representative of the average Schmid factor of the grain cluster.

The size of the simulation cell is $150 \times 150\ \mu m$ and the average size of the embedded grains is $\bar{D}_{sim} \sim 47 \mu m$. The microstructures were tessellated using the open-source software, Neper (Quey et al., 2011) and meshed with six-noded triangular elements, with quadratic interpolation, and an average element size $\sim 3 \pm 1\ \mu m$. Further, multiple such random tessellations were generated, in order to accumulate data for statistically significant number of grains. We have ensured the average grain size is similar for all the tessellations.

Loading and boundary conditions are similar to the simulations given Section 3.2.3.4. All simulations were performed till 10% applied strain, as in the experiments. It is important to note here that the experimental microstructures were not utilized directly as input to our idealized SGCP simulations. This is primarily due to the presence of non-smooth grain boundaries in pixel-based EBSD maps. These may result in erroneous prediction due to

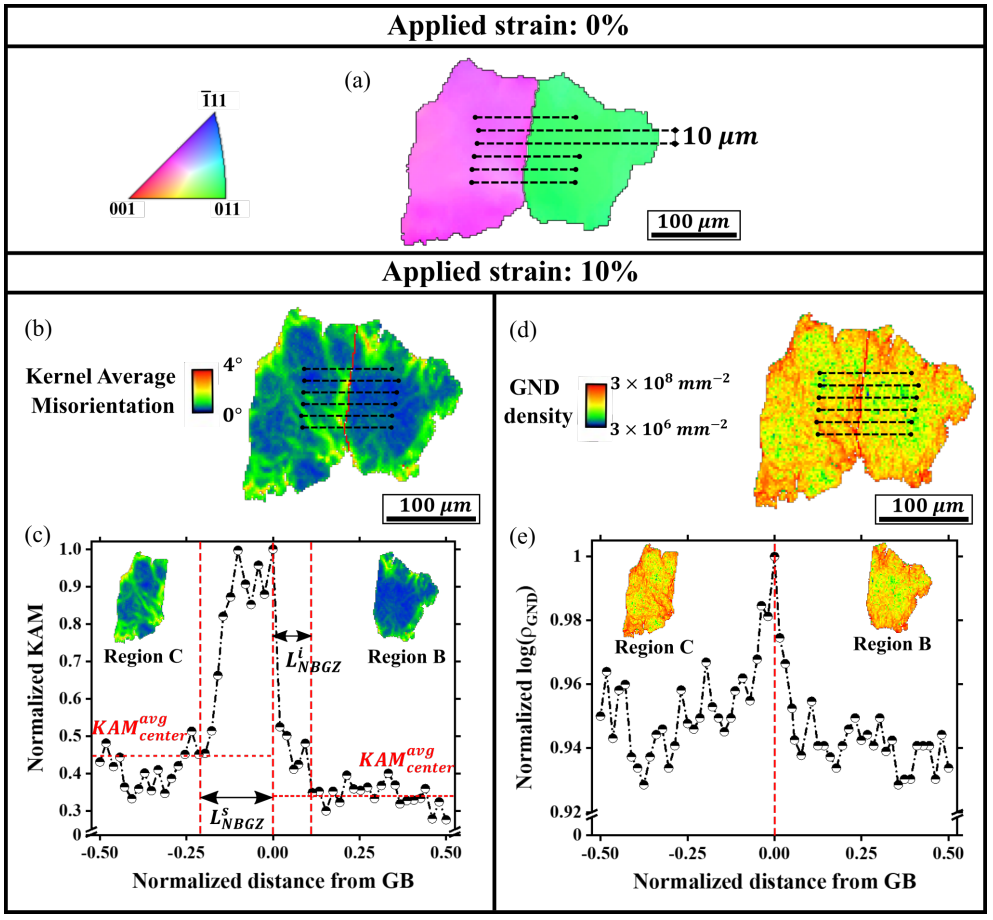

FIGURE 3.6: A grain cluster comprising of a shared grain boundary between grains of region B-region C, shown before deformation (a) and after deformation (b), (d). The horizontal dotted lines in (a,b,d) indicate the sections along which the KAM and GND density data have been extracted. The corresponding mean profiles of KAM and GND density are shown in (c) and (e), respectively. The method for estimating L_{NBGZ} is also shown graphically in (c).

artificial GND density and backstress pile-ups in the vicinity of the grain boundary. A lower step/element size may smoothen the grain boundary pixelation, however, with higher computational costs.

Further, the area of deformation considered in the simulations is also significantly smaller than that studied in the experiments. This again is due to limitations in the computational costs. A direct comparison of experimental and simulated microstructures is, of course, ideal. However, our idealized microstructures have a grain pair embedded in a domain with mean orientation, so as negate some of the effects of neighboring grains (stress concentrations and localizations), while still representing realistic grain structures and orientations. In order to obtain a representative behavior of NBGZs, we have utilized 9 such grain pairs (total 18 grains) for our idealized SGCP simulations.

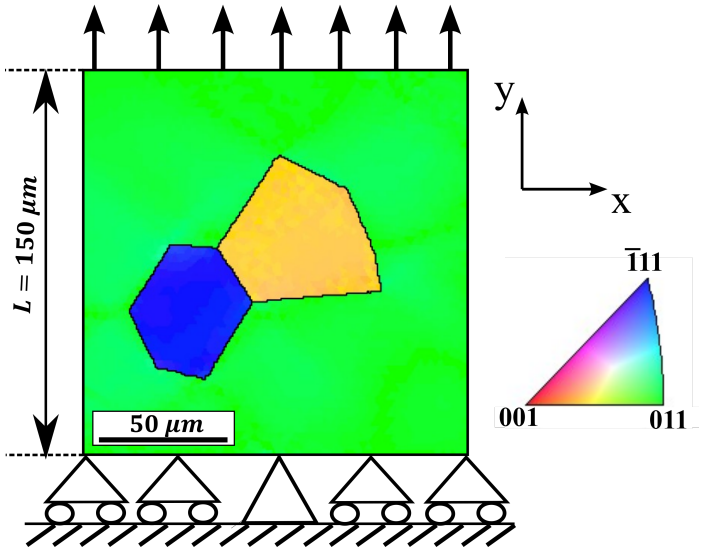

FIGURE 3.7: Simulation setup and boundary conditions for the SGCP model shown on a virtual microstructure generated using Neper (Quey et al., 2011). The colors of the grains in the simulation domain are indicative of the orientations shown on the IPF.

Before moving forward, it should be noted that the average grain size considered in the simulations ($\bar{D}_{sim} \sim 47\mu m$) is lower than those observed in the experimental microstructures (cf. Figure 3.5, $\bar{D}_{exp} \sim 92\mu m$). The choice of grain size and simulation domain size is primarily influenced by the total number of elements in the simulation domain, while using a reasonably fine mesh (3 μm) to predict orientation gradients in the regions of stress concentration. A typical simulation domain has $4000 - 5000$ elements and takes $\sim$ 150 hours to reach 10% applied strain when run on 96 parallel processors. Using a larger grain size or simulation domain size would significantly increase the simulation time. However, we have performed one set of parametric simulations by increasing the grain size and also commented on the effect of grain size on the length of NBGZs in Section 3.3.5.2.

3.3.3.1 Representative Deformation Contours Obtained from Simulations

Figure 3.8 shows the contours of the simulated von Mises effective stress, $\bar{\sigma}$, and effective plastic strain, $\bar{\varepsilon}^p$, at 2.5%, 5%, 7.5% and 10% applied strain using the SGCP model for the simulation setup shown in Figure 3.7. The corresponding results obtained using a local crystal plasticity model (GND density and the kinematic hardening parameter, k_{kh}, set to zero) are also shown in Figure 3.8. Generally speaking, an increase in flow stress is observed with increasing plastic strain. A higher effective stress is observed in the grain with lower Schmid factor ($m = 0.29$). Since, the grain is unfavorably oriented for deformation, a higher stress is needed to accommodate the imposed deformation. In contrast, the soft grain ($m = 0.49$) undergoes plastic deformation readily, thus a higher effective plastic strain

is observed for the same in Figure 3.8. The above trends are observed in both simulations, with and without strain gradients. Stress localizations (refer markers 1, 4 in Figure 3.8) and plastic strain localizations (refer markers 2, 5 in Figure 3.8) around triple junctions can be seen in the material deformed to 2.5% and 5% strains; the localizations become intense at higher strains (10%) (Chen et al., 2000).

The effective plastic strain contours show that the accommodated plastic strain varies between the grains, and even within the grains. Differential rotation is more evident in the softer grain, as the grain core deforms preferentially. The resulting plastic strain gradients arise primarily due to the effect of varying constraints acting on the grain (cf. Section 3.1). These plastic strain gradients result in the generation of GND density and the ensuing backstress further opposes the applied deformation. Similar contours can be observed in the $\bar{\sigma}$ map on moving from the grain interior towards the grain boundary.

Comparison of deformation contours between the SGCP model and the local model clearly shows that the SGCP model predicts sharper plastic strain concentrations and gradients even in the grain interior (refer marker 3 in Figure 3.8), as compared to the local model (refer marker 6 in Figure 3.8). These predictions by the SGCP model may be indicative of the formation of slip lines commonly observed in metallic systems (Kang et al., 2006) (also see the mesh convergence study in Figure 3.9). In contrast, deformation contours predicted by the local model appear to be more homogeneous, with little or no evidence of slip localizations in the grain interiors (refer marker 6 in Figure 3.8). These observations indicate that the SGCP model is perhaps better suited for simulating localized deformation in the regions of incompatible deformation.

As discussed previously, KAM and GND density may vary based on the consideration of element size in finite element simulations or step size in the EBSD measurements (Subedi et al., 2015). An ideal element size should be such that the KAM and GND density vary minimally with change in the mesh/step size. In order to explore this effect, we deformed a polycrystalline ensemble in 50 $\mu m \times 50$ μm simulation domain, meshed with three different element sizes, namely 1 μm, 3 μm and 5 μm, and identical grain structures and orientations. Six noded triangular elements, with quadratic interpolation, were used for these simulations. The top face of the simulation cell was subjected to uniaxial tensile deformation at a nominal strain rate of 0.0001 s^{-1} up to an applied strain of 2%. The grain in the center of the simulation cell was assigned a crystallographic orientation with Schmid factor of 0.49, while the surrounding grains were assigned random orientations.

Figure 3.9(a) shows the KAM and effective plastic strain contours for different element sizes at 2% applied strain. We have resorted to line profile analysis of the KAM in order

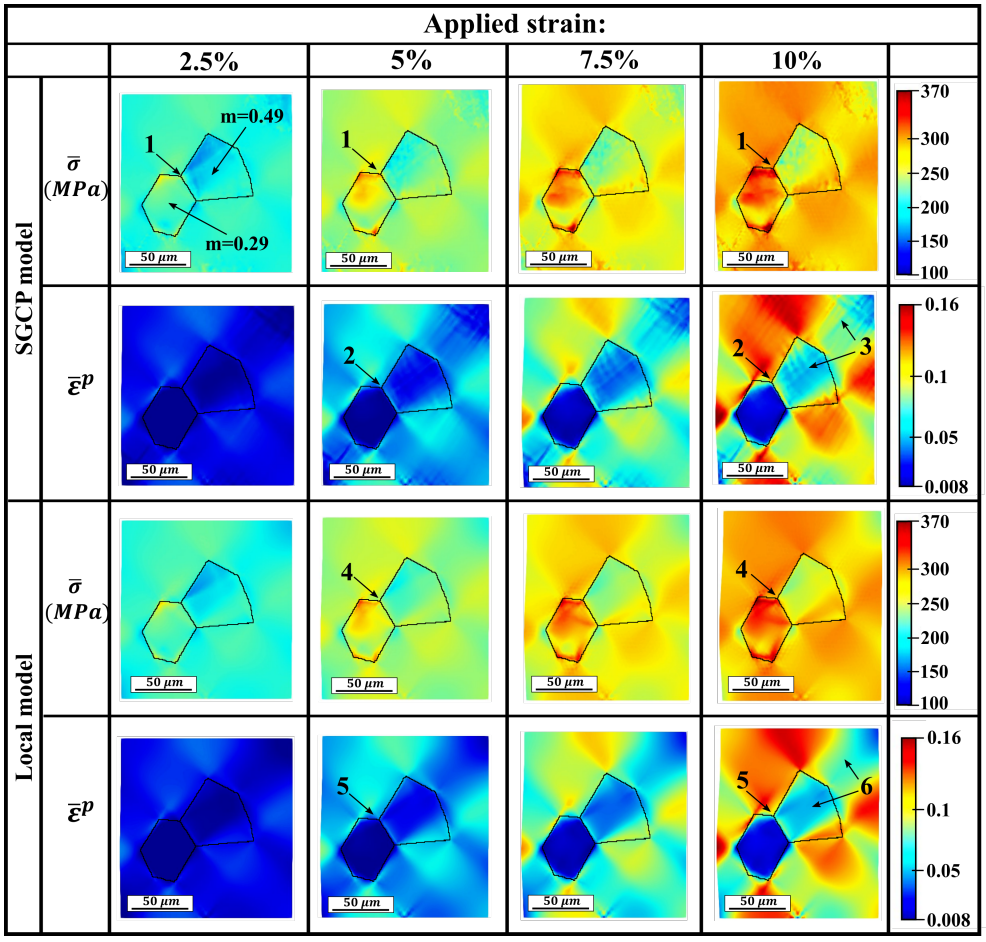

FIGURE 3.8: Evolution of effective stress ($\bar{\sigma}$ MPa) and effective plastic strain ($\bar{\varepsilon}^p$), with increasing applied strain, simulated using the SGCP model and the local crystal plasticity model. These deformation contours are for the virtual microstructure shown in Figure 3.7. Markers $1-6$ indicate various regions of stress and strain concentrations, which have been discussed in the text (Section 3.3.3.1).

to establish mesh convergence for our SGCP simulations. Figure 3.9(b) shows the KAM profile extracted along the line highlighted in Figure 3.9(a). It can be clearly seen that for the 5 μm mesh size simulation, the KAM values at the grain boundaries of the center grain are lower than that obtained using a 3 μm and 1 μm mesh size. The KAM values predicted using the 3 μm and 1 μm mesh size are similar (both at the grain boundaries and towards the grain interiors), thus establishing "qualitative" mesh convergence. Some local element-level fluctuations are, of course, observed in the mesh size 3 μm and 1 μm profiles in Figure 3.9(b). This could be potentially due to random meshing and arrangement of the triangular elements. However, these results indicate that a reasonable concurrence in the KAM profiles has been achieved using mesh sizes of 3 μm or lower.

Further, the strain contours indicate the development of strain localizations due to slip lines. For example, the markers shown in Figure 3.9(a) highlight that the slip lines can

be captured using finer element sizes in our simulations. It may be expected that the localizations can be predicted, if the element size is of the same order as the underlying deformation characteristic. Using a coarse mesh, these bands appear as diffuse localizations, while using finer mesh sizes, these bands appear as slip lines in our SGCP simulations. From a mechanistic standpoint, these slip lines are manifestations of the slip system resolved strain localizations that can be observed at finer resolutions. Presumably, the element type (triangular or quadrilateral) and their spatial arrangement during meshing could also play a role in the nature of the predicted strain localization patterns and KAM fluctuations. For example, Zhou et al. (2020) have shown that the strain contours (specifically, localizations) appear pixelated when using quadrilateral elements.

Figure 3.10 shows the evolution of the total GND density, ρ_{GND} (summed up over all slip systems), and the effective backstress, $\bar{\tau}_b$, with applied strain for the same microstructure. The simulated GND density varies from $10^6 - 10^8\ mm^{-2}$, which is in the range of experimentally observed values $3 \times 10^6 - 3 \times 10^8\ mm^{-2}$. As reported previously (Evers et al., 2004b; Liang and Dunne, 2009; Calcagnotto et al., 2010; Allain-Bonasso et al., 2012), GND concentrations are observed at the grain boundaries. Generally speaking, the backstress develops in the same regions where the GND pile-ups occur. The GND pile-up and backstress subsequently increases with increasing strain. At 10% applied strain, the peak value of backstress is $\sim 180MPa$, amounting to more than 50% of the flow stress in the regions of stress concentrations. Based on analysis of experimental measurements for Al-Zn alloys subjected to creep loading, such high values of long range internal stresses have indeed been reported (Blum and Finkel, 1982).

This indicates the development of high local residual stresses and is expected to influence the subsequent deformation and failure. Also note that not all grains have identical width of these GND concentrations, i.e., the GND concentrations are not symmetric across the grain boundary (refer makers 1,2 in Figure 3.10). The soft grain has a wider region with higher GND density (refer marker 1 in Figure 3.10). The grain core for the hard grain has remained intact (refer marker 3 in Figure 3.10) and the observed localizations are limited to a small region close to the grain boundary. Finally, these quantities are not predicted by the local crystal plasticity model and hence are not shown here.

Figure 3.11 shows the evolution of KAM at different applied strains for the SGCP model and also compared with predictions from the local crystal plasticity model. The KAM, calculated using the methodology discussed in Section 3.2.2, indicates a similar trend as observed in the GND density maps in Figure 3.10. Generally speaking, the SGCP model tends to predict higher values of KAM even in the grain interiors. In contrast, the local crystal plasticity model only predicts some KAM in the immediate vicinity of grain boundaries, with little

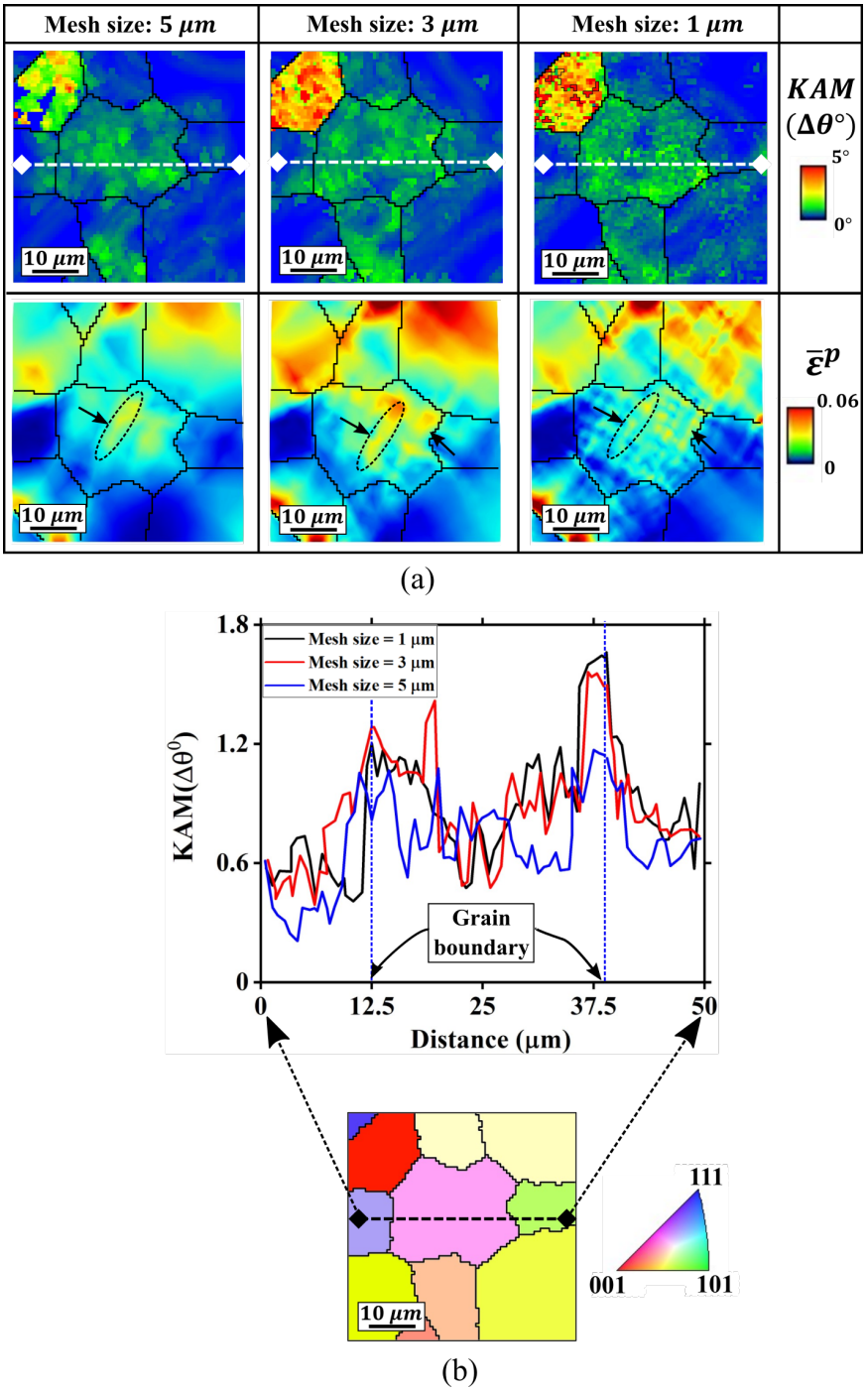

FIGURE 3.9: Mesh convergence study performed on the same polycrystalline domain with three different element sizes, $1, 3$ and 5 μm, showing (a) the KAM and effective plastic strain, $\bar{\varepsilon}^p$, contours in the three microstructures at 2% applied strain. The KAM values extracted along the dotted white line are plotted for the three different mesh sizes in (b).

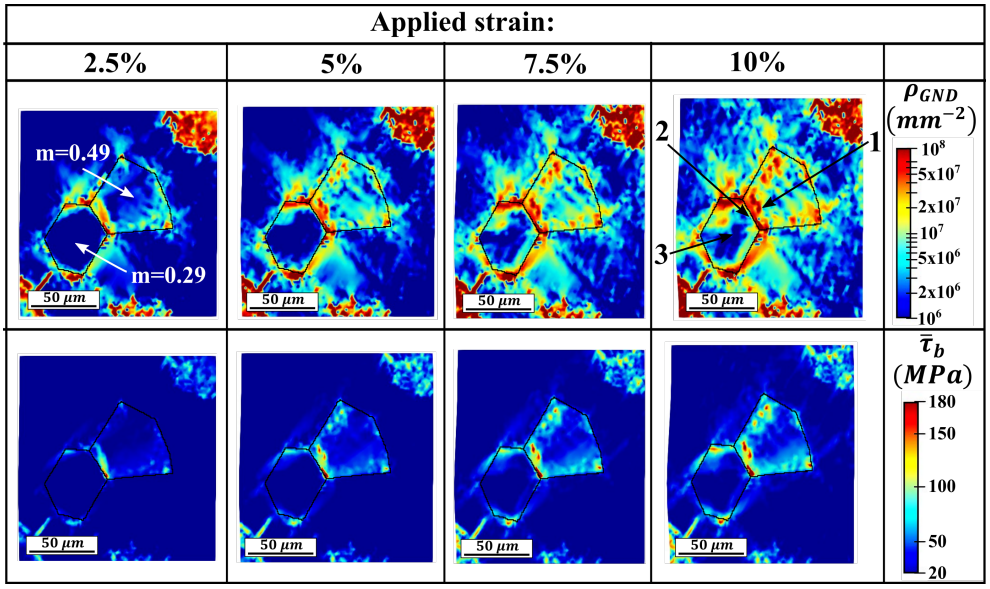

FIGURE 3.10: Evolution of total GND density,ρ_{GND} (mm^{-2}), and effective backstress, $\bar{\tau}_b$ (MPa), with increasing strain for the simulation setup shown in Figure 3.7. Markers 1 and 2 represent GND density pile-up within the NBGZ, while marker 3 represents low GND density observed at the grain core.

or no KAM in the grain interiors. Some KAM localizations observed in the local model's predictions are primarily due to the stress/strain concentrations at the triple junctions (refer markers 1,2 in Figure 3.11).

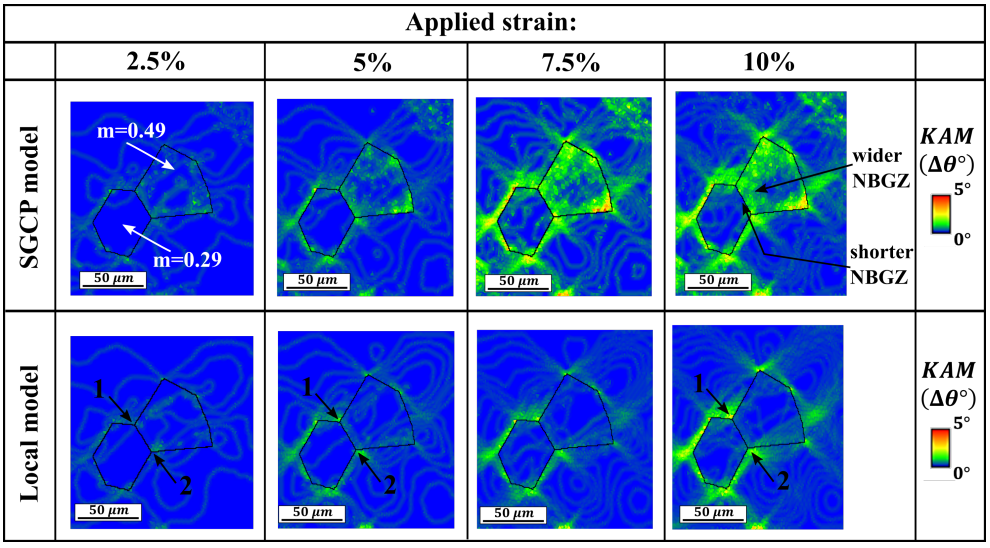

FIGURE 3.11: Evolution of KAM at different applied strains as predicted by the SGCP model and the local crystal plasticity model. These contours are for the virtual microstructure shown in figure 3.7. The Markers 1 and 2 represent the KAM buildup at triple junctions in the local CPFE model.

The following discussion is for predictions with the SGCP model. At lower applied strains, the KAM is sparsely distributed in the grain interior as well as at the grain boundaries.

However, with increasing strain (5% to 10%), the KAM tends to localize in the vicinity of the grain boundaries. Further, this localization is more diffuse in the soft grain, as compared to that in the hard grain, which shows a narrower localized region. This observation is similar to the GND and backstress predictions in Figure 3.10. For a soft grain, multiple slip systems are oriented favorably for slip, leading to significant deformation within the grain core, as compared to the hard grain (Figure 3.8). As a result of this, the GND pile-up at the grain boundary becomes diffuse, leading to a more diffuse NBGZ. It is important to note that the magnitude of differential rotation between the grain core and grain boundaries may still be large; it is only the spatial gradient of misorientation that becomes diffuse. In contrast, for the hard grain, the grain core remains intact and a severe misorientation gradient develops close to the grain boundary, leading to a sharper and shorter NBGZ. Note that similar observations were also observed in the experimental contours in Figure 3.6.

While the present study mainly focuses on the evolution of NBGZ, some important observations have also been noted with respect to KAM/ρ_{GND} concentrations near the triple junctions. Firstly, the localizations in the vicinity of triple junctions start developing much earlier than those near the grain boundaries. With increasing deformation, these localizations propagate farther across the grain boundary. This can be noted from our deformed experimental (cf. Figure 3.5) as well as simulated (cf. Figures 3.10 and 3.11) microstructures, where KAM/ρ_{GND} concentrations can be seen to originate near triple junctions even at low applied strains (2.5%). Additionally, the deformation contours reveal that localizations developing at triple junctions primarily effect the soft and intermediate grains. The hard grains are affected only at large applied strains (cf. Figures 3.10 and 3.10). Further, the deformation contours in Figure 3.2 show that the localizations developing at triple junctions are also influenced by the angle subtended between the boundaries forming the triple junctions. The ρ_{GND} concentrations are seen to primarily develop within grains whose boundaries subtend the lowest angle at the triple junction. However, this may also be influenced by the crystallographic orientation of the grains/near-neighbors, and statistics from a larger number of simulated microstructures would be needed to validate this observation.

Before moving further, we note that grain boundary migration and associated grain shape change have not been considered in the constitutive model. While such effects may indeed be present in the experiments, their effects may be neglected at the small strains considered in the present study.

3.3.3.2 Correlating Various Substructure Evolution Properties Related to Plastic Deformation

It has been generally hypothesized and also shown from experimental observations that the GND density correlates with KAM (Calcagnotto et al., 2010; Kubushiro et al., 2015; Rui et al., 2019; Fu et al., 2022). We have extracted the mean KAM and the GND density along the grain boundary and plotted the normalized values as a function of the normalized distance from the grain boundary for the simulated microstructure in Figure 3.12. This has been done using the methodology described in Section 3.3.2. It can be seen that the normalized values of KAM and $\log(\rho_{GND})$ correlate well with each other, not just in the vicinity of the grain boundary, but also in the grain interior. In a recent study, Rui et al. (2019) proposed that the total GND density includes the contribution from lattice curvatures induced by buckling, in-surface bending, torsion, out of surface bending and an additional lattice curvature component, which does not belong to any of the elastic strain modes. Additionally, they showed that the misorientation measure, KAM, can be directly correlated to the GND density. Although our simulations do not decompose the total GND density into these individual components, the simulated (total) GND density does exhibit qualitative correlation with KAM (see Figure 3.12).

Unlike GNDs, Statistically Stored Dislocations (SSDs) are generated due to dislocation bowing, trapping and multiplication processes generally associated with homogeneous plastic deformation (Ashby, 1970). Hence, the SSD density may be expected to correlate well with the effective plastic strain (Brinckmann et al., 2006; Zhang and Aifantis, 2015; Lu et al., 2020). A similar observation is reflected in the comparison of the average effective plastic strain profile with the corresponding $\log(\rho_{SSD})$ in Figure 3.12. The simulated SSD density profile qualitatively correlate with the effective plastic strain profile. An additional observation from Figure 3.12 is that the GND density/KAM profiles exhibit a significant amount of noise in comparison to the SSD density/effective plastic strain profiles. The local variability in the GND density and the resulting KAM could be due to the fact that the net flux of signed dislocations at a material point (pixel/element) would depend on the size of the corresponding pixel/element (Jiang et al., 2013b; Zhu et al., 2018).

It can also be seen from Figure 3.12 that the effective plastic strain profile has a rather steep drop as we move from the grain boundary towards the grain core for the hard grain ($m = 0.29$). This indicates that for the hard grain, the grain core has not deformed significantly and deformation is primarily restricted to the vicinity of the grain boundary. Such a sharp plastic strain gradient results in a highly concentrated localization of GND density, which in turn results in a sharp NBGZ for the hard grain. In contrast, the soft grain exhibits a

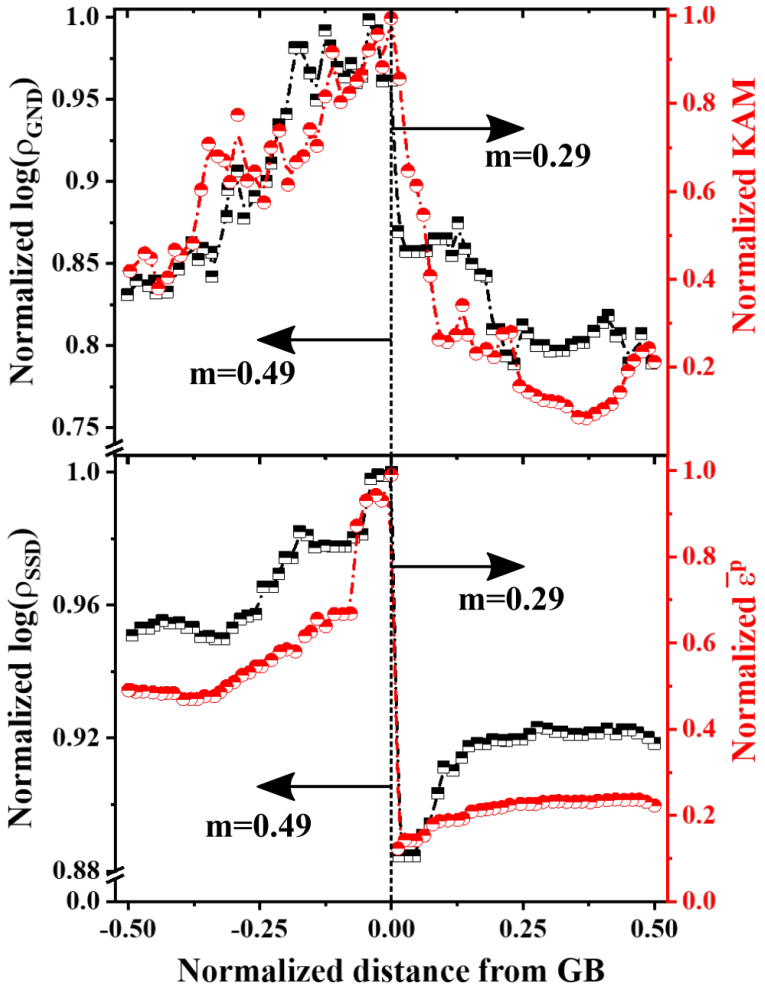

FIGURE 3.12: Mean profile of the normalized GND density and KAM (top), and the normalized SSD density and effective plastic strain (bottom) as a function of distance from the grain boundary at an applied strain of 10%. These data points have been extracted for the virtual microstructure shown in Figure 3.7.

low plastic strain gradient (Figure 3.12). This, in turn, may result in a diffuse NBGZ for the soft grain.

3.3.4 Comparison of Experimental and Simulated NBGZs

3.3.4.1 Evolution of Kernel Average Misorientation (KAM) with Applied Strain

The experimental microstructures, an example shown in Figure 3.5, indicate that the average KAM increases with applied strain. A similar trend is also observed from the simulated KAM contours shown in Figure 3.11. Here we compare the evolution of KAM between the experiments and simulations by looking at the line profiles. For this we consider a grain cluster comprising of a grain boundary shared between the grains lying in region B ($0.35 <$

$m < 0.45$) and region C ($m > 0.45$). The experimental and simulated microstructures are shown in Figure 3.13 (a), (b), and (c). Figure 3.13(b) shows the deformation contour in terms of KAM using a SGCP model, whereas Figure 3.13(c) shows the same using a local CPFE model (cf. Section 3.3.3.1). As observed previously in Figure 3.11, the local CPFE model does not predict any significant KAM buildup within the NBGZ. This proves that the SGCP model predicts a more realistic deformation behavior as compared to the local CPFE model. Figure 3.13 (d), (e), and (f) compares the normalized KAM profiles as a function of the normalized distance from the grain boundary at different applied strains for experiments and simulations. This was done using the methodology listed in Section 3.3.2. Note that all KAM values have been normalized with respect to the maximum values observed in the respective experiment or simulation. As discussed earlier, KAM (and also GND density) is a geometry-dependent quantity and depends on the step size in EBSD measurements and mesh size in simulations (Subedi et al., 2015). However, the extreme values are comparable between the experiments and simulations. For example, the peak values of KAM were observed to be 1.02° at 2.5%, 1.14° at 5%, 1.29° at 7.5% and 1.57° at 10% applied strain respectively. For simulations, the peak KAM values predicted at the grain boundaries using the SGCP model were: 0.92° at 2.5%, 1.32° at 5%, 1.46° at 7.5% and 2.32° at 10% applied strain, respectively, in grains with similar orientations. Nonetheless, normalizing the KAM allows qualitative comparison of the line profiles for dissimilar microstructures with distinct grain morphologies.

The misorientation development predicted by the local CPFE model is generally negligible, with some intermittent fluctuations, which are observed at the grain boundary as well as the grain interior. However, the normalized KAM profiles are comparable between experiments and our SGCP simulations. For example, a sharper KAM profile is observed for the relatively harder grain ($m = 0.41$) for both experiments and SGCP simulations, as compared to the soft grain ($m = 0.49$). Whereas the local CPFE model does not highlight such a pile-up within the NBGZ. At low strains (2.5%), the misorientation development at the grain boundaries is relatively small in our SGCP simulations, whereas some misorientation is observed in experiments. At higher strains, the KAM concentrations at the grain boundaries rise significantly, both in experiments and SGCP simulations. Note that similar trends were also observed by comparing the GND density profiles; the data has not been presented here for brevity.

It is noted here that the average profiles of experimental KAM saturate at higher strains, whereas, the simulated KAM (using SGCP) does not exhibit a similar saturation. This could be due to the presence of fewer number of grains present within the simulation domain. The imposed deformation is accommodated in these fewer grains in the simulation by

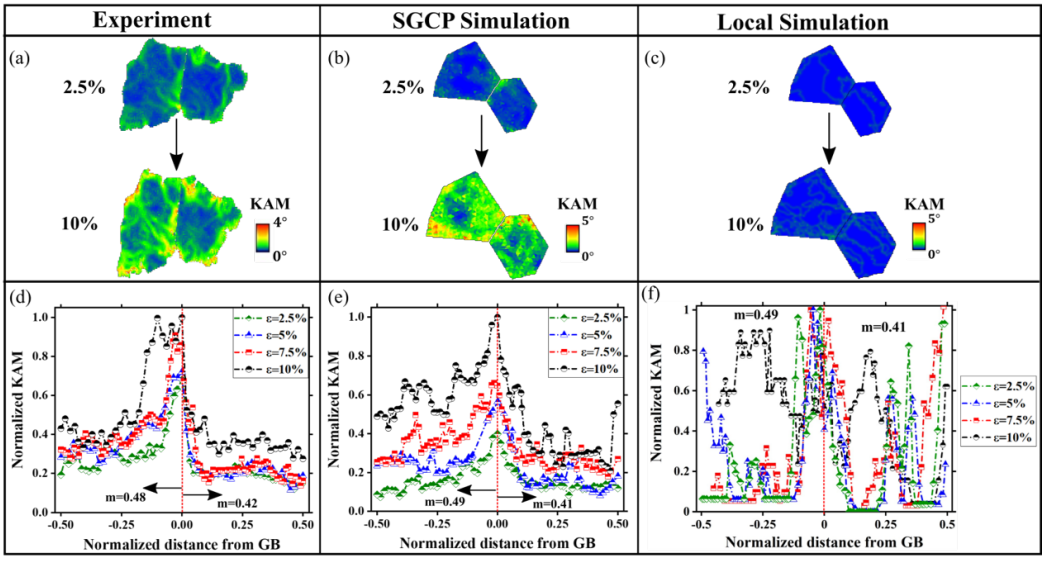

FIGURE 3.13: Comparison of representative KAM profiles with progressive deformation between experiments and simulations. The grain clusters considered for this analysis are shown in (a),(b) and (c), while the normalized KAM plotted as function of distance from the grain boundary at different applied strains is shown in (c),(d) and (e). KAM contour (b) and its respective (average) profile (d) are predicted by the SGCP model, whereas KAM contour (c) and its respective (average) profile (e) are predicted by the local CPFE framework.

deformation both in the NBGZs and the grain interior, thus making them more compliant. This may have contributed to the continuous KAM build up (and lack of saturation) in the soft grain as observed in our SGCP simulations. Additionally, the localizations developing at the triple junctions/sharp corners of the grain boundaries also contribute to higher KAM values in our SGCP simulations.

Keskar et al. (2014) attributed the development of NBGZ to the presence of large, localized Near Boundary Mesoscopic Shear (NBMS). With increasing strain, accommodation of the imposed shape change leads to a rise in the NBMS, which further results in widening of the NBGZ.

3.3.5 Comparison of KAM and GND Profiles for Different Grain Orientations

The preceding section focused on analyzing the evolution of KAM localizations within the NBGZ, with increasing strain, for a given grain cluster. Here, we analyze the buildup of mean KAM and GND density between different combination of grain pairs, with different grain orientations, at 10% applied strain and compare the same between experiments and simulations. We chose a random grain pair from the experimental microstructure and

a corresponding virtual grain pair. As mentioned earlier, normalized data was used for comparison between simulations and model predictions.

Figure 3.14 shows the comparison between experimental and simulated normalized KAM profiles, for representative individual grain pairs lying in each of the three regions A, B and C (cf. Section 3.3.2). In each of these plots in Figure 3.14, the left-hand side represents KAM profile for the softer grain (higher m), while the right-hand side represents the KAM profile for the harder grain (lower m) for the grain pair under consideration. Lines connected by symbols represent the mean values, while the scatter is represented by dotted lines. The horizontal dashed line denotes the average KAM in the grain interior. Additionally, the following abbreviations have been used: L^h_{NBGZ}: L_{NBGZ} for the hard grain (region A); L^i_{NBGZ}: L_{NBGZ} for the grain with intermediate orientation (region B) and L^s_{NBGZ}: L_{NBGZ} for the soft grain (region C). The following key observations can be summarized from Figure 3.14.

The average line profiles and L_{NBGZ} predicted by the model for each of the regions is qualitatively similar to the experimental counterparts, except for the region B-A, where the simulation underpredicts the L^h_{NBGZ} in the harder grain. This could be due to the essentially 2D nature of the simulations, where deformation beneath the surface is not accounted for. In the experiments, there may be additional compatible deformation modes beneath the surface of the specimens that can contribute to the widening of NBGZs. Also, presence of neighboring grains along the third direction (normal to the surface) would introduce non-uniform localizations at grain boundaries during deformation, which can further contribute to the widening of NBGZs. On the other hand, the simulations only consider a generalized plane strain assumption by introducing a scalar out-of-plane strain component (Li and Lim, 2005). This could play a role in the deformation of the harder grain, where the out-of-plane strain may accommodate the imposed deformation (rather than the in-plane components) and predict a wider NBGZ. Further, strain localizations from nearby triple junctions may also be influencing this behavior. Generally speaking, harder grains (lower m) have a smaller L_{NBGZ} as compared to the softer grains (higher m). As discussed earlier, the grain core of a softer grain (higher m) deforms readily, thus diffusing out the localizations developing in the NBGZ, which leads to a higher L_{NBGZ}. It can also be observed that the variation/noise observed in the KAM profiles for each of the plots in Figure 3.14 is lower for the harder grains (lower m) as compared to the softer grains (higher m). Presumably, this is because of the activation of multiple slip systems in the grain core in the softer grains, resulting in significant intragranular localizations, leading to a spatial scatter in the KAM data points.

Using a similar methodology, the GND density profiles have been plotted and compared with their experimental counterparts in Figure 3.15. The mean GND density profiles in

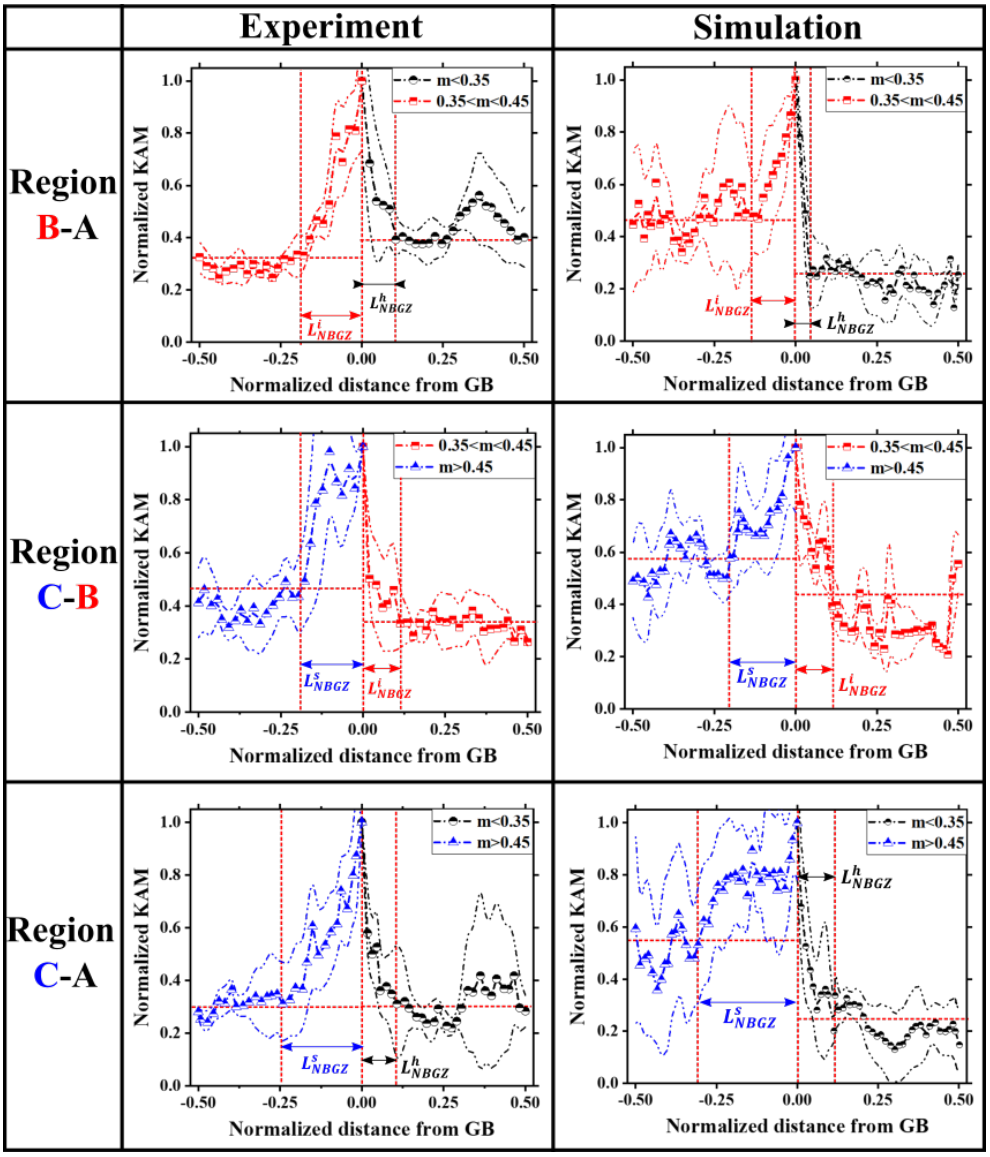

FIGURE 3.14: Comparison of representative normalized KAM profiles as a function of normalized distance from the grain boundary between experiments and simulations. The KAM profiles have been shown for representative, individual grain pairs (between the given regions) from the actual microstructures, and a corresponding grain cluster from the virtual microstructures. The lines connected by symbols represent the mean values and the dotted lines represent the scatter.

Figure 3.15 are qualitatively similar to the KAM profiles in Figure 3.14, with the exception that the GND density exhibits considerable noise compared to the KAM. This could be due to the fact that significantly less number of material points have KAM values below the noise floor (as compared to the GND density) (cf. Section 3.3.2). Moreover, these GND densities are estimated from an incomplete geometric dislocation tensor, due to lack of out of plane derivatives, which can also lead to additional noise in the data (Sun et al., 2000; Pantleon, 2008). The dependence of GND density on the window size could also contribute to the local fluctuations (cf. Section 3.3.3.2).

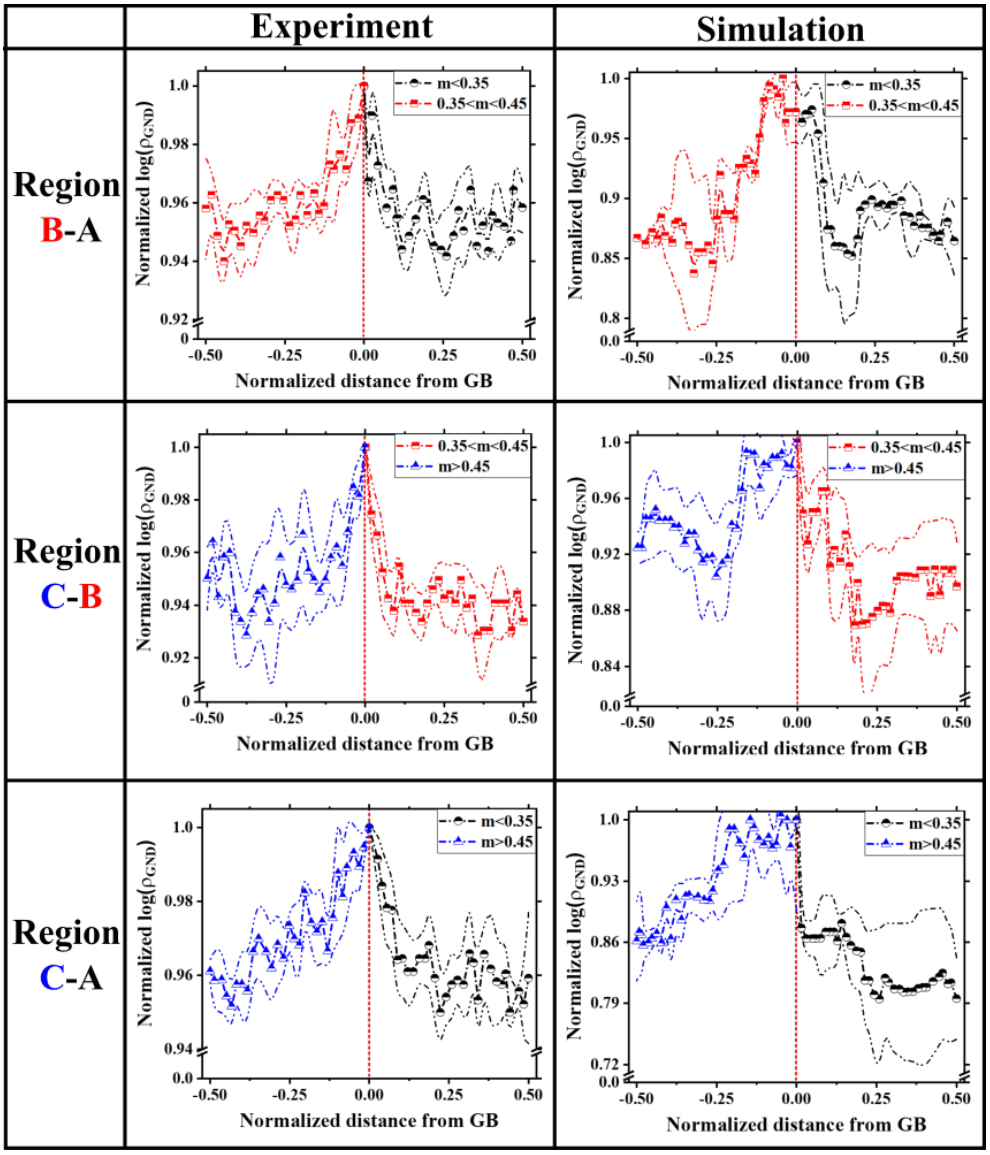

FIGURE 3.15: Comparison of representative normalized GND density profiles as a function of normalized distance from the grain boundary between experiments and simulations. The same grain clusters, used in Figure 3.14, have been employed for the current analysis. The lines connected by symbols represent the mean values and the dotted lines represent the scatter. Note that the scales are different for each of the plots.

3.3.5.1 Length of NBGZs

In this section, we compare the length of NBGZs obtained from the experiments and simulations. Figure 3.16 shows the initial crystallographic orientation for all the grains studied in the experimental and virtual microstructures, in a standard stereographic triangle. The dotted lines separate the three regions (region A, B and C or hard, intermediate and soft orientations) on the basis of their Schmid factors (m). A total of 24 grain pairs were studied in the experiments and 9 grain pairs were studied in simulations; each grain pair consisting of any of the two orientations highlighted in open circles in the figure below. Thus, the overall NBGZ analysis comprised of 48 grains from experimental microstructures and 18 grains from the virtual microstructures. Further, all results presented in this section are for individual grains, irrespective of their neighbors. While the number of grains considered in the present work may not be statistically significant, we believe that the deformation characteristics observed from these idealized grain pairs are representative. Finally, the length of NBGZs, L_{NBGZ}, is normalized with respect to their grain size, D.

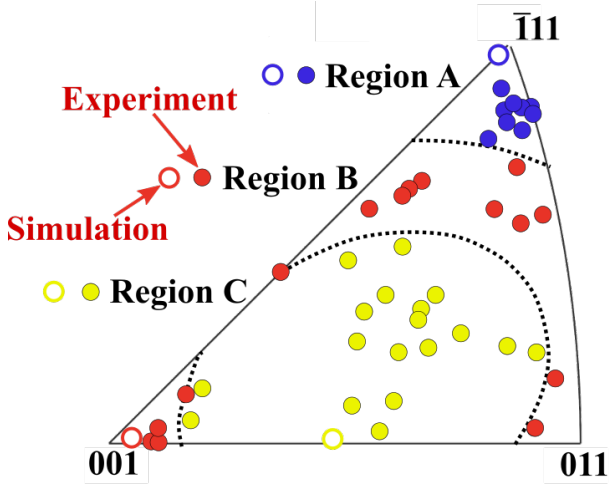

FIGURE 3.16: The orientations of the selected grain clusters for NBGZ analysis. The dotted lines divide the standard stereographic triangle into three regions (soft, intermediate and hard) on the basis of their Schmid factors (m). Solid circles represent the experimentally observed average grain orientations (from EBSD data for the undeformed specimens, cf. Figure 3.5), while open circles denote the grain orientations used in simulations.

Figure 3.17(a) shows the plot of L_{NBGZ}/D as a function of the initial grain-average Schmid factor for all the grain orientations shown in the IPF in Figure 3.16. The analysis has been carried out at an applied strain of 10%. The L_{NBGZ} calculations were done using the KAM profiles. This figure shows that the L_{NBGZ}/D scatter in data points not only increases, but also translates towards higher L_{NBGZ}/D values with increasing Schmid factor. Figure 3.17(b) represent the average values of all data points lying in each of the regions shown

in Figure 3.17(a), along with the respective scatter. Two main observations can be drawn from these data.

Firstly, this indicates that the width (mean with deviation) of the distribution of L_{NBGZ}/D scales with the initial grain-average Schmid factor of the grains studied. A similar observation can be inferred from both the experimental and simulated data.

Secondly, our results suggest a possibly strong correlation between the length of the NBGZ, L_{NBGZ}, and the grain size, D. Given that the average grain size in the experiments ($\bar{D}_{exp} \sim 92\mu m$) is relatively higher than those in the simulations ($\bar{D}_{sim} \sim 47\mu m$), there is a difference in the actual values of L_{NBGZ} observed in experiments and simulations. However, on normalizing the L_{NBGZ} with D, the mean value of L_{NBGZ}/D appears to scale with the initial grain-average Schmid factor. Further, the grain size could be the length scale parameter governing the formation of such regions.

The effect of grain size is studied in more detail in the next section to understand this length scale dependence further.

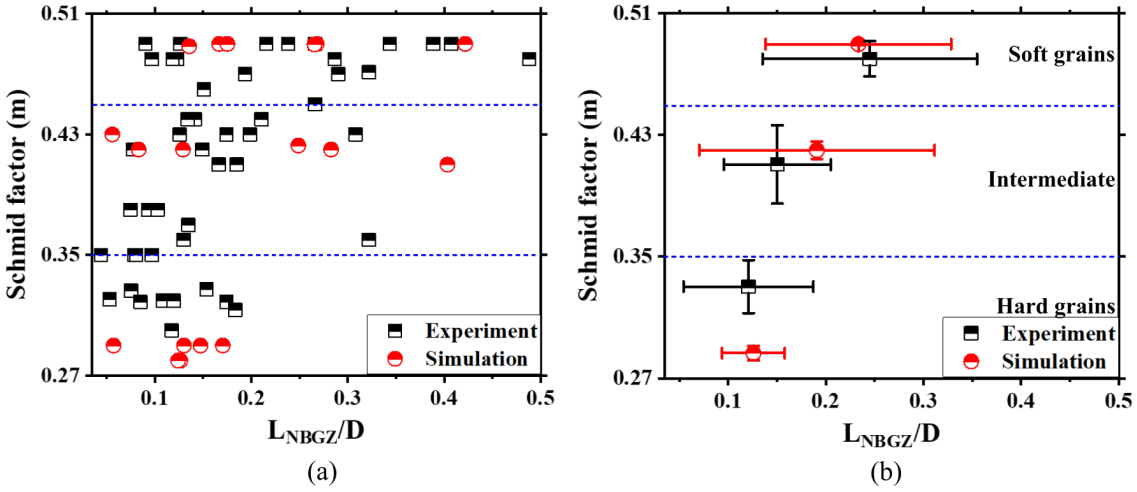

FIGURE 3.17: (a) Variation of the length of the NBGZ, L_{NBGZ}, normalized with respect to the grain size D, plotted as a function of the Schmid factor (m) for each of the grains shown in Figure 3.16 at 10% applied strain. The corresponding average values of L_{NBGZ}/D has been plotted as a function of the average Schmid factor in (b).

3.3.5.2 Effect of Grain Size on the Length of NBGZ

In order to further explore the effect of grain size on the length of NBGZs, virtual microstructures with three different grain sizes ($47\ \mu m, 71\ \mu m, 94\ \mu m$) were instantiated using Neper (Quey et al., 2011) and deformed in tension up to an applied strain of 10%. Essentially, the

tessellation was increased in size by a factor of 1.5 and 2, while keeping the grain orientations and boundary conditions identical. The average element size was also kept constant ($\sim 3\ \mu m$) for all three simulations, in order to preclude any mesh effects. Note that there is no appreciable difference in the stress-strain response for simulations with the different grain sizes (results not presented here). This is primarily because of the nature of the idealized simulations, where *only* two grains are embedded in a matrix, whose crystallographic orientation is representative of the average Schmid factor of the grain cluster. As a result, not enough GNDs (and deformation heterogeneities) are present in the simulation domain to contribute to the expected grain size strengthening on the macroscopic response in these simulations. Generally speaking, the *intrinsic* grain size effects on the macroscopic response can be observed only in polycrystalline aggregates, where a representative number of grains are present in the domain to induce appropriate GND densities due to the intergranular heterogeneities (cf. Section 3.2.3.4). Hence, the differences in mechanical properties and microstructure evolution are only restricted to a region in the vicinity of a grain boundary in our rather idealized simulations.

Figure 3.18(a) shows the KAM contours for the three microstructures after 10% applied strain. The Schmid factors of the selected grain orientations have also been highlighted in Figure 3.18(a). The grain pairs considered here lie in the Region B-A discussed earlier.

The 94 μm grain size used in our simulations here corresponds to the experimentally observed mean grain size. A direct one-to-one comparison is not possible due to difference in grain morphologies and arrangements between the experiments and the idealized simulations. If, however, one compares the simulated KAM profiles in Figure 3.18(b), with the corresponding experimental KAM profiles for Region B-A in Figure 3.14, qualitative similarities are observed. For example, there is a sharp drop in KAM as a function of distance from the grain boundary in the hard grain. Further, the ratio of the mean KAM in the grain center (0.6°) to that at the grain boundary (1.8°) for the 94 μm simulation in Figure 3.18(b) is qualitatively similar to the corresponding ratio of normalized KAM values observed experimentally for a similar grain pair in Figure 3.14 (~ 0.35).

Note that the KAM values have not been normalized (with respect to the peak value) here in order to highlight the absolute variation of KAM. The absolute values of KAM at the grain boundary are similar, irrespective of the grain size. For $\bar{D}_{sim} = 71\ \mu m$, the peak value of KAM is shifted inwards, i.e., towards the interior of the softer grain. Such a shift in the mean KAM profile could be due to strain localizations initiated at grain corners and triple junctions in the vicinity.

More importantly, it can be seen from Figure 3.18(b) that the KAM concentrations at the grain boundaries are spread over a wider region (L_{NBGZ}/D higher) and are more diffuse for the smaller grain sizes. This could possibly be due to the decrease in differential deformation between the grain mantle and the grain core as the grain size decreases for the softer grains. Strain localizations from neighboring grain corners and triple junctions may also contribute towards increasing the KAM values of the smaller and softer grains. However, it should be noted that the change in the apparent L_{NBGZ}/D is *not significant* and there is no appreciable difference in the KAM profiles (and the length of NBGZs) for the harder grain. These are discussed further in the context of our experimental results below. Further, such a comparison of KAM contours has not been done for the experimental data, since the grain size cannot be parametrically varied, while keeping all other microstructural factors same in the experiments.

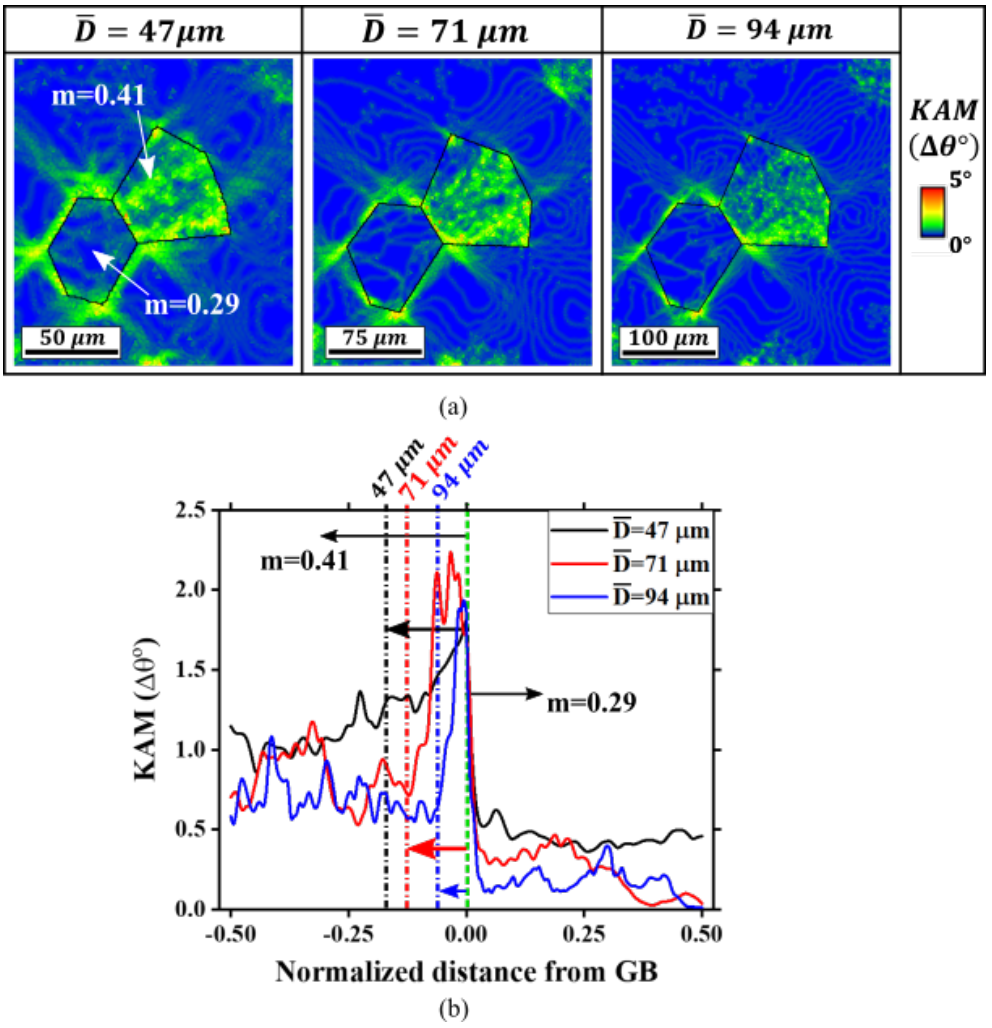

FIGURE 3.18: (a) KAM contours for simulations with different grain sizes. (b) KAM profiles as a function of distance from the grain boundary for three different grain sizes. All datapoints are plotted for simulations deformed to 10% strain respectively.

The experimental data points in Figure 3.17(a) were binned on the basis on their grain sizes, and the distribution of L_{NBGZ}/D plotted as a function of m is shown in Figure 3.19(a). Further, model predictions from the limited simulations (cf. Figure 3.18) are also shown in Figure 3.19(b). It can be observed from Figure 3.19(a) that smaller grains tend to have a larger L_{NBGZ}/D and vice-versa for soft grains with high Schmid factors. However, no clear trends emerge from the experimental data for grains with intermediate and low Schmid factors. Differences in grain morphology, crystallographic orientations of neighboring grains and influence of strain localizations from the neighboring points of stress concentration could be factors contributing to this.

As mentioned earlier, the model predictions presented in Figure 3.18 indicate that L_{NBGZ}/D decreases for the soft grain, but only to a small extent, as D increases. This is also evident from Figure 3.19(b). This could be due to the fact that for smaller D, the area fraction of grain mantle region is relatively smaller and is inadequate to accommodate the strain localizations in the NBGZs. This forces the grain core to undergo plastic deformation for accommodating the imposed deformation and results in lower differential deformation between the grain mantle and core, and hence a wider L_{NBGZ}/D. For larger grain sizes, however, the area fraction of the grain mantle region may be sufficient to accommodate the imposed strain, thus leading to a smaller L_{NBGZ}/D.

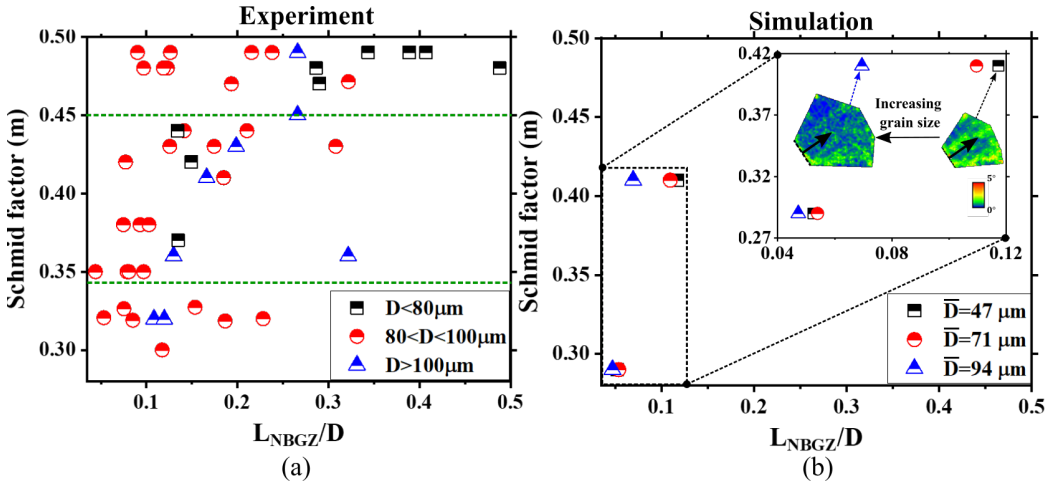

FIGURE 3.19: Variation of L_{NBGZ}/D as a function of m plotted by (a) binning the experimental data (from Figure 3.17(a)) into different grain sizes, and (b) from the simulation data in Figure 3.18

It should also be noted that the experimental data shows a much larger scatter in the L_{NBGZ}/D as compared to the simulation data. Since only a few specific instances were considered in the simulations, statistics of the distribution of L_{NBGZ}/D, similar to the experimental data in Figure 3.19(a), have not been captured. Such a reduced simulation data set was primarily due to the limitation of our computational resources. The simulation

with $\bar{D}_{sim} \sim 94\mu m$ ($\approx 14,000$ elements) took ~ 300 hours to reach 10% applied strain when run on 96 parallel processors. This imposes a constraint on generating additional data points using virtual microstructures. Nonetheless, qualitative trends between experiments and simulations are similar, i.e., L_{NBGZ}/D decreases to a small extent with increase in grain size for the soft grains.

Finally, the effect of grain size on L_{NBGZ}/D is negligible for the harder grains (low m). Since the grain core in a hard grain does not undergo deformation, the localizations remain restricted to the grain mantle region only. Thus, no significant grain size effects are observed for the harder grains, either from experiments or simulations.

The results presented in Figures 3.18 and 3.19 show that smaller grain sizes lead to a diffused NBGZ, i.e., the differential deformation between the core and the mantle vanishes, especially for softer orientations. Based on these observations, it can be deduced that the NBGZs would not exist for ultrafine ($\leq 1\ \mu m$) and nano ($\leq 100\ nm$) grained materials. At such fine length-scales, the imposed strains would necessitate that the entire grain deforms plastically, and that the deformation is not restricted to a finite region in the vicinity of grain boundaries. Hence, the concept of NBGZ would vanish for microstructures where NBGZ width approaches the order of grain diameter. This can also be inferred from the SGCP simulated deformation contours presented in Figure 3.2, where the NBGZs, visualized in terms of the ρ_{GND}, are much more prominent in simulation domains with larger grain sizes ($\bar{D} \geq 24\ \mu m$). Finally, in order to accurately predict the substructure evolution at such fine length scales (for ultra and nano grained materials), it would be crucial to incorporate additional mechanisms such as grain boundary sliding within the material model.

While the experiments and simulations performed in the present study point to a strong correlation between the length of NBGZ and the grain size, this rather simplified analysis has not considered the effect of factors such as the orientation of neighboring grains, grain morphology, triple junctions, and the role played by activated slip systems, in the NBGZ and the grain interior towards the development of such regions. Additionally, SGCP simulations for predicting substructure developments during deformation of 3D microstructures have also been reported in the existing literature (Liang and Dunne, 2009; Das et al., 2018; Sharma et al., 2024). The orientation gradients are expected to be more diffuse in 3D simulations as compared to our 2D simulations, due to lesser constraints and availability of more deformation modes in 3D. These shortcomings shall be explored in detail in the forthcoming studies.

Moreover, the grain size has not been varied significantly in our experiments to study their influence on the length of the NBGZs. Presumably, these factors may be expected

to contribute to the scatter observed in Figures 3.17(a) and 3.19(a). However, based on the limited number of grains studied in the experiments and simulations, some interesting correlations do emerge between the mean values of L_{NBGZ} and the initial grain averaged Schmid factor, as well as the mean grain sizes. In future work, we will perform parametric studies to isolate the individual effects of these other factors mentioned above. Further, statistics will also be collected from a larger number of grains to support the observations presented here.

3.4 Conclusions

We have studied the microstructural factors contributing to the formation of Near Boundary Gradient Zones (NBGZs) in an aluminum-magnesium alloy using combined experiments and modeling in the present work. We note that there have been earlier attempts at implementing strain gradient plasticity models using the MOOSE framework (see Barker et al. (2013), for example). The present implementation of strain gradient crystal plasticity using MOOSE is an advancement (compared to this previous implementation) in that the prediction of size-dependent strengthening effects (both grain size- and specimen size-dependent strengthening) and the development of misorientation gradients near grain boundaries has been demonstrated using our model.

Based on the detailed analysis of the results, the following conclusions can be drawn from our work:

1. The strain gradient crystal plasticity model is able to predict heterogeneous deformation in the vicinity of the grain boundaries. This is evident from the KAM localization within the NBGZ, which is significantly higher as compared to the local model predictions.

2. A correlation between the SSD density and the effective plastic strain, and between the GND density and KAM within the NBGZ is naturally observed from our SGCP simulations.

3. Both experimental and simulation data indicated that the KAM values, plotted as a function of distance from the grain boundary, increase with applied strain.

4. The width (mean with deviation) of the distribution of L_{NBGZ}/D scales with the initial grain-average Schmid factor of the grains studied.

5. Our results also suggest a possibly strong correlation between the length of the NBGZ, L_{NBGZ}, and the grain size, D.

6. The limited data available from experiments and simulations indicate that L_{NBGZ}/D decreases to a small extent as D increases for the soft grains, while this effect is negligible for the hard grains.

Chapter 4

Effect of Precipitates on the Development of Near Boundary Gradient Zones

4.1 Objectives of the Work

The study extends the conclusions drawn in Chapter 3 on the substructure developments within the Near Boundary Gradient Zones (NBGZs) during plastic deformation, to a precipitation strengthened Aluminum-Copper (Al-Cu) alloy, which has Al_2Cu precipitates at a majority of the grain boundaries, in addition to traces of solute (Cu) segregation. While Chapter 3 studied the NBGZ developments in a (relatively) homogeneous alloy, Chapter 4 focuses on examining the microstructural and mechanistic factors influencing the NBGZ developments in the presence of precipitates and solute atoms. Such a study is of significant practical interest, as various grades of Al-Cu alloys are routinely employed in the aerospace as well as automobile sectors, where they are subjected to complex thermomechanical treatments leading to the formation of additional phases/precipitates (Verlinden et al., 2007; Prakash et al., 2019).

The study presents a combined experimental and modeling framework to examine the role of precipitates and solute in the substructure evolution within the NBGZs in deformed microstructures. The NBGZs have been quantified in terms of the (mis)orientation and (mis)orientation gradients, across grain boundaries with and without the presence of precipitates. Following this, the Taylor hardening based Strain Gradient Crystal Plasticity (SGCP) framework presented in Chapter 3 has been modified to account for the additional

effects of solid solution strengthening during deformation. The Electron Backscatter Diffraction (EBSD) derived experimental microstructures, along with the information on the local chemical composition derived from Energy Dispersive Spectroscopy (EDS) serve as input to our SGCP framework. Finally, statistical correlations have been established between the experimental and simulated NBGZs and the local crystallographic orientations to understand the hierarchy of factors influencing the NBGZs during the deformation of Al-Cu alloys.

4.2 Materials and Methods

4.2.1 Materials

This study uses a precipitation strengthened Aluminum-Copper (Al – 4wt.% Cu) alloy. Its composition was determined using optical emission spectrometry and is given in Table 4.1. This alloy manifests Cu rich, or primarily Al_2Cu precipitates, at most of the grain boundaries (Bahl et al., 2022). The alloy was procured in a hot-forged and annealed state in the form of cylindrical bars of 30 mm diameter and 100 mm length. As will be seen in the subsequent sections, the as-received material shows a mean grain size of 168.06 ± 60.32 μm (see Figure 4.2 later in the study) and a near random crystallographic texture (Texture Index: 1.1) (see Figure 4.1(a) later in the study).

TABLE 4.1: Chemical composition of the Aluminum-Copper (Al – 4wt.% Cu) alloy used in the present study.

	Si	Fe	Cu	Mn	Mg	Cr	Zn	Ti	Al
Comp.(wt%)	0.5	0.5	~ 4.2	0.5	1.4	0.1	0.25	0.15	bal

4.2.2 Experimental Methodology

The as-received specimens were machined into cylindrical blocks of $D = 10$ mm diameter and $L = 15$ mm length each. These were then subjected to compressive deformation (single stroke) in a Gleeble 3800^{TM} thermomechanical simulator at a constant strain rate $\dot{\varepsilon} = 0.001$ s^{-1} up to nominal strains of -0.05, -0.10, -0.15 and -0.18, respectively. Three such experiments were carried out for each of the cases, to ensure sufficient reproducibility in the reported data. Note that an interrupted deformation study, as in Chapter 3, was not attempted here, because the sample surfaces get degraded during compression; graphite lubricant/sheets were used in between the cylinders and the specimen holder to minimize friction during compressive loading. Moreover, compressive loading was used over tensile

loading due to the fact that these specimens showed poor tensile ductility (total elongation< 5%).

Detailed microstructural characterizations were performed on the as-received and the deformed (half-cut, or at $\frac{L}{2}$) specimens ($\varepsilon_{zz} = -0.05,\ -0.10,\ -0.15,\ -0.18$). The samples were prepared by standard metallographic polishing followed by sub-micron colloidal silica polishing. In order to identify/crystallographically index the Al_2Cu precipitates often reported in these Al-Cu alloys, the final round of polishing involved the use of ion milling technique. In this regard, a GATAN^{TM} Precision Etching System (PES Model 682) was used for argon ion milling (3 kV beam energy, $\sim$ 2 hours). Following this, the polished specimens were characterized using Electron Backscatter Diffraction (EBSD) on an EDAX^{TM}-Tridant system, integrated with a FEI^{TM} Quanta-3D Field Emission Gun-Scanning Electron Microscope (FEG-SEM). A fixed step size of 0.25 μm, accelerating voltage of 20 kV, a current of 16 nA, detector binning of 2×2 and a working distance of 13.5 mm were employed during the EBSD data acquisition. The acquired orientation data was re-indexed using Neighbor Pattern Averaging (NPAR), in order to improve the quality of EBSD patterns as well as the subsequent indexing.

In addition to the orientation data, Pattern Region of Interest (PRIAS) maps were also acquired for all the specimens, in order to analyze the topography/atomic number contrast. Finally, the same region was characterized using TSL-EDX^{TM}, in order to quantify the local elemental composition. Note that the elemental composition maps were acquired from the chi-scan (combined EBSD-EDS) and from the SEM-EDS configurations. As will be seen later in the study, though the former subtends poor energy as well as spatial resolution due to a lower dwell time, it can be utilized in assistance with the PRIAS data to identify the Al_2Cu precipitates. Impression from micro-hardness indents were used to identify similar regions during the EBSD and SEM-EDS scans. Note that the Region of Interest (ROI) for EBSD/PRIAS/EDS characterization was limited to smaller regions close to center of the half-cut cylinder, to avoid edge effects. Finally, the scans were analyzed in an EDAX^{TM}-OIM Analysis software. A fixed confidence cut-off of 0.1 was used to ensure the removal of any erroneous EBSD data. In addition to these focused ROIs, wide area EBSD scans (1900 $\mu m \times 2000\ \mu m$) were performed on the half-cut undeformed ($\varepsilon_{zz} = 0.0$) and deformed ($\varepsilon_{zz} = -0.18$) specimens, to examine the bulk crystallographic texture. These were however, performed at a relatively coarser step size of 0.75 μm and only indexed using the (bulk) Aluminum phase.

In order to estimate the volume fraction of Al_2Cu precipitates in the bulk specimen, Rietveld analysis (Rietveld, 1969) was performed on X-ray Diffraction (XRD) based 2θ profiles. XRD measurements were performed on a Panalytical^{TM} Empyrean XRD system, hosting a 3 kW

sealed Copper tube and a K-β filter (Nickel) on the emission side, an Eulerian cradle having a reproducibility of $\sim 0.01^{\circ}$ and a 1-Der^{TM} solid state linear (1D) detector with a soller slit of 0.04 radian on the diffracted beam side. A spot size of 2 mm with an oscillation of ± 2 mm was provided, in order to acquire data from a statistically representative volume. A commercial software, Xpert^{TM} HighScore was used for the Rietveld analysis (Rietveld, 1969).

The Kernel Average Misorientation (KAM) and OIM-based Geometrically Necessary Dislocation (GND) density were used to quantify the heterogeneous deformation taking place within the NBGZ. The reader is referred to Chapter 3 for a detailed review of the mathematical formulations involved in estimating the KAM and GND density (ρ_{GND}) from the OIM data. Finally, note that these analyses on the development of NBGZs were limited to the bulk Al phase only, since the relatively harder Al_2Cu precipitates were expected to deform elastically and not contribute towards accommodating the (imposed) shear.

4.2.3 Modeling Framework

A similar model as in Chapter 3 was used in this study to account for the role of Geometrically Necessary Dislocations (GNDs) (and hence, the backstress) on the local as well as aggregate properties of the Al matrix, with additional consideration for solid solution strengthening. The relevant constitutive equations are briefly summarized in Table 4.2. The reader is referred to Chapter 3 for a detailed understanding on the terminologies used in Table 4.2.

As a first order approximation, we assume that the Al_2Cu precipitates, which possess a much higher elastic stiffness (Liu et al., 2020b) and yield stress (Bahl et al., 2022) in comparison to the Al matrix, only deform elastically and accommodate the applied load. However, note that the EBSD derived crystallographic orientation along with appropriate anisotropic elastic constants (see Table 4.4) have been employed for the Al_2Cu precipitates, to account for their anisotropic elastic deformation.

Although the present study used a precipitation strengthened Al-Cu alloy, minor traces of Cu segregation were noted at the grain boundaries from the SEM-EDS based elemental composition data (shown later in Figure 4.2). The presence of these solute atoms in the crystalline lattice have often been attributed to increase the frictional resistance for dislocation glide (Labusch, 1972; Nabarro, 1977). In order to we account for these effects, we modify the short range thermal slip resistance based on a formalism proposed by Zander

TABLE 4.2: Constitutive Equations used in our Strain Gradient Crystal Plasticity (SGCP) formulation (cf. Chapter 3).

Constitutive Equation	**Description**
Crystallographic shearing rate due to dislocation glide: $\dot{\gamma}^{\alpha} = \dot{\gamma}_0 \exp\left\{\frac{-\Delta F}{kT}\left(1-\left(\frac{\left\|\tau^{\alpha}-\tau_b^{\alpha}\right\|-s_a^{\alpha}}{s_t^{\alpha}}\right)^{p}\right)^{q}\right\}$ $\operatorname{sgn}(\tau^{\alpha}-\tau_b^{\alpha})$; $\|\tau^{\alpha}-\tau_b^{\alpha}\| > s_a^{\alpha}$	$\alpha \propto 1,2...,12$: slip system, τ^{α}: resolved shear stress, τ_b^{α}: slip system-level (directional) backstress, s_a^{α}: (non-directional) athermal slip resistance, s_t^{α}: (non-directional) thermal slip resistance, ΔF: activation energy for dislocation glide in the absence of external stress, p and q: shape parameters, k: Boltzmann constant, T: absolute temperature.
Resolved shear stress: $\tau^{\alpha} = \boldsymbol{m}^{\alpha} \cdot \boldsymbol{\sigma} \cdot \boldsymbol{n}^{\alpha}$	$\boldsymbol{m}^{\alpha}$: slip direction, $\boldsymbol{n}^{\alpha}$: slip plane normal, $\boldsymbol{t}^{\alpha} = \boldsymbol{n}^{\alpha} \times \boldsymbol{m}^{\alpha}$
Athermal slip resistance: $s_a^{\alpha} = \tau_0 + k_{ih} G b \sqrt{\sum_{\xi=1}^{Ns} A^{\alpha\xi} \rho_{SSD}^{\xi}}$	τ_0: threshold slip resistance, k_{ih}: hardening coefficient associated with isotropic hardening due to Statistically Stored Dislocations (SSDs), $A^{\alpha\xi}$: interaction matrix, accounting for hardening due to junctions formed between dislocations gliding on slip systems α and ξ ($\alpha, \xi = 1,2,...,N_s$), G: shear modulus, b: Burgers vector, N_s: total number of slip systems, i.e., 12.
Evolution of SSD density: $\dot{\rho}_{SSD}^{\alpha} = \frac{k_{mul}}{b}\sqrt{\rho_{SSD}^{\alpha}+\rho_{GND}^{\alpha}}\left\|\dot{\gamma}^{\alpha}\right\| - k_{dyn}\rho_{SSD}^{\alpha}\left\|\dot{\gamma}^{\alpha}\right\|$	k_{mul}: parameter accounting for dislocation multiplication at the existing junctions, k_{dyn}: parameter accounting for annihilation of dislocations due to dynamic recovery.
Evolution of Nye tensor: $\dot{\boldsymbol{\Lambda}} = -\left(\boldsymbol{\nabla} \times \dot{\boldsymbol{F}}^{pT}\right)^{T}$	$\boldsymbol{F^p}$: plastic deformation gradient tensor.
Evolution of GND density: $\dot{\rho}_{GND}^{\xi} = \left(\boldsymbol{A}^{T} \cdot \boldsymbol{A}\right)^{-1} \cdot \boldsymbol{A}^{T} \cdot \dot{\boldsymbol{\Lambda}}$	$\boldsymbol{A} = \sum_{\xi} b^{\xi} \boldsymbol{m}_0^{\xi} \otimes \boldsymbol{t}_0^{\xi}$
Slip-system level backstress: $\dot{\tau}_b^{\alpha} = k_{kh} \frac{Gb}{2\sqrt{\left\|\rho_{GND}^{\alpha}\right\|}} \dot{\rho}_{GND}^{\alpha}$	k_{kh}: hardening coefficient accounting for the (directional) kinematic hardening.

et al. (2007) as,

$$s_t^{\alpha} = s_t^0 + \sum_i k_{ln} (\varepsilon_b^{4/3})_i \; c_i^{2/3} \tag{4.1}$$

where, s_t^0 and k_{ln} are numerical constants and ε_b accounts for the misfit strain associated with the solute atoms of element i in the Al matrix.

The above equations (Table 4.2 and Equation 4.1) have been implemented and interfaced with an open source finite element library, Multiphysics Object Oriented Simulation Environment (MOOSE) (Permann et al., 2020). We refer the reader to Chapter 3 for further description on the model implementation involved in development of the above-mentioned SGCP framework.

4.2.4 SGCP Model Calibration

A 512 grain cube shaped domain, with 8 elements per grain and a grain size of 100 μm was generated using an in-house algorithm. Normal displacements were constrained on the left, x, bottom, y, and back, z, faces of the simulation domain during deformation. The domain was then deformed quasi-statically in uniaxial compression along the front, z, face, at a nominal strain rate of 10^{-3} s^{-1}.

Rietveld analysis (Rietveld, 1969) on the XRD measured 2θ profiles showed that the volume fraction of Al_2Cu precipitates was ~ 0.0247. Further, the precipitate volume fraction reported here is the average of the data measured from XRD scans on 3 randomly chosen (as-received) specimens. Based on this, 13 out of the 512 discrete grains in the cubic domain were (randomly) chosen to correspond to the Al_2Cu phase, to approximately represent the volume fraction of the precipitates in the simulation domain.

The input crystallographic texture for the Al matrix acquired from the wide-area EBSD scans was reduced to 499 discrete orientations using an open-source software, MTEX (Bachmann et al., 2010). Figure 4.1(a) shows the EBSD-measured experimental texture, in terms of the (001), (110) and (111) pole figures. The reduced texture used for the simulations is also shown in Figure 4.1(a). As can be seen, the reduced pole figures are qualitatively comparable with their experimental counterparts. This was also verified by estimating the Texture Indices (TI) (Verlinden et al., 2007; Bachmann et al., 2010). The TI was found to be 1.01 for the experimental texture and 1.08 for the reduced texture. This reduced texture was then input (randomly) to the grains corresponding to the Al phase in the simulation domain. An approximate random texture was assigned to the Al_2Cu precipitates.

The Al matrix has a Face Centered Cubic (FCC) crystal structure, which permits dislocation glide on the 12 $\{111\} < 110 >$ (octahedral) slip systems. The SSDs were assumed to be composed of only edge type of dislocations, thus leading to 12 distinct SSD configurations, whereas both edge and screw type of GNDs were considered, thus resulting in 18 distinct GND configurations (Evers et al., 2004b). These have been summarized in Table 3.2 of Chapter 3.

The anisotropic elastic constants for the FCC Al ($Fm\bar{3}m$) and tetragonal (I4/mcm) Al_2Cu phases were adopted from Chapter 3 and from Liu et al. (2020b). The parameters p and q, which control the shape of the enthalpy curve, ΔF, the reference shear strain rate, $\dot{\gamma}_0$, and the threshold slip resistance, s_t^0, were chosen so as to obtain a best fit simulated yield stress with the experimental value. Since the as-received material was procured in a hot forged and annealed state, a low value of initial slip system level SSD density, $\rho_{SSD}^0 = 10^5\ mm^{-2}$ was chosen. The parameters k_M, k_D and k_{ih}, which govern the substructure evolution and Taylor hardening contribution were obtained by calibrating the model to the hardening response of the material. The parameter governing the kinematic hardening contribution of GNDs, k_{kh}, has been adopted from Chapter 3, where it was used to predict the deformation of an Al-Mg alloy. Since k_{kh} is sensitive to the mesh size used in the simulations, we have ensured that the initial microstructures imported from the EBSD data too have a mesh size identical to those used in Chapter 3, where it was shown that $k_{kh} = 0.87$ sufficiently reproduced the Hall-Petch coefficient values reported in the existing literature for Al alloys. As mentioned earlier in Section 4.2.3, the Al matrix was assumed to deform plastically, while only elastic deformation was allowed in the Al_2Cu precipitates. Such an approximation was primarily motivated by the fact that the elastic stiffness (Liu et al., 2020b) and yield stress (Bahl et al., 2022) of Al_2Cu precipitates were sufficiently higher, in comparison to the relatively softer Al matrix. The calibrated model parameters have been summarized in Tables 4.3 and 4.4.

4.3 Results

4.3.1 Mechanical Response and Bulk Texture

Figure 4.1(b) presents a comparison of the SGCP predicted aggregate mechanical response with their experimental counterparts. As can be seen, a reasonable match is observed between the two entities. Further, Figure 4.1(c) presents the comparison of the predicted deformed textures with the measured deformed texture for the Al phase, at $|\varepsilon_{zz}| = 0.18$, in terms of the (001), (110) and (111) pole figures. The corresponding Loading Direction (LD,

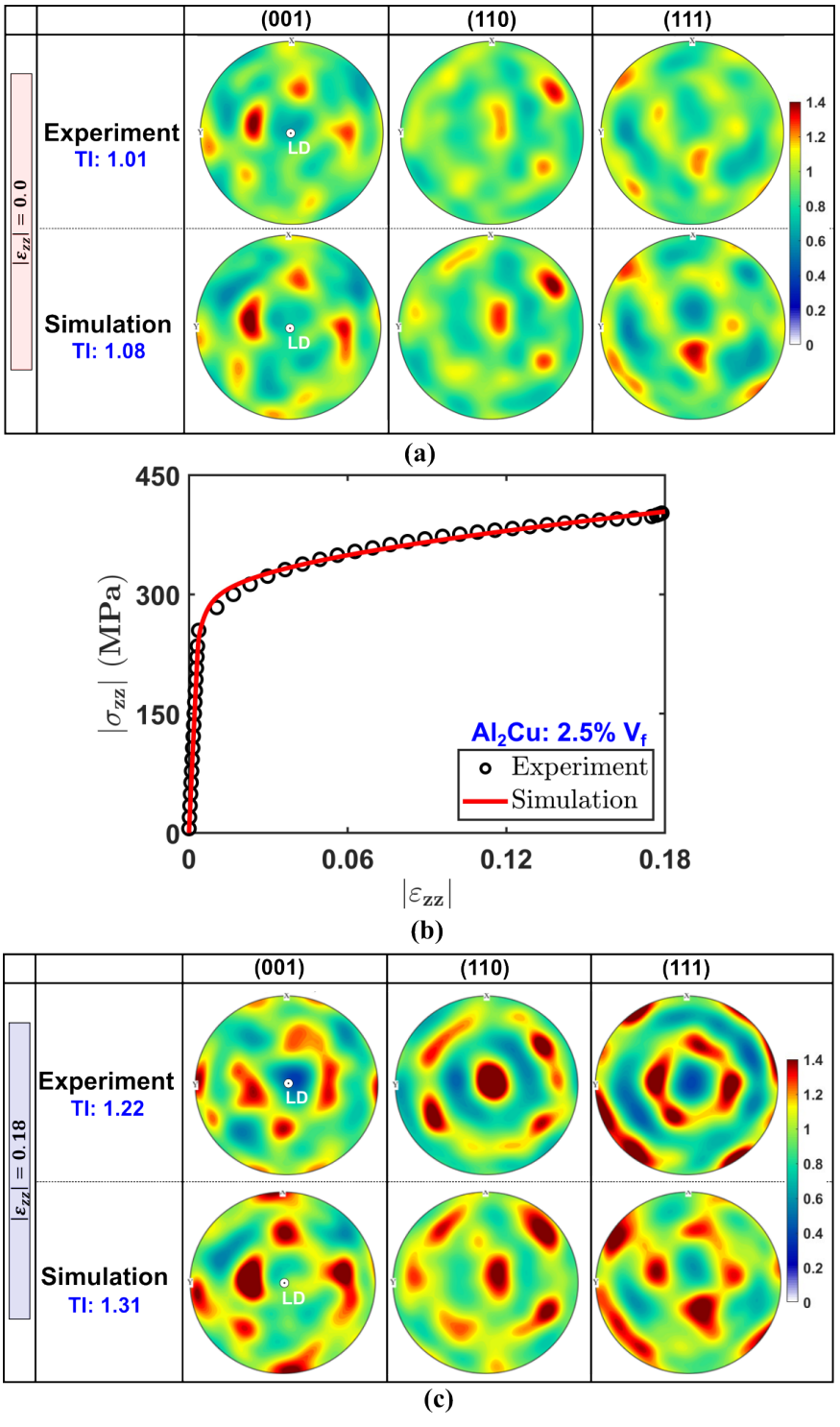

FIGURE 4.1: (a) The experimentally measured and reduced crystallographic texture of the as-received specimen, shown in terms of the (001), (110) and (111) pole figures along with their respective texture indices. The Loading Direction (LD) has been marked on the (001) pole figure. Comparison of the experimental and SGCP predicted (b) mechanical response and (c) deformed crystallographic texture ($|\varepsilon_{zz}| = 0.18$, measured on the half-cut specimen). Note that the mechanical response has been presented in terms of absolute magnitudes of σ_{zz} and ε_{zz}, for better visualization of the data.

TABLE 4.3: Model parameters calibrated to the experimental mechanical response.

Parameter	Value	Meaning
C_{11}	108 GPa	
C_{12}	61.3 GPa	Elastic constants for Al
C_{44}	28.5 GPa	
G	$\sqrt{\frac{(C_{11}-C_{12})C_{44}}{2}}$ GPa	Shear modulus
b	2.86 Å	Burger's vector magnitude
$\dot{\gamma}_0$	$4 \times 10^2\ s^{-1}$	Reference shear strain rate
ΔF	$0.45Gb^3$	Activation energy barrier
p	0.5	Shape parameter
q	1.7	Shape parameter
τ_0	34.8 MPa	Threshold slip resistance
$A^{\alpha\xi}$	0.055 if $\alpha \neq \xi$, else 1	Interaction matrix
s_t^0	0 MPa	Numerical constants associated with s_t^α
k_{ln}	246 MPa	
k_{mul}	0.05	Dislocation multiplication constant
k_{dyn}	32	Dynamic recovery constant
k_{ih}	0.23	Isotropic hardening parameter (due to SSDs)
k_{kh}	0.87	Kinematic hardening parameter (due to GNDs)
ρ^0_{SSD}	$1 \times 10^5\ mm^{-2}$	Initial SSD density
ρ^0_{GND}	0	Initial GND density

TABLE 4.4: Elastic constants for the Al_2Cu precipitates.

Parameter	Value	Meaning
C_{11}	175.6 GPa	
C_{12}	64.8 GPa	
C_{13}	59.3 GPa	Elastic constants for Al_2Cu
C_{33}	167.2 GPa	
C_{44}	31.7 GPa	
C_{66}	64.5 GPa	

z) has been marked on the (001) pole figure (cf. Figure 4.1(c)). A qualitative match can be observed between the pole figure contours. The predicted texture index of 1.31 also compares reasonably with the measured texture index of 1.22. We do note here that some minor differences exist between the predictions and experiments, for example, at $(\alpha, \beta) \sim (40, 179)$ in the deformed (001) pole figure. This might be due to the fact that relatively less number of grains were considered in our simulation domain. Nonetheless, qualitative trends have been reasonably predicted by our SGCP simulations, for example, increasing pole figure intensity around the $\sim \{011\}$ grain family at $|\varepsilon_{zz}| = 0.18$ in comparison to their undeformed counterparts.

4.3.2 Microstructure Characterization

Figure 4.2(a) presents results from the microstructural characterization carried out on the half-cut (at $\frac{L}{2}$) undeformed specimen, shown in terms of the PRIAS image, EDS counts acquired from chi-scan (combined EBSD-EDS mapping), Inverse Pole Figure (IPF) and Kernel Average Misorientation (KAM) map. The PRIAS image clearly shows that a majority of the grain boundaries have been decorated by the Al_2Cu precipitates (see yellow markers in Figure 4.2(a)). Note here that the phase identification for these precipitates was carried out using Rietveld analysis on the XRD-measured 2θ profiles (cf. Section 4.2). The chi-scan data, indicative of the local chemical composition, also convey that these precipitates are rich in Cu. Finally, since the as-received specimens were obtained in a hot-forged and annealed condition, low magnitudes of KAM can be noted in Figure 4.2(a). Moreover, the IPF maps do not display any large intragranular orientation gradients. Note here that Figure 4.2(a) was indexed only using the Al phase, hence a large fraction of unindexed points (black regions) are seen in the vicinity of grain boundaries and triple junctions. The identification as well as indexing of the Al_2Cu precipitates through EBSD has been explained in the subsequent paragraphs.

Figure 4.2(b) presents the elemental composition maps derived from SEM-EDS, along with a line profile analysis of the SEM-EDS counts across two different types of grain boundaries, with (marker A) and without (marker B) the presence of precipitates. Note that the scans shown in Figure 4.2(b) and thereafter, have been carried out on a cross-section parallel to the Loading Direction (LD) of the half-cut specimen (at $\frac{L}{2}$), since they have been directly utilized as input to our SGCP framework. As can be seen, the grain boundaries decorated by the precipitates display a significantly higher Cu concentration (maximum$\sim$ 0.32 wt.%) as compared to those without precipitates. Further, we have also characterized the Cu segregation at the grain boundaries which did not show evidence of Al_2Cu precipitates, using high magnification (focused area) SEM-EDS scans. The inset presented within the Cu SEM-EDS counts in Figure 4.2(b) shows the Cu segregation at one such grain boundary. However, since the Al-Cu alloys belong to the family of precipitation strengthened Al alloys, only few grain boundaries (which were not decorated by the Al_2Cu precipitates) display evidences of Cu segregation. These may be attributed to the limited solubility and insufficient time for precipitation kinetics during the thermomechanical processing.

Finally, Figure 4.2(c) presents the IPF maps for the Al matrix and Al_2Cu precipitates. Note that the Rietveld analysis was first used to identify the presence of Al_2Cu precipitates. Following this, the dynamic pattern simulations using OIM-Matrix^{TM} in TSL-OIM^{TM}, presented for two representative pixels in Figure 4.2(c), were generated and used to validate the

presence/indexing of Al_2Cu precipitates. The micron sized grain boundary Al_2Cu precipitates displayed a tetragonal (I4/mcm) crystal structure and formed an incoherent interface with the surrounding matrix. As can be seen in Figure 4.2(b, c), the morphology of these precipitates varied significantly based on the shape of the grain boundary, with the average (horizontal) intercept size typically of the order of $\sim 2.2\ \mu m$ and an aspect ratio of ~ 1.7. The highlighted plane traces on the Kikuchi patterns in Figure 4.2(c) also show a reasonable similarity between the experimental and simulated patterns for the Al_2Cu precipitates. An average confidence index of ~ 0.4 was noted while indexing the Al_2Cu precipitates. Finally, Neighboring Pattern Averaging (NPAR) was used to improve the quality of indexing of the EBSD patterns.

4.3.3 Experimental Measurements of L_{NBGZ}

As discussed previously, the as-received specimens were deformed in compression up to a maximum applied strain of $|\varepsilon_{zz}| = 0.18$ (cf. Section 4.2). Similarly, note that the microstructural characterizations to examine the substructure evolution within the NBGZ have been performed on a cross-section parallel to the loading direction of the half-cut (at $\frac{L}{2}$) deformed specimen. To begin with, the acquired EBSD and SEM-EDS datasets were categorized into two separate classes, grains boundaries with and without Al_2Cu precipitates. Since, only a fraction of the grain boundaries which did not have Al_2Cu precipitates showed traces of Cu segregation, they were not categorized separately and were accounted in the latter class.

Following this, an analysis determining the length of the NBGZ, L_{NBGZ}, similar to the one reported in Chapter 3 was carried out for the hard (A: $m \leq 0.35$), intermediate (B: $0.35 < m \leq 0.45$) and soft (C: $m > 0.45$) oriented grains based on the line profiles of KAM and GND density, ρ_{GND}, across grain boundaries. This exercise was carried out for 50 grains having Al_2Cu precipitates at the grain boundaries and 10 grains which did not show evidence of any such precipitates. Note that a fewer number of data points for the latter were primarily due to the fact that only few of the grain boundaries did not show any precipitates. This can also be confirmed from the PRIAS map as well as chi-scan based EDS counts shown in Figure 4.2(a). The corresponding KAM profiles for a few grain boundaries, with and without the Al_2Cu precipitates, have been presented in Figure 4.3(a) and Figure 4.3(b), respectively. Finally, to correlate these substructure developments with the local crystallographic orientation, their corresponding Schmid factor contours have also been attached (cf. Figure 4.3).

Further, note that the statistical correlations established in this study between the L_{NBGZ} and the crystallographic orientation, represented in terms of the Schmid factor, m, are with

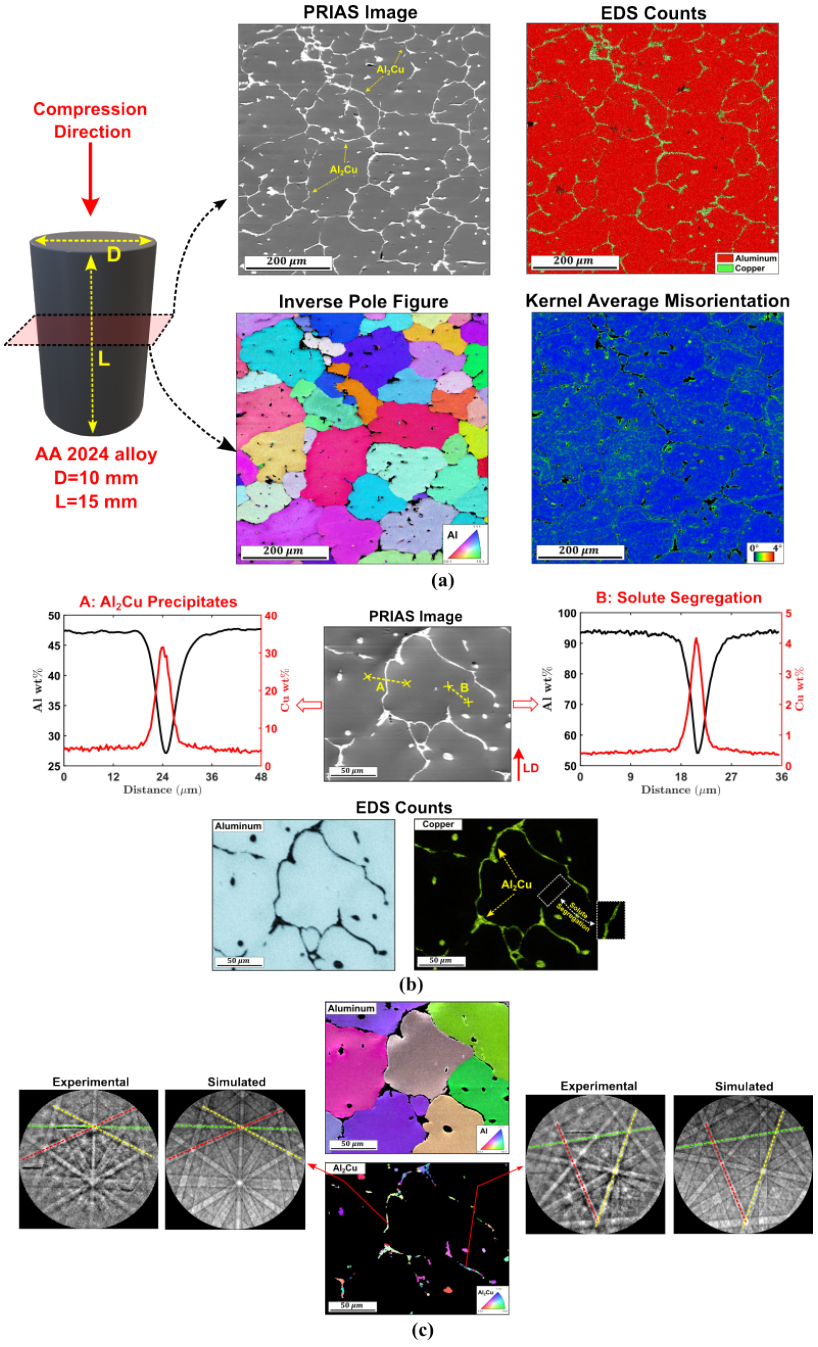

FIGURE 4.2: Schematic showing the specimen geometry, with region of interest marked in red and its corresponding microstructure, in terms of the PRIAS image, chi-scan (combined EBSD-EDS mapping) derived EDS counts, IPF and KAM maps. (b) SEM-EDS line profile analysis along with the spatial distribution of Al and Cu elements, along a grain boundary with and without the Al_2Cu precipitates. Note that the inset presents the SEM-EDS data acquired from high magnification scans along a grain boundary without precipitates, carried out to examine the presence of local Cu segregation, if any. (c) Identification of Al and Al_2Cu phases in EBSD using dynamically simulated Kikuchi patterns, generated using OIM-Matrix^{TM}. Three (random) plane traces have also been marked to indicate the similarity between the experimental and simulated patterns.

respect to the current or the deformed grain-average orientations, unlike those reported in Chapter 3, which employed the initial grain-average orientations. Acquiring the initial grain-average orientations necessitates the tracking of ROIs during deformation, which is only possible during interrupted, albeit progressive deformation experiments. Such an exercise could not be carried out in the present case due to constraints associated with compression experiments.

Figure 4.3 presents a comparison of the NBGZ development near grain boundaries with and without the presence of Al_2Cu precipitates, in terms of the GND density, ρ_{GND}, and KAM contours. The corresponding Schmid factor maps have also been shown. To begin with, Figure 4.3 shows localized deformation in the vicinity of grain boundaries for both classes, those with (Figure 4.3(a)) and those without (Figure 4.3(b)) the Al_2Cu precipitates. As can be seen in Figure 4.3(b), the (plastically) softer grain develops a much wider L_{NBGZ} over its intermediate and hard counterpart, for grain boundaries which are not decorated by the Al_2Cu precipitates. The hierarchy of NBGZ width in the absence of Al_2Cu precipitates can hence be stated as: soft (C: $m > 0.45$) > intermediate (B: $0.35 < m \leq 0.45$) > hard (A: $m \leq 0.35$). These trends are qualitatively similar to those reported in Chapter 3.

Following the method used in Chapter 3, the L_{NBGZ} analysis presented in Figure 4.3 relied on the use of KAM over ρ_{GND}. This is because only a marginal fraction of data points had their KAM magnitudes lower than the noise floor ($KAM_{nf} \sim 0.38°$) (Genée et al., 2021). Further, an interesting trend can be observed for grain boundaries decorated by the Al_2Cu precipitates (cf. Figure 4.3(a)). Over here, the the (plastically) harder and the intermediate oriented grains manifest a nearly similar L_{NBGZ}. As can be seen in Figure 4.3(b), the presence of precipitates accentuates the development of NBGZs, i.e., harder grains show higher L_{NBGZ} in the presence of Al_2Cu precipitates. The softer grain, still shows a relatively wider L_{NBGZ} in comparison to the hard and intermediate oriented grains.

The presence of Al_2Cu precipitates results in additional constraints for the deformation in the vicinity of grain boundaries. This leads to a significant (local) heterogeneity in the deformation within the NBGZ, necessitating the generation of ρ_{GND}. As can be seen in Figure 4.3(a), large ρ_{GND} concentrations are evident near the grain boundaries manifesting Al_2Cu precipitates. In addition to the crystallographic mismatch at the grain boundaries, the dislocation pileups and orientation gradients arising during deformation are enhanced due to the presence of harder, non-deforming second phase precipitates. The above-mentioned analysis is then repeated over multiple such grain boundaries, in order to obtain statistical correlations between the $\frac{L_{NBGZ}}{D}$ and m.

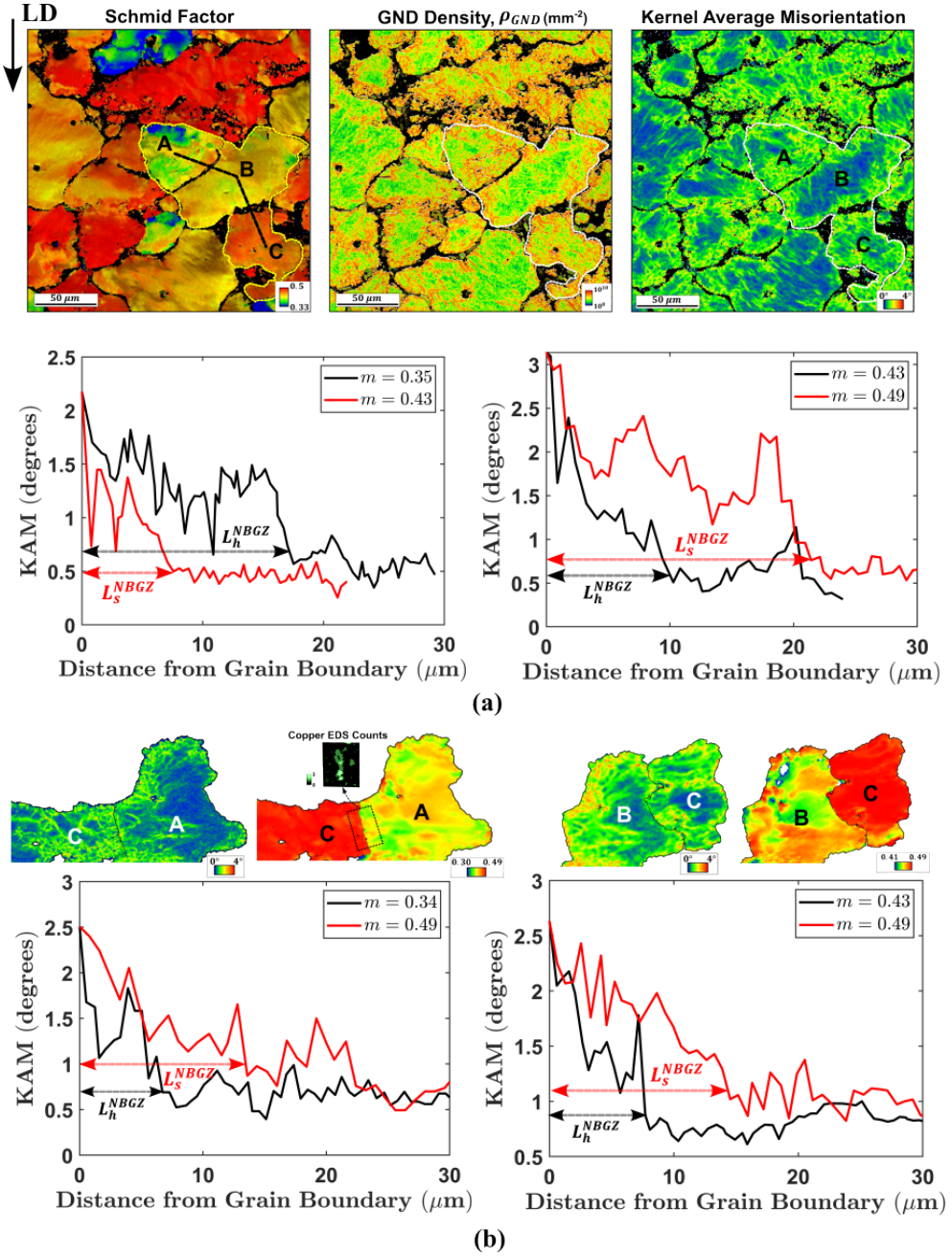

FIGURE 4.3: (a) EBSD derived Schmid Factor, m, total GND density, ρ_{GND}, and KAM contour maps for the specimen deformed up to $|\varepsilon_{zz}| = 0.18$. The NBGZ, in terms of KAM, across hard (A)-intermediate(B) and intermediate(B)–soft(C) grains having Al_2Cu precipitates has also been shown. (b) The NBGZ development, across a grain boundary between A-C and B-C type grains without Al_2Cu precipitates. Note that (Cu) solute segregation was observed across the A-C type grains shown in (b), while no such segregation was noted across B-C type grains.

4.3.4 Model Predictions of L_{NBGZ}

Figure 4.4(a) presents a representative focused-area EBSD microstructure, in terms of the phase map, which has been used as input for our SGCP framework. The colors in Figure 4.4(a) are indicative of the Al and Al_2Cu phases, respectively. These EBSD derived microstructures were meshed using 3D hexahedral elements of size 2 μm and with linear interpolation. Since the parameter k_{kh} is sensitive to the element/mesh size (Kapoor et al., 2018; Patra et al., 2023b), it has been kept identical to those in Chapter 3. Further, the simulation cell comprises of a single element along the thickness or out-of-plane direction (Patra et al., 2023a). We do note here that the addition of elements along the out-of-plane direction have been shown to improve the strain field predictions (Lim et al., 2014; Hestroffer et al., 2022). However, the computational costs associated with such large simulation domains/number of elements is substantial. In addition, employing a non-local framework that accounts for the deformation behavior of neighboring material points would limit the application of such large simulation domains to small deformations, in contrast to the strain magnitudes ($|\varepsilon_{zz}| = 0.18$) used for the present study. Further, similar to Chaudhary et al. (2023), axisymmetric boundary conditions, i.e., constraints on displacements normal to the left, bottom and back faces were applied. As can be seen in Figure 4.4(a), the microstructure was loaded in uniaxial compression along the top face at a nominal strain rate of 10^{-3} s^{-1}. The remaining faces were kept traction free.

In addition to the simulation domain shown in Figure 4.4(a), two additional EBSD-acquired microstructures were deformed virtually to obtain a statistically representative dataset on the substructure evolution within NBGZ, in particular, across grain boundaries with and without the Al_2Cu precipitates. Their corresponding grain-average crystallographic orientations in the initial or undeformed configuration have been marked on an inverse pole figure projection in Figure 4.4(b). As can be seen, the chosen crystallographic orientations span across the entire inverse pole figure, thus providing a sufficient number of data points for examining the NBGZ buildup across the hard (A: $m \leq 0.35$), intermediate (B: $0.35 < m \leq 0.45$) and soft (C: $m > 0.45$) oriented grains.

Figure 4.4(c) presents the SGCP predicted deformed microstructure, shown in terms of the grain-average Schmid factor, m, total GND density, ρ_{GND}, Kernal Average Misorientation (KAM), effective plastic strain, $\bar{\varepsilon}^p$, and the local residual strains, transverse, ε^{TD}, and parallel, ε^{LD}, to the loading direction at an applied strain of $|\varepsilon_{zz}| = 0.18$ and in the deformed configuration. Note that the loading direction has been kept identical to their experimental counterparts shown in Figure 4.2(b). As can be seen, the ρ_{GND}, and KAM accumulations are visible primarily in the vicinity of grain boundaries. Further, two important inferences can

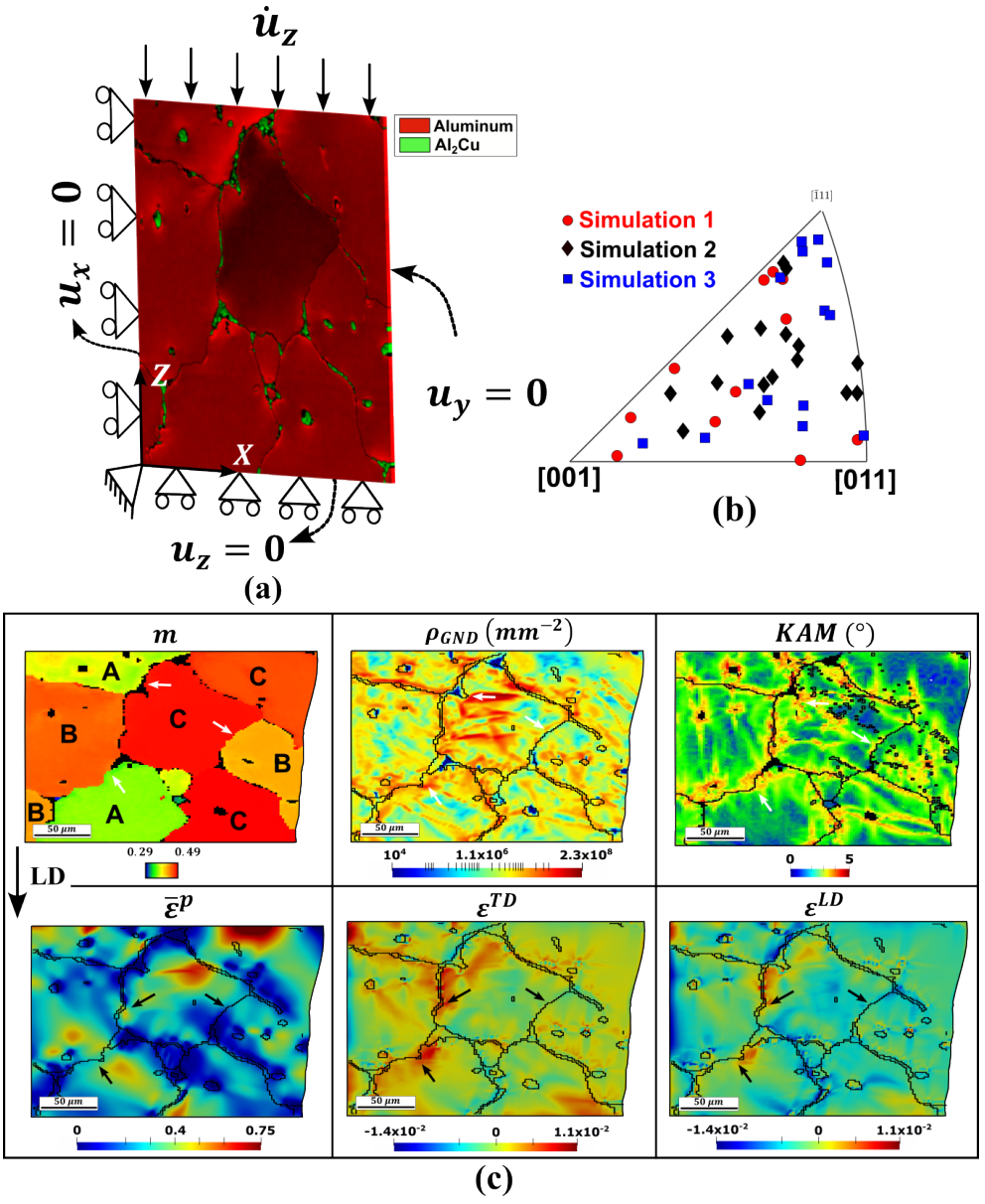

FIGURE 4.4: (a) Schematic of the simulation set-up and boundary conditions employed for deformation of EBSD microstructures. The colors are indicative of the Al and Al_2Cu phases, respectively. (b) Crystallographic (grain-average) orientations, plotted on an inverse pole figure, of the grains considered for analyzing the NBGZ development using SGCP. (c) Deformation contours, represented in terms of the grain-average Schmid factor, m, total GND density, ρ_{GND}, Kernel Average Misorientation (KAM), effective plastic strain, $\bar{\varepsilon}^p$, transverse, ε^{TD}, and longitudinal, ε^{LD}, local residual strains at an applied strain of $|\varepsilon_{zz}| = 0.18$. The black and white markers denote regions showing large magnitudes of local (residual) strains and ρ_{GND}, respectively. The markers A, B and C denote the hard ($m \leq 0.35$), intermediate ($0.35 < m \leq 0.45$) and soft ($m > 0.45$) oriented grains, respectively.

be clearly noted from these deformation contours. Firstly, for grain boundaries decorated by Al_2Cu precipitates, the NBGZs are significantly wider in comparison to their counterparts without precipitates. More importantly, the grains belonging to hard (A) and intermediate (B) orientations display nearly similar L_{NBGZ} (see white markers in Figure 4.4(c)) in the presence of Al_2Cu precipitates, with the former even showing wider L_{NBGZ} for certain grain boundaries.

The softer or C type grains on the other hand, display a wider L_{NBGZ} compared to the hard as well as intermediate grains, with or without the presence of Al_2Cu precipitates. The former, grain boundaries with Al_2Cu precipitates, however, shows a substantially wider L_{NBGZ} as compared to the ones without precipitates. This is similar to our observations for their experimental counterparts in Figure 4.3. Additionally, Figure 4.4(c) shows significant residual strain hotspots in the vicinity of grain boundaries manifesting Al_2Cu precipitates. The local lattice incompatibilities arising due to the presence of Al_2Cu precipitates during deformation necessitates the presence of GNDs. The resulting local stress fields arising due to these GNDs are not fully relaxed upon the removal of external load, thus resulting in large magnitudes of local residual (elastic) strains. Since heterogeneous deformation is much more prominent at the phase boundaries in comparison to the grain boundaries, the resulting local strains are also higher for the former over the latter (cf. black markers in Figure 4.4(c)).

Finally, statistical correlations between substructure developments within the NBGZ and the grain average Schmid factors, from experimental as well as SGCP predictions have been discussed in detail in the subsequent Section (Section 4.4).

4.4 Discussion: Comparison of Experimental and Simulated Predictions of L_{NBGZ}

Figure 4.5 presents a statistical analysis of the $\frac{L_{NBGZ}}{D}$ development as a function of the grain-average Schmid factor, obtained from experimental measurements (Figure 4.5(a,c)) and SGCP predictions (Figure 4.5(b,d)). As explained earlier, the EBSD-acquired datasets have been categorized into two broad classes, namely, the grain boundaries with and without the presence of Al_2Cu precipitates. Additionally, note that a few of the grain boundaries belonging to the latter class did show traces of Cu solute segregation. However, since they were few in numbers, they have not been categorized as a separate entity.

To begin with, the $\frac{L_{NBGZ}}{D}$ is always wider for cases where grain boundaries are decorated by Al_2Cu precipitates, in comparison to those without precipitates. This trend becomes

clearly visible in the case of soft grains, where the NBGZ development has even spread up to the grain center, or $\frac{L_{NBGZ}}{D} \sim 0.5$. This might be due to the fact that localizations developing as a result of the incompatible deformation between the matrix and precipitates gets diffused out much easily in the softer grains, which has slip systems readily available for deformation. This diffusing out of localizations near grain boundaries leads to the formation of a wider $\frac{L_{NBGZ}}{D}$. In addition, the readily available slip systems in the soft grains leads to the easy deformation of the grain core as well, especially at such large imposed strains. This capability of the grain core to accommodate the shear further diffuses the localizations at the grain boundaries, thus widening the NBGZ. On the other hand, the grains belonging to the hard orientations do not have such slip systems readily available, and hence deformation is relatively localized to a smaller region near the grain boundary.

Generally speaking, the hard grains should develop a much smaller $\frac{L_{NBGZ}}{D}$ in comparison to grains belonging to intermediate orientations, as noted in Chapter 3 and visible in our data for grain boundaries without the Al_2Cu precipitates (cf. Figure 4.5). However, the presence of Al_2Cu precipitates results in the development of pronounced strain localizations near the grain boundaries, even for the hard grains. These heterogeneities, and their resulting compatibility constraints causes (localized) lattice rotations, thus activating additional slip systems and widening the $\frac{L_{NBGZ}}{D}$ for hard grains. This results in a nearly comparable $\frac{L_{NBGZ}}{D}$ for the hard as well as intermediate grains. The soft grains on the other hand, continuing manifesting a wider $\frac{L_{NBGZ}}{D}$ even in the presence of precipitates. Such a trend is clearly observed in the mean values of $\frac{L_{NBGZ}}{D}$ shown in Figure 4.5(c,d). Another interesting difference is in the spread (deviation from the mean) of $\frac{L_{NBGZ}}{D}$, which is significantly larger for grain boundaries with Al_2Cu precipitates. This indicates that the local heterogeneity, and hence the ρ_{GND} and $\varepsilon_{LD/TD}$, are much more prominent in the vicinity of phase boundaries than the grain boundaries. Such trends are captured by our SGCP predictions as well, see Figure 4.4(d). More importantly, this states the crystallographic orientation is not the sole factor governing the NBGZ development in these alloys.

Similar trends can also be observed in our virtually deformed microstructures, see Figure 4.5(b,d). However, note that the our SGCP predictions manifested a significant noise in the dataset. This could be due to the presence of a fewer number of grains in the undeformed simulation cell, thus elevating the edge/boundary effects of a voxel-based mesh. However, a qualitative concurrence does exist between the experimental and simulated dataset. This can also be confirmed from Figure 4.5(c,d), which presents a qualitative match between the experimental (cf. Figure 4.5(c)) and simulated (cf. Figure 4.5(d)) mean and standard deviation of $\frac{L_{NBGZ}}{D}$.

Based on these results, two of the key observations from experiments, i.e., (i) wider $\frac{L_{NBGZ}}{D}$ in the presence of Al_2Cu precipitates in comparison to those without precipitates, and (ii) similar $\frac{L_{NBGZ}}{D}$ in the hard and intermediate oriented grains, while much larger $\frac{L_{NBGZ}}{D}$ in the softer grain in the presence of precipitates, have been qualitatively predicted by our SGCP simulations (cf. Figure 4.5(b,d)).

The available dataset, though limited, suggests that the Cu solute segregation does not alter or deviate the dependence of $\frac{L_{NBGZ}}{D}$ on m. This might be because the Al matrix displays a very low solid solubility for Cu (Verlinden et al., 2007), unlike the Al-Mg alloys used in Chapter 3. Hence solute segregation is not spontaneous, especially at room temperature and mesoscale, in these alloys. Moreover, the thermomechanical treatments for Al-Cu alloys are primarily designed to optimize the precipitate size, volume fraction and morphology, in order to attain the desired mechanical properties (Verlinden et al., 2007; Prakash et al., 2019; Bahl et al., 2022). As the solute segregation is limited to small regions in the vicinity of grain boundaries, it does not significantly affect the local substructure evolution during deformation (cf. Figure 4.2(b) and 4.3(b)).

Finally, as discussed in Section 4.3.2, the EBSD scan parameters as well as the post-processing techniques employed here resulted in the Al_2Cu precipitates being indexed with a confidence index of ~ 0.4. Additionally, the step size used in our EBSD scans were chosen so as to accurately capture the NBGZ and therefore did not involve sufficient number of pixels within the Al_2Cu precipitates to accurately capture the intragranular deformation occurring within them. Hence, we have not focused on exploring the deformation evolution within the Al_2Cu precipitates in this study.

4.5 Conclusions

The present study explored the local substructure developments within the NBGZ, specifically in terms of KAM and ρ_{GND}, in a precipitation strengthened Aluminum-Copper (Al-Cu) alloy using combined experiments and modeling. XRD as well as combined SEM-EBSD-EDS characterization showed that the Al_2Cu precipitates decorated a majority of the grain boundaries in the as-received specimen. These were then subjected to compressive loading at room temperatures up to a nominal strain of $|\varepsilon_{zz}| = 0.18$. The entire EBSD derived dataset was categorized into two classes, namely, the grain boundaries with and without the Al_2Cu precipitates. Following this, line profiles of KAM and ρ_{GND} were extracted from the EBSD data on deformed microstructures as also described in Chapter 3. The NBGZ

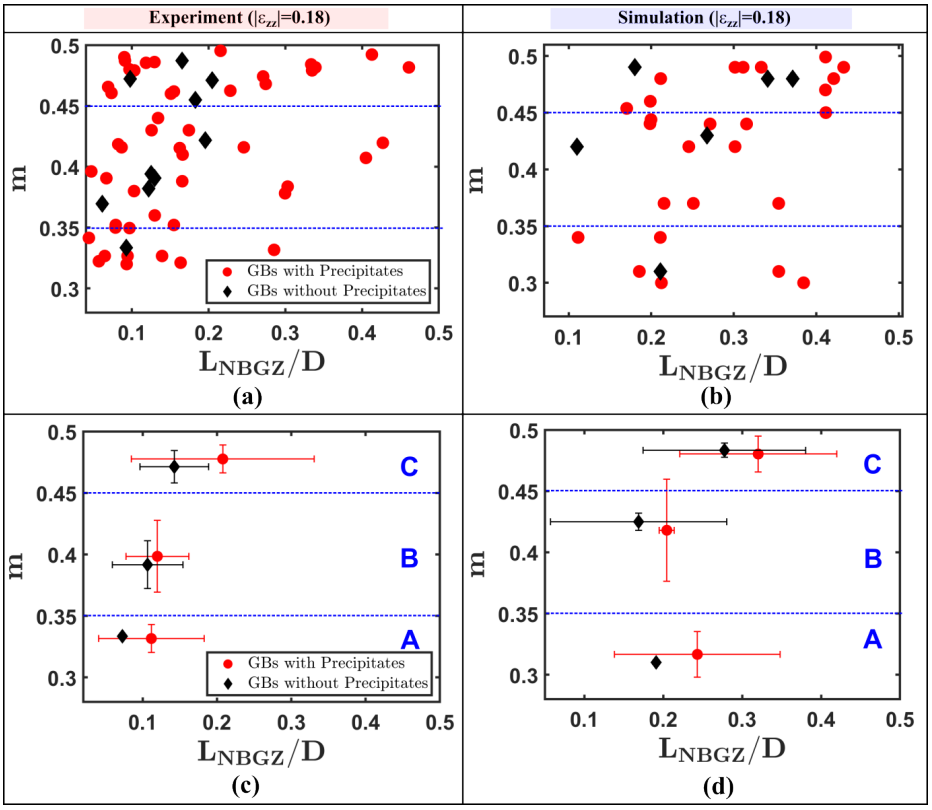

FIGURE 4.5: (a) Normalized length of the Near Boundary Gradient Zone, $\frac{L_{NBGZ}}{D}$, at $|\varepsilon_{zz}| = 0.18$, as estimated from the (a) experimental dataset and (b) SGCP predictions. The (c) experimental and (d) SGCP predicted mean and standard deviation in $\frac{L_{NBGZ}}{D}$, for the hard (A: $m \leq 0.35$), intermediate (B: $0.35 < m \leq 0.45$) and soft (C: $m > 0.45$) oriented grains at an applied strain of $|\varepsilon_{zz}| = 0.18$.

development was quantified in terms of the width of KAM accumulations and their correlation with the grain-average Schmid factor. In parallel, a Strain Gradient Crystal Plasticity (SGCP) model was developed and implemented in an open source finite element solver MOOSE (Permann et al., 2020). A similar line profile analysis of KAM/ρ_{GND} was carried out on the SGCP-predicted deformed microstructures as well.

Following are the key takeaways that can be drawn from the present study:

1. The SGCP framework qualitatively predicted the heterogeneous deformation trends in the vicinity of grain boundaries. The predicted KAM and ρ_{GND} localizations near the grain boundaries for a representative microstructure were qualitatively similar to those observed for their experimental counterparts (cf. Figure 4.3 and 4.4).

2. Our line profile analysis showed that the presence of Al_2Cu precipitates at the grain boundaries resulted in significant KAM and ρ_{GND} accumulation and a much wider NBGZ for all grains, in comparison to its counterparts (without Al_2Cu precipitates).

3. The plastically hard (A: $m \leq 0.35$) and intermediate (B: $0.35 < m \leq 0.45$) grains displayed a similar distribution in the width of length of NBGZ, $\frac{L_{NBGZ}}{D}$, while the softer (C: $m > 0.45$) grains showed significantly larger $\frac{L_{NBGZ}}{D}$, in cases where Al_2Cu precipitates decorated the grain boundaries.

4. For grain boundaries which did not manifest any Al_2Cu precipitates, an orientation dependence similar to those reported in Chapter 3, where the $\frac{L_{NBGZ}}{D}$ increases with increasing m was observed.

5. The hierarchy of $\frac{L_{NBGZ}}{D}$ as a function of the grain-average orientation can hence be given by: soft $>$ intermediate $\sim$ hard in the presence of Al_2Cu precipitates and soft $>$ intermediate $>$ hard without precipitates.

6. The presence of grain boundary precipitates or second phase (agglomerates) plays a larger role than the crystallographic orientation in influencing the substructure developments within the NBGZ.

7. The solute segregation, though limited to only a few of the grain boundaries, does not manifest any notable deviation on the dependence of NBGZ width on the crystallographic orientation.

Chapter 5

Microstructural Factors Influencing the Tension-Compression Asymmetry of Rapidly Solidified Alloys

5.1 Introduction

Additive Manufacturing (AM) of metallic systems can be used for fabrication of complex geometries via incremental deposition of the rapidly solidified melt to conform to the desired geometry, thus reducing the need for post-deposition machining of the AM-ed parts (Murr et al., 2012; Gao et al., 2015; Herzog et al., 2016; DebRoy et al., 2018). However, this manufacturing technique is generally associated with high solidification (and cooling) rates ($> 10^3\ K/s$) (Farshidianfar et al., 2016; Prasad et al., 2020) and severe thermal gradients ($10^4 - 10^6\ K/m$) (Bertoli et al., 2019; Pinomaa et al., 2020a), which may result in non-equilibrium microstructures, with significant defect densities (Gao et al., 2015; Du Plessis et al., 2020; Sanaei and Fatemi, 2021). These defects range from the nanoscale, such as dislocation entrapments at the chemical cell walls (Chen et al., 2019; Zhang et al., 2022), to the macroscale, such as fusion defects and porosities (Beretta and Romano, 2017; Sanaei and Fatemi, 2021). Further, this may also result in an incomplete solute partitioning at the solid-liquid interface, especially in steels containing a significant concentration of solute elements. This phenomenon of solute trapping leads to the segregation of solute atoms

[1] Significant parts of this Chapter have been published in (Pai et al., 2024b)

as well as precipitates along the cell walls and geometrically necessary boundaries, thus promoting dislocation pinning (Bertsch et al., 2020; Voisin et al., 2021) and increasing the material's strength, without sacrificing the tensile ductility (Liu et al., 2018a; Wang et al., 2018). Such a superior strength-ductility combination has been attributed to the development of *hierarchically* heterogeneous microstructures in AM materials (Wang et al., 2018).

Understanding these dislocation substructures is hence essential for developing AM microstructures exhibiting superior mechanical properties. Various mechanisms have been identified for the development of such heterogeneous dislocation substructures (Saeidi et al., 2015; Liu et al., 2018a; Yoo et al., 2018; Birnbaum et al., 2019; Bertsch et al., 2020; Voisin et al., 2021; Zhang et al., 2021b). For example, Saeidi et al. (2015) reported the accommodation of distortion induced by the solute enriched sub-grain and inter-dendritic boundaries via dislocation networks and substructures in AM austenitic Stainless Steel (SS 316L). The formation of cell boundaries in AM Inconel 718 has also been attributed to a combination of solute supersaturation at the solid-liquid interface and subsequent dislocation generation to accommodate the lattice incompatibilities (Yoo et al., 2018). The Geometrically Necessary Dislocations (GNDs), which originate during solidification for accommodating the inter-dendritic misorientations, further act as a scaffold for the mobile dislocations (Bertsch et al., 2020). Ramirez et al. (2011) attributed the presence of fine cuprite precipitates, along the inter-dendritic as well as grain boundary regions, for the development of complex precipitate-dislocation networks in AM copper components. An alternative mechanism suggests that the thermal distortion occurring due to rapid solidification (and cooling) results in the formation of cellular structures, which then act as sinks for the solute and precipitate atoms in AM SS 316L (Birnbaum et al., 2019). In addition, the boundary constraints surrounding the molten pool too play a role in deciding the dislocation substructures during rapid solidification (Bertsch et al., 2020). In summary, the printing induced stresses, solute atoms, precipitates and the local inter-dendritic misorientation play an important role in the formation of the observed dislocation cells during rapid solidification.

In terms of the mechanical properties, rapid solidification leads to the development of internal (residual) stresses, which govern the ensuing deformation behavior of AM-ed parts (Wu et al., 2014; Brown et al., 2017, 2019; Chen et al., 2019). Briefly, these can be divided into macroscale (bulk or type-I) and microscale (type-II and type-III) residual stresses. The former are mainly attributed to the specimen geometry, AM process parameters, scanning strategy, clamping constraints, etc. (Ding et al., 2011; Wu et al., 2014; Kumar and Nagamani Jaya, 2023), and can be reduced by optimizing the process parameters or relaxed by

subsequent annealing. The latter can be further classified into two categories: intergranular (type-II) and intragranular (type-III) internal stresses (Chen et al., 2019; Zhang et al., 2022). The intergranular internal stresses are a consequence of the compatibility conditions arising at the grain boundaries, and self-equilibrate over the length scale of a few grains (Zhang et al., 2022). The type-III stresses are primarily due to the printing-induced dislocation substructures, specifically the GND components of these dislocation clusters (Zhang et al., 2022). The heterogeneous distribution of GNDs thus gives rise to backstresses, and are hypothesized to be responsible for the anisotropic mechanical properties, including Tension-Compression (TC) asymmetry in rapidly solidified alloys (Chen et al., 2019; Zhang et al., 2022; Wang et al., 2023). Further, the as-printed dislocation substructures act as forest obstacles to dislocation slip, and influence the associated mechanical properties (Wang et al., 2018; Bean et al., 2022). For example, AM austenitic steels (SS 316L) exhibit a significantly higher yield strength and total elongation to failure, in comparison to the as-cast and wrought counterparts (Sun et al., 2018; Wang et al., 2018). The substructure development is generally dependent on the local thermal history, which is governed by the imposed thermal gradient and the pulling velocity during AM (Pinomaa et al., 2020a; Lindroos et al., 2022).

Much work has been done on modeling the mechanical properties of AM metals post-solidification by accounting for the effect of microstructure and residual stresses (Kapoor et al., 2018; Chen et al., 2019; Pokharel et al., 2019; Zhang et al., 2022; Wang et al., 2023). Further, multiscale models coupled with the phase field method (Azizi et al., 2021; Hu et al., 2022; Lindroos et al., 2022; Pinomaa et al., 2022) have been developed for simulating the solidification and grain growth processes as well. Macroscale finite element methods have been used to mimic the temperature profiles of various AM processes, for example, Selective Electron Beam Melting (SEBM) and Laser Powder Bed Fusion Process (LPBF), which then served as an input to a temperature-dependent phase field model (Liu et al., 2018b, 2020a; Azizi et al., 2021). Moreover, the preferred growth direction and crystallographic orientation based anisotropy were also accounted for by altering the gradient energy coefficients (Liu et al., 2018b). Several studies have utilized mechanics coupled phase field models to analyze the effect of solidification parameters (and consequent thermal profiles) on the microsegregation, Primary and Secondary Dendrite Arm Spacing (PDAS/SDAS), grain nucleation and growth and interface morphologies in rapidly solidified microstructures (Farzadi et al., 2008; Yu et al., 2018; Lingda et al., 2021).

These frameworks have also been coupled with crystal plasticity models, to study the microsegregation, grain-level residual stresses and dislocation structure developments during AM (Pinomaa et al., 2020b; Lindroos et al., 2022; Hu et al., 2022, 2023). Pinomaa et al.

(2020a); Lindroos et al. (2022) have used a phase field-crystal plasticity model to simulate the microstructure evolution (dislocation structure and solute segregation) during solidification and the subsequent mechanical properties. Hu et al. (2022) also utilized such an approach and observed significant plastic deformation in (a few) elongated grains along the laser track, as a result of the imposed thermal and geometric constraints. Homogenization of these plastic strains lead to reduction in the residual stresses in the AM microstructure (Hu et al., 2022). Further, Hu et al. (2023) have used the temperature as well as microstructure histories that act as input to a 3D Continuum Dislocation Dynamics (CDD) model to study the local evolution of dislocation structures during a laser-based AM process. However, these models do not account for the strain gradient plasticity induced backstresses, and its subsequent influence on the anisotropic mechanical properties. In this regard, (Chen et al., 2019; Zhang et al., 2022) have shown that by phenomenologically introducing a constant value of printing-induced backstress in their crystal plasticity model, the experimentally observed TC asymmetry of rapidly solidified microstructures can be predicted. However, their models did not simulate the *in-situ* development of printing induced backstress. In the present work, we try to address these gaps in the literature by developing a unified modeling framework for the predicting the development of GND-induced backstress in rapidly solidified microstructures and the ensuing anisotropic mechanical properties.

This manuscript proposes a coupled phase field (PF) - strain gradient plasticity (SGP) framework, for simulating microstructure evolution due to dislocation substructures and (micro) segregation, and predicting the Tension-Compression (TC) asymmetry in rapidly solidified iron-chromium (Fe-Cr) alloys. Essential features of the framework include consideration for solute segregation, anisotropic elastic and plastic deformation, GND and backstress evolution during solidification, multi-grain interaction effects, as well as thermally-induced residual stress development and their accommodation via plastic deformation during solidification. Simulations are performed for a range of solidification conditions, representative of AM conditions, to identify the microstructural origins of TC asymmetry in rapidly solidified Fe-Cr alloys. Finally, an analysis of the modeling framework itself is performed to identify the essential features of the model necessary for predicting the TC asymmetry.

5.2 Model Description

This work uses a combined phase field (PF)-strain gradient plasticity (SGP) modeling approach for studying the factors contributing to the development of microscale residual stresses in rapidly solidified microstructures and their effect on the mechanical properties of iron-chromium (Fe-Cr) alloys. The phase field model is used to simulate solidification in

idealized 2D polycrystalline microstructures, along with consideration for the solute (Cr) segregation during solidification. Further, the phase field model is coupled with a J_2 SGP model that allows consideration for the directional, GND-induced backstresses in the solidified phase. These backstresses are expected to be induced while accommodating the thermal Eigen strains during solidification and cooling and also the residual stresses due to Cr segregation during solidification. Solid solution strengthening due to the Cr atoms is also considered. The solidified microstructures are then virtually deformed using the SGP model to study the anisotropy of mechanical properties, more specifically, the Tension-Compression (TC) asymmetry along the build and transverse directions in these rapidly solidified microstructures.

The PF model and the SGP model are loosely coupled in the sense that the dissipation of work due to plastic deformation in the solidified phase is not considered in the free energy minimization of the PF model. Similar assumption has also been made in prior studies (Pinomaa et al., 2020a; Hu et al., 2022; Lindroos et al., 2022). Further, the use of a J_2 SGP model, instead of a strain gradient crystal plasticity model, is necessitated by the feasibility of running these coupled phase field-plasticity simulations, which are computationally intensive. We note that there are more advanced strain gradient crystal plasticity models (Evers et al., 2004a) and thermo-mechanical crystal plasticity models (Chen et al., 2019; Pokharel et al., 2019) in the literature, for example. However, coupling these crystal plasticity models with the PF models led to a significant increase in the computational costs and meaningful results could not be realized for the problem of interest here. This is also the reason that idealized 2D microstructures have been simulated here, instead of 3D polycrystalline microstructures. The following sections provide details on the development and implementation of our coupled PF-SGP model.

5.2.1 Phase Field Model

The phase field method is a versatile technique for simulating the mesoscale microstructure evolution during solidification, grain growth and phase transformation phenomena that models the evolution of the order parameter, representative of the transformation from one phase/state to another, by minimizing the free energy of the system (Kobayashi, 1993; Yeon et al., 2001; Militzer, 2011; Permann et al., 2016; Acharya et al., 2017; Biswas et al., 2022). In the present phase field model, the microstructural features are modeled in terms of a set of continuous variables that evolve in the spatial as well as temporal coordinates:

1. The non-conserved order parameters, ϕ_i ($0 \leq \phi_i \leq 1$ and $i \in 1, 2, \ldots .N$), which describe the microstructure in terms of the phase (i.e., liquid, $\phi_i = 0$, or solid, $\phi_i = 1$) for the N grains, with unique crystal orientations, considered in the simulation.

2. The conserved variable, c_{Cr}, representing the concentration of the solute (Cr) in the Fe system.

5.2.1.1 Evolution of the Order Parameter, ϕ_i

We adopt the formulation given by Kobayashi (1993) to describe the evolution of our order parameter/phase field variable, ϕ_i, and further modify it to account for the interaction between i^{th} and j^{th} grain of the solid phase (Pinomaa et al., 2020b; Biswas et al., 2022). This is given as:

$$\tau\frac{\partial\phi_i}{\partial t} = -\frac{\partial}{\partial x}\left(WW'\frac{\partial\phi_i}{\partial y}\right)+\frac{\partial}{\partial y}\left(WW'\frac{\partial\phi_i}{\partial x}\right)+\boldsymbol{\nabla}\cdot\left(W^2\boldsymbol{\nabla}\phi_i\right)+\phi_i\left(1-\phi_i\right)\left(\phi_i-\frac{1}{2}+m\right)+2\phi_i\sum_i\sum_j\gamma_{s_{ij}}\phi_j^2 \tag{5.1}$$

where, τ and W represent the interface relaxation time and the anisotropic interface layer width, respectively. $W^{'}$ denotes the first derivative of W with respect to ψ, the angle subtended between the interface normal and the global X direction. Mathematically, this can be written as (Kobayashi, 1993):

$$\psi = \tan^{-1}\left(\frac{\partial\phi_i/\partial y}{\partial\phi_i/\partial x}\right) \tag{5.2}$$

Further, γ_{sij} is representative of the interfacial energy, γ_s, between the i^{th} and j^{th} grain (Pinomaa et al., 2020b; Biswas et al., 2022). The thermodynamic driving force for microstructure evolution is written in terms of the parameter, m, as (Kobayashi, 1993):

$$m = \frac{\beta}{\pi}\tan^{-1}\left(\Gamma\left(\theta_e-\theta_r\right)\right) \tag{5.3}$$

where, β and Γ are material constants and θ_e is the non-dimensional equilibrium temperature, which has been set to unity. Further, θ_r is the non-dimensional temperature ranging from 0 to 1 and can be written as a function of the local temperature, θ, as:

$$\theta_r = \frac{\theta_m-\theta}{\theta_m-\theta_{ref}} \tag{5.4}$$

where, θ_m and θ_{ref} denote the melting point and reference temperature, respectively. The local temperature in absolute units, θ, which evolves spatially and temporally, has been non-dimensionalized here to θ_r, such that $\theta_r = 1$ indicates a fully solidified melt and $\theta_r = 0$ indicates a fully liquid region (Kobayashi, 1993). The thermodynamic driving force is

directly proportional to the degree of undercooling, $\theta_e - \theta_r$, i.e., higher undercooling results in a rapid evolution of ϕ_i fields across the liquid region. The evolution of the local temperature θ is governed by the imposed thermal gradient G during directional solidification. This has been discussed later in Section 5.2.3.

Using the law of conservation of enthalpy, we can write (Kobayashi, 1993; Acharya et al., 2017):

$$\frac{\partial \theta_r}{\partial t} = \nabla^2 \theta_r + K \sum_{i=1}^{N} \frac{\partial \phi_i}{\partial t} \tag{5.5}$$

where, K is the dimensionless latent heat, which varies directly with the latent heat, L, and inversely with the specific heat, C_p, i.e., $K = f(L/C_p)$ (Kobayashi, 1993; Acharya et al., 2017). The moving heat source term, $K \sum_{i=1}^{N} \partial \phi_i / \partial t$, is only present at the interface where the phase field variable, ϕ_i, transitions from zero to unity and is zero elsewhere (Kobayashi, 1993).

Prior studies have shown that the anisotropy in thermal conductivity, elastic modulus and surface energy of a grain can inherently determine its preferred growth direction (Lee et al., 1997). More importantly, these properties influence the favored growth direction by minimizing the strain and the crystal/liquid interface energy. In the present work, the interface layer width, W, has been modified to take into account the inherent anisotropy as a function of the growth direction (Kobayashi, 1993; Acharya et al., 2017), as:

$$W = \bar{W} \left(1 + \varsigma_i \cos(\Omega \psi)\right) \tag{5.6}$$

where, $\bar{W}$ is the mean value of the interface width W, ς_i is the anisotropy strength of the i^{th} grain and Ω is the anisotropy mode number. Liu et al. (2018b) accounted for anisotropic grain growth by altering the gradient energy coefficients, such that the grains with $< 001 >$ axis oriented closer to the thermal gradient have a competitive advantage during grain growth. Accordingly, the anisotropy strength, ς_i, has been rewritten as a function of the crystallographic orientation of the grain i as (Liu et al., 2018b):

$$\varsigma_i = \bar{\varsigma} \left| \cos \angle \left(< 001 >_{\text{axis}} , \nabla T \right) \right| \tag{5.7}$$

where, $\bar{\varsigma}$ is a numerical constant, signifying the average anisotropic strength. Physically, the above equation indicates that grains having $< 001 >$ axis oriented closer to the direction of thermal gradient have a higher ς_i, thus exhibiting a stronger preference during the grain growth.

The interface between two grains i and j is given by a smooth variation of the order parameter ϕ_i from 1 to 0 and vice-versa for ϕ_j (cf. Equation 5.1). This is in contrast to the sharp interface models, that inherently assume that the grain/phase interfaces are infinitely sharp, i.e., the properties exhibit a sudden discontinuity at these interfaces (Liu and Kirchheim, 2004; Detor and Schuh, 2007). On the other hand, the diffuse interface models are defined by a set of variables that are continuous functions of space and time (Cha et al., 2002; Kim et al., 2016b; Zhou, 2020).

5.2.1.2 Evolution of Cr Concentration, c_{Cr}

Chemically, the system is considered to be a single phase, i.e., the chemical activity of all grains in the system is denoted by a single (continuous) conserved parameter representing the Cr concentration, c_{Cr}, as opposed to the non-conserved order parameters, ϕ_i, which are considered for individual grains (Pinomaa et al., 2020b).

We use a regular solution model to predict the evolution of the conserved variable, c_{Cr}. In this context, an idealized pseudo binary Fe-Cr alloy has been assumed, with the Cr solute randomly distributed in the Fe solvent. This is motivated from prior studies (Bertsch et al., 2020; Voisin et al., 2021) that have reported Cr as the primary segregating element in AM stainless steels. Accordingly, the chemical free energy of the system can be written as:

$$F_{\text{chem}} = G^0_{\text{liq}}\ (1-\phi_i) + \phi_i(G^0_{Fe}c_{Fe} + G^0_{Cr}c_{Cr} + G^E_m + RT\left(c_{Fe}\ln\left(c_{Fe}\right) + c_{Cr}\ln\left(c_{Cr}\right)\right)) \quad (5.8)$$

where, c_{Cr} and c_{Fe} represents the concentration of Cr (solute) and Fe (solvent) atoms, respectively. The terms accounting for the free energy contributions from pure components (G^0_{Cr}, G^0_{Fe}), liquid melt (G^0_{liq}) and the heat of mixing (G^E_m) are obtained from thermodynamic databases of equilibrium phase diagrams (Dinsdale, 1991; Miettinen, 1999; Koyama and Onodera, 2004; Kim et al., 2021). Here, R is the gas constant. Further, by substituting $c_{Fe} = 1 - c_{Cr}$, the individual terms in Equation 5.8 can be written as:

$$G^0_{Cr} = -8856.9 + 157.48\theta - 26.908\theta\ln(\theta) + 0.00189\theta^2 - 1.477\times10^{-6}\theta^3 + \frac{139250}{\theta}\text{J/mol} \quad (5.9)$$

$$G^0_{Fe} = -236.7 + 132.416\theta - 24.66\theta\ln(\theta) - 0.003757\theta^2 - 5.86\times10^{-8}\theta^3 + \frac{77358.5}{\theta}\text{J/mol} \quad (5.10)$$

$$G^0_{\text{liq}} = -180383.83 + 291302\theta - 46.01\theta\ln(\theta)\text{J/mol} \quad (5.11)$$

$$G^E_m = \left((10833 - 7.477) - 1410\left(1 - 2c_{Cr}\right)\right)(1 - c_{Cr})c_{Cr}\text{J/mol} \quad (5.12)$$

The solute diffusivity in the solid is expected to be significantly lower than that in the liquid (Lindroos et al., 2022). Moreover, increasing the interface thickness results in a magnification of the solute trapping effect (Echebarria et al., 2004; Ghosh et al., 2017). In order to restore the local equilibrium at the interface, an additional solute back current is introduced that pushes the solute out of the solidified region. This back current is referred to as the anti-trapping current (Plapp, 2011; Biswas et al., 2022). The modified Cahn-Hilliard equations governing the evolution of solute concentration can then be written as (Pinomaa et al., 2020a; Lindroos et al., 2022; Pinomaa et al., 2022):

$$\frac{\partial c_{Cr}}{\partial t} = \boldsymbol{\nabla} \cdot \left[M \boldsymbol{\nabla} \frac{\partial F_{\text{chem}}}{\partial c_{Cr}} + W_0 \left(1 - k_e\right) \frac{c_{Cr}}{c_{Cr}^{eq}} \sum_i a_t' \frac{\partial \phi_i}{\partial t} \frac{\boldsymbol{\nabla} \phi_i}{|\boldsymbol{\nabla} \phi_i|} \right] \tag{5.13}$$

where, c_{Cr}^{eq} can be derived using the equilibrium partition coefficient, k_e, as $c_{Cr}^{eq} = \frac{1+k_e-(1-k_e)h}{2}$, where $h = N - 1 + \Sigma_i \phi_i$ (Pinomaa et al., 2020b). Further, W_0 is the magnitude of interface width and $a_t^{'}$ represents the modified anti-trapping coefficient, given by (Pinomaa et al., 2020a; Lindroos et al., 2022; Pinomaa et al., 2022):

$$a_t' = \frac{1}{2\sqrt{2}} \left(1 - A \left(1 - \phi_i^2\right)\right) \tag{5.14}$$

Here, A represents the solute trapping parameter. Further, using the approach given by Koyama and Onodera (2004), the interface mobility, M, is written as:

$$M = \left[c_{Cr}(1 - c_{Cr}) D_{Fe}^* + (1 - c_{Cr})^2 D_{Cr}^*\right] \left(\frac{c}{R\theta}\right) \tag{5.15}$$

where, D_{Fe}^* and D_{Cr}^* denote the self-diffusion constant of the solvent and the solute, respectively.

We have used the open-source finite element library, Multiphysics Object Oriented Simulation Environment (MOOSE) (Permann et al., 2020) for the phase field and plasticity simulations. A Kobayashi formulation-based single crystal dendritic growth framework (Kobayashi, 1993) is already implemented in MOOSE (Zhou, 2020). The existing PF models in MOOSE have been modified from their existing form to those given in Equations 5.1-5.7 and Equations 5.8-5.15, respectively. Specifically, we have modified the existing formulation to account for the multigrain interaction effects (5^{th} term in Equation 5.1) and the crystallographic orientation-based anisotropy during grain growth (Equation 5.7). In addition, we have modified the existing Cahn-Hilliard model to account for the regular solution free energy given in Equation 5.8.

5.2.1.3 Parameters for the Phase Field Model

The model parameters used to study the evolution of the above-mentioned phase field variables are summarized in Table 5.1. The constants β and Γ, which define the double-well potential curve, the numerical constant τ, governing the interface attachment timescale and the dimensionless latent heat, L have been taken directly from Kobayashi's work (Kobayashi, 1993). The average anisotropic strength, $\bar{\varepsilon}$, and the mode number, Ω, were obtained from Zhou (2020).The interfacial energy constant was taken from Pinomaa et al. (2020b) .The equilibrium Cr concentration c^0_{Cr} and melting temperature and θ_m were taken from McGuire (2008), while the parameters k_e and A were adopted from Lindroos et al. (2022), which also modeled a similar Fe-Cr alloy system. The average interface width, $\bar{W}$, was selected such that sufficient number of mesh elements existed within the interface, to achieve a continuous transition from liquid to the solid phase. The self-diffusion constants for Fe and Cr were taken from Koyama and Onodera (2004).

TABLE 5.1: Phase field model parameters for a representative pseudo binary Fe-Cr alloy.

Parameter	Description	Value
β, Γ	Constants governing the slope of double well potential (Kobayashi, 1993)	0.9, 10
τ	Numerical constant (Kobayashi, 1993)	0.0003
$\gamma_{s_{ij}} \forall\ i, j$	Interfacial energy constant (Pinomaa et al., 2020b)	20
$\bar{\varsigma}$	Average anisotropic strength (Kobayashi, 1993; Zhou, 2020)	0.04
Ω	Mode number	4
$\bar{W}$	Average interface width (μm)	0.14
K	Dimensionless latent heat (Kobayashi, 1993)	1.20
θ_m	Melting temperature (K) (McGuire, 2008)	1789
k_e	Equilibrium partition coefficient (Lindroos et al., 2022)	0.79
c^0_{Cr}	Equilibrium Cr concentration (wt. fraction) (McGuire, 2008)	0.21
A	Solute trapping parameter (Lindroos et al., 2022)	0.88
D^*_{Fe}	Self-diffusion constant for Fe (m^2/s) (Koyama and Onodera, 2004)	$1 \times 10^{-4} \exp\left(-\frac{294\times10^3}{RT}\right)$
D^*_{Cr}	Self-diffusion constant for Cr (m^2/s) (Koyama and Onodera, 2004)	$2 \times 10^{-5} \exp\left(-\frac{308\times10^3}{RT}\right)$

5.2.2 Strain Gradient Plasticity (SGP) Model

The finite deformation J_2 plasticity model is adapted from Patra et al. (2023b), and is based on the multiplicative decomposition of the deformation gradient, $\boldsymbol{F}$, into the elastic, $\boldsymbol{F}^e$, plastic, $\boldsymbol{F}^p$, and thermal, $\boldsymbol{F}^\theta$, parts (Musinski and McDowell, 2015; Pokharel et al., 2019), i.e.,

$$\boldsymbol{F} = \boldsymbol{F}^e \cdot \boldsymbol{F}^p \cdot \boldsymbol{F}^\theta \tag{5.16}$$

Here, $\boldsymbol{F}^e$ accounts for the elastic deformation, $\boldsymbol{F}^p$ accounts for the shear due to plastic deformation, and $\boldsymbol{F}^\theta$ accounts for the Eigen strain due to thermal expansion/contraction

(see Figure 5.3). Assuming isotropic thermal expansion/contraction, $\boldsymbol{F}^{\theta}$ can be written as (Musinski and McDowell, 2015):

$$\boldsymbol{F^{\theta}} = \sqrt{1 + 2\alpha^{\theta}\Delta\theta}\ \boldsymbol{\delta} \tag{5.17}$$

where, α^{θ} is the thermal expansion coefficient, which is a function of the temperature, θ, i.e., $\Delta\theta = \theta_{ref} - \theta$ represents the deviation from the stress-free temperature, θ_{ref}, and $\boldsymbol{\delta}$ is the second rank identity tensor. The resulting "stress-free" Eigen strains can thus be written as:

$$\boldsymbol{E}^{\theta} = \frac{\mathbf{1}}{\mathbf{2}}\left(\boldsymbol{F}^{\theta^T} \cdot \boldsymbol{F}^{\theta} - \boldsymbol{\delta}\right) = \alpha^{\theta}\Delta\theta\ \boldsymbol{\delta} \tag{5.18}$$

The evolution of the plastic deformation gradient, $\boldsymbol{F}^{p}$, can be written in terms of the plastic part of the spatial velocity gradient, $\boldsymbol{L}^{p}$, as $\dot{\boldsymbol{F}}^{p} = \boldsymbol{L}^{p} \cdot \boldsymbol{F}^{p}$. In this J_2 plasticity model, $\boldsymbol{L}^{p}$ is simply given by (Patra et al., 2023b):

$$\boldsymbol{L}^{p} = \sqrt{\frac{3}{2}}\dot{\bar{\varepsilon}}^{p}\boldsymbol{N}^{p} \tag{5.19}$$

where, $\dot{\bar{\varepsilon}}^{p}$ is the effective plastic strain rate and $\boldsymbol{N}^{p}$ is the unit tensor along the direction of plastic flow. $\boldsymbol{N}^{p}$ can be further written in terms of the deviatoric stress, $\boldsymbol{S}$, and the backstress tensor, $\boldsymbol{\chi}$, as (Patra et al., 2023b):

$$\boldsymbol{N}^{p} = \sqrt{\frac{3}{2}}\frac{\boldsymbol{S} - \boldsymbol{\chi}}{\bar{\sigma}^{*}} \tag{5.20}$$

Here, $\bar{\sigma}^{*}$ describes the modified effective stress, which is given by: $\bar{\sigma}^{*} = \sqrt{\frac{3}{2}(\boldsymbol{S} - \boldsymbol{\chi}) : (\boldsymbol{S} - \boldsymbol{\chi})}$. Generally speaking, $\boldsymbol{L}^{p}$ can be additively decomposed into a symmetric part, $\overline{\boldsymbol{D}}^{\boldsymbol{p}} = \text{sym}\left[\dot{\boldsymbol{F}}^{p} \cdot \boldsymbol{F}^{\boldsymbol{p}^{-1}}\right]$, which is representative of the plastic strain rate and an anti-symmetric part, $\overline{\boldsymbol{W}}^{p} = \text{ant}\left[\dot{\boldsymbol{F}}^{p} \cdot \boldsymbol{F}^{\boldsymbol{p}^{-1}}\right]$, representative of the plastic spin or the substructure rotation (Hashiguchi, 2020; Weber and Anand, 1990). The formulations presented in Equations 5.19-5.20 for $\boldsymbol{L}^{p}$ have been adopted from Weber and Anand (1990), where it was assumed that $\overline{\boldsymbol{D}}^{\boldsymbol{p}} = \text{sym}\left[\dot{\boldsymbol{F}}^{\boldsymbol{p}} \cdot \boldsymbol{F}^{\boldsymbol{p}^{-1}}\right] = \sqrt{\frac{3}{2}}\dot{\bar{\varepsilon}}^{p}\boldsymbol{N}^{\boldsymbol{p}}$ and $\overline{\boldsymbol{W}}^{p} = \text{ant}\left[\dot{\boldsymbol{F}}^{p} \cdot \boldsymbol{F}^{\boldsymbol{p}^{-1}}\right] = 0$, thus neglecting the anti-symmetric part of $\boldsymbol{L}^{p}$ for isotropic plasticity. As a first order approximation, we have also not considered the rotation of the substructure in our anisotropic model. While the effect of plastic spin may be negligible for small deformations, we note that such an approximation may not hold for large plastic strains and appropriate modifications can be made in future work (see Dafalias (1985), for example).

The effective plastic strain rate is modeled using a Kocks-type thermally activated flow rule

that can account for temperature- and strain rate-dependent effects (Kocks et al., 1975), i.e.,

$$\dot{\bar{\varepsilon}}^p = \dot{\bar{\varepsilon}}_0^p \exp\left\{\frac{-\Delta F_g}{k\theta}\left(1 - \left(\frac{\bar{\sigma}^* - s_a}{s_t}\right)^p\right)^q\right\}; \bar{\sigma}^* > s_a \tag{5.21}$$

where, $\dot{\bar{\varepsilon}}_0^p$ denotes the reference strain rate, ΔF_g is the activation energy for dislocation glide, the athermal slip resistance, s_a, accounts for slip resistance due to long range stress fields of dislocation junctions, and the thermal slip resistance, s_t, accounts for slip resistance due to short range barriers. k denotes the Boltzmann constant and θ denotes the absolute temperature, respectively. Further, p and q are parameters governing the shape of the activation enthalpy curve.

The athermal slip resistance, s_a, is represented using a typical Taylor-type hardening model as (Taylor, 1934):

$$s_a = a\left(\tau_0 + k_{ih} G b \sqrt{\rho_{SSD}}\right) \tag{5.22}$$

where, τ_0 is the threshold resistance, k_{ih} is the (isotropic) Taylor hardening coefficient due to the Statistically Stored Dislocation (SSD) densities, ρ_{SSD}, G is the shear modulus, and b is the Burgers vector magnitude.

The SGP model is by definition isotropic, i.e., it does not take into account the anisotropy induced by the crystallographic orientation or texture of a microstructure. However, this assumption may not be appropriate in the present work, where we intend to simulate solidification in polycrystalline microstructures. As described earlier, the phase field model accounts for the growth of grains with different crystal orientations. Hence, in order to incorporate the effect of anisotropy (due to crystallographic orientation) on the yield surface, the above equation is multiplied by an anisotropy factor, a, which is representative of the Taylor factor. Inspired from Patra et al. (2023b), the factor a is modeled as the inverse of the maximum Schmid factor over all possible slip systems of the crystal structure under consideration, i.e.,

$$a = \frac{1}{\max\left(m^\alpha\right)}; \alpha = 1, 2, \ldots, N_s \tag{5.23}$$

where, m^α represents the Schmid factor associated with the α^{th} slip system of the crystal with N_s possible slip systems. Here, $\boldsymbol{s}^\alpha$ and $\boldsymbol{n}^\alpha$, denote the unit slip and slip plane normal directions, respectively. Further, m_α is defined as:

$$m^\alpha = \frac{\boldsymbol{\sigma}}{\|\boldsymbol{\sigma}\|} : \boldsymbol{s}^\alpha \otimes \boldsymbol{n}^\alpha \tag{5.24}$$

where, $\boldsymbol{\sigma}$ is the Cauchy stress. m^α may be considered as the equivalent of the Schmid factor commonly used in crystal plasticity models. Essentially, the factor, a, introduces anisotropy along the slip system with the maximum Schmid factor under the assumption of single slip

in our J_2 plasticity model. Further, the slip system information is only used to compute the anisotropy factor in this otherwise "macro-plasticity" model. We note that such an assumption may not be valid at large plastic strains, when multiple slip is to be expected.

Anisotropic yield has generally been incorporated in macro-plasticity models using the Hill's stress potential (Hill, 1948) and the associated anisotropic material constants can be derived by testing bulk specimens (sizes greater than a few mm) along different orientations. Given that we do not have much experimental data regarding orientation-dependent yield anisotropy for the idealized Fe-Cr alloy under study, we resort to a crystal plasticity-motivated model, by introducing the anisotropy factor, a, which accounts for the orientation-dependence of the slip resistance. The emphasis in the present work is on predicting the anisotropic elastic and plastic deformation in smaller microstructures (less than 100 μm size) at the single crystal and polycrystal level using a macro-plasticity model. Predictions from verification simulations are also presented in Section 5.2.2.2, which demonstrate the model's ability to predict the crystalline anisotropy-induced deformation at small strains in single crystals. Additionally, it should be noted that a crystal plasticity model naturally accounts for the orientation effect in terms of the resolved shear stress, rather than altering the slip resistance. In our SGP framework, the stress potential is based on the second invariant, J_2, of the deviatoric stress tensor minus the backstress tensor and resembles a von Mises yield criterion (cf. Equation 5.20). Without altering this stress potential, we introduce crystalline anisotropy in the model by proposing the anisotropy factor, a, which modifies the slip resistance based on the crystal orientation.

Similar to crystal plasticity models, elastic anisotropy has also been considered in our model as:

$$\boldsymbol{C} = \boldsymbol{R} \cdot \boldsymbol{R} \cdot \boldsymbol{C}_0 \cdot \boldsymbol{R}^T \cdot \boldsymbol{R}^T \tag{5.25}$$

where, $\boldsymbol{C}$ and $\boldsymbol{C}_0$ denote the fourth rank elasticity tensor in the sample and crystal reference frame, respectively, and $\boldsymbol{R}$ is the rotation tensor that transforms the elasticity tensor from the crystal frame to the sample frame.

Note that although we consider the elastic anisotropy and the anisotropy factor, a, here, unlike crystal plasticity models, their respective evolutions are not considered in the J_2 plasticity model. This approximation may not be valid at large plastic strains, where the grain/crystal may rotate significantly.

The solid solution strengthening due to alloying elements may contribute to the short range barriers to dislocation glide. In order to account for such effects, the thermal slip resistance

has been formulated as (Sieurin et al., 2006; Lindgren et al., 2017):

$$s_t = a\left(s_t^0 + k_{ln}\ \varepsilon_b^{\frac{4}{3}} c_{Cr}^{\frac{2}{3}}\right) \tag{5.26}$$

where, a is the anisotropy factor described earlier (cf. Equation 5.23), ε_b accounts for the misfit strain due to solute (Cr) atoms with concentration c_{Cr} and s_t^0 and k_{ln} are associated constants. In the coupled phase field-plasticity simulations, the spatially resolved local solute concentrations are used to the solid solution strengthening model.

The evolution of the SSD density is modeled using a Kocks-Meckings type hardening equation (Kocks and Mecking, 2003), which has been modified to account for the GND density (see Chapters 3 and 4 and Evers et al. (2004a); Patra et al. (2023b)), as given below:

$$\dot{\rho}_{SSD} = \frac{k_{mul}}{b}\sqrt{\rho_{SSD} + \rho_{GND}}\dot{\bar{\varepsilon}}^p - k_{rec}\rho_{SSD}^{\alpha}\dot{\bar{\varepsilon}}^p \tag{5.27}$$

where, the first term on the RHS accounts for the dislocation evolution at forest obstacles and pre-existing junctions, while the second term accounts for the dislocation annihilation due to recovery. Here, ρ_{GND} represents the GND density, and k_{mul} and k_{rec} are material parameters associated with the SSD density evolution.

The Nye tensor, $\boldsymbol{\Lambda}$, can be derived from the curvature of the plastic deformation gradient (Nye, 1953; Dai, 1997; Arsenlis and Parks, 1999; Arsenlis et al., 2004). We have used the same here in the rate form as (Patra et al., 2023b):

$$\dot{\boldsymbol{\Lambda}} = -\left(\boldsymbol{\nabla} \times \dot{\boldsymbol{F}}^{pT}\right)^T \tag{5.28}$$

The corresponding rate of evolution of GND density is given as:

$$\dot{\rho}_{GND} = \frac{1}{b}||\dot{\boldsymbol{\Lambda}}|| \tag{5.29}$$

where, $||\dot{\boldsymbol{\Lambda}}||$ denotes the L_2 norm of $\dot{\boldsymbol{\Lambda}}$. The rate of evolution of backstress due to the GND density is given as (Patra et al., 2023b):

$$\dot{\boldsymbol{\chi}} = a\ k_{kh} G b \frac{\dot{\rho}_{GND}}{2\sqrt{\rho_{GND}}}\boldsymbol{N}^p \tag{5.30}$$

where, k_{kh} is the kinematic hardening coefficient. The incremental form of the backstress model allows development of backstress due to GNDs along the direction of plastic flow, while also capturing the history of backstress evolution upon load reversals (Patra et al.,

2023b). The reader is referred to Chapter 3 and Patra et al. (2023b) for a detailed description of the backstress model and physical implications of the k_{kh} parameter.

In summary, we have developed a J_2 SGP model that can also account for the effect of crystalline anisotropy on the elastic and plastic deformation in the limit of small strains. Numerical integration of the SGP model is described in Patra et al. (2023b). The SGP model has been implemented as a material model and interfaced with the open source finite element solver, MOOSE (Permann et al., 2020).

5.2.2.1 Parameters for the SGP Model

This work primarily focuses on the rapid solidification and deformation of a model Fe-Cr alloy. In this regard, the SGP model was first calibrated to nominally predict the temperature-dependent yield stress of a representative austenitic steel (Nikulin et al., 2010) and the representative flow stress at room temperature (Brown et al., 2017). A three dimensional (3D) cube-shaped simulation domain, comprised of 512 randomly oriented cubic grains, was generated using an in-house algorithm. These 3D ensembles were meshed using hexahedral elements of 50 μm size, with linear interpolation and full integration. The ensembles were deformed quasi-statically in tension at a fixed strain rate of $2 \times 10^{-4}\text{s}^{-1}$. Note that while the SGP constitutive model was calibrated to the experimental response using 3D simulations, the coupled PF-SGP simulations shown later have been performed in 2D, with a generalized plane strain assumption.

Flow parameters, primarily the reference strain rate, $\dot{\bar{\varepsilon}}_0^p$, activation energy for dislocation glide, ΔF_g, the shape parameters, p and q, and the threshold slip resistance, τ_0, were calibrated to predict the experimentally observed yield stress as a function of temperature. Since this work involves simulating processing-induced thermomechanical deformation across a wide range of temperatures, temperature-dependence of the elastic constants needs to be considered as well. Temperature dependence of the anisotropic elastic constants in the range $278 - 1473$ K was taken from Neuhaus et al. (2014); Magagnosc et al. (2021). The temperature dependent thermal expansion coefficient, α^θ, was taken from Pokharel et al. (2019). As a first order approximation, we have extrapolated these values for temperatures beyond the specified limits. FCC crystallography, with twelve $111 < 110 >$ slip systems, was considered for the calculation of the anisotropy factor, a.

Model predictions of the temperature-dependent yield stress from the standalone SGP model as compared with the experimental counterparts is shown in Figure 5.1(a). Experimental data for the temperature-dependent yield stress for SS 304L alloy were obtained from Nikulin

et al. (2010). Following this, the strain rate-dependent response of our SGP model was predicted by deforming the 3D ensembles at various strain rates ranging from $\dot{\varepsilon} = 2\times10^{-4}\text{s}^{-1}$ to $\dot{\varepsilon} = 2\text{s}^{-1}$. The 0.2% offset yield strength obtained for each of the simulations, was normalized with the value obtained at the lowest strain rate, i.e., at $\dot{\varepsilon} = 2\times10^{-4}\text{s}^{-1}$. These results, along with the experimental values for two different steels (i.e., low carbon steel: 0.035 wt. % C and micro-alloyed steel: 0.062 wt. % C) (Paul et al., 2014), have been shown in Figure 5.1(b). The model predicted strain rate sensitivity is in the same range as these representative experimental values. The hardening and substructure evolution parameters were estimated by fitting the Room Temperature (RT) stress-strain response to the experimental data for an AM SS304L deformed in tension (Brown et al., 2017). Analytical estimates of the initial SSD density, ρ^0_{SSD}, and Taylor hardening coefficient for isotropic hardening, k_{ih}, were directly taken from Brown et al. (2017), whereas the dislocation multiplication constant, k_{mul}, and the dynamic recovery constant, k_{rec}, were estimated by fitting to the experimental RT stress-strain response. This is shown in Figure 5.1(c).

Subsequent to identifying the flow and isotropic hardening parameters, the kinematic hardening parameters were identified using a separate set of simulations in 2D polygrain ensembles. This is necessitated as the model predicted size-dependent strengthening from our first order SGP model is expected to be mesh size-dependent (cf. Chapter 3). The GND density was assumed to be negligible at the start of the calibration simulations, i.e., $\rho^0_{GND} = 0$. The kinematic hardening coefficient, k_{kh}, was determined using the methodology discussed in Chapter 3 to nominally predict the Hall-Petch coefficients in the range of experimental observed values. In this regard, 2D microstructure ensembles of 100×100 μm with different mean grain sizes, D, were first instantiated using an open source tessellation and meshing software Neper (Quey et al., 2011). These microstructures were then meshed using 8 node square-shaped elements, with quadratic interpolation and 0.5 μm mesh size. The model-predicted Hall-Petch coefficients were well within the range of experimental values reported in the literature ($\sim$ 320 MPa $\mu\text{m}^{-0.5}$) (Astafurov et al., 2019). This has been shown in Figure 5.1(d) at different values of applied strain. Values of the SGP model parameters are given in Table 5.2.

5.2.2.2 Strain Gradient Plasticity Model Predictions of Single Crystal Deformation

Figure 5.2 shows the uniaxial stress-strain behavior for single crystal simulations performed in 3D (Figure 5.2(a)) and in 2D-plane strain (Figure 5.2(b)), with crystals oriented along

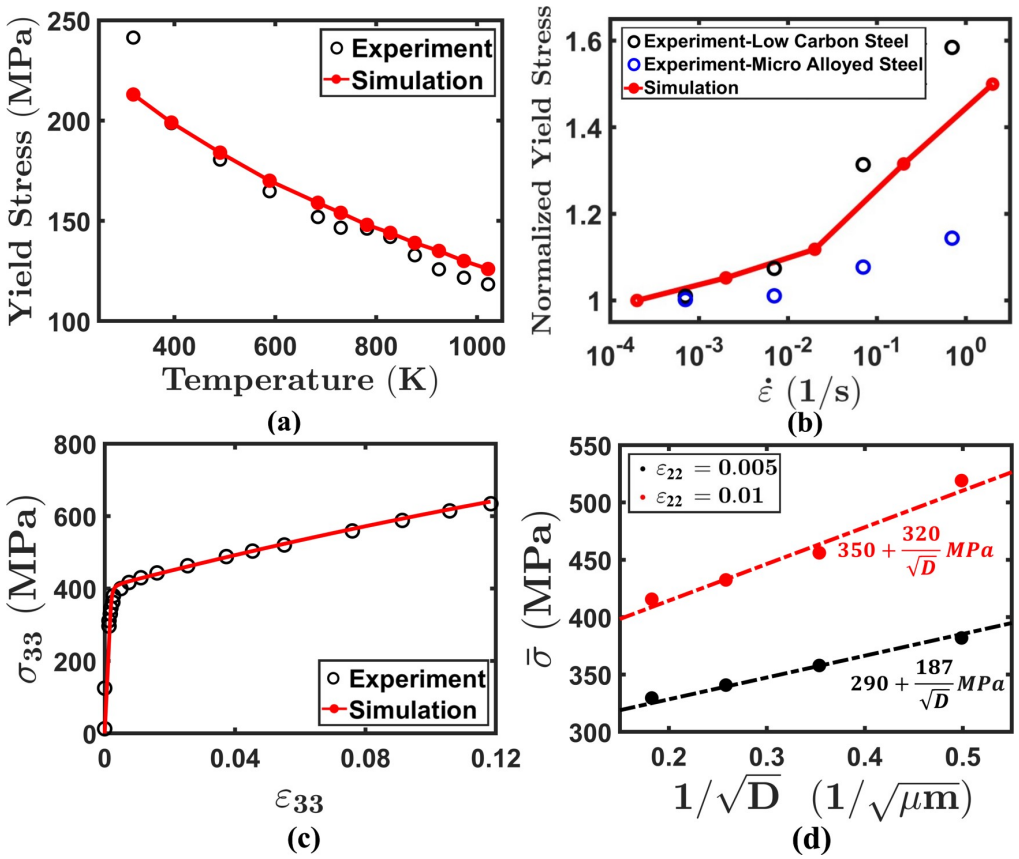

FIGURE 5.1: (a) SGP model prediction of the temperature-dependent yield stress as compared with representative experimental data from Nikulin et al. (2010). (b) SGP model prediction of the normalized strain rate-dependent yield stress as compared with the representative experimental data for similar steels from Paul et al. (2014). (c) Comparison of SGP predicted room temperature stress-strain response with the experimental data from Brown et al. (2017). (d) Prediction of grain size effect shown in terms of $\bar{\sigma}$ versus $1/\sqrt{D}$ for different values of applied strain. Here, D represents the mean grain size in the randomly instantiated microstructures.

the $< 001 >$, $< 011 >$ and $< 111 >$ directions, respectively. A comparison of the predicted elastic modulus and yield strength with their corresponding analytical estimates has been provided in Table 5.3. For a three dimensional domain, the analytical elastic modulus (Dieter and Bacon, 1976) and yield strength (Patra et al., 2023b) is given by:

$$\frac{1}{E_{hkl}} = S_{11} - 2\left[(S_{11} - S_{12}) - \frac{1}{2}S_{44}\right]\left(l^2m^2 + m^2n^2 + l^2n^2\right) \tag{5.31}$$

$$\bar{\sigma}_y \approx \bar{\chi} + a\left(\tau_0 + k_{ih}Gb\sqrt{\rho_{SSD}}\right) + a\left(s_t^0 + k_{ln}\varepsilon_b^{\frac{4}{3}}c_{Cr}^{\frac{2}{3}}\right)\left(1 - \left(\frac{kT}{\Delta F_g}\log\left(\frac{\dot{\varepsilon}_0^p}{\bar{\varepsilon}^p}\right)\right)^{\frac{1}{q}}\right)^{\frac{1}{p}} \tag{5.32}$$

TABLE 5.2: SGP model parameters for a representative Fe-Cr alloy.

Parameter	Description	Value
C_{11}	Temperature dependent elastic constants (GPa)	$(266.36 - 0.0677\theta)$
C_{12}		$(169.6 - 0.0196\theta)$
C_{44}		$(97.7 - 0.00604\theta)$
G	Shear modulus (GPa)	$(97.7 - 0.00604\theta)$
α	Thermal expansion coefficient (K^{-1})	$9.472 \times 10^{-6} + 2.062 \times 10^{-8}\ \theta - 8.934^{-12}\ \theta^2$
b	Burgers vector magnitude (nm)	0.258
$\dot{\bar{\varepsilon}}_0^p$	Reference shear strain rate (s^{-1})	1.73×10^{-1}
p, q	Activation energy shape parameters	0.35, 1.95
τ_0	Threshold slip resistance (MPa)	32
ΔF_g	Activation energy barrier	$0.5Gb^3$
s_t^0	Thermal slip resistance (MPa)	62.048
ε_b	Misfit parameter	0.031
k_{ln}	Self-diffusion constant for Cr (MPa)	18×10^3
k_{mul}	Dislocation multiplication constant	0.14
k_{rec}	Dynamic recovery constant	6
k_{ih}	Isotropic hardening coefficient due to SSDs	0.19
k_{kh}	Kinematic hardening coefficient due to GNDs	0.8
ρ_{GND}^0	Initial GND density (mm^{-2})	0.0
ρ_{SSD}^0	Initial SSD density (mm^{-2})	2.4×10^8

where, S_{ij} are the components of the compliance tensor, $\boldsymbol{S}$, and l,m,n are the direction cosines for the crystal orientation under consideration. Equation 5.32 is obtained by inverting the flow rule given in Equation 5.21 and the reader is referred to Patra et al. (2023b) for further description. Note that the value of $\bar{\chi}$ has been directly added from our simulations. For the 2D simulations, we rotate the elastic tensor to a plane strain coordinate system (Shishvan et al., 2011). The resulting plane strain elastic modulus E^* can be analytically estimated as (Shishvan et al., 2011):

$$E^* = \left[S'_{11}\cos^4\phi + 2\left(S'_{12} + 2S'_{66}\right)\cos^2\phi\sin^2\phi + S'_{22}\sin^4\phi - \frac{\left(S'_{13}\cos^2\phi + S'_{12}\sin^2\phi\right)^2}{S'_{33}} \right]^{-1} \tag{5.33}$$

where, S'_{ij} denotes the components of the compliance tensor in the plane strain coordinate system, and ϕ is the angle between X axis of the global and the plane strain coordinate system. Further, the methodology for estimating yield strength for a 2D domain is identical to that explained for its 3D counterpart.

Table 5.3 shows that the SGP predicted elastic moduli and yield stresses are in concurrence with the analytical values for all orientations. Generally speaking, the $< 111 >$ orientation is elastically stiffer (Brown et al., 2017) and also has a lower Schmid factor ($max(m^\alpha)$), in comparison to the $< 011 >$ and $< 001 >$ oriented single crystals. Similar observations have been noted for the 2D plane strain simulations, see Table 5.3. In summary, these results

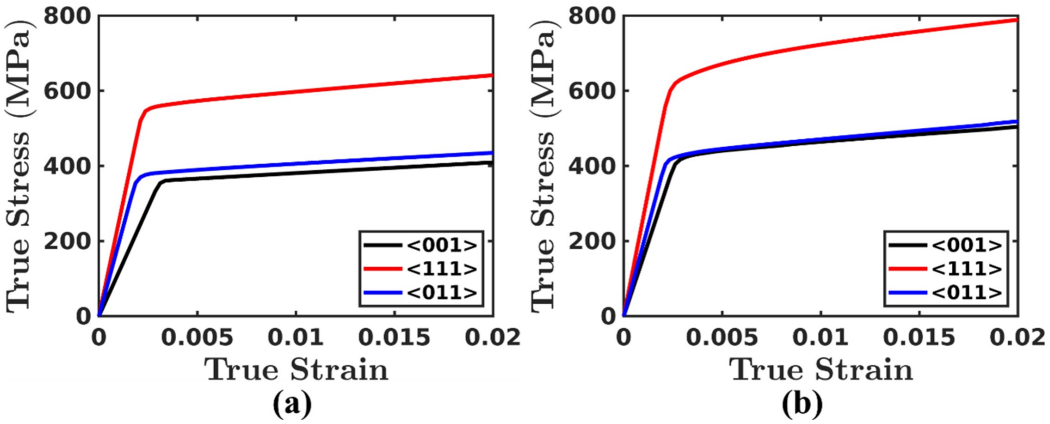

FIGURE 5.2: Model Predictions of mechanical response of $< 001 >$, $< 011 >$ and $< 111 >$ oriented single crystals obtained from (a) 3D and (b) 2D (plane strain) SGP simulations.

indicate that the proposed SGP model demonstrates the capabilities to predict the crystal anisotropy induced deformations similar to a crystal plasticity model, at least for small strains, but at much lower computational costs in comparison to a crystal plasticity model.

TABLE 5.3: Comparison of the elastic modulus, E, and yield stress, σ_y, values between the single crystal SGP simulations and analytical calculations.

Simulation domain	Property	Crystal orientation	J_2 SGP predictions	Analytical calculations
3D	E (GPa)	$< 001 >$	116.51	115.22
		$< 011 >$	192.81	191.81
		$< 111 >$	247.67	246.45
	σ_y (MPa)	$< 001 >$	303.51	317.91
		$< 011 >$	320.65	318.92
		$< 111 >$	528.81	507.36
2D	E (GPa)	$< 001 >$	157.80	156.93
		$< 011 >$	194.24	191.83
		$< 111 >$	266.18	263.10
	σ_y (MPa)	$< 001 >$	326.30	326.10
		$< 011 >$	333.60	326.34
		$< 111 >$	495.89	516.32

5.2.3 Coupled Phase Field and Strain Gradient Plasticity Simulations

Figure 5.3 schematically describes our coupled PF-SGP framework. The solidification and deformation simulations have been performed in three stages:

1. The first stage involved simulation of the phase transformation due to solidification, up to the point of complete solidification, i.e., $\phi_i = 1$ in the entire simulation domain, using the coupled PF-SGP model. Consideration for SGP allows the development of dislocation substructures and residual stresses during solidification.

2. Following complete solidification, the simulation domains are allowed to cool down to RT using only the SGP model. The PF model is turned off during this stage to save computational costs. This assumption is justified based on the limited diffusivity of Cr in solid Fe in these rapidly solidified microstructures (Lindroos et al., 2022), such that the Cr concentration may not evolve significantly. Moreover, the primary purpose of this stage of the simulation is to allow the development of thermally-induced residual stresses (cf. Pokharel et al. (2019)).

3. After cooling to RT, the microstructures are deformed using the SGP model, with the "residual" state of stresses, deformation gradients, SSD and GND densities, and backstresses.

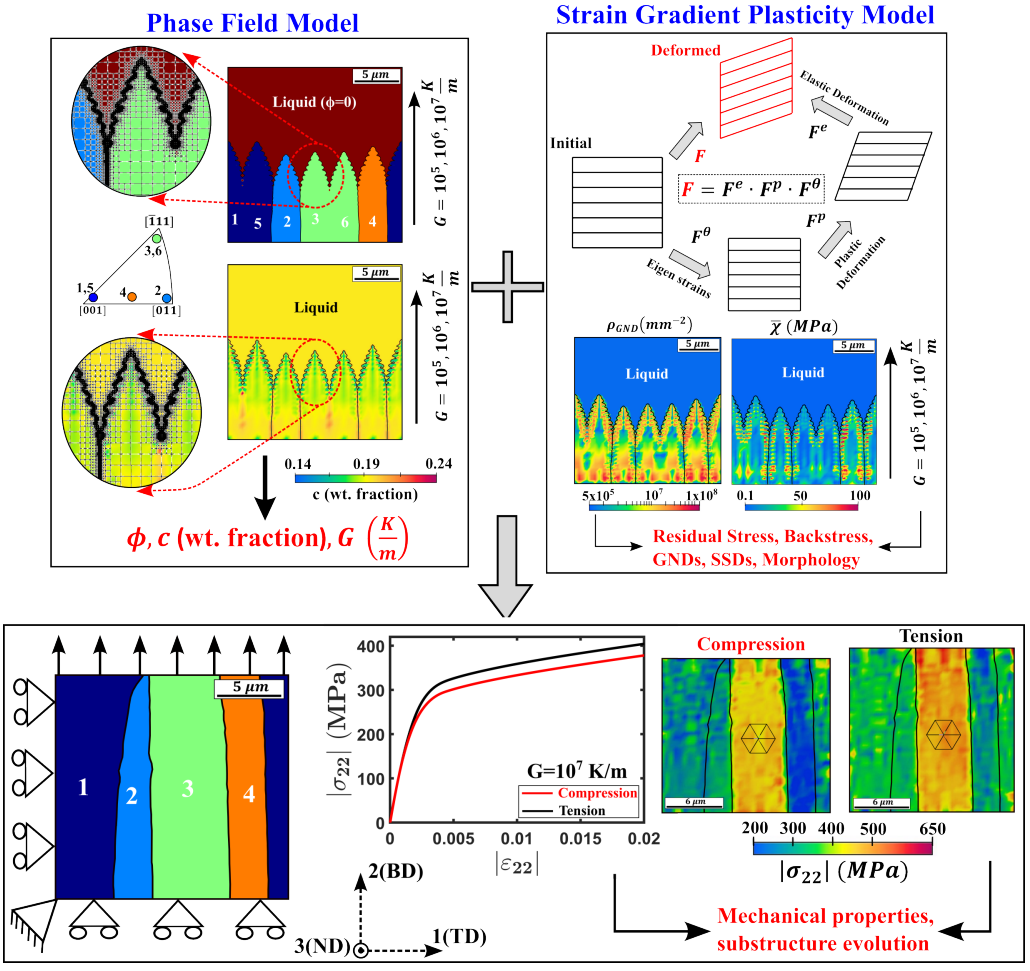

FIGURE 5.3: Schematic of the coupled phase field-strain gradient plasticity framework and its application in simulating solidification as well as post-solidification Tension-Compression asymmetry in rapidly solidified microstructures.

The simulation domain of 18×18 μm was meshed using square-shaped finite elements, with linear interpolation and full integration. This relatively small domain size was considered primarily to mitigate computational costs (also see Section 5.4). An initial mesh size of 0.125 μm was used at the start of the first time step. Following this, adaptive mesh refinement was employed to efficiently resolve the growing interface (Biswas et al., 2022). The mesh was allowed to selectively refine around regions depicting the largest error (of all variables, conserved as well as non-conserved). Such high error values are typical for the solid-liquid interfaces, inter-dendritic regions and for regions in the vicinity of grain boundaries. This resulted in the element size varying from 0.5 μm (maximum) up to 0.015 μm (minimum) within the simulation domain. Since the SGP model is a non-local formulation, the element size does affect the predicted strength contribution via the kinematic hardening coefficient, k_{kh} (see Chapter 3 and Patra et al. (2023b)). As a first order approximation, we assume that the k_{kh} remains constant ($k_{kh} = 0.8$) over all element sizes ($0.015 - 0.5$ μm) lying within the simulation domain. Following the approach of Pinomaa, Lindroos and co-authors (Pinomaa et al., 2020a; Lindroos et al., 2022), six equally spaced nuclei, with an initial radius of 0.07 μm and an interface width of 0.14μm, were initialized at the bottom edge of the simulation domain. Of the six nuclei, four have random crystallographic orientations (see orientations 1, 2, 3 and 4 in the Inverse Pole Figure (IPF) in Figure 5.3), whereas the remaining two nuclei are assumed to have an orientation identical to their neighbors (cf. nuclei 5 and 6 in Figure 5.3). Such an instantiation was deliberate, in order to analyze the solute behavior near Low Angle (LAGBs) or identical grain boundaries and the High Angle Grain Boundaries (HAGBs) during rapid solidification. Additionally, grains 1 and 2 represent the so-called intermediate orientations, having a Schmid factor $m = 0.42$, whereas grain 3 represents the hard orientation, having a $m = 0.31$. The grain 4 represents the soft orientation, having a Schmid factor of $m = 0.48$, respectively.

For the seed nuclei, we have assumed an initial SSD density (ρ^0_{SSD}) of 10^2mm^{-2} and an initial GND density (ρ^0_{GND}) of 10^2mm^{-2}. Note that these magnitudes vary from those used in our calibration simulations reported in Section 5.2.2.1. This is because the seed nuclei are instantiated in a liquid melt pool, i.e., at $\theta \sim \theta_m$, when dislocation densities are expected to be low. However, the remaining parameters of the SGP model have been kept identical to those mentioned in Table 5.2. The anisotropic strength, ς_i ($i \in [1, 4]$), was varied to incorporate the effect of crystallographic orientation on the growth morphology. A crystal with $< 001 >$ axis lying closer to the thermal gradient would always have a higher ς_i, thus exhibiting a stronger preference for growth (cf. Equation 5.7). In a similar manner, based on the crystallographic orientation allotted to the seed nuclei (see standard IPF triangle in Figure 5.3), ς_i calculations were performed for each of the four grains considered in this study. These values have been summarized in Table 5.4.

TABLE 5.4: Anisotropic strength values, ς_i, assigned to each of the grains using Equation 5.6.

Grain number	Crystal Orientation (Axis)	Value
1	$< 0\ 0\ 1 >$	0.04
2	$< 0\ 1\ 1 >$	0.029
3	$< 1\ 1\ 1 >$	0.024
4	$< 0\ 4\ 11 >$	0.035

The Cr concentration, c_{Cr}, was initialized to be 0.13 (in wt. fraction) within the domain of the initial nuclei, while it was 0.21 (in wt. fraction) inside the liquid. The Cr concentration was intentionally kept lower within the initial nuclei, to mimic realistic conditions, where initial nuclei formation results in solute rejection into the liquid (Spittle and Brown, 1989). During the solidification step, the temperature of the top edge of the simulation cell was kept equal to the melting temperature, θ_m, whereas the temperature at the bottom edge varied depending on the applied thermal gradient, G, and according to the following equation:

$$\theta(y) = \theta_m - G(H - y)\ \forall x \tag{5.34}$$

Here, $H = 18\mu$m is the height of the simulation domain and y represents the spatial coordinate along the solidification direction ($y \in [0, 18]\ \mu$m). The thermal gradient, G, varied from 10^5 K/m to 10^7 K/m in our simulations.

As described earlier, the phase field model operates in terms of the reduced temperature, θ_r, while the deformation model operates in terms of the absolute temperature, θ. In order to scale this variable, the reference temperature, θ_{ref}, used in Equation 5.4 to non-dimensionalize the absolute temperature, θ, was kept equal to the minimum (imposed) temperature among all solidification simulations used in the present study, i.e., $\theta_{ref} = \theta_m - 10^7\ H = 1609$ K. For the solidification simulations, the bottom left corner was fixed in all directions to prevent rigid body translation. Periodic boundary conditions were imposed on the left and right edges in all degrees of freedom, while the top and bottom faces were kept traction free. These non-linear partial differential equations were solved using the preconditioned Jacobian-free Newton–Krylov (PJFNK) solver in the MOOSE finite element framework (Permann et al., 2020). The solver parameters and tolerances were adapted from Biswas et al. (2022).

Post the completion of the solidification step, i.e., $\phi_i = 1$ in the entire domain, the PF model was turned off and the mesh was regularized to a uniform mesh size of 0.5 μm, while ensuring smooth interpolation of the phase field variables, deformation gradient, stress tensor, SSD, GND, and the backstress tensor, from the adaptively refined mesh to the uniform mesh. Subsequent simulations were performed with the standalone SGP model for cooling the

microstructures to room temperature. The microstructure solidified with the largest thermal gradient ($G = 10^7$ K/m), was subjected to a cooling rate of 3×10^5 K/s, whereas the microstructure solidified with intermediate ($G = 10^6$ K/m) and low ($G = 10^5$ K/m) thermal gradients were cooled at 3×10^4 K/s and 3×10^3 K/s to room temperature, respectively. Such large thermal gradients, and corresponding cooling rates, were chosen to mimic realistic solidification environments which are typical in an AM process (Farshidianfar et al., 2016; Prasad et al., 2020). Finally, the solidified and cooled microstructures were then subjected to tensile and compressive deformations up to a nominal strain of 0.02 to obtain their mechanical properties.

5.3 Model Predictions

In the present study, solidification simulations have been performed for three different thermal gradients, namely, 10^5 K/m, 10^6 K/m, and 10^7 K/m. We first present model predictions of microstructure evolution during solidification, followed by the mechanical properties.

5.3.1 Evolution of the Conserved Parameter, c_{Cr}

Figure 5.4 shows the distribution of Cr solute, c_{Cr} (in wt. fraction), after $\sim 50\%$ solidification for three different thermal gradients. The crystallographic orientation of the individual grains has been highlighted in the corresponding standard inverse pole figure (IPF) key. Two important observations emerge from these contours. Firstly, a transition from cellular to dendritic grain morphology can be seen with increasing values of G from 10^5 K/m to 10^7 K/m. Such grain morphologies are typical in welded structures, where a sharp thermal gradient, G, leads to a planar-cellular-dendritic transition on moving from the base metal towards the weld region (Zhu et al., 2021b; Fisher et al., 2023). Further, the solidification front is non-uniform, i.e., grains oriented favorably tend to grow faster than their neighbors. The anisotropy strength, ς_i, plays a key role here. Grains with $< 001 >$ axis oriented closer to the thermal gradient direction have a higher value of anisotropy strength, thus giving them a competitive advantage over their neighbors (Liu et al., 2018b). However, it is important to note that this heterogeneity in grain morphology is observed only for large thermal gradients. Lower thermal gradients provide a diminished driving force for grain growth, thus reducing the competitive advantage of favorably oriented grains and resulting in a cellular front.

Identical grain boundaries (same orientations between the grains) are marked as 'A', while the HAGBs are marked as 'B' in Figure 5.4. It is observed that the Cr segregation at 'A' type

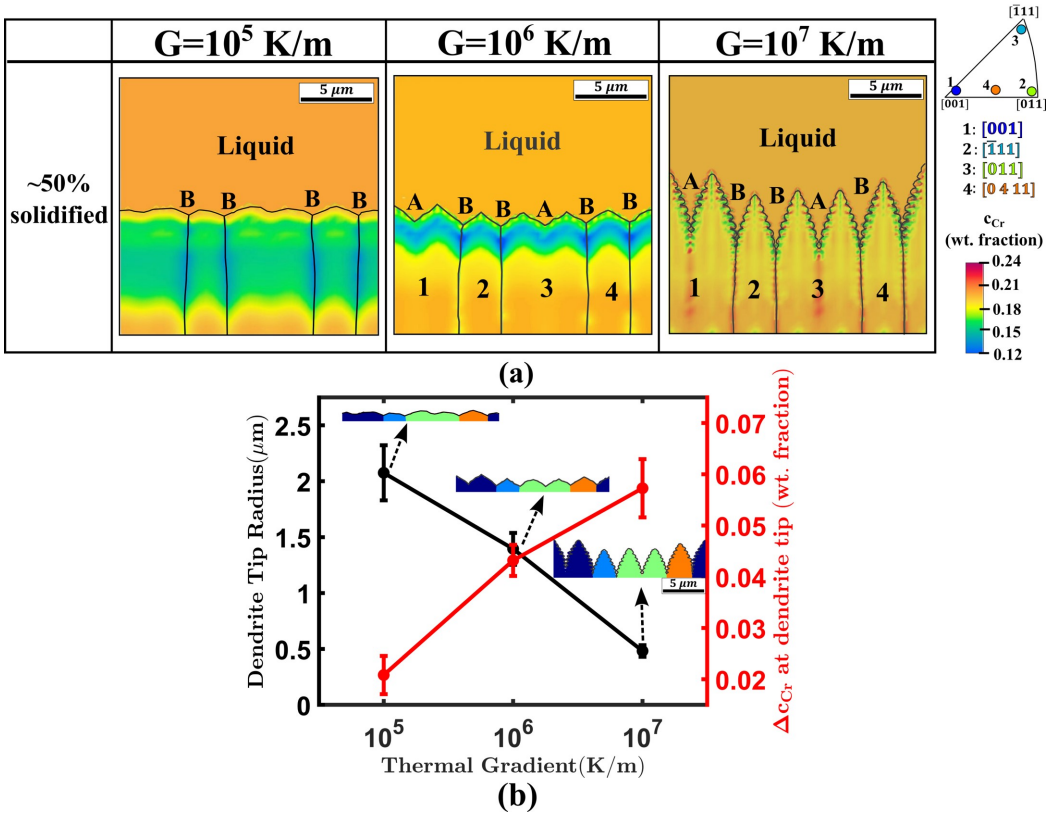

FIGURE 5.4: Cr concentration, c_{Cr}, in the $\sim 50\%$ solidified microstructure for three different thermal gradients, G. The crystallographic orientations of the grains have been marked in the standard inverse pole figure (IPF) key. The boundaries at the grain interfaces have been added during post-processing. The markers "A" and "B" refer to identical (same orientation between grains) and high angle grain boundaries, respectively. (b) Effect of the imposed thermal gradient, G, on the radius and Cr solute segregation at the dendrite tip.

boundaries is quite prominent for the largest G, i.e., 10^7 K/m. However, such a prominent Cr segregation does not develop at the 'A' type boundaries for $G = 10^5$ K/m and $G = 10^6$ K/m. This is primarily because the lower thermal gradients associated with lower cooling rates provide sufficient time and thermal activation for the Cr solute for diffusion, thus leading to segregation at only 'B' type grain boundaries (Mun et al., 2012; Li et al., 2022). For the microstructures solidifying at thermal gradients of $G = 10^5$ K/m and $G = 10^6$ K/m, the temperatures in these microstructures remains close to the melting point ($\theta_m = 1789$ K) even after complete solidification. Hence, no significant solute segregation can be seen at 'A' as well 'B' type boundaries in Figure 5.4. Another observation from the contours shown in Figure 5.4(a) is the variation in the Cr solute distribution within the solidified grains (along the direction of thermal gradient), specifically at low and intermediate thermal gradients. Such a behavior can arise by neglecting the effects of interface velocity on the partition coefficient (Pinomaa et al., 2020a), thus altering the evolution of (spatial as well temporal) Cr solute distribution (see Equation 5.13).

In order to further explore the effect of cooling rates on the microstructure evolution, the dendrite tip radius was estimated for the $\sim 50\%$ solidified microstructures. Figure 5.4(b) shows a decrease in the dendrite tip radius with increasing cooling rate. The observed scatter is primarily due to the anisotropy associated with the randomly assigned crystallographic orientation of the growing nuclei. The dendrite tip radius provides an alternative indication of the wavelength of instability at the solid-liquid interface (Fisher et al., 2023). Moreover, large thermal gradients, associated with high cooling rates result in a significant undercooling at the solid-liquid interface. This is due to the imposed temperature boundary conditions that alter the local temperature as well as composition equilibrium from the calculated solidus temperature, and are primarily responsible for the complex non-equilibrium microstructures observed in rapidly solidified microstructures (Zhu et al., 2021b).

Further, the Cr diffusivity in the solid phase is significantly lower as compared to the liquid phase. This, in conjunction with the higher undercooling and enhanced boundary layer thickness, leads to a higher ΔCr at the solid-liquid interface for simulations with large thermal gradients (and hence higher cooling rates). This phenomenon has been quantified in Figure 5.4(b), by extracting the Cr concentration from the line profiles at the solid-liquid interface from the $\sim 50\%$ solidified microstructure.

The results presented in this section highlight the effect of thermal gradients on solute (Cr) partitioning to the grain boundaries. Presumably, these may be expected to affect the deformation behavior and mechanical properties as well. In order to account for such effects, the thermal slip resistance in our SGP model accounts for solid solution strengthening due to the local Cr concentration (cf. Equation 5.26). Based on the local Cr concentration, the local thermal slip resistance is also allowed to vary during solidification.

5.3.2 Evolution of GND Density and Backstress

Figure 5.5 shows the evolution of the GND density, ρ_{GND}, and the effective backstress, $\bar{\chi}$, in the $\sim 50\%$ and the fully solidified microstructures under three different (imposed) thermal gradients. Corresponding line profiles for ρ_{GND} and $\bar{\chi}$ obtained at $H/2$ for the fully solidified microstructures are shown in Figures 5.6(a) and 5.6(b), respectively. In addition, the contour plots and the corresponding line profiles at $H/2$ for the SSD density, ρ_{SSD}, have been shown in Figure 5.7(a) and 5.7(b). Localizations of ρ_{GND}, and the corresponding $\bar{\chi}$ are evident along the primary as well as secondary dendrite arms for the microstructure solidified at $G = 10^7$ K/m. Insufficient supply of liquid metal to fill the empty gaps between the dendritic arms results in the development of significant strain gradients within these regions. The Cr solute segregation, especially at larger imposed thermal gradients, in the

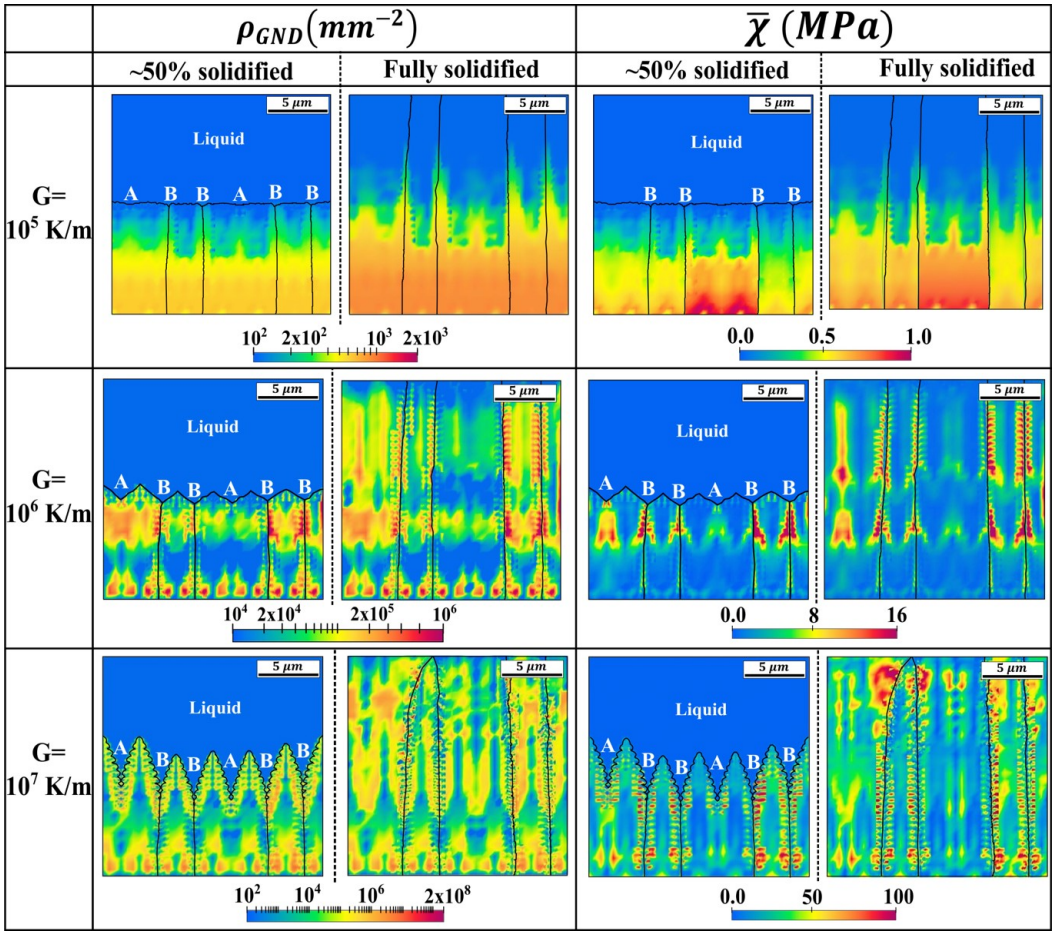

FIGURE 5.5: Contours of the GND density, ρ_{GND}, and effective backstress, $\bar{\chi}$, in the $\sim 50\%$ and the fully solidified microstructures for three different thermal gradients.

dendrite arms adds up to the local microstructural heterogeneity as well (cf. Figure 5.4). This leads to the development of geometrically necessary dislocations in these regions.

An important observation from Figure 5.5 and 5.6(b) is the development of backstress along the 'A' type boundaries. Especially, the microstructure solidified under the largest thermal gradient shows a significant backstress accumulation (Figure 5.5) and solute segregation (cf. Figure 5.4) along the 'A' type boundaries. At lower thermal gradients, the microstructure tends to homogenize, thus diffusing out the ρ_{GND} (Figure 5.6(a)) and backstress (Figure 5.6(b)) accumulations. This indicates that the development of local GNDs and backstress is also dependent on the underlying solute segregation. Generally speaking, the grain boundary energy associated with identical grain boundaries is significantly lower than their HAGB counterparts (Humphreys and Hatherly, 2012). Hence, the heterogeneities developed across 'A' type boundaries depict a much lower magnitude than the ones developed across HAGBs (see Figure 5.5). With decrease in G, no significant GND density and backstress accumulations were observed along the 'A' type boundaries for the intermediate and low thermal

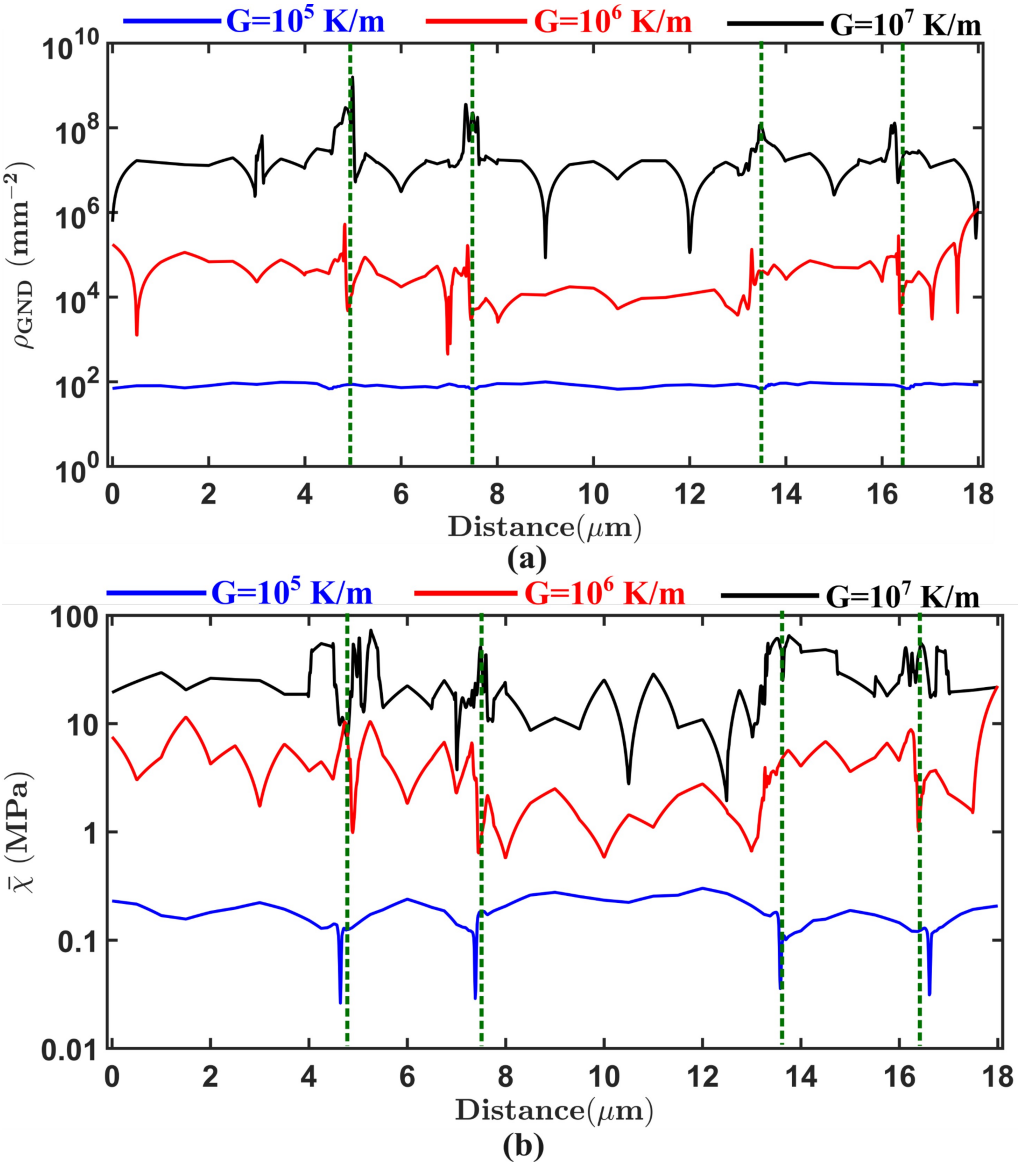

FIGURE 5.6: Line profiles of (a) GND density, ρ_{GND}, and (b) effective backstress, $\bar{\chi}$, in the fully solidified microstructures at $H/2$ for simulations with three different thermal gradients.

gradients (cf. Figure 5.6).

It can be seen from Figure 5.6 that the GND density increases by $\sim 1-2$ orders of magnitude and the effective backstress increases by about an order of magnitude per order of magnitude increase in G. While the value of backstress is still insignificant (< 6 MPa) for thermal gradients of 10^6 K/m and lower, the values increase to ~ 30 MPa for a thermal gradient of 10^7 K/m, which is typical of AM processes. Bertsch et al. (2020) measured the dislocation density in TEM lamellae of AM SS316L, where the cooling rate were derived from the corresponding SDAS spacing. Similar to the present work, they have observed a net rise

in the total dislocation density by $\sim$ 2 orders of magnitude with increase in the cooling rate from 3×10^3 K/s to 7×10^4 K/s. Additionally, similar magnitudes of total dislocation density have also been reported by Hu et al. (2023) at the end of the cooling stage using their multi-scale modeling framework of laser-based AM process. Yoo et al. (2018) calculated High Resolution- Electron Back Scattered Diffraction (HR-EBSD) based GND densities in an AM Inconel 718, and reported GND localizations similar to those shown in Figure 5.5 in the inter-dendritic regions. Godec et al. (2020) reported an average GND density of 1.34×10^7 mm^{-2} in their AM SS316L from the EBSD based Kernel Average Misorientation (KAM) data. Similar magnitudes of GND densities can also be seen in Figure 5.5 for the specimen solidifying with the highest G. Small and Taheri (2021) reported a rise in EBSD based average GND densities from 2.2×10^7 mm^{-2} to 1.2×10^8 mm^{-2} on moving from Binder Jet 3D Printing (BJ3P), with low thermal gradient, to Direct Metal Laser Sintered (DMLS), with higher thermal gradient for AM Inconel 625. Such an effect of the imposed thermal gradient can be clearly observed in Figure 5.5 and 5.6(a). The above observations provide validation of the model predicted dislocation densities near the inter-dendritic and grain boundaries.

The ρ_{SSD} contours and corresponding line profiles shown in Figure 5.7(a) and 5.7(b) do not show any notable variation for the lower and intermediate G, with their average magnitude being close to that of the initial SSD density, 10^2 mm^{-2}. Variations are somewhat visible at 'A' as well as 'B' type boundaries for the microstructure solidified under $G = 10^6$ K/m, however the subtended magnitudes are not that significant. On the other hand, the microstructure solidified under $G = 10^7$ K/m does indicate a notable rise in the ρ_{SSD}, although the average magnitude is still two orders lower than its ρ_{GND} counterpart. It is important to note here that the exponential rise in ρ_{GND} with increasing G also influences the ρ_{SSD} evolution through Equation 5.27. The sudden in rise in ρ_{SSD} for microstructure solidified under $G = 10^7$ K/m, and similarity in contour plots shown in Figure 5.5 and 5.7(a) do conform the above conclusion. This is interesting, considering that although our SGP model is rate-sensitive (cf. Figure 5.1(b)), the SSD density, which is a function of the plastic strain, does not vary significantly for the different thermal gradients. Given that the GND density is much higher than the SSD density for the highest G, the dislocation structures could be expected to be primarily of GND type. These results also indicate that the thermal gradient induced GND density and backstress could not be predicted by *local* plasticity models that do not account for the effect of strain gradients. *Non-local* strain gradient plasticity formulations are required to simulate the heterogeneous microstructure and residual stress developments during rapid solidification.

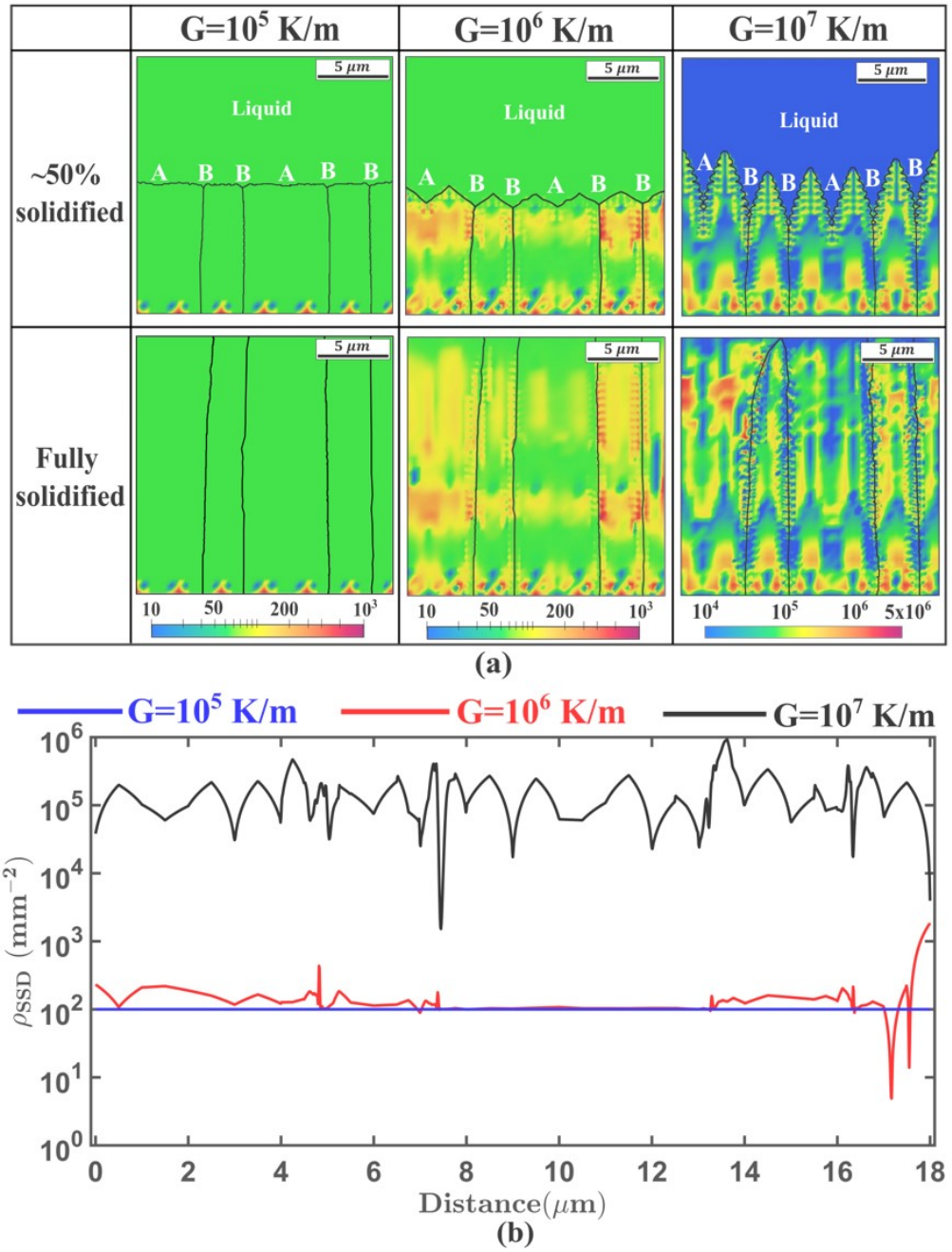

FIGURE 5.7: (a) Contours of the SSD density, ρ_{SSD}, in the $\sim 50\%$ and the fully solidified microstructures for three different thermal gradients. (b) Line profiles of the SSD density in the fully solidified microstructures at $H/2$ for simulations with three different thermal gradients.

5.3.3 Uniaxial Deformation of Solidified Microstructures

The solidified microstructures were first cooled to room temperature and then loaded in uniaxial tension and compression along the build (BD) and transverse (TD) directions at a quasi-static strain rate of 2×10^{-4} s^{-1} up to 0.02 nominal strain. As explained earlier, the microstructure solidified with the largest thermal gradient ($G = 10^7$ K/m) was cooled to RT with a cooling rate of 3×10^5 K/s, whereas its lower ($G = 10^5$ K/m) and intermediate ($G = 10^6$ K/m) counterparts were subjected to a cooling rate of $G = 3 \times 10^3$ K/s and $G = 3 \times 10^4$ K/s. As shown in Figure 5.3, the bottom and left faces were subjected to roller boundary conditions, whereas the bottom left corner was fixed in all dimensions to avoid rigid body motion. The remaining surfaces were kept traction free. As discussed previously in Section 5.2.3, the PF model was turned off and only the SGP model was employed for these deformation simulations.

Figure 5.8 shows the predicted mechanical response when loaded in both tension and compression, and separately along the BD and TD, for the microstructures solidified (and further cooled) with different thermal gradients. Generally speaking, the flow stress is higher during compression loading as compared to tension loading for the microstructures loaded along the TD and vice-versa for those loaded along the BD. Moreover, the observed difference in flow stress between tension and compression increases with increase in the (imposed) thermal gradient G. For $G = 10^5$ K/m, this effect is almost negligible. With a thermal gradient of 10^6 K/m, this effect increased somewhat, but is still very small. However, under large thermal gradients ($G = 10^7$ K/m), the anisotropy in predicted mechanical response is clearly visible. This behavior could be attributed to the significant ρ_{GND} and back-stress localizations developing in the microstructure, as seen in Figure 5.5 and is discussed later. Further, no appreciable difference is observed in the work-hardening regime for the different microstructures. This could possibly be due to the observation that ρ_{SSD} spatial distribution was nearly homogeneous, and did not display any significant localizations for the different thermal gradients (cf. Figure 5.7(a)) used in this study. The contours of $|\sigma_{22}|$ (for BD loading) and $|\sigma_{11}|$ (for TD loading), shown as inset in Figure 5.8, show an appreciable difference in the magnitude as well as distribution between the tensile and compressive deformations for the highest G. This is observed for the BD as well as TD loaded microstructures. While this effect is still present at lower G, the difference in the stress magnitudes between the two loadings are relatively lower. Additionally, the Cauchy stress contours for the different solidified and cooled microstructures are presented below to verify the self-equilibration of the residual stresses.

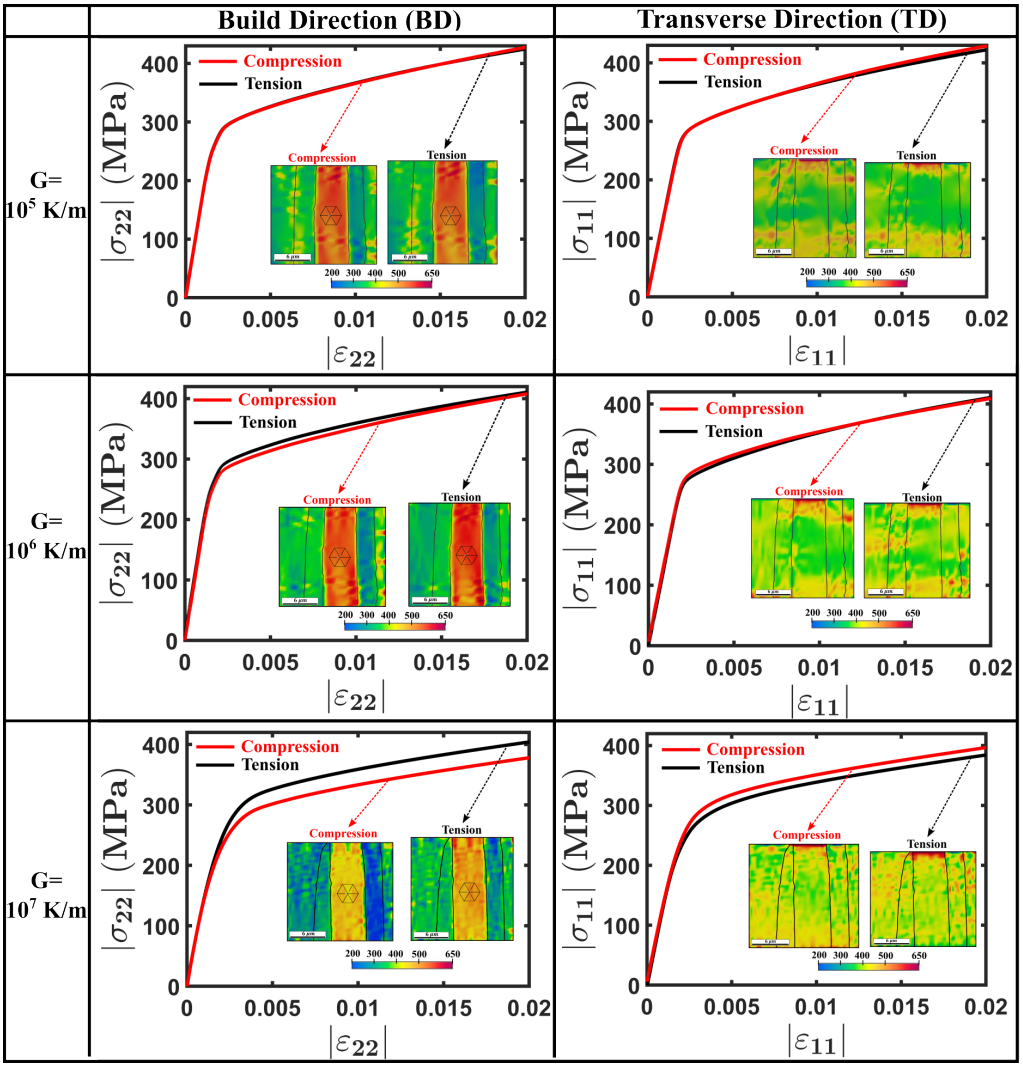

FIGURE 5.8: Stress-strain responses of the microstructures solidified and cooled under three different thermal gradients, loaded in uniaxial tension and compression along the build direction (BD) and the transverse direction (TD). The $|\sigma_{22}|$ (for BD loading) and $|\sigma_{11}|$ (for TD loading) deformation contours at a nominal strain of 0.02 have been added as an inset for each of the thermal gradients, respectively.

In the absence of any external loads, the residual Cauchy stresses within a simulation domain should self-equilibrate (Kapoor et al., 2018; Bandyopadhyay et al., 2024), i.e., the net sum of the stress components should be equal to zero over the simulation domain. To verify this, the $\bar{\sigma}$, σ_{11} and σ_{22} contours were plotted for the fully solidified and cooled microstructures for the three different thermal gradients (prior to deformation) in Figure 5.9. Further, the element area-weighted sum of the individual Cauchy stress components over the entire domain, i.e., $\langle\sigma_{ij}\rangle = \sum \frac{A_k}{A_{\text{total}}}\sigma_{ij}$, are also shown in Figure 5.9. It can be seen that $|\langle\sigma_{ij}\rangle| \leq 1\ MPa$ for all three thermal gradients, thus verifying self-equilibration of residual stresses along the BD and TD. It can also be seen that the residual stresses are high in the regions where

the backstress is high (see hotspots for $G = 10^7$ K/m in Figure 5.5 and the corresponding regions in Figure 5.9, for example).

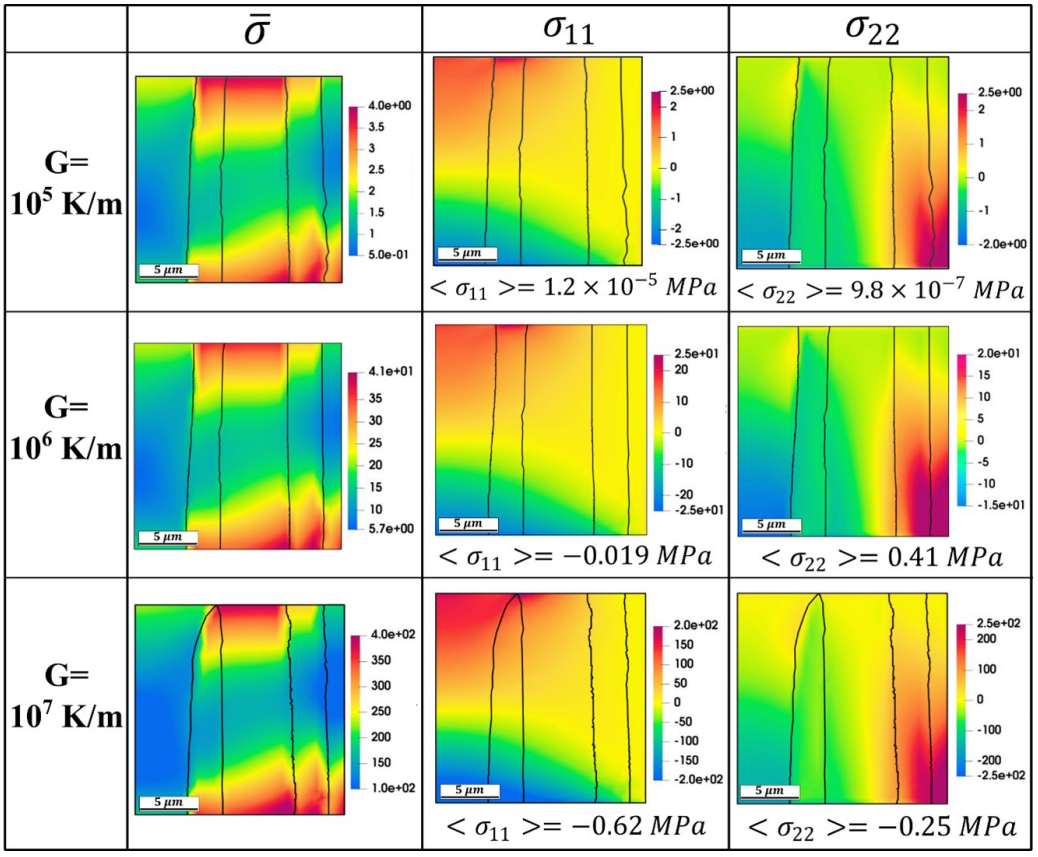

FIGURE 5.9: $\bar{\sigma}$, σ_{11} and σ_{22} contours in the fully solidified and cooled microstructures for the three different thermal gradients. Note that the scales (in MPa) are different in all three cases.

In addition, the hard grain ($m = 0.31$, grain 3 in Figure 5.3) displays significantly large stress magnitudes as compared to the intermediate grains ($m = 0.42$, orientation 1 and 2 in Figure 5.3), which in turn, accommodate higher stresses when compared to the softer grain ($m = 0.49$, orientation 4 in Figure 5.3). Such an effect is much more prominent when loaded along the BD than along the TD. Similar correlations between the accommodated residual stresses and (grain average) orientations have been noted by employing a thermo-mechanical crystal plasticity model during LPBF-based solidification of a fully austenitic SS316L by (Kuna et al., 2023). These results further indicate that the proposed SGP model has the ability to capture orientation-based anisotropy in directionally solidified microstructures at a computational cost significantly lower than its CPFE counterpart.

To further understand the role played by printing-induced backstresses on the anisotropy in mechanical response, the average values of individual backstress components, i.e., χ_{11}, χ_{22} and χ_{33}, were analyzed at the end of the cooling regime. This is described schematically

in terms of the translation of the von-Mises yield surface in Figure 5.10. The tabulated (average) backstress magnitudes show a clear increase with increase in thermal gradients, irrespective of the component under consideration. Using a two dimensional approximation of 3D yield surface, we now try to explain the effect of these (directional) backstress components on the subsequent yield surface. Assuming an initially negligible backstress (which is conventionally assumed to be the center of the yield surface), the initial yield surface (schematically shown using the dotted black line in Figure 5.10) is centered at the origin, A. Dislocation substructure and backstress evolution during solidification leads to the translation of the center of the yield surface to the point B, which also varies as a function of the thermal gradient. The negative values of χ_{11} leads to a leftward translation of the yield surface along direction 1 (TD) (see Figure 5.1), along with a upward translation along direction 2 (BD) due to a positive χ_{22}. The post-solidification yield surface is schematically shown using the dotted red line in Figure 5.10. On subjecting to uniaxial deformation, the resulting yield stress is thus higher in compression as compared to tension for TD loading, and vice-versa for BD loading. This explains the mechanistic origin of TC asymmetry in rapidly solidified Fe-Cr alloys due to the GND-induced directional backstress.

Given that a generalized plane strain assumption was used in our mechanics model, χ_{33} is also predicted in our essentially 2D simulations (which is similar in magnitude to χ_{11}). However, the qualitative arguments regarding the translation of the yield surface due to the printing-induced directional backstress would not change under the assumption of different boundary conditions, such as plane stress or full 3D.

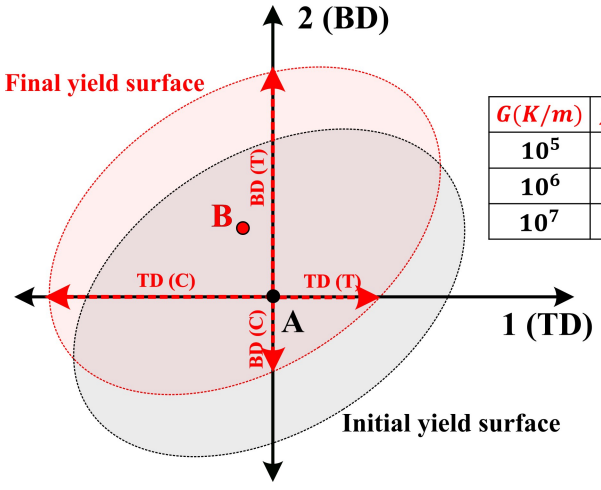

$G(K/m)$	χ_{11} (MPa)	χ_{22} (MPa)	χ_{33} (MPa)
10^5	-0.02	0.04	-0.02
10^6	-0.68	1.36	-0.72
10^7	-3.67	8.34	-4.96

FIGURE 5.10: Schematic showing the effect of the backstress tensor, $\boldsymbol{\chi}$, on the translation of the yield surface due to dislocation substructure development during solidification. The table on the right gives the values of the individual components of the backstress tensor, χ_{11}, χ_{22} and χ_{33}, at the end of solidification and cooling for the microstructures with three different thermal gradients.

In order to quantify the predicted TC asymmetry, we have adopted the metric of Strength Differential, SD, as given by (Bassani and Racherla, 2011; Patra et al., 2014):

$$SD = \frac{|\sigma_y^t| - |\sigma_y^c|}{\left(|\sigma_y^t| + |\sigma_y^c|\right)/2} \tag{5.35}$$

where, σ_y^t and σ_y^c denote the yield strength in tension and compression, respectively. Figure 5.11 shows a direct comparison of the SD obtained under BD and TD loading for the various thermal gradients simulated in this study. The SD values indicate that the TC asymmetry gets enhanced with increase in the thermal gradients. Available SD data from the literature for similar Fe-Cr alloys (under TD loading) have also been plotted in Figure 5.11. It can be seen that the predicted SD values, under TD loading, are qualitatively comparable to the experimental SD values reported in literature, thus validating our model predictions. It should be noted that the present study used only six initial seeds with (four) random crystallographic orientations (see Figure 5.3), for the (directional) solidification simulations. The number of seeds used, their orientations, the imposed thermal gradient and the volume of the ensemble may also effect the ensuing mechanical properties, and hence the SD magnitudes. Further, it should also be noted that our model was not calibrated to any specific material data and hence only qualitative trends should be inferred from our predictions.

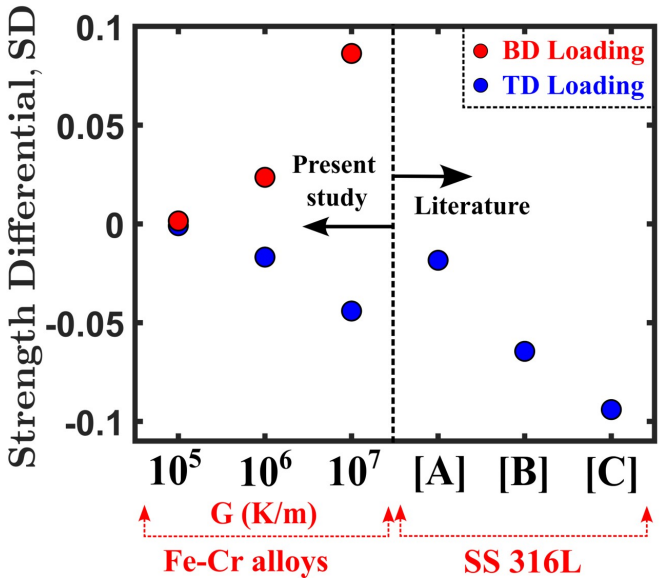

FIGURE 5.11: Strength Differential (SD) values for the three thermal gradients under BD and TD loading, in comparison with the available experimental data. The markers [A], [B] and [C] refer to the literature values from Wang et al. (2023), Jeon et al. (2019), and Chen et al. (2019), respectively.

Two important observations can be further derived over here. Firstly, the microstructures

solidified (and further cooled) under the intermediate and largest thermal gradients have predicted a non-negligible TC asymmetry, with the simulated SD values being qualitatively similar to those reported in the literature (Chen et al., 2019; Jeon et al., 2019; Wang et al., 2023). For the TD loading of the microstructure with $G = 10^7$ K/m, the yield stress values in tension were 293.1 MPa and compression were 305.1 MPa, respectively. This resulted in a SD of -0.0401. Note here that the difference between the yield stresses in compression and tension ($\sim$ 12.0 MPa) roughly correspond to twice of the mean effective (average) backstress accumulated in the microstructure ($\sim$ 7.4 MPa). Chen et al. (2019) also reported similar observations from their deformation studies on AM SS 316L. An identical analysis for the microstructure with $G = 10^6$ K/m reveals that the difference between the yield stress in compression and tension ($\sim$ 4.0 MPa) follows a similar relationship with the effective (average) backstress ($\sim$ 1.7 MPa). Moreover, with increasing thermal gradients, the SD values display an exponential increase, as seen in Figure 5.11 for BD as well as TD loading scenarios. This could be attributed to the order of magnitude increase in backstress values (due to the printing-induced GND density) as described in Figure 5.10. Presumably, local solute segregation may also play a role in the TC asymmetry of rapidly solidified microstructures. Individual contributions of these competing mechanisms are delineated in Section 5.4.

5.4 Discussion

It has been previously reported that the microscale intragranular residual stresses, an outcome of printing induced dislocation substructures, are primarily responsible for the TC asymmetry observed in rapidly solidified metals (Chen et al., 2019; Zhang et al., 2022). The present work developed a coupled PF – SGP framework to simulate these microscale residual stresses and their effect on the anisotropic mechanical properties, specifically the TC asymmetry. The prior studies (Chen et al., 2019; Zhang et al., 2022), assumed a constant initial value of backstress during the deformation simulations to predict this TC asymmetry. In our work, the backstress, due to the GND densities, were allowed to develop *in situ* during the solidification. While Pinomaa, Lindroos and co-authors (Pinomaa et al., 2020b,a; Lindroos et al., 2022) have previously used coupled phase field-crystal plasticity models to predict the dislocation structures and also predicted the mechanical properties of rapidly solidified microstructures, they did not explicitly model the *directional* backstress due to these dislocation structures and did not attempt to predict the anisotropic mechanical properties of rapidly solidified microstructures. Consideration for the said effects in our

coupled PF-SGP modeling framework to predict the TC asymmetry of rapidly solidified microstructures represents an advancement over these prior modeling studies.

We further delineate the role played by the two potentially competing mechanisms on the TC asymmetry: (a) the thermal distortion induced GNDs (and directional backstress), and (b) local Cr solute segregation at the solid-liquid interface, which necessitates the presence of GNDs to accommodate the ensuing lattice incompatibilities. As discussed in (Yoo et al., 2018; Bertsch et al., 2020), these solute segregation-induced GNDs then interact with the moving dislocations and contribute to additional hardening. In this regard, the solidification simulations for $G = 10^7$ K/m were re-run, *albeit* with two modifications. In one case, the backstress tensor, $\boldsymbol{\chi}$, was forced to be equal to zero, i.e., suppressing the contribution of GNDs to the directional residual stresses. In the second case, a uniform solute concentration was artificially imposed by setting the Cr concentration equal to the equilibrium concentration of $c^0_{Cr} = 0.21$, i.e., suppressing solute segregation and its contribution to the GND development and backstress. Post-solidification, these simulations were cooled (at a cooling rate of 3×10^5 K/s) and subsequently deformed in tension and compression along the BD as well as TD directions, respectively. Figure 5.12(a) shows the mechanical response in terms of the stress-strain curves and Figure 5.12(b) shows the predicted values of SD for these two cases, as compared with the predictions from a fully coupled PF-SGP model. These results clearly point out that the contribution of GND-induced backstress to the SD is higher than that due to solute segregation. Such an observation can be seen for the microstructrures loaded along both BD and TD. Modeling frameworks for predicting the anisotropic mechanical response of rapidly solidified microstructures therefore need to consider both these effects. In experiments, both the mechanisms are expected to act concurrently during rapid solidification, although the dominant mechanism may vary based on the microstructural factors and the boundary conditions imposed on the specimen.

Further, the PF-SGP framework proposed here has been used to study cellular microstructures which are expected to develop at the subgrain level. While the model can be applied for larger polycrystalline structures, the computational expenses involved would be substantial.

We note that strain gradient crystal plasticity models (instead of J_2 plasticity models) could be better suited for predicting heterogeneous substructure development at the slip-system level during rapid solidification. However, these simulations become significantly computationally intensive when coupled with PF due to the fact that adaptive remeshing at the solidification front in our coupled simulations lead to over $300,000$ finite elements in the simulation domain during the solidification process. A representative solidification and cooling simulation takes ≈ 250 hours on 200 processors in parallel. A crystal plasticity simulation would take at least an order of magnitude longer time to run. Nonetheless, our J_2

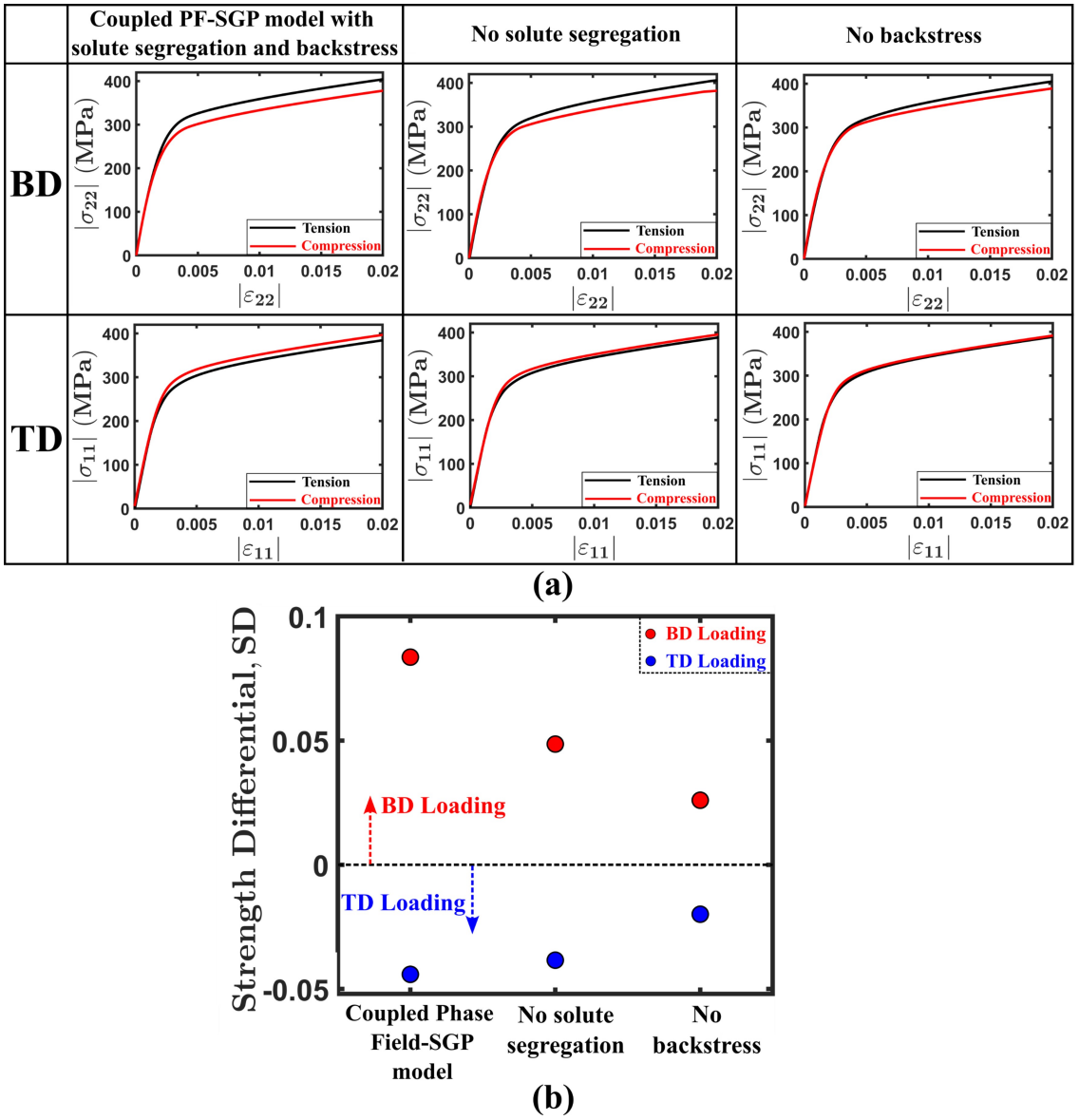

FIGURE 5.12: (a) Predicted stress-strain responses along the BD and TD, and (b) Strength Differential, SD, values for microstructures solidified under $G = 10^7$ K/m and then cooled with a cooling rate of 3×10^5 K/s using the fully coupled PF-SGP model (with solute segregation and directional backstress), and those without consideration for solute segregation, and backstress, respectively.

SGP model has consideration for anisotropic elasticity and the crystallographic orientation based anisotropic factor, which are expected to influence to heterogeneous microstructure development and mechanical properties. As has been shown in Figures 5.4 - 5.12, our model is able predict these heterogeneous microstructural attributes and anisotropic mechanical properties. We also note that a generalized plane strain was used in our 2D simulations. This implies that the microstructure is scalar along the third direction, 3, and is a deviation from realistic rapid solidification. Presumably, the heterogeneity of microstructure development and mechanical properties would be further enhanced on consideration of 3D simulations. This will be explored in future work. Additionally, the inherent crystallographic texture of rapidly solidified microstructures has also been shown to be one of the factors contributing to the anisotropy in mechanical response (Geiger et al., 2016; Jeon et al., 2019), but in this work we have focused primarily on the role of microscale residual stresses on the TC asymmetry effect. The combined role of texture and microscale residual stresses on the TC asymmetry of AM microstructures may be explored in future work.

5.5 Conclusions

We propose a coupled phase field-strain gradient plasticity (PF-SGP) framework, to predict the TC asymmetry in rapidly solidified Fe-Cr alloys. The numerical framework, summarized in Equations 5.1-5.30, accounts for multi-grain interaction effects, solute segregation, anisotropy of elastic and plastic deformation, GND density, directional backstress, local solute strengthening and thermally induced residual stress development in the microstructures during rapid solidification. The model was implemented in an open source finite element framework, MOOSE (Permann et al., 2020), using a two-step scheme: firstly, the coupled PF-SGP framework was used to predict the microstructure evolution in terms of solute segregation, dislocation substructures and backstresses during rapid solidification of the liquid melt, under three different thermal gradients ($G = 10^5$ K/m, 10^6 K/m and 10^7 K/m). Following this, only the SGP model was employed while cooling the microstructures (to RT) (with a cooling rate of 3×10^3 K/s, 3×10^4 K/s and 3×10^5 K/s), and subsequently deforming them in tension and compression along the build and the transverse directions separately.

The coupled framework successfully captured the development of several microstructural features, such as Cr solute segregation, GND localizations and backstress evolution, during the rapid solidification of Fe-Cr alloys under different (imposed) thermal gradients. The significant model predictions can be summarized as follows:

1. Inter-dendritic regions or HAGBs accumulated large magnitudes of ρ_{GND}. Solute segregation introduced additional local lattice incompatibilities, further enhancing these ρ_{GND} localizations.

2. A rise in ρ_{GND} by $\sim 1-2$ orders of magnitude, and by an order of magnitude in $\bar{\chi}$ was observed per order of magnitude increase in G (cf. Figures 5.7(a,b)).

3. Post solidification and cooling, the room temperature mechanical response of these rapidly solidified microstructures, indicated that the predicted TC asymmetry, quantified in terms of the Strength Differential (SD), is in the range of reported experimental data (cf. Figure 5.11). Additionally, the SD values showed a rise with increase in the thermal gradient.

4. The observed TC asymmetry could be explained in terms of the negative (average) backstress component along the transverse direction and a positive (average) backstress component along the build direction (cf. Figure 5.10).

5. Simulations without solute segregation and those without backstress indicate that the thermal distortion induced GNDs (and hence backstresses) play a primary role in the observed TC asymmetry, although the TC contribution due to solute segregation is not negligible either (cf. Figure 5.12).

The novelty of this modeling framework lies in its ability to predict the *in situ* development of dislocation substructures and backstresses during rapid solidification that influence its post-solidification anisotropic mechanical properties. The modeling tools and analysis of model predictions in this study could be used to develop process-microstructure-mechanical property correlations in rapidly solidified microstructures and inform the appropriate choice of AM process parameters. The modeling framework will be extended in future work to simulate post-solidification heat treatments and their effects on the mechanical properties.

Chapter 6

Diffraction-Based Multiscale Residual Strain Measurements

6.1 Introduction

Residual strains, and corresponding elastic stresses, develop when a specimen is subjected to non-uniform elastic-plastic strain gradients (Verlinden et al., 2007; Lodh et al., 2018; Thool et al., 2020). The latter may be imposed from a variety of processes (Osgood, 1954; Cullity, 1956; Almen and Black, 1963; Noyan and Cohen, 2013; Lodh et al., 2017, 2018; Thool et al., 2020). In a crystalline material, the residual strains represent lattice distortions or changes in the unit cells (Verlinden et al., 2007). Corresponding non-equilibrium structures are retained by defects, such as dislocations and dislocation boundaries. Based on the scale, the strains and stresses differ (Lodh et al., 2017, 2018; Thool et al., 2020). They are referred as macro (type I) to meso (type II) and micro (type III) (Verlinden et al., 2007). To a designer, the macroscopic residual stresses are important (Wang and Gong, 2002; Kumar et al., 2016), but micro and mesoscopic stresses and strains are also emerging as an important aspect in any microstructural investigation (Lodh et al., 2017, 2018, 2019; Thool et al., 2020). Information on local lattice distortions is a critical but often invisible component of the overall microstructure (Verlinden et al., 2007). This is the subject of multiscale residual strain measurements, the focus of the present study.

Traditional residual strain measurements include techniques ranging from dimensional changes (mechanical) to property alterations (Osgood, 1954; Withers and Bhadeshia, 2001; Verlinden et al., 2007). However, only diffraction based measurements can bring out the full

[1] Significant parts of this Chapter have been published in (Pai et al., 2024a)

strain matrix, which may then be converted with appropriate continuum elasticity model(s) to residual stress values (Van Houtte and De Buyser, 1993). Further, modern analytical tools, from micro-focus X-Ray Diffraction (XRD) to electron microscopy based microtexture determination, hold tremendous potential for multiscale diffraction based residual strain measurements (Wilkinson et al., 2006; Ghamarian et al., 2014; Lodh et al., 2019; Yu et al., 2019; Prakash et al., 2023). Among these techniques, micro-Laue based single-crystal residual stress measurement (Lodh et al., 2017, 2018, 2019; Thool et al., 2020) is non-trivial to implement in a laboratory XRD setup. However, this can be effectively used to measure grain-by-grain residual strain(s) with progressive plastic deformation or annealing (Lodh et al., 2017; Thool et al., 2020). The limitation of this technique is in the X-ray micro-focus, which is ~ 50 micron based on the spot size achievable in our laboratory setup. The XRD approach estimates relative strain from changes in the interplanar spacing ($\Delta d/d$), which is also a traditional estimate of lattice distortion (He, 2003; Lodh et al., 2017).

Similar to XRD, neutron diffraction also quantifies the changes in ($\Delta d/d$). This has been routinely employed for measurement of residual strains (Krawitz and Holden, 1990), and for estimating diffraction-based elastic constants (Baczmanski et al., 1993) and differential scattering (Soper, 2011) experiments. The key advantage lies in the greater penetration depth of neutrons. Alternatively, μ-Raman spectroscopy, with a reported strain precision of 10^{-4}, relies on the Raman peak shifts and quantifies the local (hydrostatic) stresses (Mehtani et al., 2020). This technique has excellent application potentials (Senez et al., 2003; Choi and Griffin, 2016; Srinivasan et al., 2018; Mehtani et al., 2020) and can be used to measure residual strains in sub-micron scale (Mehtani et al., 2020). However, typical measurements are "restricted" mostly to ceramics and oxides, and numerical conversion of Raman peak shift to residual stress values require high pressure data of the corresponding system.

This study, in particular, focuses on the use of laboratory scale micro-Laue single crystal XRD technique for measurement of residual strains within a single grain (Lodh et al., 2018, 2019). Other notable techniques, used in this study, are the related methods of High Resolution Electron Backscatter Diffraction (HR-EBSD) (Wilkinson et al., 2006; Fullwood et al., 2015) and High Resolution Transmission Kikuchi Diffraction (HR-TKD) (Yu et al., 2019). Both involve the same algorithm of the so-called cross-correlation, and are sensitive to changes in interplanar angle ($\Delta\theta/\theta$). Their spatial resolution is determined by the electron-atom interaction volume (Goodhew and Humphreys, 2000); and is arguably ~ 20 nm in EBSD (Zaefferer, 2007; Schwarzer et al., 2009; Ruggles et al., 2016) and even smaller in TKD performed on thin foils (Humphreys et al., 1999; Trimby, 2012; Ghamarian et al., 2014; Sneddon et al., 2016).

The technique of Transmission Electron Microscope (TEM) based Precession Electron Diffraction (PED) (Rauch et al., 2010) has originally been proposed $\sim$ 2009. This is based on measurements of interplanar spacing, $(\Delta d/d)$, from the diffraction spots (Ghamarian et al., 2014; Ghamarian, 2017). The method has the potential of providing spatial resolution of below 2 nm but is restricted by the sensitivity of the respective diffraction vectors (Ghamarian et al., 2014). The key advantage of TEM lies is in its adaptability, as the same instrument can be utilized to measure strains adopting different strain mapping techniques. Béché et al. (2013) provides a comparison between five such TEM-based residual strain measurement techniques. They all offer below 5 nm spatial resolution. These include the Convergent and Nano Beam Electron Diffraction (CBED and NBED), High Resolution TEM (HR-TEM) and High Resolution Scanning TEM (HR-STEM) and the Dark Field Electron Holography (DFEH). These deliver different strain precision, ranging from 2×10^{-4} (for CBED) to 10^{-3} (for HR-STEM) (Armigliato et al., 2006; Hüe et al., 2008; Béché et al., 2013) and varied spatial resolution. Further, they have (Béché et al., 2013) also accounted for sample specifications (thickness and geometry), data analysis time and associated computational resources (ranging from 1 day (for CBED) to $<$ 1 minute (for HR-TEM and DFEH)) together with the selection of reference frame.

In brief, TEM based strain mapping depends on the selection of an appropriate technique suitable for the problem in-hand (Béché et al., 2013). For example, the nano-scale strain distributions on strained Germanium (Ge) microdisks have been studied using the PED technique in STEM (Bashir et al., 2019). The corresponding experimental strain contours showed reasonable agreement with three-dimensional finite element simulations. Further, utilizing the scanning NBED with direct electron detectors in combination with efficient (diffraction) pattern recognition algorithms have enabled mapping of strains with relatively large field of view ($\sim$ 1 μm) even in the microstructures with large defect concentrations (Ozdol et al., 2015).

In summary, a range of micro to nanoscale diffraction techniques presently exist for effective strain mapping. Each of these possesses their own merits and demerits. The selection of a technique is hence based on the research objectives, length scale and material. The present study explores a few of them, namely the micro-Laue XRD, HR-EBSD, HR-TKD and TEM-PED. Each of these multiscale diffraction-based technique subtends a different scale and resolution. More importantly, their measurements are sensitive to two different aspects of lattice distortion, $(\Delta\theta/\theta)$ (for HR-EBSD and HR-TKD) versus $(\Delta d/d)$ (for micro-Laue and TEM-PED). It is hence essential to examine the numerical convergence/similarity between the strain magnitudes estimated by each of these techniques, and in particular, determine a (numerical) scaling factor between them. Addressing these gaps along with a general

comparison of the strengths and weaknesses of each of the techniques were the motivations behind this study.

6.2 Experimental Details

This study used fully recrystallized interstitial free (Body Centered Cubic or BCC) steel of $\sim 130\ \mu m$ micron average grain size. For details on the prior processing and chemistry, the reader may refer to Manda et al. (2023). In particular, sub-size micro-tensile specimen(s) (for dimensions refer to Figure 6.1) were fabricated by electro discharge machining. The gauge regions were prepared by a combination of mechanical polishing, followed by electropolishing. The latter involved an electrolyte of 80 : 20 methanol and perchloric acid, and 18 volts dc at 253 K. As in Figure 6.1, EBSD scans were performed with interrupted but progressive tensile deformations. These were conducted with a Deben^{TM} 1 kN stage operated at $10^{-3}\ s^{-1}$, and a maximum strain of 0.15 was imposed. It is to be noted that this stage was compatible with both our XRD and Scanning Electron Microscope (SEM). This enabled us to conduct multiscale diffraction based residual strain measurements on the same progressively deformed tensile specimens. In particular, we have used XRD based micro-Laue diffraction and SEM based HR-EBSD. Further, we have also performed post-deformation characterizations with TKD in the SEM and TEM based PED.

Micro-Laue diffraction was conducted in a Bruker^{TM} D8 Discover XRD system. The critical components were a X-ray micro-source with Montel^{TM} multi-layer focusing mirrors, laser plus video tracking, and Vantec^{TM} area detector. The reader may refer to Lodh et al. (2017, 2018, 2019) and Section 6.3, for a detailed description of this setup and associated algorithm. A FEI^{TM} Quanta 3D-FEG (Field Emission Gun) SEM equipped with an EDAX^{TM} Velocity-plus EBSD system was used for HR-EBSD (0.5 μm step size) as well as HR-TKD (10 nm step size) measurements. Patterns were acquired at an accelerating voltage of 20 kV, current of 16 nA and a working distance of 12.5 mm, with a sample tilt of 70° (for HR-EBSD). 16-bit Kikuchi patterns with a 2×2 binning size (each image comprising of 230×230 pixels), were acquired and stored for all points within the region of interest for further offline post-processing. All measurements involved identical beam plus detector conditions. Additionally, all experimentally measured (HR-EBSD) residual elastic strains reported in the present work are averaged out over a $70\ \mu m \times 70\ \mu m$ region near the geometric center of the grains. Such a scheme was followed to avoid erroneous strain measurements, primarily due to large orientation gradients occurring near the grain boundaries (see Figure 6.10 later in this Chapter).

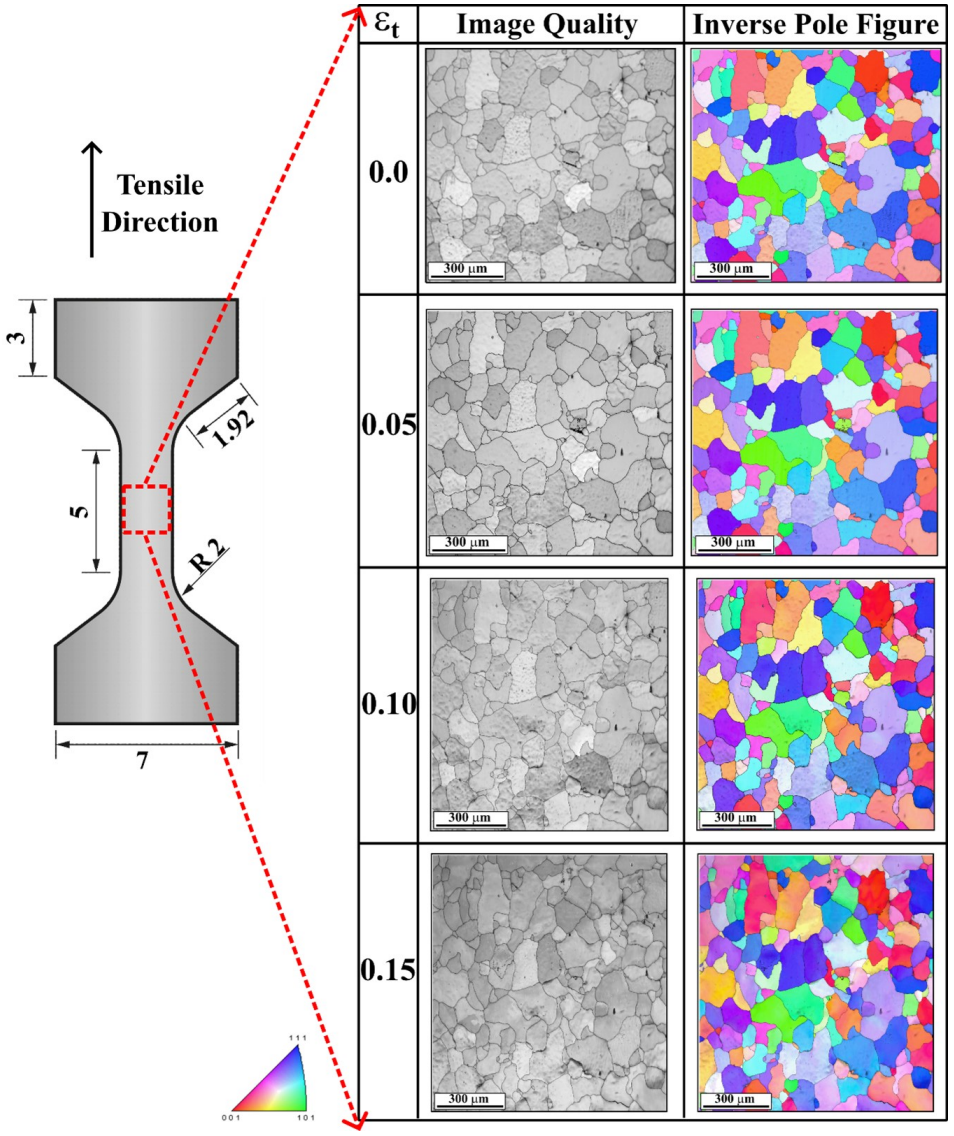

FIGURE 6.1: Schematic of a micro-tensile specimen used in this study. The Electron Backscattered Diffraction (EBSD) Image Quality (IQ) and Inverse Pole Figure (IPF) maps of the highlighted gauge region, with progressive tensile deformation.

TEM thin foils, used in HR-TKD as well as PED, were prepared from 3 mm discs using a Struers^{TM} Tenupol-5 twin-jet electropolisher. A sample tilt of $-20°$ was used for the (off-axis) HR-TKD measurements. The TEM-PED residual strain measurements were conducted on a NanoMegas^{TM} system within a Thermofisher^{TM} Themis 300 TEM, at an operating voltage of 300 kV. Further details on these measurement techniques are given in the next Section.

6.3 Diffraction-Based Multiscale Residual Strain Measurements

The different residual strain measurement techniques are described in the subsequent Sections: XRD based micro-Laue diffraction (Section 6.3.1), SEM based HR-EBSD and HR-TKD (Section 6.3.2), and TEM based PED (Section 6.3.3). These techniques differed in algorithm, and also in spatial plus angular resolutions. At this stage, it is important to note the rationale in referring micro-Laue XRD and TEM-PED as techniques sensitive to $\Delta d/d$ and HR-EBSD and HR-TKD as techniques sensitive to $\Delta\theta/\theta$. The strain measurement using TEM-PED technique primarily relies on the shift of the diffraction spots, which alters the resulting distortion matrix D. The in-plane residual strain components are then estimated using Equation 6.5 (listed subsequently). The shift in diffraction spots in TEM-PED, irrespective of (direction of) $\boldsymbol{g}$, is an outcome of the changes in the interplanar spacing of the crystal ($\Delta d/d$). In a similar manner, any change in $d_{\phi\psi}$, irrespective of the goniometer rotations, is an outcome of the changes in interplanar spacing ($\Delta d/d$). However, HR-EBSD as well as HR-TKD techniques rely on the shift in $\boldsymbol{q}$ (see subsequent Equations 6.2 and 6.3), which is primarily sensitive to changes in interplanar angles ($\Delta\theta/\theta$).

The micro-Laue setup in our study uses an approximate circular X-ray spot of $\sim 50\ \mu m$ with an estimated depth of penetration of less than $5\ \mu m$. The technique has an angular reproducibility of $\sim 0.01°$ (He, 2003; Słowik and Zieba, 2005; Krost and Bläsing, 2009). HR-EBSD and TKD offer similar angular resolution (0.006°) and a higher spatial resolution restricted by electron-atom interaction volume ($\sim 20\ nm$) (Humphreys, 2004; Wilkinson et al., 2006; Jiang et al., 2013a; Yu et al., 2021). It is important to note that the spatial resolution in EBSD, including HR-EBSD, is non-isotropic (Farooq et al., 2008). The tilting of the sample by 70° in EBSD results in the intersection shape of the electron beam (at the entry point of the specimen) to take on an elliptical shape, with an aspect ratio of 1 : 3 (Schwarzer et al., 2009; Sneddon et al., 2016; Fullwood et al., 2022). The beam subsequently enters the sample to a certain depth, where a "virtual point source" is generated by inelastic scattering, which then produces the outwards directed elastically scattered electrons, that form the EBSD patterns (Winkelmann, 2010). The non-isotropic nature of the EBSD/HR-EBSD resolution is hence an outcome of the intersection of this internal cone of electrons with the tilted sample surface. In summary, this leads to the reduction of spatial resolution along the vertical direction by ~ 3 times (Schwarzer et al., 2009; Sneddon et al., 2016). Further, the interaction volumes and diffraction paths for HR-EBSD on a bulk sample and HR-TKD on thin-foil are quite different. For a bulk sample, the information depth lies in the range $10 - 40\ nm$ at $20\ kV$. The depth values can decrease further for denser materials

(Dingley, 2004; Winkelmann, 2010). In HR-TKD the lateral resolution is defined by the effective beam diameter at the exit point (bottom surface) of the TEM foil. This would typically be of the order of 10 nm and is defined by the actual beam spread in the sample (by the foil thickness, material density, and keV). TEM-PED offers the very best in spatial (below ~ 2 nm) but less so in angular resolution ($\leq 0.4°$). This technique is restricted to very thin TEM foils (Viladot et al., 2013; Ghamarian et al., 2014; Ghamarian, 2017).

6.3.1 XRD based micro-Laue diffraction

Unlike the traditional XRD based residual strain measurements (Van Houtte and De Buyser, 1993; Verlinden et al., 2007), which are relatively routine for polycrystalline material, single crystal micro-Laue diffraction remains extremely specialized. Such measurements have been restricted to high energy synchrotron radiation (Margulies et al., 2002). More recently, however, Lodh et al. (2017, 2018, 2019) have developed a similar, though not identical, approach utilizing laboratory micro-focus XRD. We have adopted the same in this study. As indicated in Figure 6.2, and further described by Thool et al. (2020), the gauge of the micro-tensile specimen(s) has been subjected to prior EBSD scan(s) at different stages of tensile deformation (see Figure 6.1). We have tracked the corresponding grains delineated by appropriate fiducial markers. Laser plus video tracking has been used to facilitate placing the $\sim$ 50-micron X-ray beam in the center of individual grains. Appropriate rotations (θ, ϕ, ψ) in goniometer angles, derived from EBSD-estimated grain orientations, were imposed. As stated earlier, the average orientations from a 70 $\mu m \times 70$ μm region near the geometric center of the grains were used to determine the rotations (θ, ϕ, ψ) in goniometer angles. This was done to minimize the errors associated with the determination of goniometer angles due to the spread in EBSD estimated average grain orientations, especially in the deformed specimens. In addition, the laser plus video tracking facility along with a $\sim 0.01°$ of angular reproducibility ensured that no significant errors were introduced in the determination of (θ, ϕ, ψ) angles for micro-Laue residual strain measurements. We have obtained six different brightest Laue spots (Lodh et al., 2017), and the centroids were used to estimate $d_{\phi\psi}$ for each grain. Following this, $\varepsilon_{\phi\psi}$ was calculated as $\varepsilon_{\phi\psi} = \frac{d_{\phi\psi} - d_0}{d_0}$, where d_0 is the estimated unstrained interplanar spacing obtained from the annealed powder specimen (Noyan and Cohen, 2013; Kumar et al., 2016). In this study, we have obtained and used $d_0^{011} = 2.0266$ $\mathring{A}$, $d_0^{200} = 1.4309$ $\mathring{A}$ and $d_0^{211} = 1.1697\mathring{A}$, respectively. The resulting $\varepsilon_{\phi\psi}$ was then transformed to the grain average strain ε_{kl} in the specimen co-ordinate system as given in Lodh et al. (2017, 2018, 2019, 2022):

$$\varepsilon_{\phi\psi} = \varepsilon_{11}\cos^2\phi\sin^2\psi + \varepsilon_{12}\sin 2\phi\sin^2\psi + \varepsilon_{22}\sin^2\psi\sin^2\phi + \varepsilon_{33}\cos^2\psi + \varepsilon_{13}\cos\phi\sin 2\psi + \varepsilon_{23}\sin\phi\sin 2\psi \tag{6.1}$$

The solution of Equation 7.1 gives the residual strain tensor for an individual grain. Since there are six unknown strain components, at least six independent reflections are needed to solve the linear equations. All these make the technique fairly sophisticated. The schematic shown in Figure 6.2 briefly explains the above methodology. We have conducted these measurements, of intergranular residual strain, on 50 different (and randomly selected) grains subjected to progressive tensile deformation. It is to be noted that the micro-Laue residual strains, measured in the present study as well as those reported in literature (Lodh et al., 2017), show negligible spherical or hydrostatic strains.

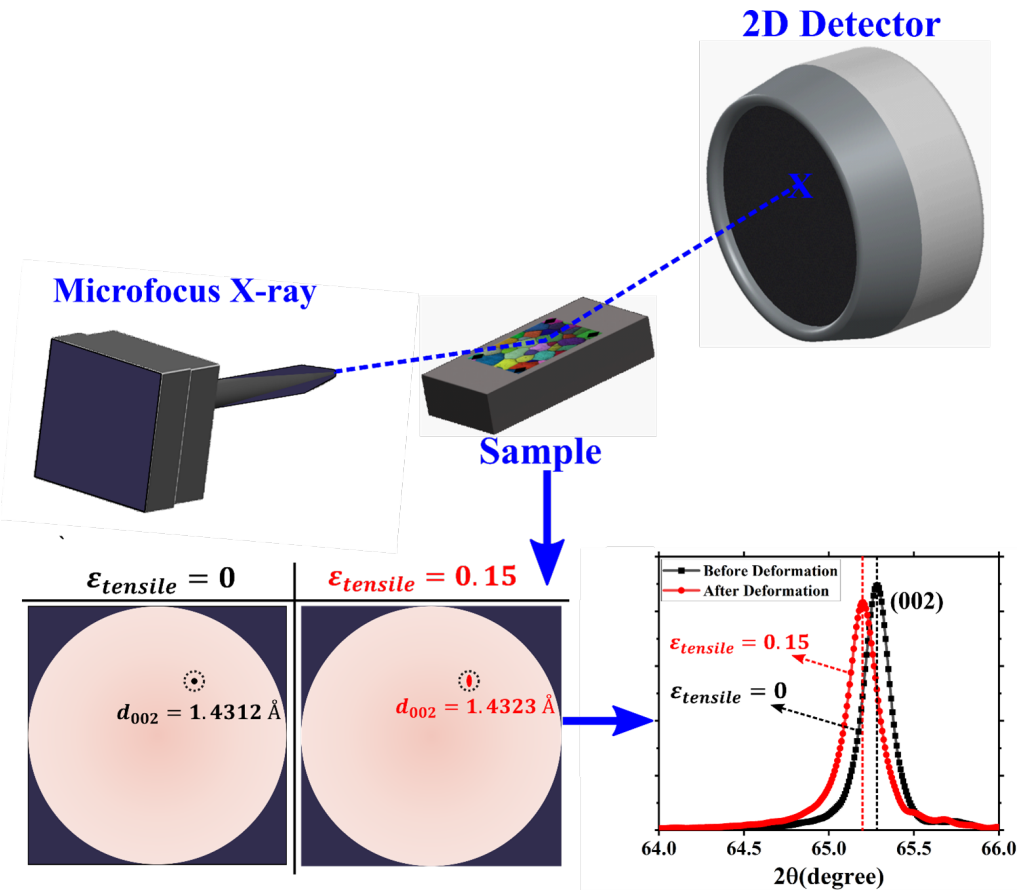

FIGURE 6.2: Schematic indicating the micro-Laue based single-crystal X-ray diffraction (XRD) technique for diffraction based residual strain measurements.

6.3.2 SEM based HR-EBSD and TKD

The automated EBSD or TKD measurements involve the Hough transformation to extract the approximate lattice plane traces found in the Kikuchi diffraction patterns (Adams et al., 1993; Wright and Adams, 1992). These measurements are usually based on the angle(s) between the planes or Kikuchi bands, which are then analyzed, using a "look-up" table, to obtain corresponding crystallographic orientations. The primary difference between the EBSD and TKD lie in the mode of pattern generation. Though both techniques rely on an incoherent scattering event to act as a basis (virtual point source) for further elastic scattering events, the exit beam diameter of the scattered electrons is much lower in TKD, compared to its EBSD counterparts (van Bremen et al., 2016). In addition, the negative tilt angles used in TKD leads to incident electrons being forward scattered, in-contrast to the EBSD technique, where (incident) electrons are backscattered from the sample surface to the detector.

The use of an electron transparent specimen, in conjunction with the negative tilt angle, results in the diffraction patterns originating from a small region close to lower surface of the specimen (Trimby, 2012; Sneddon et al., 2016). This leads to a significant improvement in the spatial resolution in TKD/HR-TKD as compared to the EBSD/HR-EBSD. It is to be noted (Trimby, 2012) that TKD/HR-TKD subtends to a smaller interaction volume and hence superior spatial resolution. More recently, the use of on-axis TKD technique, which utilizes a zero-tilt condition, was reported to provide significant improvements in the pattern intensities and data acquisition rates (Niessen et al., 2018). Additionally, unlike the conventional TKD measurements used in the present study, the on-axis TKD technique does not result in a gnomonic distortion of the diffraction patterns (Yuan et al., 2017; Niessen et al., 2018).

Kikuchi patterns from both techniques can be further analyzed by comparing appropriate Regions of Interest (ROI) with a reference pattern. This technique is often referred as cross-correlation or HR-EBSD (Wilkinson et al., 2006; Wright et al., 2011; Fullwood et al., 2015). HR-EBSD, for example, can be used to determine relative orientations of the reference and current sample point to very high angular resolution, and to estimate relatively minor lattice strains (Wilkinson et al., 2006; Yu et al., 2021).

We have processed high resolution Kikuchi patterns, both EBSD and TKD, using background division and dynamic background subtraction. Kikuchi patterns from the grain center, having maximum image quality (Small et al., 2020), were used as the reference patterns. A comparison between reference and the strained pattern(s), see Figure 6.3, provided

pattern shift ($\boldsymbol{q}$) and change(s) in interplanar angles ($\Delta\theta/\theta$). As described latter in the results section, this technique needs selection of appropriate ROIs (we have used 48 as well as 64 in our study) and information on accurate pattern center (Basinger et al., 2011; Fullwood et al., 2015). Note that the selection of the reference patterns, ideally from a strain-free crystal, is always relative (Britton and Wilkinson, 2012; Small et al., 2020). The measured $\boldsymbol{q}$ vectors are related to both lattice distortion and rotation as (Wilkinson et al., 2006, 2009; Britton and Wilkinson, 2011),

$$r_2 r_3 \left[\frac{\partial u_2}{\partial x_2} - \frac{\partial u_3}{\partial x_3}\right] + r_1 r_3 \frac{\partial u_2}{\partial x_1} + r_3^2 \frac{\partial u_2}{\partial x_3} - r_1 r_2 \frac{\partial u_3}{\partial x_1} - r_2^2 \frac{\partial u_3}{\partial x_2} = r_3 q_2 - r_2 q_3 \tag{6.2}$$

$$r_1 r_3 \left[\frac{\partial u_1}{\partial x_1} - \frac{\partial u_3}{\partial x_3}\right] + r_2 r_3 \frac{\partial u_1}{\partial x_2} + r_3^2 \frac{\partial u_1}{\partial x_3} - r_1^2 \frac{\partial u_3}{\partial x_1} - r_2 r_1 \frac{\partial u_3}{\partial x_2} = r_3 q_1 - r_1 q_3 \tag{6.3}$$

In brief, when a crystal lattice is subjected to an imposed deformation, the zone axes direction vector $\boldsymbol{r}$ shifts by $\boldsymbol{q}$ resulting in a lattice distortion of $\frac{\partial u_i}{\partial x_j}$. The elastic strains can then be derived as $\boldsymbol{E}^e = \frac{1}{2}\left(\boldsymbol{F}^{\boldsymbol{e}^T} \cdot \boldsymbol{F}^{\boldsymbol{e}} - \boldsymbol{\delta}\right)$, where $\boldsymbol{\delta}$ denotes the identity tensor and $\boldsymbol{F}^e$ represents the elastic deformation gradient, given by $\boldsymbol{F}^{\boldsymbol{e}} = \boldsymbol{\delta} + \frac{\partial u_i}{\partial x_j}$. Here, i and j denote the basis directions, respectively. Further, to separate the normal strains, a boundary condition has to be utilized that forces the stress σ_{33}, normal to the sample surface, to zero. This can be expressed as (Wilkinson et al., 2006, 2009):

$$\sigma_{33} = 0 = C_{33}\varepsilon_{33} + C_{32}\varepsilon_{22} + C_{32}\varepsilon_{11} \tag{6.4}$$

where $C_{33} = C_{11} = 231.4\ GPa$ and $C_{32} = C_{12} = 134\ GPa$ are anisotropic elastic constants for the Ferrite (Fe) phase. This defines the so-called traction free boundary condition (Hardin et al., 2015). An alternative boundary condition, more recently proposed (Ruggles et al., 2020), specifies that the trace of the lattice distortion tensor should be zero. As shown in Figure 6.12, both provided similar results. We have hence performed off-line cross-correlations, under traction free boundary condition, to estimate elastic (or residual) strains. These were performed on experimental, HR-EBSD and TKD, as well as simulated (Winkelmann et al., 2007; Callahan and De Graef, 2013) Kikuchi patterns. Our cross-correlations used an open source (OpenXY$^{\text{TM}}$) software (Fullwood, 2020).

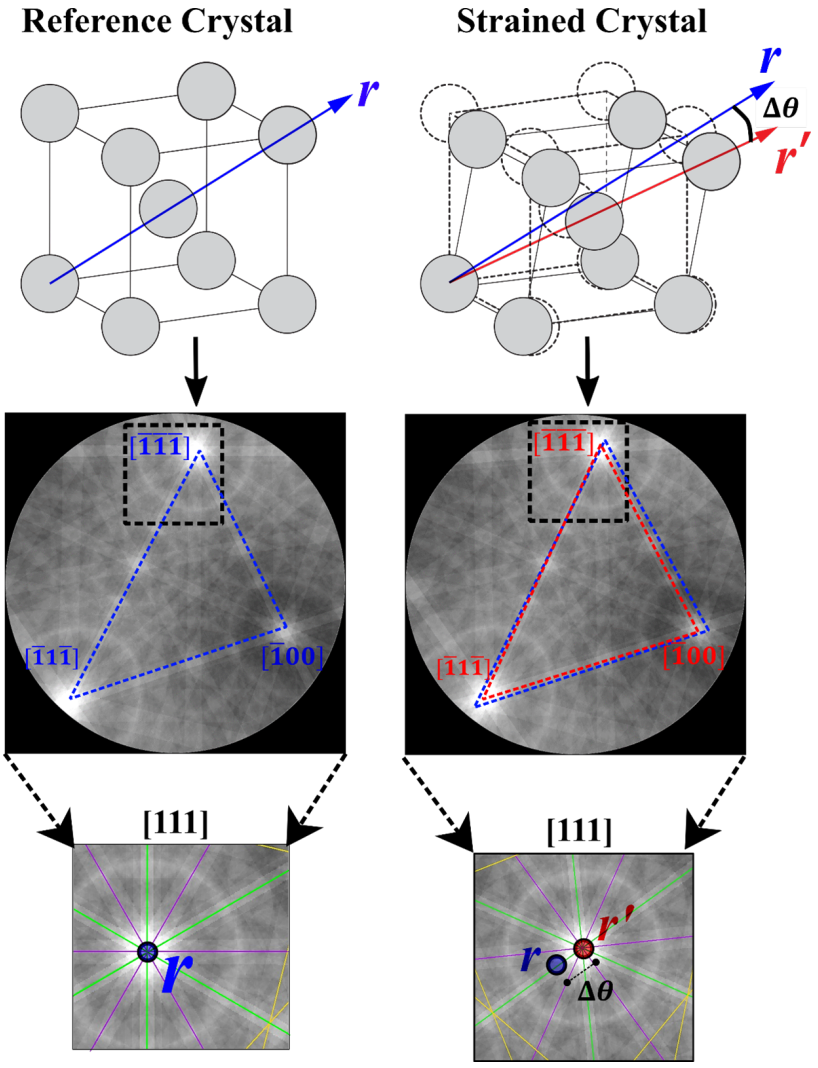

FIGURE 6.3: Schematic indicating the High Resolution Electron Backscattered Diffraction (HR-EBSD) in Scanning Electron Microscope (SEM) technique for diffraction based residual strain measurements.

6.3.3 TEM based PED

TEM offers excellent spatial resolution. TEM spot diffraction, however, has relatively poor angular resolution. This is decided by the so-called $\boldsymbol{s}$ vector, or deviation from the exact Bragg, and the electron atom-interaction volume (Ghamarian et al., 2014; Ghamarian, 2017). The latter determines the kinematic or dynamical interaction of the transmitted and diffracted beam(s). The recent incorporation of the PED technique (see Figure 6.4) in thin (below 1/3 of extinction distance) TEM foils can improve the angular resolution of TEM spot diffraction patterns (Vincent and Midgley, 1994). In brief, introduction of an appropriate precession angle provides ability to resolve very small angular deviations ($\leq 4°$) in TEM-PED (Viladot et al., 2013; Ghamarian et al., 2014; Ghamarian, 2017). Naturally,

the technique can be used in both orientation and residual strain measurements (Rauch and Veron, 2005; Rauch et al., 2010; Portillo et al., 2010; Viladot et al., 2013; Ghamarian et al., 2014; Ghamarian, 2017). Of course, the latter would still require a reference pattern which is then compared to the strained patterns, see Figure 6.5.

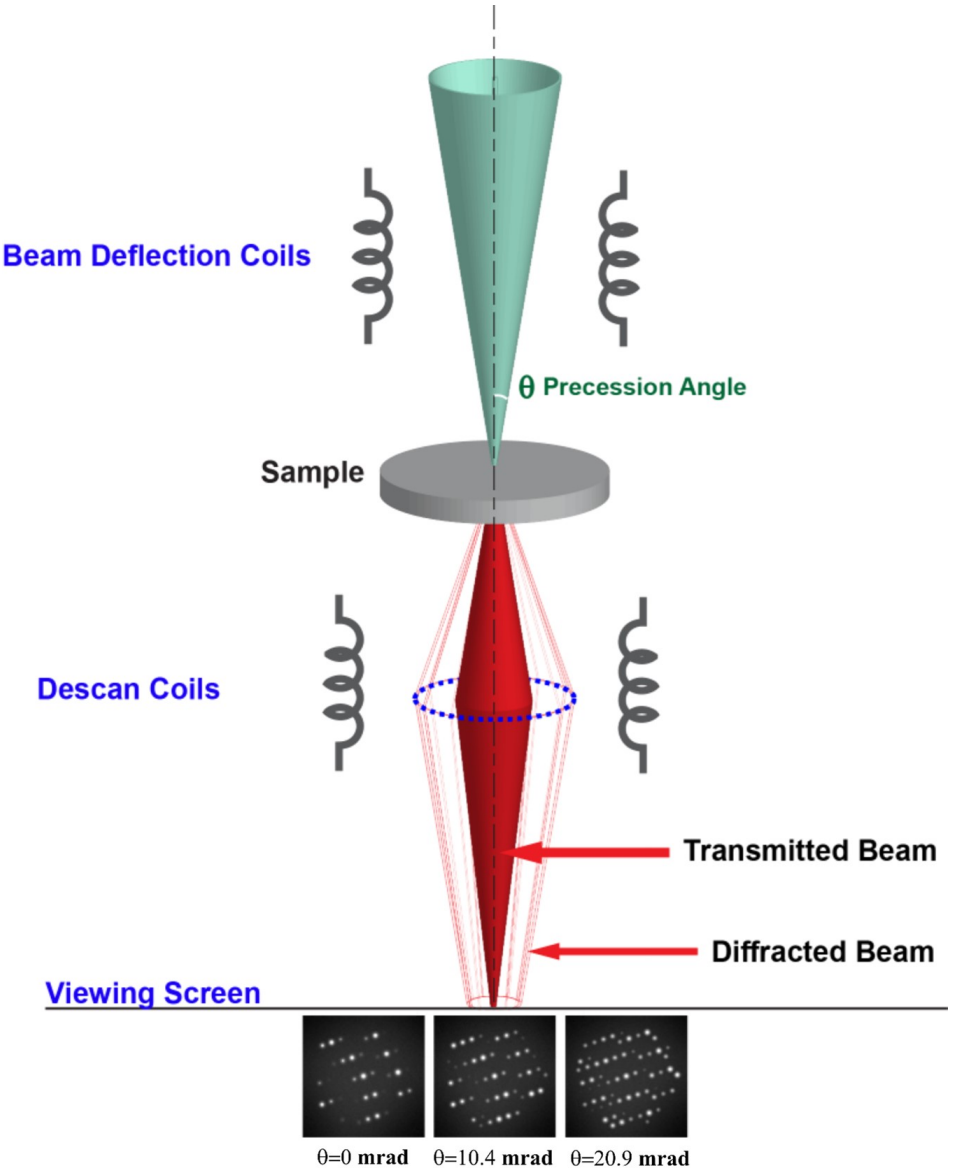

FIGURE 6.4: Schematic describing the Precession Electron Diffraction (PED) technique in TEM. Introduction of a precession angle (θ) helps in obtaining additional diffraction spots.

As shown in Figure 6.5 two non-collinear diffraction spot patterns ($\boldsymbol{g}_1$, $\boldsymbol{g}_2$ for the reference and the strained crystals, respectively) are acquired. The respective diffraction matrices can be stated as $\boldsymbol{G_0} = [g_{x_1} g_{x_2}; g_{y_1} g_{y_2}]$ and $\boldsymbol{G} = [g'_{x_1} g'_{x_2}; g'_{y_1} g'_{y_2}]$ (Zhao et al., 2023). The lattice distortion is then given as the distortion matrix $\boldsymbol{D} = \left(\boldsymbol{G_0 G^{-1}}\right)^T$, where T indicates a transpose operation (Zhao et al., 2023). The in-plane residual strain components can be

extracted from the distortion matrix using the infinitesimal strain theory, see Pekin et al. (2017), as:

$$\begin{bmatrix} \varepsilon_{xx} & \frac{1}{2}(\varepsilon_{xy} - \theta) \\ \frac{1}{2}(\varepsilon_{yx} + \theta) & \varepsilon_{yy} \end{bmatrix} = \boldsymbol{D} - \boldsymbol{\delta} \tag{6.5}$$

where, ε_{xx} and ε_{yy} are the strains in X and Y direction, respectively. ε_{xy} represents the in-plane shear component and θ here denotes the lattice rotation. It is important to note that the above expression estimates lattice strain in the reciprocal space, and ε_{xx}, ε_{yy} and ε_{xy} must be flipped to produce strain measurements in the specimen space. The present study uses the TopSpin^{TM} module of NanoMegas^{TM} PED software for data acquisition and subsequent analysis. Alternative algorithms, based on the polar decomposition of transformation matrix between the strained and unstrained diffraction vectors have also been proposed in literature estimate residual elastic strains with very high precisions ($\sim 0.1\%$) (Ozdol et al., 2015). Further, the reader is referred to Béché et al. (2013) for a detailed analysis on the various strain mapping techniques and its associated merits and demerits.

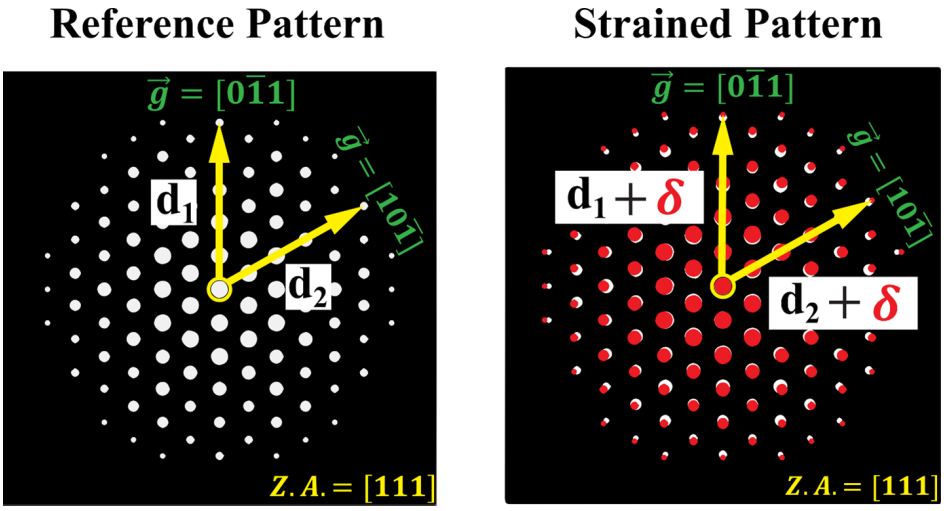

FIGURE 6.5: Schematic indicating the Precession Electron Diffraction (PED) in Transmission Electron Microscope (TEM) technique for diffraction based residual strain measurements.

6.4 Results from Experiments and Pattern Simulations

Figure 6.6 shows a direct comparison in the development of intergranular von-Mises residual strains, as estimated by the micro-Laue or ($\Delta d/d$) and the HR-EBSD or ($\Delta\theta/\theta$). This is shown for three randomly selected grains - $G1$, $G2$ and $G3$. It is to be noted that we

have taken similar grain surface areas for the two measurements, making the data in Figure 6.6 spatially comparable. It is to be noted that past HR-EBSD studies have also reported higher residual elastic strain values, higher than the theoretical yield limit of 0.2% (Basinger et al., 2011; Zhang et al., 2014, 2016; Mehtani et al., 2020; Small et al., 2020; Zhao and Li, 2021). For example, Small et al. (2020) reported equivalent residual elastic strains of $0.007 - 0.008$ in additively manufactured Inconel 625 specimen. Further, the reported strain values, representing multiple grains, also had an extremely large spread. It is to be noted that fast cooling associated with additive manufacturing resulted in large intragranular orientation gradients ($> 10°$) and a significant variation in the intragranular residual strain values. Zhang et al. (2014) have noted strains greater than 0.002 (specifically, in grains near non-metallic inclusions) in their nickel-based superalloy subjected to thermal loading; Zhao and Li (2021) too reported strain components with peak magnitude of up to 0.01 in stainless steel specimens subjected to three-point bending tests. Similarly, (Mehtani et al., 2020) have reported von-Mises residual elastic strains of magnitude $0.01 - 0.03$ in the pseudo-epitaxially grown magnetite grains, during their studies on oxidation kinetics of interstitial free steel.

There have been efforts to cross-validate HR-EBSD results with an alternative measurement approach. For example, dislocation density measurements from HR-EBSD and XRD have been compared (Kalácska et al., 2017, 2020; Gallet et al., 2023). Similar comparison has also been attempted between residual strain measurements from HR-EBSD and synchrotron X-ray diffraction (Deal et al., 2021). An earlier study, on a patterned $Si_{1-x}Ge_x$ thin film, have even reported (Fullwood et al., 2015; Vaudin et al., 2015) a reasonable convergence between the HR-EBSD and XRD strain estimates. However, any comparison in semi-conductor/thin film structures have intrinsic limitations of constraints and mechanical properties, as compared to bulk metallic materials. In addition, such studies, reporting similar elastic strains from HR-EBSD and XRD (Fullwood et al., 2015; Vaudin et al., 2015), also involved relatively minor plastic deformation. Even in the present study, Figures 6.6-6.7, reported a numerical convergence at lower values of imposed plastic deformation. This study, in particular, provided a direct grain-by-grain evolution of residual strains, as estimated by HR-EBSD and micro-Laue XRD. It is to be noted that such a comparison (see Figure 6.6) has never been attempted/reported in the past. The difference between the strain estimates did depend on the magnitude of the imposed plastic deformation as well as the elastic stiffness of corresponding grain(s). At large tensile deformations, HR-EBSD clearly showed higher residual elastic strain values. The authors would like to state here that the term "higher residual elastic strains", used henceforth, refer to residual elastic strains significantly greater than the theoretical yield limit of 0.2%.

Further, the data in Figure 6.6 is based on only three randomly selected grains. From

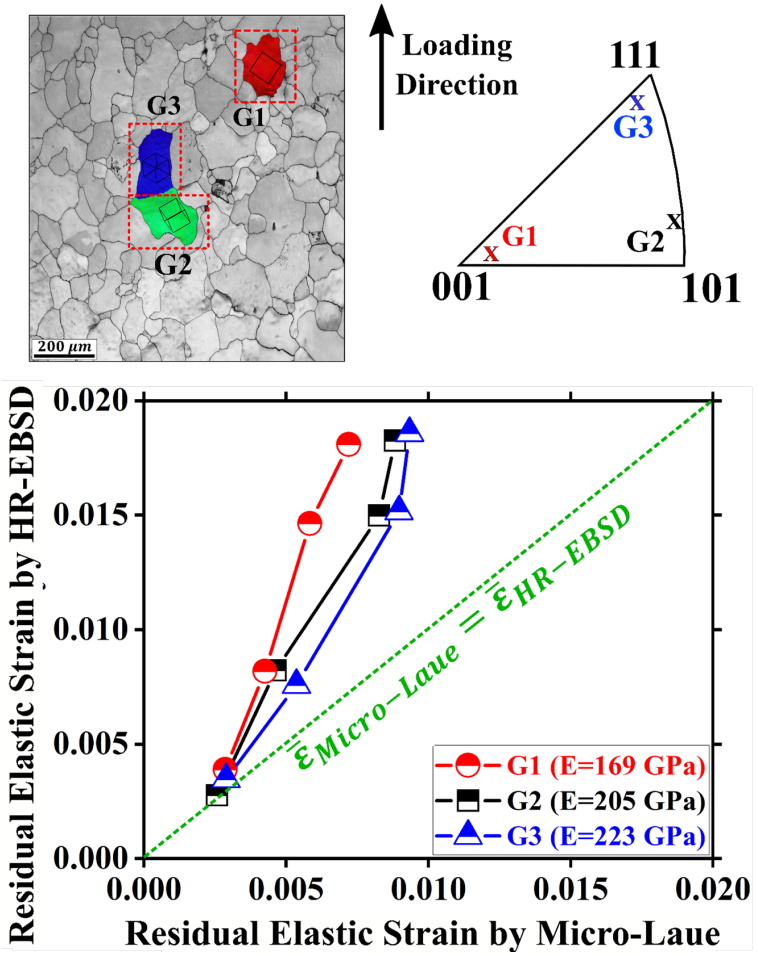

FIGURE 6.6: Comparison of residual strain measured using micro-Laue XRD ($\Delta d/d$) and HR-EBSD ($\Delta\theta/\theta$). These measurements were performed, with progressive tensile deformation, on three identical grains G1,G2 and G3.

the large number of grains characterized in this study, 50 were randomly selected for a statistical comparison (see Figure 6.7(a)). The residual strain(s) increased as expected with imposed tensile deformation. There were, however, significant scatter between different grains (see Figure 6.7(a) and error bars in Figure 6.7(b)). Statistically, but definitively, the relative increase in residual strain, with tensile deformation, was more in HR-EBSD than in the micro-Laue XRD. This last point is further represented in Figure 6.7(c) as strain distributions at the highest tensile deformation step (0.15 imposed tensile strain). In particular, HR-EBSD average residual strain was $\sim$ 2.06 times of that of micro-Laue. Further, the HR-EBSD strain estimates had wider distribution or scatter. This last point, to be deliberated latter in the manuscript, actually indicated higher angular resolution for HR-EBSD and/or HR-TKD.

It is important to note here that the micro-Laue residual elastic strain measurements, which are sensitive to ($\Delta d/d$), do show large magnitudes for certain grains/orientations. This

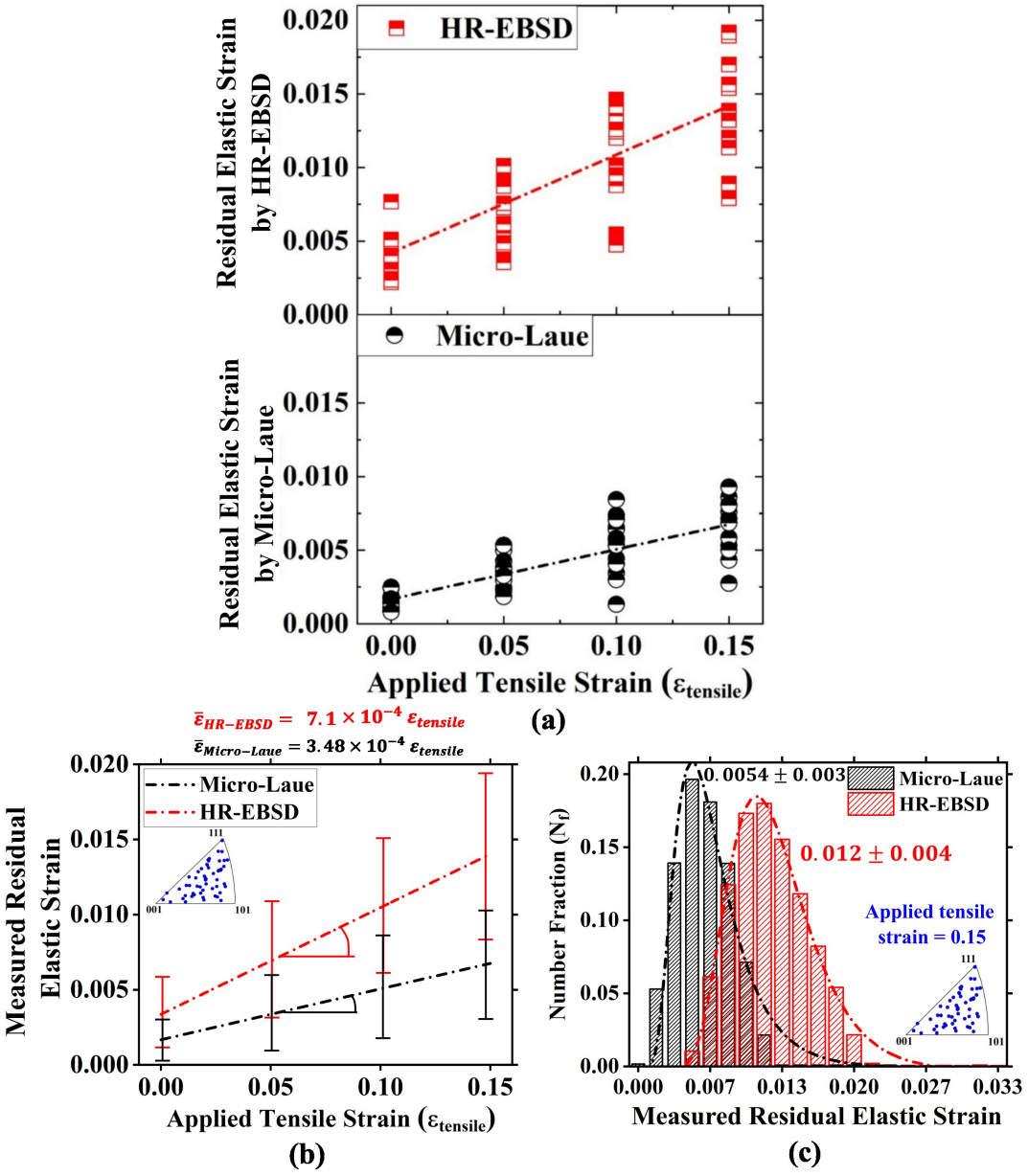

FIGURE 6.7: Comparison of residual strains measured measured using micro-Laue XRD ($\Delta d/d$) and HR-EBSD ($\Delta\theta/\theta$) on 50 grains. The corresponding best fit slopes are shown in (b). (a,b) show higher residual elastic strains in HR-EBSD and (c) shows the same as statistical distributions.

can be attributed to multiple factors, more specifically, the improper strain free lattice spacing substitution in Equation 7.1, as well as the geometrical errors associated with the determination of the Laue spot centroids. In addition, it is important to note that minor variation in lattice parameters can result in large difference in the measured strains. This point has been discussed latter in the manuscript. We have ensured that all such possible errors were minimized in the present study. For brevity, we did not discuss this point further in this manuscript. The measurement uncertainty for micro-Laue based von-Mises residual strains were estimated. This came from repeating the measurements, at least thrice, in five randomly selected grains subjected to controlled tensile deformation. It is to be noted that we estimated/observed a measurement uncertainty of 8.4×10^{-4} (at 0.15 imposed tensile strain) in our micro-Laue strain measurements. Further, for the HR-EBSD measurements, the measurement uncertainty was nearly negligible.

There have been attempts to improve HR-EBSD based residual strain measurements (Basinger et al., 2011; Wright et al., 2011; Jiang et al., 2013a; Fullwood et al., 2015). Potential errors might arise due to (A) insufficient ROIs, (B) inappropriate selection of the reference pattern and (C) choice of pattern center and (D) remapping, which accounts for orientation gradients in the material (Britton and Wilkinson, 2012; Maurice et al., 2012; Small et al., 2020). In particular, we have considered factors A-D, see Figure 6.9(a). Increase in ROIs, from 48 to 64, for example, reduced the HR-EBSD estimated single crystal residual elastic strains. However, this drop was marginal. Combining more ROIs with manual selection of reference pattern and correcting for pattern center shift, based on an algorithm proposed by Fullwood et al. (2015), reduced the HR-EBSD residual elastic strain more significantly. The remapping technique (Britton and Wilkinson, 2012; Maurice et al., 2012; Small et al., 2020), which uses the finite rotation component of the elastic deformation gradient tensor ($\mathbf{F^e}$) to derive the rotated reference pattern, and then estimate the residual shifts ($\boldsymbol{q}$) between the rotated reference pattern and Kikuchi pattern from the current pixel, further improves the residual elastic strain estimation. Subsequently, the slope of HR-EBSD versus micro-Laue residual elastic strain dropped from ~ 2.06 to ~ 1.57, see Figure 6.9(b). However, an absolute numerical, albeit statistical, convergence of the two techniques would require a slope of 1, which appears to be unachievable by simply optimizing HR-EBSD parameters.

It is to be noted that for large grains, pattern center shifts are significant but expected. Such shifts can be compensated by the HR-EBSD code (Britton and Wilkinson, 2012). As shown in Figure 6.8(a), though shifts were real; but even if incorrectly compensated, they affected the HR-EBSD estimated residual elastic strain value(s) only marginally (1% <). Further, the HR-EBSD residual elastic strains emerge from the shift in the $\boldsymbol{q}$ vector. As illustrated in the Figure 6.8(b), this is affected by the relative positioning of the zone axes. In brief, zone

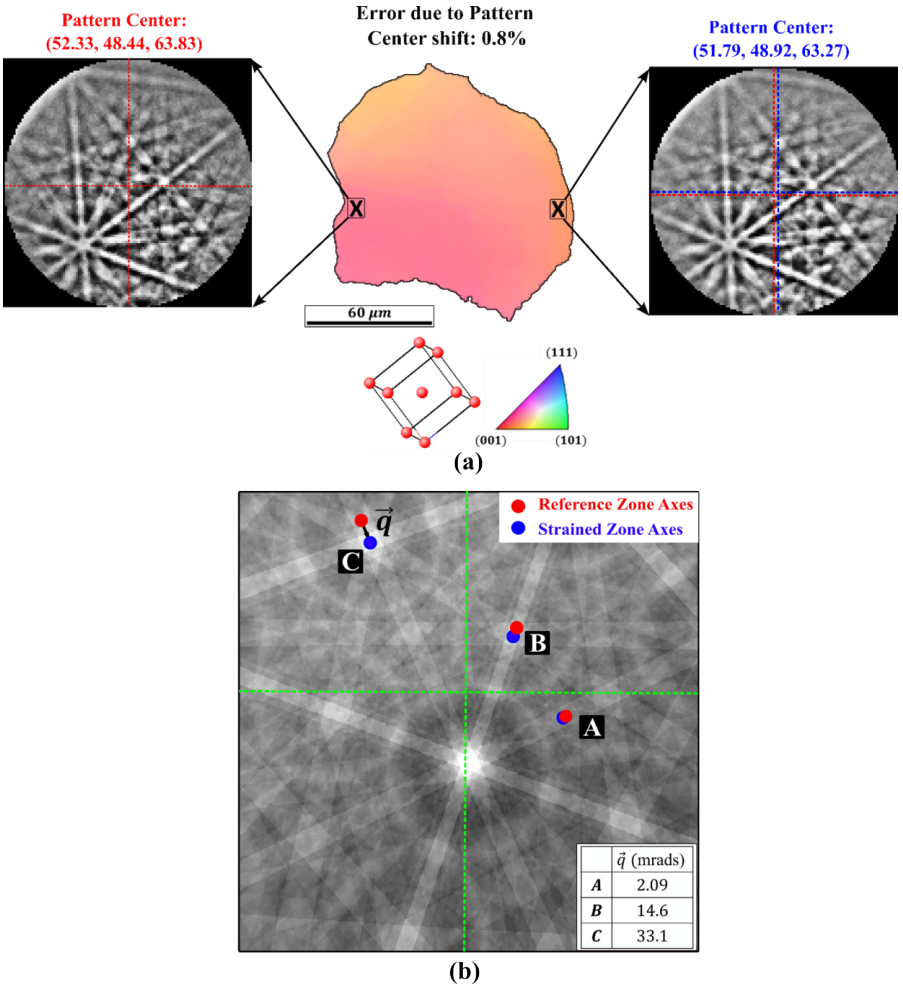

FIGURE 6.8: (a) Shift of pattern centers between the two edges of a large ($\sim$ 82 micron) grain. (b) Zone axis shift (or shift in the $\boldsymbol{q}$ vector), when axes near and away from the pattern center (see green line) were taken.

axes further from the pattern center show numerically higher $\boldsymbol{q}$ vector. However, both these factors also do not justify the very large difference, see Figure 6.9(b), estimated from our statistical data. Clearly, the HR-EBSD provides larger residual elastic strain estimates than the micro-Laue. To further explore the deviation in numerical convergence between micro-Laue and HR-EBSD techniques, the reader is referred to Section 6.4.1. Briefly, Figure 6.10(a) shows a grain-level comparison, while Figure 6.10(b) depicts a component wise comparison of the residual elastic strains measured using the two techniques.

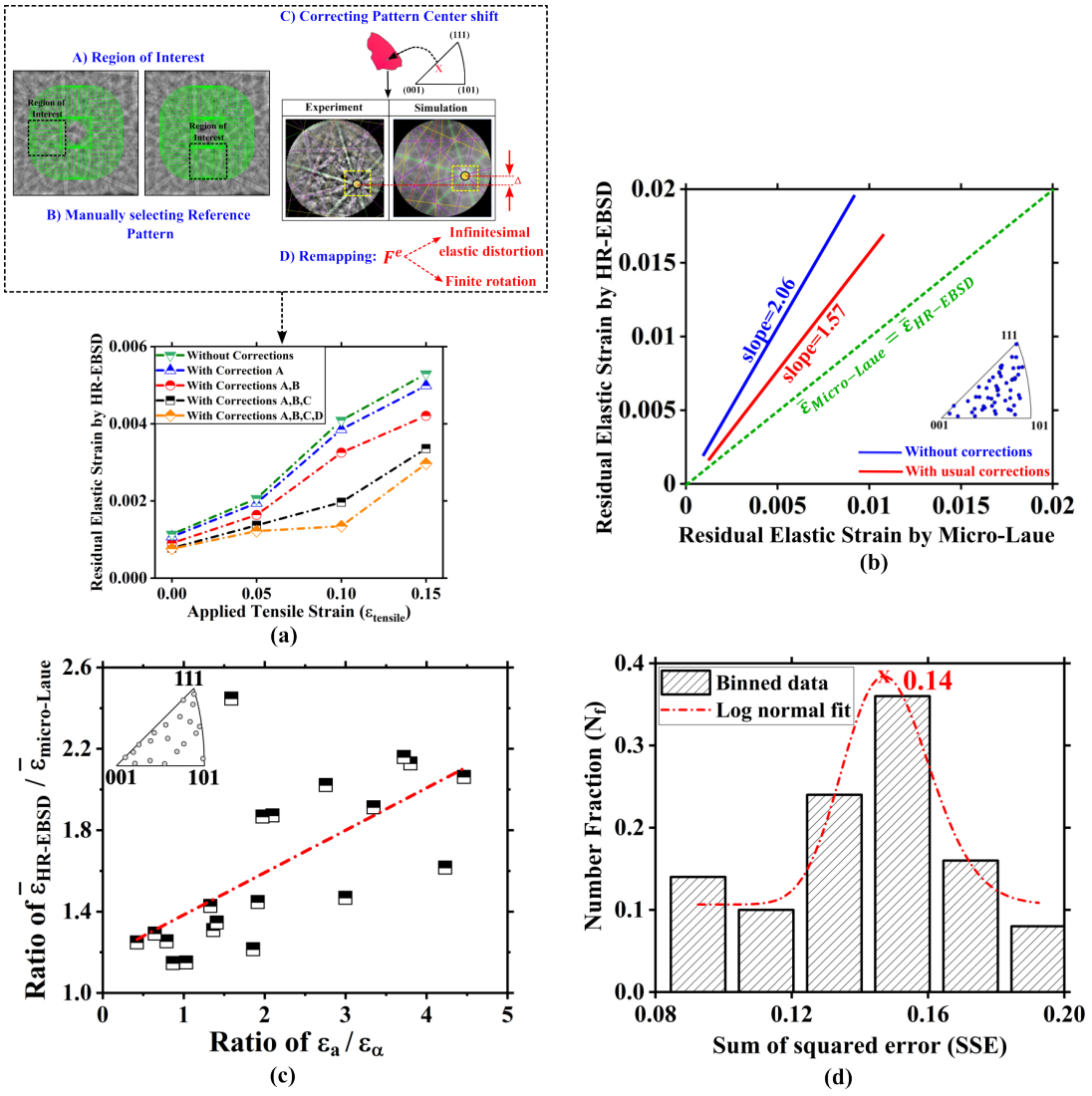

FIGURE 6.9: (a) Frequently reported errors in HR-EBSD and corresponding corrections. (b) These corrections were applied to our statistical data on HR-EBSD versus micro-Laue residual strains. However, even the 'corrected' data did not bring an equivalence between the two approaches.(c) Comparison of the ratios of 'a' type (effect on Δd) and 'α' type (effect on $\Delta\theta$) residual elastic strains with experimental HR-EBSD and micro-Laue (von-Mises) strains. The red dotted best fit line indicates a direct linear relationship between the two entities. (d) Sum of squared error (SSE) distribution, shown as a lognormal fit (red dotted line), for all grains analyzed in Figure 6.9(c).

6.4.1 Analyzing Residual Strains from Experimental HR-EBSD Measurements

Figure 6.10(a) shows the evolution of the Grain Reference Orientation Deviation (GROD) and von-Mises residual elastic strains with increasing tensile deformation, measured using the HR-EBSD technique. The corresponding average values from its $\Delta d/d$ counterpart (micro-Laue) have also been provided. It is to be noted that the HR-EBSD strain measurements have been shown after accounting for the corrections, i.e., (A) insufficient ROI, (B) inappropriate selection of the reference pattern, (C) choice of pattern center and (D) Remapping, discussed previously. It can be seen that HR-EBSD provides significantly larger residual strains in comparison to the micro-Laue; the differences get amplified with increasing deformation. This observation can also be noted from the component level comparison shown in Figure 6.10(b), albeit the scaling factor differs significantly for each individual strain component.

To further analyze and explore the HR-EBSD residual elastic strain measurements, we estimate the amount of 'a' type (effect on Δd) and 'α' type (effect on $\Delta\theta$) strains from the residual elastic strain tensor $\mathbf{E^e}$ as:

$$\varepsilon_a = |E^e_{11}| + |E^e_{22}| + |E^e_{33}| \tag{6.6}$$

$$\varepsilon_\alpha = |E^e_{12}| + |E^e_{13}| + |E^e_{23}| \tag{6.7}$$

where, ε_a and ε_α denotes the 'a' and 'α' type residual elastic strains, respectively. Since the elastic strain tensor $\mathbf{E^e}$ is calculated in the crystal reference frame, a first order approximation has been utilized, i.e., the absolute values of the diagonal and non-diagonal components of the elastic strain tensor $\mathbf{E^e}$ are used, to estimate the 'a' type and 'α' type strains, respectively. Physically, ε_a defines the portion of $\mathbf{E^e}$ that would affect the interplanar spacing of a crystal lattice, whereas ε_α is indicative of the shear deformation or the change in interplanar angles in a crystal lattice.

The ratio of these entities, i.e., $\varepsilon_a/\varepsilon_\alpha$, has then been compared with existing experimental datasets (see Figure 6.6, 6.7). 20 randomly oriented grains were selected from the specimen deformed up to 0.15 (imposed) tensile strain; the corresponding results have been shown in Figure 6.9(c). In an ideal scenario, i.e., if numerical convergence were established, these above-mentioned ratios should be identical, i.e., equal to one. However, it can be clearly observed that with increasing magnitude of $\varepsilon_a/\varepsilon_\alpha$, i.e., when the '$\alpha$' type strains are underpredicted, the difference in von-Mises residual strains estimated by the HR-EBSD (sensitive to $(\Delta\theta/\theta)$) from its counterpart (micro-Laue: sensitive to $(\Delta d/d)$) increases linearly. It is

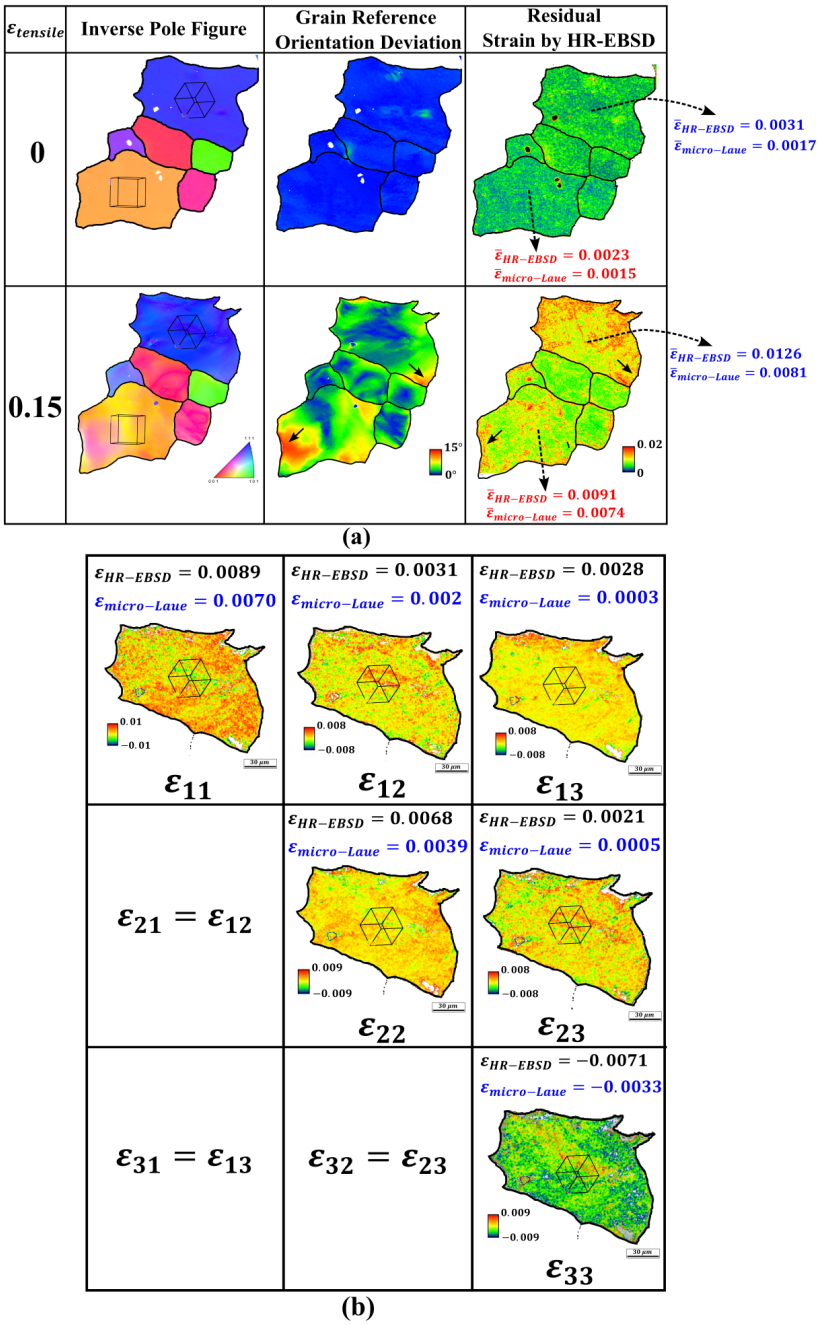

FIGURE 6.10: Comparison of residual elastic strains measured using the micro-Laue (sensitive to $\Delta d/d$) and HR-EBSD (sensitive to $\Delta\theta/\theta$) technique in terms of (a) von-Mises strain and (b) component-level comparison. The markers refer to regions depicting large orientation gradients and hence, the strain concentrations.

important to note that the error in estimated von-Mises strains can rise as high as $\sim 120\%$ for large variations in $\varepsilon_a/\varepsilon_\alpha$ (see Figure 6.9(c)). The significant scatter in the data is primarily due to consideration of randomly oriented grains in the specimen (0.15 imposed tensile strain), each of which behaves differently under the imposed deformation.

We have further validated our observations on the 'a' type and 'α' type strains (see Figure 6.9(c)) and its effects on the error in strain measurements (between HR-EBSD and micro-Laue) by conducting an identical analysis on the micro-Laue residual strain tensors. This exercise was carried out for three distant scenarios. These were taken for the grains where HR-EBSD residual strains resulted in a ratio of $\varepsilon_a/\varepsilon_\alpha$=1.1, 2.99 and 4.43, respectively. The corresponding strain matrices have been shown in Table 6.1. Clearly, it can be seen that when $\varepsilon_a/\varepsilon_\alpha$=1.1 (from HR-EBSD), the resulting strain tensors are nearly identical (in magnitude), with the ratio of $\bar{\varepsilon}_{HR-EBSD}/\bar{\varepsilon}_{micro-Laue}$=1.18. It is important to note that the ratio is not exactly equal to one; the minor difference may be attributed to the different sensitivities of the two measurement techniques to lattice distortion, $(\Delta\theta/\theta)$ versus $(\Delta d/d)$. Additionally, the differences in interaction volume for the two techniques, errors in geometric centroid determination and the noise in the HR-EBSD patterns may also contribute to the error.

In contrast, when $\varepsilon_a/\varepsilon_\alpha$=2.99 and 4.43, the micro-Laue strain is significantly lower than the HR-EBSD strain, with the ratio of $\bar{\varepsilon}_{HR-EBSD}/\bar{\varepsilon}_{micro-Laue}$ being 1.42 and 2.05, respectively (see Table 6.1). A component wise comparison of the residual strain tensors (along with the respective strain contours), shown in Figure 6.10(b), also points out towards a similar conclusion. In summary, Figure 6.9(c) and Table 6.1 conforms to the fact that as the 'a' type (effect on Δd) strain increases relative to the 'α' type (effect on $\Delta\theta$) component, the error in strain measured by HR-EBSD (sensitive to $(\Delta\theta/\theta)$), relative to the measurements from micro-Laue (sensitive to $(\Delta d/d)$), also increases.

TABLE 6.1: Comparison of residual elastic strain tensors obtained from the micro-Laue (sensitive to $(\Delta d/d)$) and HR-EBSD (sensitive to $(\Delta\theta/\theta)$) techniques

$\varepsilon_a/\varepsilon_\alpha$ (from HR-EBSD)	HR-EBSD strain tensor	micro-Laue strain tensor	$\bar{\varepsilon}_{HR-EBSD}/\bar{\varepsilon}_{micro-Laue}$
1.1	$\begin{bmatrix} 0.0021 & 0.0007 & -0.0009 \\ 0.0007 & -0.001 & -0.0023 \\ -0.0009 & -0.0023 & -0.0012 \end{bmatrix}$	$\begin{bmatrix} 0.0018 & 0.0003 & -0.0012 \\ 0.0003 & -0.0011 & -0.0019 \\ -0.0012 & -0.0019 & -0.0007 \end{bmatrix}$	1.18
2.99	$\begin{bmatrix} -0.0082 & 0.0015 & -0.0015 \\ 0.0015 & 0.0037 & 0.0025 \\ -0.0015 & 0.0025 & 0.0046 \end{bmatrix}$	$\begin{bmatrix} -0.0055 & 0.0008 & -0.0018 \\ 0.0008 & 0.0019 & -0.0006 \\ -0.0018 & -0.0006 & 0.0043 \end{bmatrix}$	1.42
4.43	$\begin{bmatrix} 0.0137 & 0.0032 & -0.0001 \\ 0.0032 & -0.0013 & -0.0029 \\ -0.0001 & -0.0029 & -0.0125 \end{bmatrix}$	$\begin{bmatrix} 0.0066 & 0.0031 & 0.0012 \\ 0.0031 & -0.0035 & -0.0008 \\ 0.0012 & -0.0008 & -0.0038 \end{bmatrix}$	2.05

Further, we have also shown the Sum of Squared Error (SSE), a standard output of OpenXY^{TM}, for all grains analyzed in Figure 6.9(c). The SSE values (see Figure 6.9(d)) range from 0.08 (minimum) to 0.2 (maximum) with a mean of 0.14. These results indicate that the conclusions derived from Figure 6.9(c), representing errors in HR-EBSD strains relative to the micro-Laue strains, are not largely influenced by the noise in the derived HR-EBSD patterns.

The reference patterns for HR-EBSD as well as HR-TKD were selected from a region near the geometric center of the grain, having the maximum image quality. In all cases, it was assumed that the reference patterns were relatively strain-free. Owing to the large size of grains used in the present study, the geometric center of the grains remained nearly unaffected with progressive deformation, even at an imposed tensile strain of 0.15 (see GROD maps in Figure 6.10(a)). As discussed in Section 6.3.1, the reference d_0 for micro-Laue single crystal XRD, was obtained from annealed powder specimens (Noyan and Cohen, 2013; Kumar et al., 2016). The measured residual elastic strains using the $(\Delta\theta/\theta)$ sensitive and $(\Delta d/d)$ sensitive methods do not show any notable errors at lower imposed tensile strains (Figures 6.6, 6.7 and 6.9), thus indicating residual elastic strain estimations for all measurement techniques have initiated from an identical baseline.

One potential cause of this difference is perhaps the different levels of sensitivity, of the respective measurement techniques, to different measures of elastic strain. After all, HR-EBSD and micro-Laue XRD are sensitive to measurements of interplanar angle $(\Delta\theta/\theta)$ and spacing $(\Delta d/d)$, respectively. To investigate this possibility, virtual experiments were conducted using HR-EBSD pattern simulations (Winkelmann et al., 2007; Zaefferer, 2007; Callahan and De Graef, 2013).

6.4.2 Residual Strain Estimates from Simulated HR-EBSD Patterns

To investigate the difference between the measurement of residual strains based on $(\Delta\theta/\theta)$ and $(\Delta d/d)$, we have conducted simulations of HR-EBSD patterns. An ideal strain free (BCC) lattice, see Figure 6.11(a), was subjected to progressive strains of two types. The corresponding deformation gradients were estimated as:

1. Idealized expansions were applied along the 'a' direction with no Poisson contraction in the perpendicular directions, see Figure 6.11(a). The corresponding deformation

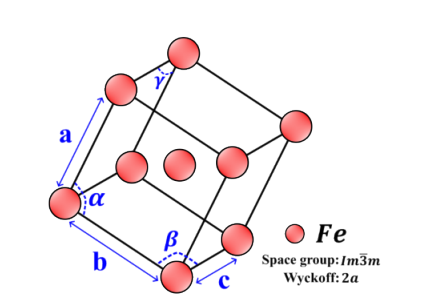

Applied Strain	Δd/d approach (a)Å	$\Delta\theta/\theta$ approach (α)°
0.0049	2.8837	89.5
0.0080	2.8944	89.21
0.0098	2.9007	89.12
0.012	2.9083	88.81
0.013	2.9118	88.7
0.015	2.9185	88.5

(a)

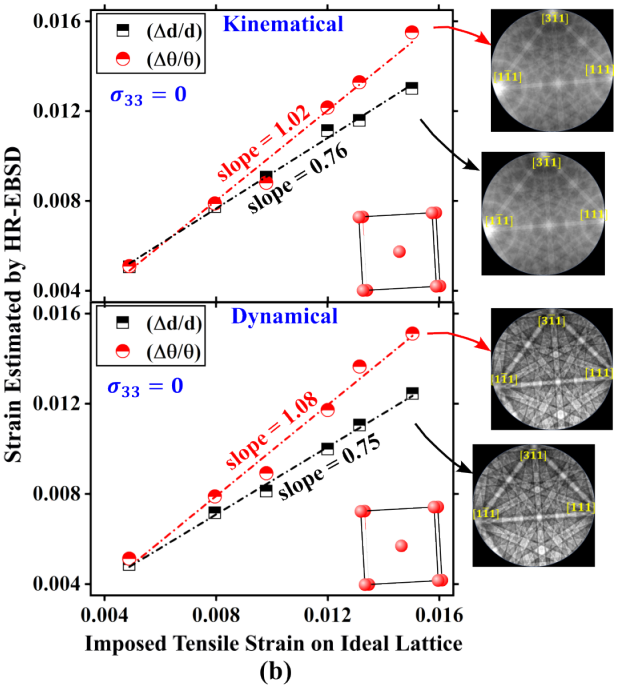

(b)

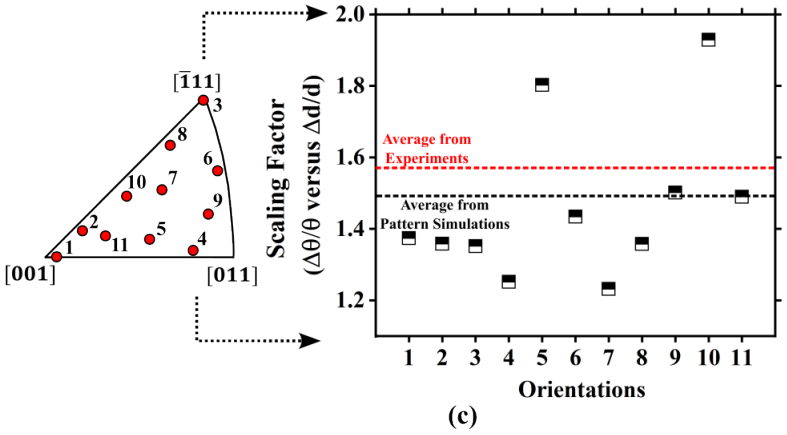

(c)

FIGURE 6.11: Results from virtual experiments conducted on simulated HR-EBSD patterns. (a) Progressive tensile strains were introduced in an ideal BCC iron (Fe) strain-free lattice ($a = b = c = 2.8667$ Åand $\alpha = \beta = \gamma = 90°$). This was implemented by altering lattice parameter 'a' (while keeping b and c constant) and by changing 'α' (while holding β and γ constant). The corresponding von-Mises strains, as estimated by $\Delta d/d$ and $\Delta\theta/\theta$, ranged from 0.0049 to 0.015. (b) For these strained, and unstrained, lattices HR-EBSD patterns were simulated both kinematically and dynamically. These strains were then estimated using HR-EBSD or cross-correlation algorithm. (c) Scaling factor from patterns simulations (as in Figure 6.11(c)) from 11 different crystallographic orientations, using traction free boundary conditions. Average scaling factors from pattern simulations (~ 1.47) and experiments (~ 1.57, Figure 6.9(b)) have also been included.

gradient:

$$\boldsymbol{F} = \begin{bmatrix} \lambda & 0 & 0 \\ 0 & 1 & 0 \\ 0 & 0 & 1 \end{bmatrix} \tag{6.8}$$

where, $\lambda = d/d_0$. d and d_0 represent the strained and unstrained lattice spacings, respectively. The residual strains (see Figure 6.11(a)) were represented as type $(\Delta d/d)$.

2. Idealized shear strains were applied at 45 deg to the 'a' direction, see Figure 6.11(a). The corresponding deformation gradient:

$$\boldsymbol{F} = \begin{bmatrix} 1 & \tan(\theta) & 0 \\ \tan(\theta) & 1 & 0 \\ 0 & 0 & 1 \end{bmatrix} \tag{6.9}$$

where, θ denotes the change in interplanar angle. This approach represented residual strain as type $(\Delta\theta/\theta)$.

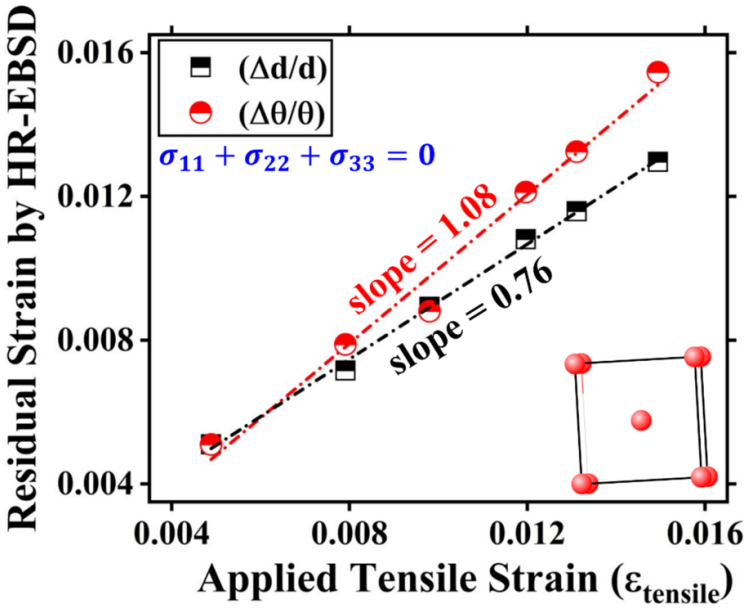

FIGURE 6.12: Kinematical pattern simulations, similar to Figure 6.11(b), but conducted using trace free boundary conditions ($\sigma_{11}+\sigma_{22}+\sigma_{33}=0$). The slopes were similar to those obtained by adopting traction free boundary conditions (Figure 6.11(b)).

As shown in Figure 6.11(a), an ideal strain-free BCC iron lattice (Fe) was subjected to progressive strain(s) by systematically increasing a 'single' lattice parameter (a) or an interplanar angle (α). The corresponding infinitesimal strains $\boldsymbol{\varepsilon}$, see Figure 6.11(a), were then determined from the knowledge of $(\Delta d/d)$ or $(\Delta\theta/\theta)$, respectively. The imposed von Mises strain(s) were derived as $\bar{\varepsilon} = \sqrt{\frac{2}{3}\boldsymbol{\varepsilon} : \boldsymbol{\varepsilon}}$, and were systematically altered from 0.0049 to

0.015. We have used corresponding crystal structures to simulate the HR-EBSD patterns, see Figure 6.11(a). The HR-EBSD pattern simulations were conducted with EDAX OIM-Matrix^{TM} software. It is to be noted that both kinematical, where no interaction between beam(s) were considered, and dynamical, with multi-beam interaction, simulations were used. The latter, as expected (Goodhew and Humphreys, 2000; Zaefferer, 2007; Callahan and De Graef, 2013) appeared more realistic. A description of our pattern simulations is given in the Section 6.4.2.

Figure 6.11(b) shows pattern simulations, kinematical as well as dynamical, originating from a single representative orientation. It is to be noted that strains were progressively applied on an ideal lattice. From the distorted lattice(s), pattern simulations (Winkelmann et al., 2007; Zaefferer, 2007; Callahan and De Graef, 2013) were then conducted. Finally, from the simulated patterns lattice distortions or strains were estimated by cross-correlation. As discussed earlier, the cross-correlation or HR-EBSD is sensitive to changes in $(\Delta\theta/\theta)$ only, but were performed on lattices distorted by α or $\Delta\theta$ and a or Δd, respectively. These two estimates were clearly different. As in Figure 6.11(b), the strains imposed by distorting the ideal lattice by $\Delta\theta$ showed a higher slope. More importantly, the strain estimated by HR-EBSD is nearly identical to the imposed strain on ideal lattice (slope$\sim$1), when the lattices are distorted by α or $\Delta\theta$, as compared to the case when lattice is distorted by a or Δd. Further, it was checked that the mode of pattern simulation (Figure 6.11(b)) and traction-free versus trace-free boundary conditions (cf. Section 6.4.2) did not significantly alter this strain estimate. However, crystal orientations or the relative positioning of the zone axes (see Figure 6.8(b)) appeared to affect the scaling factor. We used fitting of 11 randomly selected crystallographic orientations (and corresponding ideal lattices), and an average scaling factor of ~ 1.47 was obtained, see Figure 6.11(c). It is interesting to note that the experimental and statistical data produced a scaling factor of ~ 1.57 (Figure 6.9(b)), which was similar but not identical to the scaling factor emerging from pattern simulations (Figure 6.11(c)).

We have used this approach for 11 crystallographic orientations, see Figure 6.11(c). Out of these, Figure 6.11(b) shows results from 'orientation 1' with both kinematical and dynamical simulations. The corresponding patterns were input to OpenXY^{TM}, and estimates of residual strains were obtained by an off-line cross-correlation of simulated Kikuchi patterns. As the results for kinematical and dynamical pattern simulations were similar (Figure 6.11(b)), we have only used the computationally inexpensive kinematical simulations for the remaining calculations. It is to be noted that HR-EBSD estimates adopting traction free (Figure 6.11(b)) or trace free (Figure 6.12) boundary conditions were nearly identical (Ruggles et al., 2020). We have then determined an average scaling factor between $(\Delta\theta/\theta)$ type

strain measurements and $(\Delta d/d)$ type measurements for a given effective strain level, for all 11 orientations – see Figure 6.11(c). An average scaling factor of ~ 1.47 was thus obtained. It is to be noted that the estimated scaling factors were different for orientations 5 and 11. These were orientations where zone axes were at the edge of HR-EBSD Bragg spread, potentially introducing higher $\boldsymbol{q}$ vector (see Figure 6.8).

To further verify the simulated residual elastic strain measurements, we have estimated the change in interplanar spacing ($(\Delta d/d)$ for lattices distorted by a or Δd) and the change in interplanar angle 'α' (for lattices distorted by α or $\Delta\theta$) from the corresponding strain tensors, derived at various deformation levels (see Figure 6.11(a)). The resultant magnitudes have then been compared with their imposed counterparts. A reasonable convergence has been achieved by our HR-EBSD pattern simulations, especially in the predictions of the 'α' angle. For brevity, the results have been only been presented for the orientation 1 (see Figure 6.11(c)) in Table 6.2 and Table 6.3. The imposed change in Table 6.2 and 6.3 refer to the use of deformation gradients described in Equations 6.8 and 6.9 to distort the ideal crystal lattice, whereas the estimated changes refer to the back-calculations carried out from the OpenXY$^{\text{TM}}$ estimated deformation gradients.

TABLE 6.2: Comparison of the imposed versus estimated change in interplanar angles (for lattices distorted by α or $\Delta\theta$)

Applied tensile strain	Trace free boundary condition		Traction free boundary condition	
	Imposed	Estimated	Imposed	Estimated
0.0049	0.5	0.5215	0.5	0.5243
0.008	0.79	0.7598	0.79	0.7617
0.0098	0.88	0.7651	0.88	0.7677
0.012	1.19	1.1356	1.19	1.1374
0.013	1.3	1.2407	1.3	1.2964
0.015	1.5	1.4906	1.5	1.4973

TABLE 6.3: Comparison of the imposed versus estimated change in $(\Delta d/d)$ (for lattices distorted by a or Δd)

Applied tensile strain	Trace free boundary condition		Traction free boundary condition	
	Imposed	Estimated	Imposed	Estimated
0.0049	0.0058	0.00352	0.0058	0.0034
0.008	0.0097	0.00656	0.0097	0.0060
0.0098	0.0119	0.00802	0.0119	0.0075
0.012	0.0145	0.00973	0.0145	0.0089
0.013	0.0157	0.0103	0.0157	0.0093
0.015	0.0182	0.0126	0.0182	0.0115

6.4.3 Residual Strains Measurements at Sub-Micron Scales

Micro-Laue and HR-EBSD are significantly different in spatial resolution ($\sim 50\ \mu m$ versus $\sim 20\ nm$). Spatial resolutions of HR-TKD and TEM-PED, on the other hand, are somewhat closer. It was hence decided to explore the differences in strain measurement further with direct observations from TKD ($(\Delta\theta/\theta)$-sensitive) and PED ($(\Delta d/d)$-sensitive). It is to be noted that both these measurements were performed on an identical area (see Figure 6.15(a)) from a 3 mm TEM foil. Considering the foil thickness of a few hundred Å, we have focused on in-plane shear strain (γ_{xy}) for comparison. Reference patterns (HR-TKD and TEM-PED) were obtained from the identical spot, see Figure 6.15(a). Additionally, we have also shown standard SSE output from OpenXY^{TM} in the Figure 6.13. The low error fraction magnitudes ($\sim 12\%$), especially in a strained specimen, are indicative of the fact that the captured HR-TKD patterns (and the corresponding scan parameters, camera settings) were of sufficient quality.

Several interesting points emerged. Firstly, the orientations (shown as inverse pole figures) were similar. However, the so-called kernel average misorientation or KAM distribution (cf. Chapter 3 and Thool et al. (2020)) was higher and broader for HR-TKD (see Figure 6.14). This is not surprising. HR-TKD (or HR-EBSD) has nearly two-orders of magnitude higher angular resolution than PED. Increasing angular resolution ($\sim 0.006°$) enables HR-TKD to detect minor gradients in orientation effectively. TEM-PED on the other hand, with an angular resolution of $< 0.4°$, would neglect such minor orientation gradients and report them as a single orientation. This results in a wider/broader spread of the misorientation distribution for HR-TKD when compared to TEM-PED measurements.

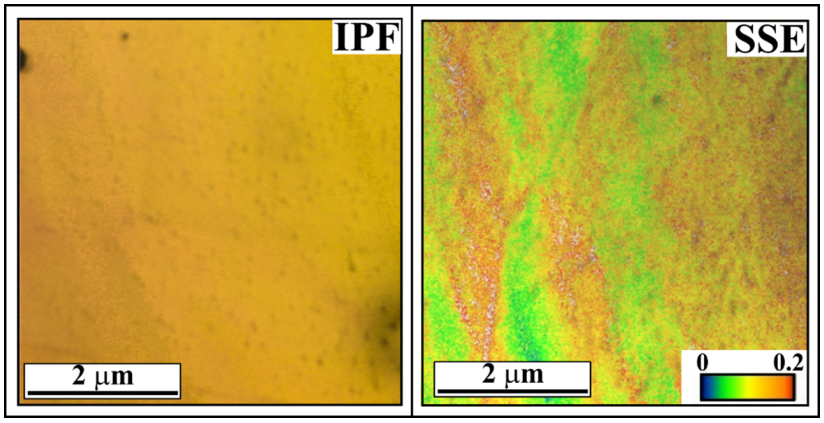

FIGURE 6.13: High resolution transmission Kikuchi diffraction (HR-TKD) results represented using Inverse Pole Figure (IPF) and the standard Sum of Squared Error (SSE) map obtained from the OpenXY^{TM} software.

Naturally, the microstructural features appeared different. Though both measurements were taken at a step size of 10 nm, HR-TKD used a beam current of 16 nA while PED involved a beam current of 0.0017 nA and a precession angle of 10.4 mrad. It is to be noted that the adopted precession angle provided excellent spatial resolution. In brief, the PED map clearly offered higher spatial resolution than the HR-TKD. The respective spatial resolutions were estimated using a MATLAB^{TM} code. This was $\sim$ 1.2 times (in pixels per μm^2) more in PED than in HR-TKD, though same step size was used. In particular, the PED appeared to be more sensitive to the presence of dislocations. In particular, the PED appeared to be more sensitive to the presence of dislocations. Though lateral resolution of TEM-PED is superior in comparison to HR-TKD, higher beam energies and the tendency to probe through the entire sample thickness results in a poor depth resolution (Sneddon et al., 2016). This study, however, clearly showed that TEM-PED had superior imaging for defects and dislocations.

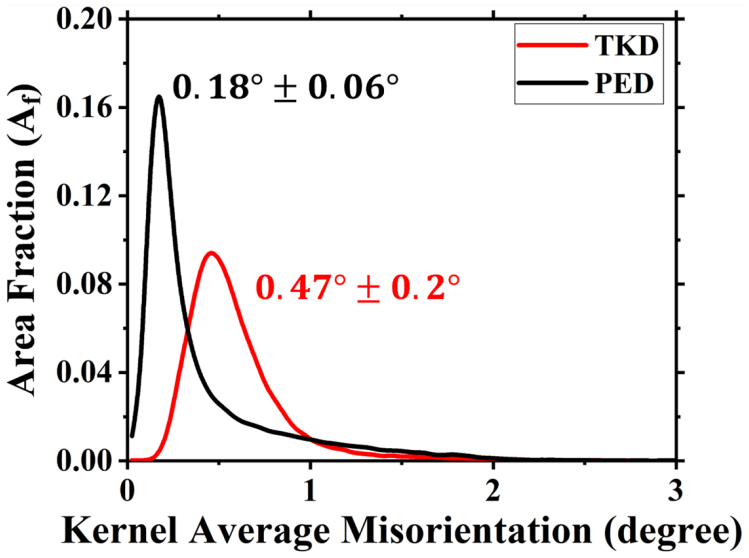

FIGURE 6.14: Kernel average misorientation (KAM) distributions between HR-TKD and TEM-PED, as obtained from Figure 6.15(b).

However, the biggest difference was in the imaging of γ_{xy}, see Figure 6.15(a). In HR-TKD, this was $\sim$ 1.73 times of the PED strain values (Figure 6.15(b)). Imposing the previously estimated scaling factor (between HR-EBSD and micro-Laue - Figure 6.9(b)), a slope of $\sim$ 1.08 was obtained (Figure 6.15(c). This is indeed striking that two different sets of experimental lattice strain estimates (Figure 6.9(b) versus Figure 6.15(b)) gave a similar scaling factor. In other words, this study not only established a difference in residual strain estimates using different measures of lattice distortions ($\Delta\theta/\theta$) versus ($\Delta d/d$), it also brought out a similar scaling adopting two different sets of analytical tools - HR-EBSD versus micro-Laue, and HR-TKD versus TEM-PED.

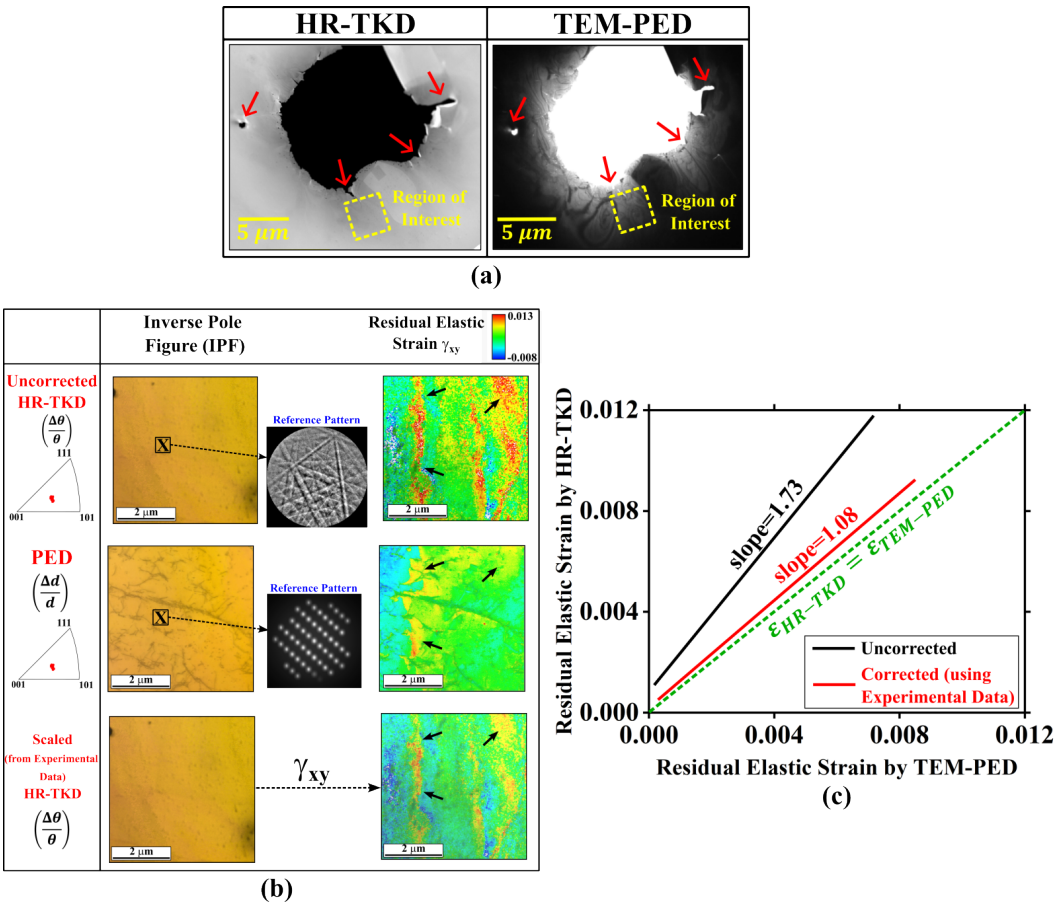

FIGURE 6.15: Exploring the numerical convergence in $\Delta\theta/\theta$ sensitive, HR-TKD and $\Delta d/d$ sensitive, TEM-PED based residual elastic strains. (a) Images showing the identical region used for mapping residual elastic strains with HR-TKD and TEM-PED. The red markers highlight the reference topological features used to ascertain identical locations for the respective scans. (b) Residual elastic strains were estimated using high resolution transmission Kikuchi diffraction (HR-TKD) and precession electron diffraction (PED) in the identical regions. The black markers highlight areas with similar strain concentrations in the HR-TKD as well as PED measurements. Correction (using experimental scaling factor of ~ 1.57) shows similar residual strain maps (in Figure 6.15(b), bottom) and (c) plot of absolute magnitudes of HR-TKD versus TEM-PED strains ($|\gamma_{xy}|$)

.

6.5 Local Lattice Distortions in Microstructures

The field of microscopy and microstructure, in metallic materials, has started by a Sheffield geologist Henry Sorby (Higham and Gentleman, 1963; Nuttall, 1981). Using thin sections of a wrought iron, deformed and then partially annealed, Sorby proposed the presence of thermodynamically unstable (deformed) and stable (recrystallized) regions. This was during a time-period, when deformation was often viewed as amorphization (Higham and Gentleman, 1963). Optical microscopy also described invariant plane strain microstructures, originally by Adolf Marten and then by Bain and Davenport, long before the phenomenological theory

of martensite crystallography was formalized (Verlinden et al., 2007). Microscopy naturally evolved further with the arrival of electron columns and then the EBSD (Wright and Adams, 1992; Adams et al., 1993). Other than attributes like resolution, the key aspect of any microscopy is in the contrast mechanism. The latter may emerge from the amplitude-phase contrast in classical TEM imaging, to more recent orientation contrast in EBSD and strain contrast in HR-EBSD.

The complete microstructural description consists of grains and phases and also defects (Verlinden et al., 2007). An important attribute of the latter is in the lattice distortions, the focus of the present study. The lattice distortion translates into residual strains and stresses, even bulk measurements of which may suffer from significant reproducibility issues (Verlinden et al., 2007). The local residual strain can be measured from high resolution TEM imaging and the so-called geometrical phase analysis (Ghamarian et al., 2014; Revelly et al., 2015; Ghamarian, 2017). However, this restricts any such measurement to aberration corrected microscopes and very limited area. Alternatives exist in the form of micro-Laue XRD (Lodh et al., 2017, 2018, 2019, 2022) and SEM (Wilkinson et al., 2006; Wright et al., 2011; Fullwood et al., 2015) plus TEM (Ghamarian et al., 2014; Ghamarian, 2017) based microtexture measurements. It is perhaps redundant to preach on the potentials for such multiscale diffraction-based measurements, as any metallurgist or materials scientist would readily appreciate this point. Such techniques hold possibilities of revealing uncharted aspects of microstructure.

A significant hurdle to any such effort, of strain-based microstructural representation, is in quantifying the differences in estimated strain magnitudes by different analytical tools. We have established that strain estimates from $(\Delta\theta/\theta)$ are higher than those from $(\Delta d/d)$. This was shown with both statistical experimental data (Figure 6.9(b)) and also with numerical simulations (Figures 6.11). Even using the same HR-EBSD algorithm, the lattices distorted by $(\Delta\theta/\theta)$ exhibited higher strain values (see Figure 6.11) than those altered by $(\Delta d/d)$. The numerical differences cannot be fixed using simple measurement algorithm adjustments (Figure 6.9) or protocol (Figure 6.8). The difference originated from the template of imposed lattice distortion. The lattices distorted by changing $\Delta\theta$ appeared more strained than those altered by Δd, see Figure 6.6. It is interesting that experiments and pattern simulation both brought out these differences, and a somewhat similar scaling factor (Figures 6.9(b) and 6.15) emerged. The clear linear relationship, with strain level, is striking, and it enabled us to obtain a convergence in strain magnitudes (Figure 6.6-6.15).

Note that the interaction volumes vary significantly between the HR-EBSD ($(\Delta\theta/\theta)$-sensitive) and micro-Laue ($(\Delta d/d)$-sensitive) residual strain measurement techniques. The penetration depth for an electron beam with a spot size of $\sim 2\ nm$ typically lies in the range of

$\sim 10-20\ nm$ (cf. Section 6.3). On the other hand, the micro-Laue technique subtends a relatively larger interaction volume, with typical penetration depths lying in the range of $5-10\ \mu m$ for a $50\ \mu m$ wide beam (cf. Section 6.3). It was hence suspected these differences may also contribute to the varying magnitudes of residual strain estimates.

To mitigate this difference, a comparison of the local residual strain estimates is presented using the HR-TKD and the TEM-PED techniques (cf. Section 6.4.3), both of which subtend nearly similar interaction volumes. As can be seen in Figure 6.15(c), employing a scaling factor of ~ 1.57 (cf. Figures 6.9 and 6.11) resulted in a numerical convergence between the $(\Delta\theta/\theta)$-sensitive HR-TKD and $(\Delta d/d)$-sensitive TEM-PED residual strain estimates. Since an identical scaling factor could be employed for $(\Delta\theta/\theta)$-sensitive and $(\Delta d/d)$-sensitive techniques with (HR-EBSD and micro-Laue) and without (HR-TKD and TEM-PED) differences in their interaction volumes, it can be concluded that the latter does not largely affect the numerical convergence between the residual strain estimates. However, our results do indicate that the interaction volumes subtended by each of the techniques significantly effects their measurement uncertainty as well as their spatial and angular resolution (cf. Figures 6.13 and 6.10).

Overall, our observations from Figures 6.6-6.9 can be justified as follows: phenomenologically, for the same state of deformation in a grain, the strain measured by HR-EBSD and micro-Laue single crystal residual elastic strain measurements should be identical. One potential cause of this difference is perhaps the different levels of sensitivity of the respective measurement techniques to different measures of elastic strain. The Kikuchi patterns are considered to be a gnomonic projection of a crystal lattice on the phosphor screen. The angles between the two bands corresponds to the interplanar angles in a crystal lattice, whereas, the width of Kikuchi band corresponds to the interplanar spacing d_{hkl} (Schwarzer et al., 2009). The cross-correlation based residual strain calculations rely on the shift in zone axes position $\boldsymbol{q}$ on the phosphor screen, to estimate the lattice distortion gradient tensor at a given pixel (Wilkinson et al., 2006, 2009). As seen in Figure 6.3, such a technique is more sensitive to $\Delta\theta/\theta$ (change in interplanar angles), in contrast to the micro-Laue technique, which is more sensitive to $\Delta d/d$ (change in interplanar spacing). The varying interpretation of the same imposed state of deformation by the two techniques can lead to the errors/discrepancies between micro-Laue and HR-EBSD/ TEM-PED and HR-TKD residual strains.

In addition, a larger 'a' type strain, which mainly results in a uniform change in the interplanar spacing (d_{hkl}) would not accurately reflect on the zone axes shifts; thus, resulting in a large deviation in the HR-EBSD/HR-TKD ($\Delta\theta/\theta$ sensitive) estimated strains as compared to the $\Delta d/d$ based techniques (see Figure 6.9(c)). It is important to note that the present

study does not comment on the reliability of either of the two diffraction-based residual strain measurement techniques, $\Delta\theta/\theta$ sensitive and $\Delta d/d$ sensitive; we only present a comparison, followed by a possible justification of the errors/discrepancies and calculation of a scaling factor to establish numerical convergence between these multiscale diffraction-based strain measurement approaches. Based on large statistical dataset as well as extensive pattern simulations, it appears that a numerical scaling factor exists between strain estimates from $\Delta d/d$ and $\Delta\theta/\theta$. Of course, the present study established this factor only in BCC iron, and it is unknown how other crystal symmetries or strain modes would exhibit such a scaling. However, the present set of experimental measurements and numerical simulations remain consistent and statistically robust. More importantly, they articulate the fundamental difference in strain estimates from $\Delta d/d$ and $\Delta\theta/\theta$. In addition, this study also brings out the potentials and challenges of multiscale diffraction-based lattice strain measurements as a microscopic technique and contrast mechanism.

6.6 Conclusions

We have used different multiscale diffraction-based residual strain measurements. These were sensitive to changes in the interplanar angle ($(\Delta\theta/\theta)$-HR-EBSD and TKD) or interplanar spacing ($(\Delta d/d)$-micro-Laue XRD and TEM-PED). A comparison of their absolute magnitudes, and possible reasons for their deviation from the ideal behavior were explored. Following were the key conclusions from this study:

1. The measurements differed in scale and resolution, but more importantly they were numerically different. For example, both HR-EBSD and micro-Laue XRD showed an increase in residual strain values with imposed tensile deformation. However, even after optimizing the HR-EBSD parameters - the increase in strains were ~ 1.57 times higher in HR-EBSD.

2. We have then distorted an ideal BCC lattice, virtually, by progressively altering its interplanar angle (α) and lattice parameter (a), respectively. These effectively changed $\Delta\theta$ and Δd. From kinematically and dynamically simulated patterns, the corresponding strains were calculated by HR-EBSD. The strain estimates were consistently higher for lattices distorted by $\Delta\theta$ compared to lattices distorted by Δd. The scaling factor (~ 1.47) was somewhat similar to the experimentally observed ratio of ~ 1.57.

3. TKD and TEM-PED measurements, conducted on the identical location, showed higher strains for TKD. However, similar magnitudes of strain distributions were obtained when scaled with the earlier (HR-EBSD versus micro-Laue) factor of ~ 1.57.

Chapter 7

Orientation-Dependent Residual Strains during Tensile and Cyclic Deformation

7.1 Introduction

The self-equilibrating strains retained in a material in the absence of external load are referred as residual strains (Cullity, 1956; Noyan and Cohen, 2013; Withers and Bhadeshia, 2001). These may arise due to heterogeneous elastic-plastic deformation, phase transformation or temperature changes during thermo-mechanical processing (Verlinden et al., 2007) and are expected to influence the ensuing mechanical properties. Based on the length-scales over which these strains self-equilibrate, they may be further classified into bulk and local residual strains (Lodh et al., 2022; Chen et al., 2022a). Alternatively, these may also be classified as Type-I (bulk), Type-II (intergranular) and Type-III (intragranular) residual strains (Verlinden et al., 2007; Chen et al., 2022a).

X-ray/neutron diffraction have been used extensively to characterize the evolution of bulk residual strains. The position, width and intensity of the diffraction peak profiles have been quantified to analyze the bulk residual strains (Clausen et al., 1999; Agnew et al., 2003; Erinosho et al., 2016; Upadhyay et al., 2019; Thool et al., 2020; Ferreri et al., 2022), while also providing information regarding the dislocation density (Ungár et al., 2001; Plotkowski et al., 2023; Wang et al., 2024) and texture development (Kocks et al., 2000; Takajo et al., 2018) during deformation. The large penetration depth and interaction volume subtended

[1] Significant parts of this Chapter have been published in (Pai et al., 2025)

by these methods ensures a statistically representative data over several grains (Randle and Engler, 2000). (hkl)-specific bulk residual strains, or lattice strains, are a measure of the change in the inter-planar spacing for specific (hkl) crystallographic planes or grain families (Verlinden et al., 2007) and are generally used to quantify the texture-dependent anisotropic residual strain development. These have also been employed to study the lattice strain/stress partitioning between the constituent phases, and subsequently quantify their influence on the local as well as aggregate properties (Kim et al., 2016a; Pokharel et al., 2019; Tran et al., 2023; Bönisch et al., 2023; Zhang et al., 2021a). For example, Zhang et al. (2021a) in their study on the Additively Manufactured AlSi10Mg subjected to tensile loading noted a clear difference in the load bearing capabilities of the Aluminum and Silicon phases. Further, their study also comments on the factors influencing the orientation-dependent lattice strains at different stages of the tensile deformation (Zhang et al., 2021a). Spatially-resolved local residual strains have also been studied using techniques such as High Energy X-ray Diffraction Microscopy (HEDM) (Kapoor and Sangid, 2018; Tayon et al., 2024), single crystal micro-Laue X-ray Diffraction (XRD) (Thool et al., 2020; Manda et al., 2024) and High Resolution Electron Back Scatter Diffraction (HR-EBSD) (Fullwood et al., 2015; Hansen et al., 2020; Das et al., 2020). The diffraction-based approaches have been used to quantify both the intragranular (Kartal et al., 2012; Jiang et al., 2015; Black et al., 2024) and intergranular local residual strains (Manda et al., 2024; Tayon et al., 2024) and their correlation with the underlying microstructure.

The development of residual strains is often anisotropic, dependent on the crystallographic texture and inherently linked to the underlying plastic deformation (Clausen et al., 1999; Korsunsky et al., 2002; Wang et al., 2003; Kanjarla et al., 2012; Zheng et al., 2013; Schröder et al., 2022). Generally speaking, the imposed deformation results in the development of substantial intragranular orientation gradients (Hartley and Kysar, 2020; Sun et al., 2022). The magnitudes of these are largely influenced by the Schmid factor of the activated slip systems as well as the misorientation it subtends with its neighbours (Nagarajan et al., 2021; Chen and Furushima, 2024). The local lattice rotation leads to the activation of additional slip systems within a grain. The resulting plastic deformation renders the grain incapable of accommodating the stress increment, thus, displaying a relaxation in the bulk residual strains (Brown et al., 2017). Similarly, Zheng et al. (2013) noted that the decay in the (hkl) lattice strain magnitudes could be directly correlated to the instantaneous Taylor factor. Further, Manda et al. (2024) reported higher local residual strain developments for the (100) grain family, followed by the (110) and (111) grains under tensile loading. Study of the effect of neighboring grains on the development of anisotropic local residual strains has been performed by (Abdolvand et al., 2018; Thool et al., 2020; Louca et al.,

2024). These observations point out that the residual strains are inherently orientation-dependent and also influenced by the texture of the neighboring grains. Anisotropic residual strains/stresses are expected to contribute to incompatible deformation and eventual failure at grain boundaries (Sudhalkar et al., 2024). However, there are only limited studies on the development of residual strains during cyclic deformation (Lorentzen et al., 2002; Wang et al., 2003; Saleh et al., 2013).

Crystal plasticity models have been used extensively to predict the development of bulk and local residual strains (Clausen et al., 1999; Dawson et al., 2001; Lorentzen et al., 2002; Li and O'Dowd, 2011; Kanjarla et al., 2012; Musinski and McDowell, 2015; Zecevic et al., 2015; Wang et al., 2017; Chen et al., 2019; Shade et al., 2019; Upadhyay et al., 2019; Jeong and Tomé, 2020; Bandyopadhyay et al., 2021; Aburakhia et al., 2022; Chen et al., 2022a; Ferreri et al., 2022; Bandyopadhyay et al., 2024). The residual strains can be predicted by projecting the simulated elastic strains onto crystallographic planes. Depending on whether the comparison is made with ex-situ or in-situ experimental measurements, the simulated residual strains need to be appropriately relaxed. While computationally cheaper, mean-field crystal plasticity models have been used for prediction of statistically representative bulk residual strains averaged over a large number of grains (Clausen et al., 1999; Lorentzen et al., 2002; Neil et al., 2010; Ferreri et al., 2022), they are generally unable to predict the development of local residual strains. Towards this end, spatially-resolved, full field crystal plasticity models have been employed (Kanjarla et al., 2012; Thool et al., 2020; Sedaghat and Abdolvand, 2021; Bandyopadhyay et al., 2024; Louca et al., 2024). Accurate prediction of the elastic-plastic transition, relaxation and load transfer among grains, and influence of neighboring orientations is often challenging. In addition, appropriate incorporation of processing induced residual strains (prior to deformation) is also a matter of ongoing study (Musinski and McDowell, 2015; Kapoor and Sangid, 2018; Bandyopadhyay et al., 2024).

Further, most of the crystal plasticity models have been used to predict residual strains during monotonic deformation. Development of residual strains and associated microstructure evolution during cyclic deformation are not very well studied. While there are several crystal plasticity studies on modeling cyclic deformation due to backstress evolution (Castelluccio and McDowell, 2017; An et al., 2020; Santus et al., 2023), evolution of residual strains during cyclic deformation has not been studied in great detail. Further, this is largely dependent on the accurate estimation of directional backstresses during cyclic loading. Recently, physically based backstress models have also been proposed to capture the underlying substructure evolution (Brahme et al., 2011; Zecevic and Knezevic, 2015; Castelluccio and McDowell, 2017; Agius et al., 2022; Bandyopadhyay et al., 2021; Zirkle et al., 2021; Zhang et al., 2023). However, their role on influencing the orientation-dependent bulk and local

residual strains has not yet been explored and needs to be studied. Further, there have been combined experimental and crystal plasticity studies examining the intragranular lattice rotation and slip activity in an Inconel 718 alloy subjected to monotonic and cyclic loading (Hestroffer et al., 2022). Recent studies have also correlated crystal plasticity-predicted slip and twin system activity with the bulk lattice strain evolution and tension-compression asymmetry (where present) due to the inherent deformation anisotropy of hexagonal closed packed crystalline materials (Wang et al., 2016; Agnew et al., 2018; Zhu et al., 2021a). Here, we further extend these correlations in terms of the development of bulk and local residual strains, the crystallographic texture and their interdependence with the underlying microstructural features, during tensile and cyclic loading.

We present a combined experimental and crystal plasticity modeling framework to study the evolution of bulk and local residual strains during tensile and cyclic deformation in an austenitic stainless steel. The bulk residual strains are quantified in terms of the lattice-specific (hkl) strains using XRD measurements, while the local residual strains are quantified in terms of the HR-EBSD measured strains. A dislocation density-based crystal plasticity finite element modeling framework is used to predict the macroscopic stress-strain response and the bulk and local residual strains during tensile and cyclic deformation. Model predictions of the bulk residual strains during tensile and cyclic deformation are compared with the XRD measurements. Further, initial microstructures obtained from EBSD scans are simulated to predict the local residual strains and compared with their HR-EBSD counterparts. The broad objectives of this work are to study the evolution of bulk and local residual strains, their correlation with the underlying microstructure, and the hierarchy in the residual strain developments during tensile and cyclic deformation.

7.2 Experimental Methodology

The material used in the present study is a commercial austenitic stainless steel (AISI 316L). This study used a fully recrystallized material (average grain size of 31 ± 6 μm) in a standard mill-annealed condition (Wasnik et al., 2002). Appropriate specimens were then subjected to tensile and cyclic deformation. Two types of specimens, standard (ASTM Standard E-606 (ASTM et al., 2012)) and sub-size (cf. Chapter 3), were used. The former were subjected to room temperature tensile tests as well as strain-controlled Low Cycle Fatigue (LCF) tests. These were performed in a servo-hydraulic axial fatigue system, MTS-Landmark, with a 100 kN loading capacity. Fully-reversed cyclic loading tests were performed for a total strain amplitude $\Delta\varepsilon/2$ of 0.01 at a nominal strain rate of 10^{-3} s^{-1}. This corresponds to an elastic

strain amplitude, $\Delta\varepsilon^e/2 \sim 0.002$ and plastic strain amplitude, $\Delta\varepsilon^p/2 \sim 0.008$. The displacement data was acquired using a fixed gauge length extensometer (having capacity of measuring strains up to 0.5) of gauge length 10 mm. For our progressive, albeit interrupted cyclic loading/LCF experiments, microstructural characterizations were carried out after deformation to 0, 10, 20, 50, 100 and 200 cycles, respectively. An identical specimen was also used to carry out the uninterrupted LCF test up to 200 cycles. Further, uninterrupted monotonic tensile testing was performed up to a nominal strain of 0.25 at a nominal strain rate of 10^{-3} s^{-1} on the standard specimen. Following this, interrupted tensile tests were carried out in a DEBEN^{TM} micro-tensile stage using a sub-size specimen, at a nominal strain rate of 10^{-3} s^{-1}. Microstructural characterizations were carried out at regular intervals during progressive tensile deformation at intervals of 0, 0.05, 0.1, 0.15, 0.2 and 0.25 nominal strains. The uninterrupted LCF/tensile experiments were used to obtain the mechanical response and the crystallographic texture (initial and deformed). The progressive LCF/tensile tests, on the other hand, were used to study the evolution of microstructure and residual strains with increasing deformation.

(hkl) specific bulk residual strain (lattice strain) measurements at various stages of the progressive tensile and cyclic deformation were carried out in a PanAlytical^{TM} Empyrean X-ray Diffraction (XRD) system. This equipment hosts a 3 kW sealed tube with a X-ray spot size of ~ 1 mm (as determined by X-ray lens) and a 1-Der^{TM} solid state linear (1D) detector. The lattice strains were measured using the standard d-sin$^2\psi$ technique (Prevéy, 1986; Van Houtte and De Buyser, 1993; Lodh et al., 2022) on four distinct crystallographic poles or (hkl) families, namely, the (111), (001), (101) and (311) poles, which satisfy the Bragg's law. As the X-ray optics (Polycap^{TM}) and solid-sate detector (1-Der^{TM}) are best suited for Cu K-α, we have used the same as the X-ray source. An angular 2-theta range of $\sim 140°$ is thus achieved in our laboratory XRD setup (PanAlytical^{TM} Empyrean). This enables covering the following (in the increasing order of 2-theta) diffraction peaks or poles: (111), (200), (220), (311), (222), (400) and (331). Thus, only the (111), (200) (denoted as (001) family), (220) (denoted as (101) family) and (311) grain families have been considered in the present work. It may also be noted that past literature (Neil et al., 2010; Chen et al., 2019; Upadhyay et al., 2019) have also considered lattice strains for these FCC crystallographic orientations. A K-β filter (Nickel) was used on the incident side to suppress the beta-emission line, whereas soller slits (with a solid angle of 0.04 rad) were used to limit the out-of-plane/angular divergence on the diffracted beam side. A commercial software, Xpert^{TM} Stress Plus, was used for analyzing the XRD data. Additionally, all measurements were performed three times for a given condition to ensure repeatability. Note that we have used ε^{LD} to refer to the *longitudinal residual strains* and ε^{TD} to refer to the *transverse residual strains*, bulk as well as local, throughout the manuscript.

The sample preparation for microscopy involved a combination of traditional metallography techniques, followed by electropolishing the specimens in an electrolyte of 80 : 20 ratio of methanol to perchloric acid solution. A Stuers^{TM} Lectropol-5 equipment at 273 K and 14 V dc was used for electropolishing the specimens. A FEI^{TM} Quanta-3D Field Emission Gun-Scanning Electron Microscope (FEG-SEM) with a EDAX^{TM} Trident system was used for Electron Back Scatter Diffraction (EBSD) scans. The EBSD scans used a fixed step size of 0.25 μm, an accelerating voltage of 20 kV, a current of 16 nA and a working distance of 14.0 mm. The scans were analyzed using EDAX^{TM}'s OIM Analysis software. For estimating local residual strains using the High Resolution EBSD (HR-EBSD) technique, the 16-bit Kikuchi patterns (acquired at 2×2 binning) were stored for all points within the region of interest. An open source HR-EBSD toolkit, OpenXY (Fullwood et al., 2015; Fullwood, 2020) was used, with the methodology given in Chapter 6. Additionally, Pattern Region of Interest Analysis (PRIAS) images (Chaudhary et al., 2023) have also been acquired at each stage of the interrupted tensile and cyclic deformation, to understand the changes in surface topography of the specimens.

A confidence index cutoff of 0.1, representing 95% accuracy in the indexing of Kikuchi patterns, was used to filter out any erroneous data during post-processing. To avoid any edge effects, regions of 200 $\mu m \times 200$ μm area near the center of tensile and cyclic specimens were used for all microstructural characterizations. Further, impressions from the microhardness indents were used to locate the region of interest during interrupted tensile and cyclic (EBSD) measurements. While studies pertaining to the detailed microstructural characterizations focused on a smaller region of interest, wide area scans (1.25 $mm \times 1.00$ mm) along the specimen cross-section with a step size of 0.75 μm were used to estimate the bulk crystallographic texture.

7.3 Modeling Framework

A dislocation density-based crystal plasticity model has been developed and integrated into the open source crystal plasticity framework, ρ-CP (Patra et al., 2023a), to predict the evolution of lattice strains during deformation. While existing models in the ρ-CP framework are based on the evolution of mobile and immobile dislocation densities during deformation, the present work has adopted a rather simpler Kocks-Mecking type formulation for evolution of statistically stored dislocation densities, combined with a Taylor hardening model for dislocation strengthening and a slip system-level Armstrong-Frederick type model for directional hardening. In addition, initial residual strains have been incorporated using the

Eigenstrain method (Musinski and McDowell, 2015) to mimic processing-induced residual strains in the as-received material.

7.3.1 Finite Deformation Kinematics

The finite deformation framework relies on the multiplicative decomposition of the deformation gradient, $\boldsymbol{F}$, into the elastic, $\boldsymbol{F^e}$, plastic, $\boldsymbol{F^p}$ and thermal, $\boldsymbol{F^\theta}$, parts (Musinski and McDowell, 2015; Pokharel et al., 2019), i.e.,

$$\boldsymbol{F} = \boldsymbol{F^e} \cdot \boldsymbol{F^p} \cdot \boldsymbol{F^\theta} \tag{7.1}$$

where, $\boldsymbol{F^\theta}$ accounts for Eigenstrains due to thermal expansion/contraction, $\boldsymbol{F^p}$ accounts for the plastic shear on the thermally-strained lattice, thus transforming it to an intermediate, isoclinic configuration. $\boldsymbol{F^\theta}$ has been added to instantiate the (initial) residual strains present in the as-received material, in the absence of any external load. Based on the assumption of isotropic thermal expansion/ contraction, $\boldsymbol{F^\theta}$ can be written as (Musinski and McDowell, 2015):

$$\boldsymbol{F^\theta} = \sqrt{1 + 2\alpha^\theta \Delta\theta}\ \boldsymbol{\delta} \tag{7.2}$$

where, α^θ denotes the temperature-dependent thermal expansion co-efficient, $\Delta\theta = \theta_{ref} - \theta$ is the deviation of the current temperature, θ, from the stress-free temperature, θ_{ref}, and $\boldsymbol{\delta}$ is the second rank identity tensor. The stress-free Eigen strains can hence be written as:

$$\boldsymbol{E}^\theta = \frac{\mathbf{1}}{\mathbf{2}}\left(\boldsymbol{F}^{\theta^T} \cdot \boldsymbol{F}^\theta - \boldsymbol{\delta}\right) = \alpha^\theta \Delta\theta\ \boldsymbol{\delta} \tag{7.3}$$

Note that the Eigenstrain approach is introduced as a means to induce the residual strains in the undeformed material. The value of θ_{ref} is hence decided by simple analytical calculations to obtain the desired residual strains. We note that alternate approaches to introduce residual strains in polycrystalline ensembles have also been proposed recently (Bandyopadhyay et al., 2024).

The plastic part of the deformation gradient, $\boldsymbol{F^p}$, can be related to the spatial velocity gradient, $\boldsymbol{L}^p$, as $\dot{\boldsymbol{F}}^p = \boldsymbol{L}^p \cdot \boldsymbol{F}^p$. Further, $\boldsymbol{L}^p$ is written as the tensorial sum of crystallographic shearing rate, $\dot{\gamma}^\alpha$, over all possible slip systems, N_s, and is given by:

$$\boldsymbol{L^p} = \sum_{\alpha=1}^{N} \dot{\gamma}^\alpha \boldsymbol{m_0^\alpha} \otimes \boldsymbol{n_0^\alpha} \tag{7.4}$$

where, $\boldsymbol{m_0^\alpha}$ and $\boldsymbol{n_0^\alpha}$ denote unit vectors along the slip and slip plane normals on slip system α in the reference configuration, respectively.

The crystallographic shearing rate due to dislocation glide is represented using a Kocks-type thermally activated flow rule as (Kocks et al., 1975):

$$\dot{\gamma}^\alpha = \dot{\gamma}_0 \exp\left\{\frac{-\Delta F_g}{kT}\left(1-\left(\frac{|\tau^\alpha - \chi^\alpha| - s_a^\alpha}{s_t^\alpha}\right)^p\right)^q\right\} \operatorname{sgn}(\tau^\alpha - \chi^\alpha)\,; |\tau^\alpha - \chi^\alpha| > s_a^\alpha \tag{7.5}$$

where, $\dot{\gamma}_0$ is the reference shearing rate, ΔF_g is the activation energy for dislocation glide, k is the Boltzmann constant, and T is the absolute temperature, respectively. The parameters p and q can be used to control the shape of the activation enthalpy curve. Further, s_a^α represents the non-directional athermal slip resistance, due to the long range stress field of obstacles, such as dislocation forests, whereas s_t^α represents the thermal slip resistance due to short range barriers, such as solute atoms. The athermal slip resistance involves contribution from the threshold lattice resistance, grain-size strengthening and dislocation strengthening, and is given by:

$$s_a^\alpha = \tau_0^\alpha + k_{ih} G b \sqrt{\sum_{\xi=1}^{N} A^{\alpha\xi} \rho_{SSD}^\xi} \tag{7.6}$$

Here, τ_0^α denotes the intrinsic lattice resistance, k_{ih} denotes the Taylor hardening coefficient due to dislocations, G is the shear modulus, b is the Burgers vector magnitude and $A^{\alpha\xi}$ represents the slip system level interaction matrix for dislocation junctions formed between dislocations on slip system α and ξ, and ρ_{SSD}^ξ is the density of Statistically Stored Dislocations (SSD) on slip system ξ.

The substructure evolution was captured using a Kocks-Mecking type model for SSD evolution of the form (Estrin, 1996; Kocks and Mecking, 2003):

$$\dot{\rho}_{SSD}^\alpha = \frac{k_M}{b}\sqrt{\rho_{SSD}^\alpha}\,|\dot{\gamma}^\alpha| - k_D \rho_{SSD}^\alpha\,|\dot{\gamma}^\alpha| \tag{7.7}$$

Here, the first term on the right-hand side accounts for dislocation multiplication at pre-existing junctions, while the second term accounts for dislocation annihilation due to dynamic recovery. The parameters, k_M and k_D are derived by fitting the model to the experimental stress-strain response.

Backstresses may contribute to directional hardening during cyclic loading. The rate of evolution of crystallographic backstress is modeled as a function of the dislocation density using a non-linear Armstrong-Frederick type kinematic hardening model (Shenoy et al.,

2008; Chaudhary et al., 2022):

$$\dot{\chi}^{\alpha} = \left(k_{\chi 1}^{\alpha} G b^{\alpha} \sqrt{\rho_{SSD}^{\alpha}}\, \mathrm{sgn}\left(\tau^{\alpha} - \chi^{\alpha}\right) - k_{\chi 2}^{\alpha} \chi^{\alpha}\right) |\dot{\gamma}^{\alpha}| \tag{7.8}$$

where, the first term accounts for the development of backstress due to dislocation pile-up and the second term accounts for the recovery, respectively. $k_{\chi 1}^{\alpha}$ and $k_{\chi 2}^{\alpha}$ are associated material parameters that can be estimated by fitting to experimental cyclic stress-strain response. As discussed earlier, more advanced physically based formulations for backstress predictions exist in the literature (Brahme et al., 2011; Zecevic and Knezevic, 2015; Castelluccio and McDowell, 2017; Zirkle et al., 2021; Agius et al., 2022; Zhang et al., 2023). In the present study, we resort to a rather simpler dislocation density based model form for backstress evolution, which has been demonstrated earlier for polycrystalline copper (Patra et al., 2023a) and Ni-based superalloys (Chaudhary et al., 2022, 2025).

The constitutive equations have been implemented as a material model in the open-source crystal plasticity framework, ρ-CP, that interfaces with the open source finite element solver, MOOSE (Permann et al., 2020), for performing crystal plasticity finite element simulations. Details of the fully implicit numerical scheme for the time step integration of the crystal plasticity model are given in Patra et al. (2023a).

7.3.2 Prediction of Lattice Strains

Based on prior studies (Li and O'Dowd, 2011; Pokharel et al., 2019; Upadhyay et al., 2019), we have adopted the following methodology for predicting the evolution of lattice strains during tensile and cyclic deformation. This method uses the crystallographic orientation (in terms of the Euler angles) at a given material point to project the elastic Green strain tensor on to specific $< hkl >$ directions or (hkl) family of planes. Given the initial Euler angles (ϕ_1, ϕ, ϕ_2) in Bunge notation, the corresponding rotation tensor, $\boldsymbol{R}_0$, can be used to rotate from the global/ laboratory frame of reference to the undeformed crystal frame of reference (and vice-versa) (Randle and Engler, 2000). Polar decomposition of the elastic deformation gradient, $\boldsymbol{F}^e$, at a given material point can be used to estimate the associated rigid rotation of the lattice, $\boldsymbol{R}^e$, as:

$$\boldsymbol{F}^e = \boldsymbol{R}^e \cdot \boldsymbol{U}^e \Rightarrow \boldsymbol{R}^e = \boldsymbol{F}^e \cdot \boldsymbol{U}^{e-1} \tag{7.9}$$

Here, $\boldsymbol{U}^e$ is the elastic stretch tensor. The total lattice rotation experienced by a material point in the deformed configuration is thus given as:

$$\boldsymbol{R} = \boldsymbol{R}^e \cdot \boldsymbol{R}_0 \tag{7.10}$$

The $< hkl >$ plane normal of the material point in the deformed configuration, $\boldsymbol{n_{hkl}}$, can be obtained by rotation of the $< hkl >$ plane normal from the undeformed frame of reference, $\boldsymbol{N_{hkl}}$, as:

$$\boldsymbol{n}_{hkl} = \boldsymbol{R} \cdot \boldsymbol{N}_{hkl} = \boldsymbol{R} \cdot \frac{(h\boldsymbol{e}_1 + k\boldsymbol{e}_2 + l\boldsymbol{e}_3)}{\sqrt{h^2 + k^2 + l^2}} \tag{7.11}$$

The lattice strain at a given material point can thus be written as:

$$\varepsilon_{hkl} = \boldsymbol{n}_{hkl} \cdot \boldsymbol{E}^e \cdot \boldsymbol{n}_{hkl} \tag{7.12}$$

where, $\boldsymbol{E^e} = (1/2)(\boldsymbol{F^{eT}} \cdot \boldsymbol{F^e} - \boldsymbol{\delta})$ is the elastic Green strain.

The average lattice strain over all possible material points contributing to a $< hkl >$ reflection is given as:

$$\langle \varepsilon_{hkl} \rangle = \frac{1}{V_{hkl}} \int_{V_{hkl}} \varepsilon_{hkl} dV \tag{7.13}$$

where, V_{hkl} denotes the volume of grains contributing to a given $< hkl >$ reflection. The possibility of a given material point contributing to the $< hkl >$ reflection depends upon the deviation of the $< hkl >$ plane normal from the diffraction vector, $\boldsymbol{g}$, and can be given by:

$$V_{hkl} \in \left| \cos^{-1} \left(\boldsymbol{g} \cdot \boldsymbol{n}_{hkl} \right) \right| \leq \omega_{tol} \tag{7.14}$$

Generally, $\omega_{tol} = 6.5 - 7.5^\circ$ has been used for neutron diffraction measurements (Pokharel et al., 2019; Upadhyay et al., 2019). We have verified that for our XRD measurements a similar tolerance is reasonable and have used the same for model predictions, as well. Finally, note that all grain families contributing to a given $< hkl >$ reflection have been referenced using the round braces, i.e., (hkl), throughout the manuscript.

We have quantified residual strains, instead of residual stresses because the latter are indirectly obtained by taking the appropriate product of the residual strains with the elastic constants. There may be error involved with this if the anisotropic elasticity tensor, rotated to the crystal axes, is not considered. On the other hand, residual strains are directly obtained from peak or zone axes shifts from X-ray diffraction or HR-EBSD.

7.4 Results and Discussion

7.4.1 Model Calibration

TABLE 7.1: Volume fraction of different texture components in the (a) undeformed and (b) deformed specimens.

(a)

Texture Component	Experimental Texture	Reduced Texture (1000 orientations)
Cube ($\{001\} < 100 >$)	0.012	0.011
Brass ($\{110\} < 112 >$)	0.068	0.070
S ($\{123\} < 634 >$)	0.053	0.048

(b)

Texture Component	$\varepsilon_{zz} = 0.25$ (Tensile)		$N = 2$ (Cyclic)	
	Experiment	Simulation	Experiment	Simulation
Cube ($\{001\} < 100 >$)	0.021	0.023	0.017	0.012
Brass ($\{110\} < 112 >$)	0.049	0.052	0.055	0.063
S ($\{123\} < 634 >$)	0.038	0.050	0.043	0.047

Figure 7.1(a) shows a schematic of the Loading Direction (LD // Z), Transverse Direction (TD // X) and Normal Direction (ND // Y) on the cross-section of a representative tensile specimen, while Figure 7.1(b) shows the representative crystallographic texture measured from the wide-area EBSD scans on the X-Y plane for the undeformed specimen. This has been shown in terms of the $\phi_2 = 0°$, 45° and 65° sections of the Orientation Distribution Function (ODF). A maximum intensity of 8.105 was observed (see Figure 7.1(b)), indicative of a mildly textured material. Note that the wide-area EBSD scan had dimensions of 1.25 $mm \times 1.00$ mm and comprised of 5082 grains. The corresponding IPF map and the grain size distribution has been shown in Figure 7.2(a,b). The representative texture derived from this wide-area EBSD scan has been used as an input to our simulations. The experimental texture was then reduced to 1000 unique orientations, which serves as an input for the crystal plasticity simulations using the MTEX open source software (Bachmann et al., 2010). Figure 7.1(b) shows the reduced crystallographic texture for the same ODF sections. Additionally, Figure 7.1(b) also shows a distribution of the ODF intensity, $f(g)$, along the ϕ_1 axis for $\phi = 45°$, $\phi_2 = 0°$ (see dotted line across $\phi_2 = 0°$ ODF section in Figure 7.1(b)). It can be seen that the line profile of the reduced texture is qualitatively similar to the experimental texture and has been used an input for the bulk simulations. The similarity is also evident from the near-similar volume fractions of the Cube, Brass and S texture components between the experimental and the reduced texture (cf. Table 7.1(a)). Moreover, one can also observe relatively higher volume fractions of the Brass component, in comparison to its counterparts in Table 7.1(a). It can also be seen in 7.2(a) that a majority of the grains in the undeformed specimen are of the $\sim$ (101) family, thus resulting in a near-Brass texture.

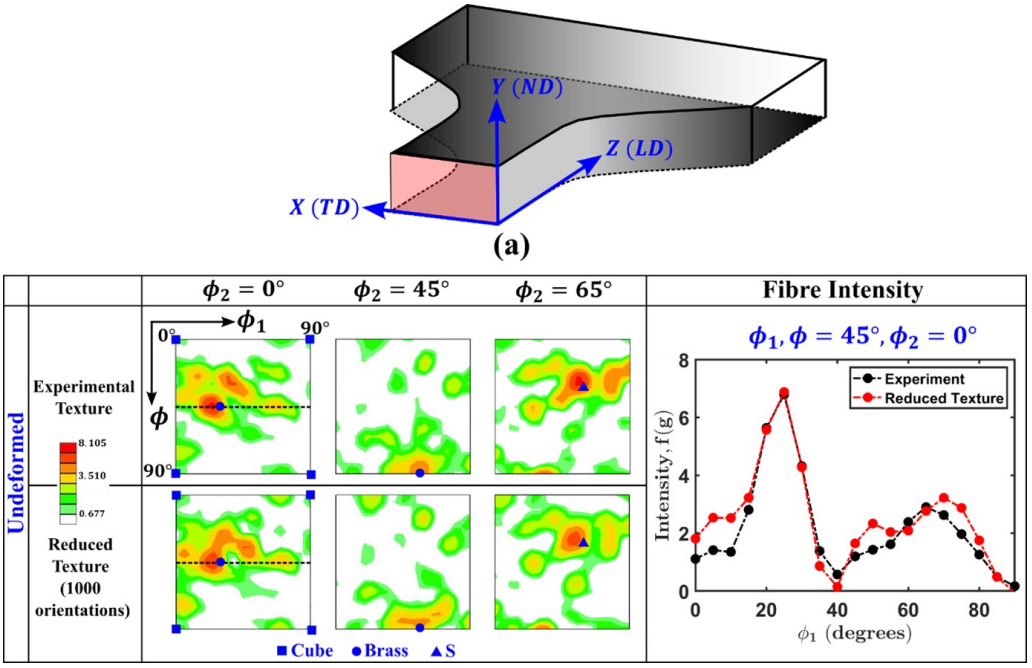

FIGURE 7.1: (a) Schematic showing the Loading (LD), Transverse (TD) and Normal (ND) directions on a tensile specimen. (b) The experimental and reduced crystallographic textures plotted in terms of the Orientation Distribution Function (ODF) $\phi_2 = 0°$, $45°$ and $65°$ sections. The corresponding intensity distribution along the α fibre (see dotted line in (b) along ϕ_1,$\phi = 45°$,$\phi_2 = 0°$ ODF section) for the experimental and reduced textures has been shown in (b). The blue markers indicate some of the typical texture components in Face Centered Cubic (FCC) metals, the volume fractions of which have been tabulated in Table 7.1(a).

TABLE 7.2: Constitutive model parameters calibrated to obtain a best-fit with the experimental tensile and cyclic stress-strain response.

Parameter	Value	Meaning
C_{11}	$207.98 + 0.0724\theta - 1.75 \times 10^{-4}\theta^2 + 5.26 \times 10^{-8}\theta^3$ GPa	
C_{12}	$135.77 + 0.0405\theta - 1.25 \times 10^{-4}\theta^2 + 5.26 \times 10^{-8}\theta^3$ GPa	Elastic constants
C_{44}	$121.83 + 0.02413\theta - 8.20 \times 10^{-5}\theta^2 + 3.49 \times 10^{-8}\theta^3$ GPa	
G	$\sqrt{\frac{(C_{11}-C_{12})C_{44}}{2}}$	Shear modulus
α	$9.472 \times 10^{-6} + 2.062 \times 10^{-8}\theta - 8.934^{-12}\ \theta^2$	Thermal expansion coefficient (K^{-1})
b	2.51×10^{-7} mm	Burgers vector magnitude
$\dot{\gamma}_0^\alpha$	0.8 s^{-1}	Reference shear strain rate
ΔF_g	$1.4Gb^3$	Activation energy barrier
p	0.48	Shape parameter
q	1.8	Shape parameter
τ_0	5.1 MPa	Threshold slip resistance
$A^{\alpha\xi}$	0.1 if $\alpha \neq \xi$, else 1	Slip system interaction matrix
s_t^α	130 MPa	Thermal slip resistance
k_{ih}	0.036	Taylor hardening coefficient
k_M	0.00205	Dislocation multiplication constant
k_D	35	Dynamic recovery constant
$k_{\chi 1}$	1639	Backstress evolution parameters
$k_{\chi 2}$	250	
ρ_{SSD}^0	1.2×10^5 mm^{-2}	Initial SSD density

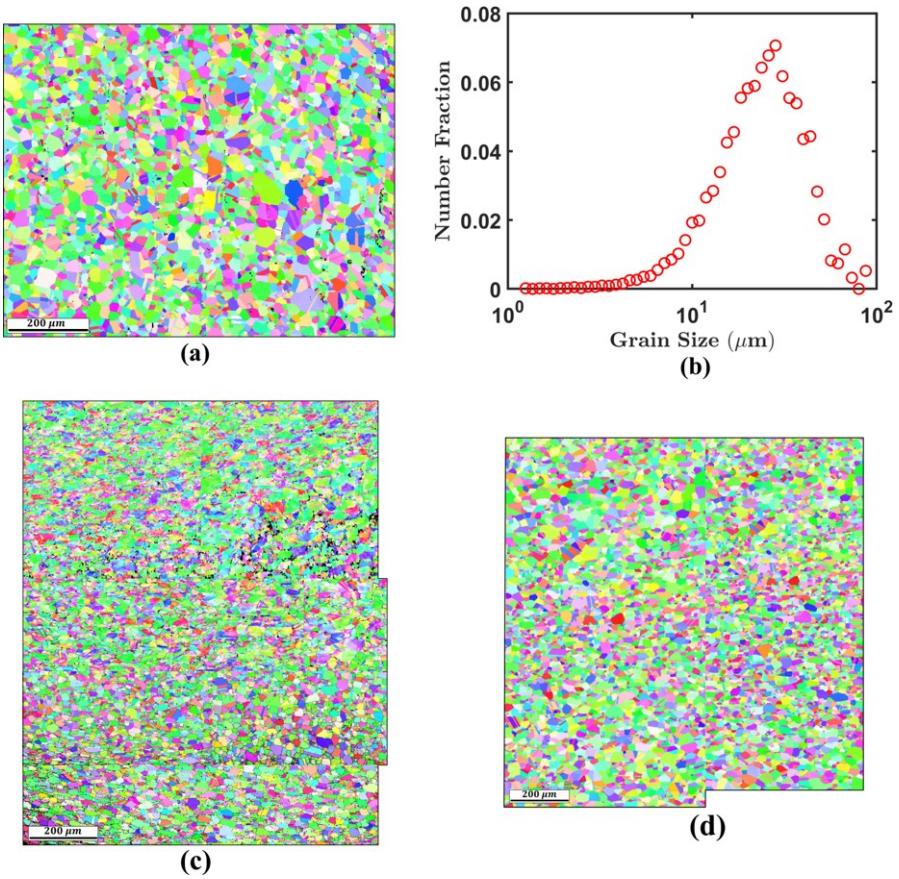

FIGURE 7.2: (a) Wide area Electron Backscatter Diffraction (EBSD) scan along the specimen cross-section to map the crystallographic texture of the specimen. (b) Grain size distribution presented in the logarithmic scale. Wide area EBSD scan along the cross-section of the specimen deformed in (c) uniaxial tension ($\varepsilon_{zz} = 0.25$) and (d) completely reverse cyclic loading (N=200). Note that multiple randomly chosen areas were mapped and stitched to obtain the microstructure presented in (c, d).

A 1000 grain cube-shaped simulation domain, with 27 elements per grain, was instantiated using an in-house algorithm. It has been shown previously that a simulation domain with 512 discrete grains/orientations (or more) can provide a representative response, both in terms of the macroscopic stress-strain response and the distribution of residual stress components developed during deformation (Patra and Tomé, 2024). Moreover, this domain size is comparable to those used in the literature (Chen et al., 2022a; Zhang et al., 2019). While adding more number of elements per grain may lead to the prediction of slightly compliant response, the computational costs are increased significantly. The 3D ensemble was meshed using hexahedral finite elements, with linear interpolation and full integration. The reduced texture, shown in Figure 7.1(b), was assigned randomly to the cube-shaped grains within the simulation domain. As stated in Section 7.2, the SS 316L was received in a standard mill annealed condition. In order to account for the prior material processing induced residual strains in the undeformed state, we have introduced initial residual strains in our crystal

plasticity finite element model (Musinski and McDowell, 2015). This is based on our experimental measurements, which indicate a non-negligible magnitude of residual strains for all grain families in the undeformed specimens (see Figures 7.8 and 7.10). To induce these residual strains, normal displacements were constrained on all surfaces of the simulation domain and the simulation domain was subjected to a quenching from $\theta_{ref} = 345\ K$ to the room temperature $\theta = 300\ K$, at a cooling rate of 45 K/s. This resulted in an average residual strain of 626.38 $\mu\varepsilon$. Following this, symmetric boundary conditions were applied and the simulation domain was deformed quasi-statically at a nominal strain rate of $10^{-3}\ s^{-1}$ to predict the tensile (see Figure 7.3(a,c)) and the cyclic stress-strain response for a strain amplitude of 0.01 up to 200 cycles (see Figure 7.3(b,d,e)).

SS 316L was assumed to have a Face Centered Cubic (FCC) austenite phase, with dislocation glide permitted on 12 possible octahedral $\{111\}< 110 >$ slip systems. The temperature dependent-anisotropic elastic constants, C_{11}, C_{12} and C_{44}, were derived from prior studies (Upadhyay et al., 2019). Parameters governing the shape of the enthalpy curve, p and q, the activation enthalpy for dislocation glide, ΔF_g, the reference shear strain rate, $\dot{\gamma}_0$ and thermal slip resistance, s_t, were chosen so as to obtain a best fit of the simulated yield stress with the experimental yield stress. These are in the range of values used for representative materials from previous studies (Patra et al., 2023a). Since the as-received material was obtained in a fully annealed condition, a low value of initial SSD density, $\rho_{SSD} = 1.2{\times}10^5\ mm^{-2}$ was used. Subsequently, the parameters governing substructure evolution and Taylor hardening, k_M, k_D and k_{ih} were calibrated by fitting the simulated mechanical response to its experimental counterpart during tensile loading. Finally, the backstress evolution parameters, $k^{\alpha}_{\chi 1}$ and $k^{\alpha}_{\chi 2}$, were calibrated to capture the experimentally observed cyclic loading response. The best-fit constitutive model parameters are given in Table 7.2. Note that the same set of model parameters were used to predict the response during tensile and cyclic deformation.

While we note that there is some under-prediction of the flow stress during tensile deformation for strains greater than $\varepsilon_{zz} = 0.1$, we have calibrated the model parameters such that they are able to predict the mechanical response under both tensile and cyclic deformation. This presents a challenge in partitioning the strengthening between the isotropic hardening and backstress hardening and the presented model predictions represent the best fit after several calibration attempts. It can be seen that the model predictions are representative for both tensile and cyclic deformation, since the predicted flow stress is within the error bars from three repeatable experiments performed for both cases (cf. Figure 7.3). Moreover, the model is also able to predict the stabilized hysteresis loop after $N = 100$ cycles (cf. Figure 7.3(d)).

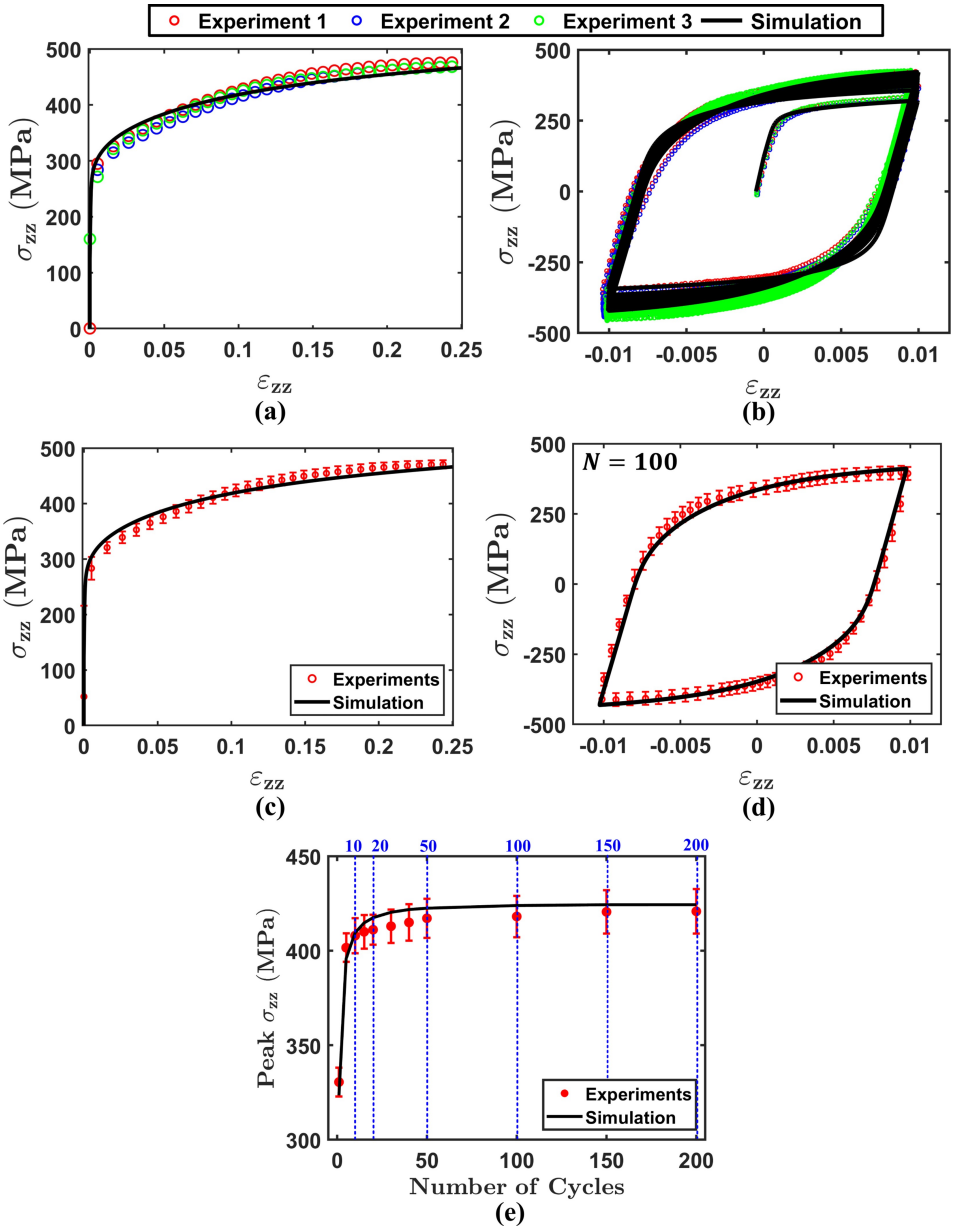

FIGURE 7.3: Comparison of the predicted stress-strain response with their experimental counterpart during (a, c) tensile, and (b, d) fully reversed cyclic loading. Three experiments were performed for both tensile and cyclic deformation and they are shown in (a) and (b). The same data is plotted in (c) and (d) in terms of the mean and the scatter from the three experiments for each case, along with the respective simulated response. (e) Comparison of the simulated peak stress with the experimental peak stress, σ_{zz}, at the end of the tensile part of loading cycle as a function of the number of cycles. The blue lines represent N=10, 20, 50, 100, 150 and 200 cycles, respectively. The scatter in the data is also plotted from the LCF experiments.

The model parameters presented in Table 7.2 are obtained by calibrating our crystal plasticity simulations with their tensile and cyclically loaded experimental counterparts (cf. Figure 7.3). Note that the same set of model parameters have been employed to predict the tensile and cyclic responses. Further, we present a validation of these model parameters by comparing the experimental and simulated mechanical response under plane strain compression. The plane strain compression experiments were performed in a Gleeble 3800^{TM} thermomechanical simulator.

The loading and boundary conditions employed in our simulations have been presented in Figure 7.4(a). The corresponding stress-strain behavior has been presented in Figure 7.4(b). The labels, Experiment 1, 2 and 3 refer to the experimental dataset generated from three different deformation experiments. Firstly, a sufficient reproducibility can be noted in our experiments. Further, as can be seen in Figure 7.4(b), our model has reasonably predicted the macroscopic experimental response and this validates the constitutive model parameters. Due to constraints in the sample size, the deformation was restricted up to a nominal strain of $|\varepsilon_{zz}| = 0.12$.

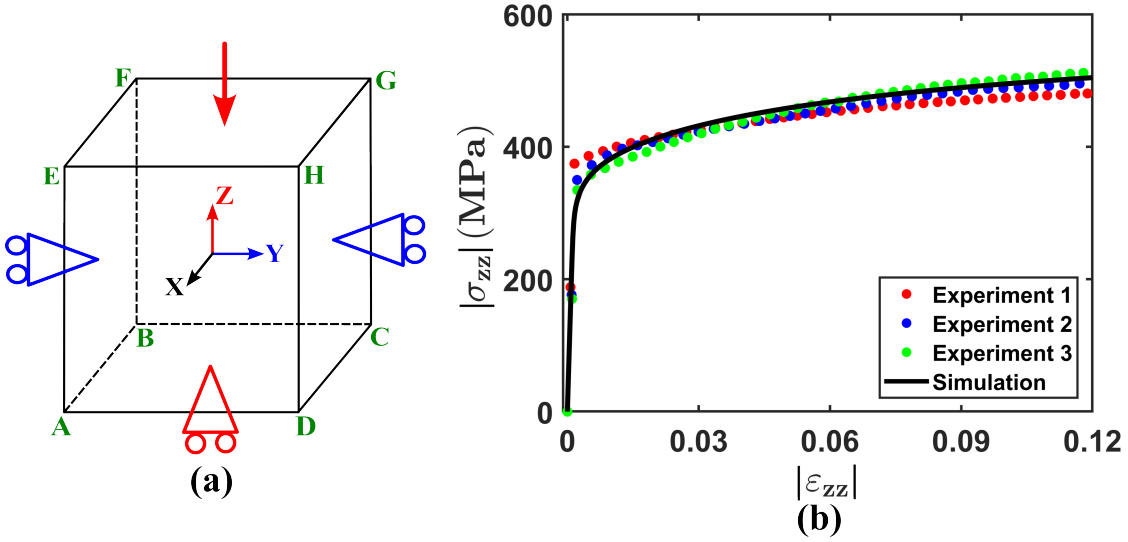

FIGURE 7.4: (a) Schematic of the loading and boundary conditions employed during plane strain compression. (b) The corresponding experimental and simulated mechanical response up to an applied strain of $|\varepsilon_{zz}| = 0.12$. The labels in (b), Experiment 1, 2 and 3, refer to the experimental dataset generated from three different deformation experiments.

Figure 7.5 shows the deformed textures after loading to $\varepsilon_{zz} = 0.25$ under tensile loading, and cyclic loading for $N = 200$ cycles at a strain amplitude of 0.01, in terms of the $\phi_2 = 0°$, 45° and 65° sections of the ODF from both experiments and simulations. The predicted deformed textures show a qualitative match with their experimental counterparts, for both tensile and cyclic loading. This is observed from the contour plots of the ODF sections, as well as from the intensity distribution along the α fibre. The tabulated volume fraction

of various texture components in Table 7.1(b) too indicates a reasonable match between the simulated and experimental textures. The discrepancies between the simulated and experimental crystallographic textures can be attributed to the relatively small simulation domain, with 1000 grains and 27 elements per grain. A larger simulation domain with a larger number of grains and finer mesh resolution may improve the prediction accuracy for micro-texture developments and orientation gradients during deformation. Further, non-local, strain gradient plasticity models may also be used for improved prediction of orientation gradients at the grain interfaces, as in Chapters 3 and 4. In the present work, we have resorted to a local crystal plasticity model, with limited number of grains and elements, in order to limit the computational costs for running simulations up to 200 cycles.

Both the experimental and the simulated line profiles in Figure 7.5 show that the texture intensity of the sample reduces after tensile and cyclic deformation. This is because the imposed deformation results in a gradual rotation of crystalline lattice (Verlinden et al., 2007; Nagarajan et al., 2021). The grain core rotates such that its slip systems are aligned favorably to the loading direction during tensile deformation. The grain mantle too undergoes a rotation, though at a lower rate, since it has to accommodate the constraints imposed by the neighboring grains (cf. Chapters 3 and 4). With increasing deformation, this lattice rotation leads to diffusing out of the hotspots noted in crystallographic texture of the undeformed specimen (cf. Figures 7.1(b)). While a similar phenomenon also occurs during cyclic deformation, its role in diffusing the texture is limited due to reversal of the grain rotations during loading in the opposite direction. Hence, it can be observed that the texture distribution for the specimen deformed under tensile loading appears diffused in comparison to that deformed under cyclic loading, for simulations as well as experiments.

The peak intensity ($f(g)$) along the α fibre (at $\phi_1 = 23°$ in Figure 7.5(a)), too, has reduced significantly in comparison to the undeformed texture (see Figure 7.1(b)) for the tensile case, as compared to its cyclic counterpart. Similarly, the near-Brass texture, which majorly dominates in the undeformed condition (cf. Figure 7.1 and Table 7.1(a)) is found to diffuse significantly during tensile deformation as opposed to its cyclic counterpart (cf. Figure 7.5 and Table 7.1(b)). This suggests that lattice rotation, contributing to the diffused texture, is more dominant in the material deformed under tensile loading, in comparison to the specimen subjected to cyclic loading. This point shall be further examined in Section 7.4.3, where these lattice rotations, quantified in terms of the intragranular orientation gradients, have been correlated to the lattice strain evolution under tensile and cyclic loading.

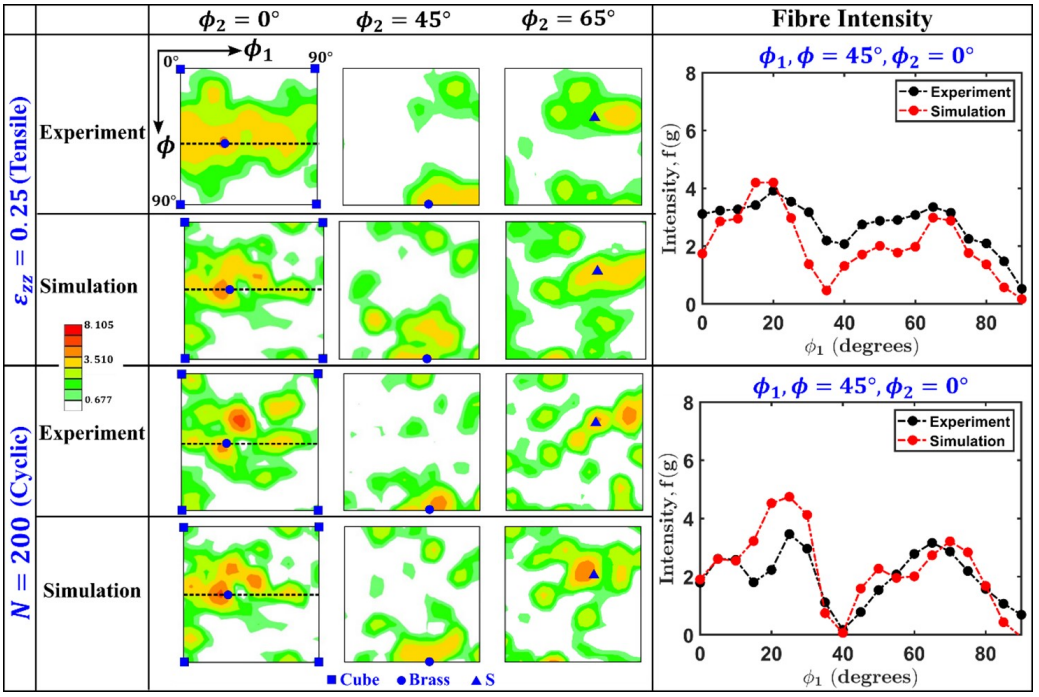

FIGURE 7.5: Comparison of the experimental and simulated Orientation Distribution Function (ODF) contours represented using $\phi_2 = 0°$, 45° and 65° ODF sections, for specimens deformed under tensile and cyclic loading. The corresponding intensity distribution along the α-fibre (see dotted line along the ϕ_1 axis for $\phi = 45°$, $\phi_2 = 0°$) has also been shown. The blue markers indicate some of the typical texture components in Face Centered Cubic (FCC) metals, the volume fractions of which have been tabulated in Table 7.1(b).

7.4.2 Evolution of Bulk Lattice Strains

We have performed ex-situ measurements of bulk lattice strains during the interrupted tensile and cyclic deformation. The specimen was first deformed in an ex-situ (tensile or cyclic) setup, followed by unloading and measurement of lattice strains using the d-sin$^2\psi$ technique in the XRD setup (Cullity, 1956; Noyan and Cohen, 2013). To ensure reliability in the measured data, all reported lattice strain values involved three measurements at different regions close to the center of the gauge for each deformation case. In order to account for the strain relaxation during the sample unloading and residual strain measurement, the simulated residual strains were recorded 1000 s after the removal of imposed deformation (by setting $\dot{\varepsilon} = 0$) for each of the cases. This methodology is followed for both tensile (cf. Figure 7.6(a)) and cyclic loading simulations (cf. Figure 7.6(b)).

Figure 7.6 shows the evolution of the stress and the longitudinal lattice strain on the (001) plane ($\vec{g}||LD$), as a function of the time after tensile deformation (Figure 7.6(a)), and cyclic deformation (Figure 7.6(b)). As can be seen, non-negligible relaxation of residual strains are observed after both tensile and cyclic deformation. The high value of residual stress

is reflective of residual state of strain. For example, the residual strain after relaxation is $\varepsilon_{001}^{LD} \sim 3500\ \mu\varepsilon$. The corresponding approximate residual stress can be estimated by multiplying this with the directional elastic modulus of ~ 100 GPa, which gives a residual stress of ~ 400 MPa.

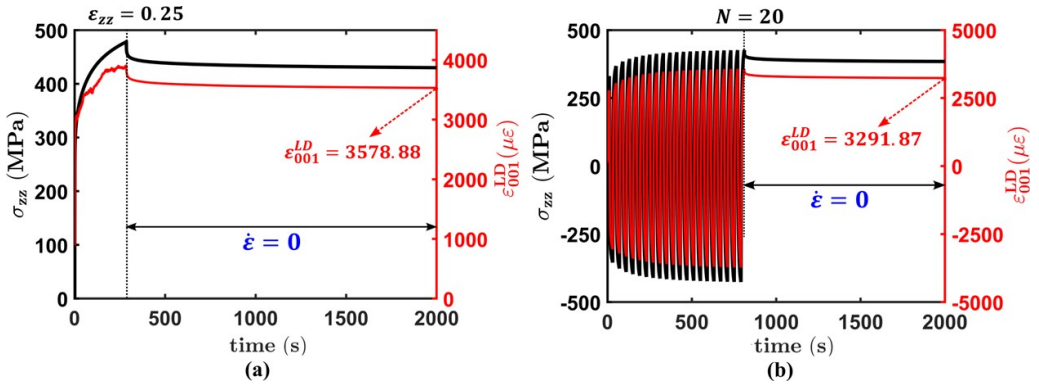

FIGURE 7.6: Predicted evolution of the longitudinal lattice strains (ε^{LD}) during relaxation after unloading for (a) tensile and (b) cyclic deformation.

Further, single crystal simulations have also been performed to verify the model's ability to predict (hkl) lattice strains. Figure 7.7(a) shows the predicted stress-strain response from three single crystal simulations oriented for tensile deformation along $< 001 >$, $< 011 >$ and $< 111 >$ directions. The corresponding lattice strains, ε_{001}, ε_{011}, ε_{111}, for a scattering vector parallel to the loading direction have been shown in Figure 7.7(b). A comparison of the predicted elastic modulii, which is obtained from the slopes of the curves in Figure 7.7(b), with the corresponding analytical values has been summarized in Table 7.3.

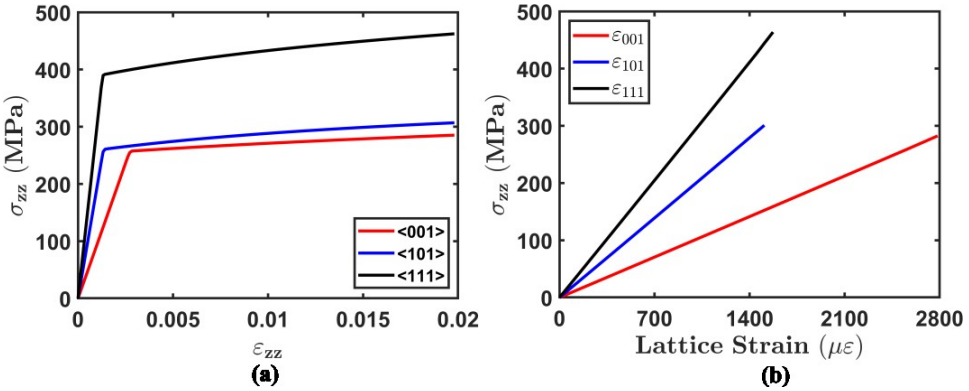

FIGURE 7.7: Prediction of (a) stress-strain response, and (b) lattice strains for single crystals oriented for tensile deformation along $< 001 >$, $< 011 >$ and $< 111 >$ directions up to an applied strain of $\varepsilon = 0.02$.

A comparison of the experimental and simulated lattice strain evolution is shown as a function of the imposed tensile strain, ε_{zz}, for the (111) family in Figure 7.8(a), (001) family in Figure 7.8(b), (101) in Figure 7.8(c), and (311) family of planes in Figure 7.8(d).

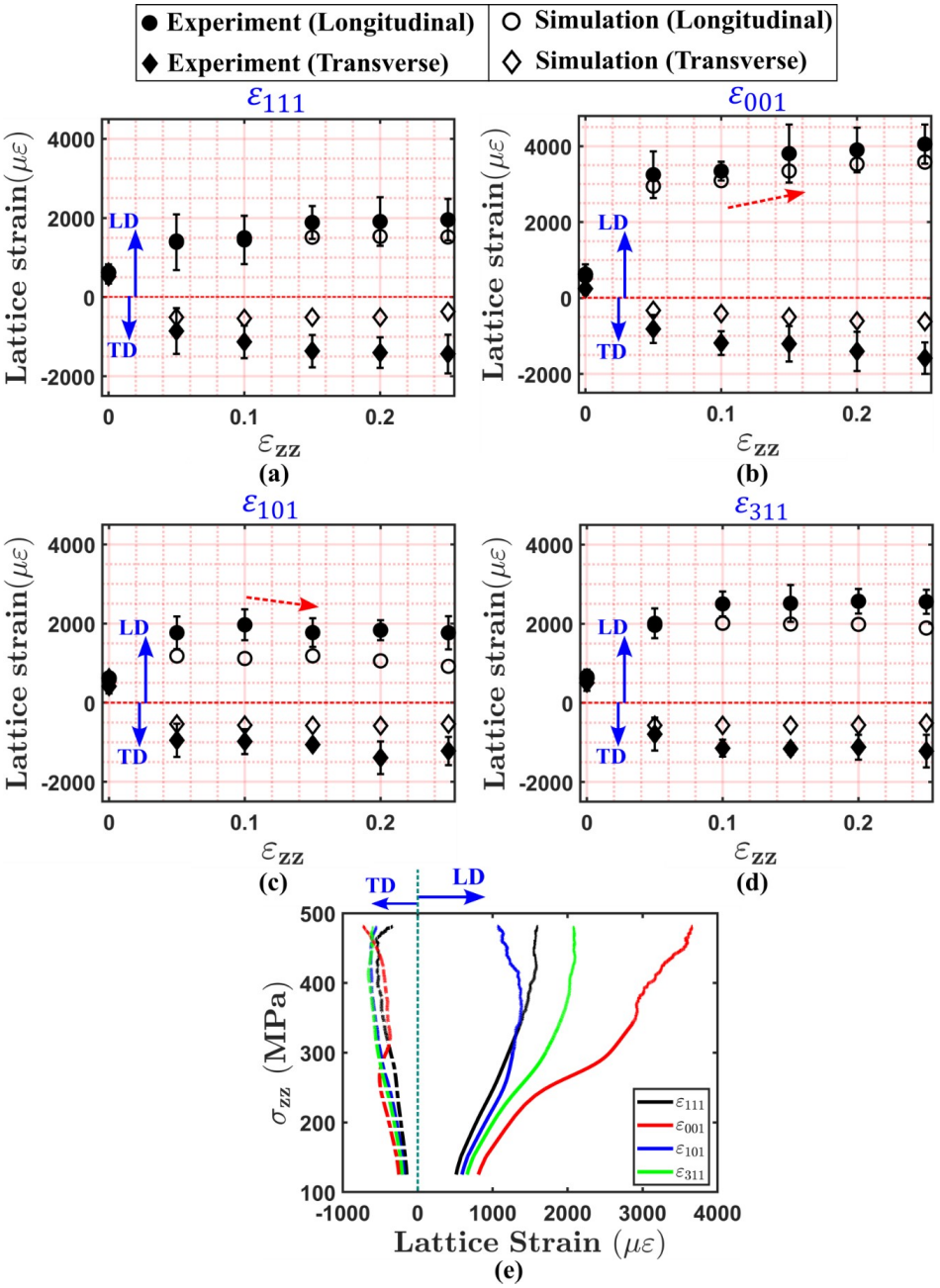

FIGURE 7.8: Evolution of the bulk lattice strains during tensile loading for the (a) (111), (b) (001), (c) (101) and (d) (311) family of planes as a function of the nominal strains along the loading direction, ε_{zz}. The arrows highlight lattice strain relaxations noted on the (101) planes and corresponding load transfer to the (001) planes. (e) Evolution of simulated bulk lattice strains as a function of the true stress along the loading direction, σ_{zz}.

TABLE 7.3: Comparison of the single crystal elastic modulus, E (in GPa), obtained from simulations and analytical calculations.

Crystal Orientation	Simulation	Analytical
$< 001 >$	100.097	93.80
$< 101 >$	197.520	193.21
$< 111 >$	295.346	293.97

Strain components parallel to the loading direction are marked as LD, while those along the transverse direction are marked as TD. As discussed earlier, initial residual strains were introduced in the simulations to induce residual strains comparable to the experimentally measured values prior to deformation (cf. Section 7.3). The simulated evolution of bulk lattice strains (without relaxation) as a function of the true stress along the loading direction, σ_{zz}, is also shown in Figure 7.8(e).

As reported in the literature (Lorentzen et al., 2002; Brown et al., 2017; Upadhyay et al., 2019), the elastically compliant (001) grains accommodate the maximum elastic strains. During the initial stages of deformation, this is followed by the (311), (101) and the (111) family of grains in the increasing order of elastic stiffness, the latter being the stiffest orientation and hence carrying the least amount of lattice strain. The simulated strains show a qualitative match with the experimental lattice strains along the LD. However, the simulations under predict the lattice strain along the TD for all grain families. The reader is referred to the subsequent paragraphs for a detailed discussion on the mismatch in the magnitudes of experimental and simulated transverse lattice strains.

As can be seen in Figures 7.8 and 7.10, the simulated transverse lattice strains are generally underpredicted in comparison to their experimental counterparts, though there is a qualitative match. Such a difference has been primarily attributed to the dispersion of the transverse scattering vector (Neil et al., 2010). Physically, this can be noted from Tables 7.4 and 7.5 (later in the Chapter), which present a lower ratio of the absolute mean to standard deviation, $|\mu|$/SD, for the transverse lattice strains, ε^{TD}, as compared to the longitudinal strains, ε^{LD}. This is due to a smaller number of material points satisfying the tolerance criterion given in Equation 7.14 for ε^{TD}, thus not contributing to the lattice strain estimation. We have plotted the number fraction of material points contributing to the longitudinal and transverse lattice strains for the various grain families with increasing tensile and cyclic deformation in Figure 7.9. It can be seen that the number fraction of material points contributing to ε^{TD} are generally lower for most of the grain families in comparison to ε^{LD}, thus leading to a quantitative inaccuracy in the prediction of ε^{TD}. Employing a

large number of grains within the simulation domain may improve the predictions of the transverse lattice strains, however with additional computational costs.

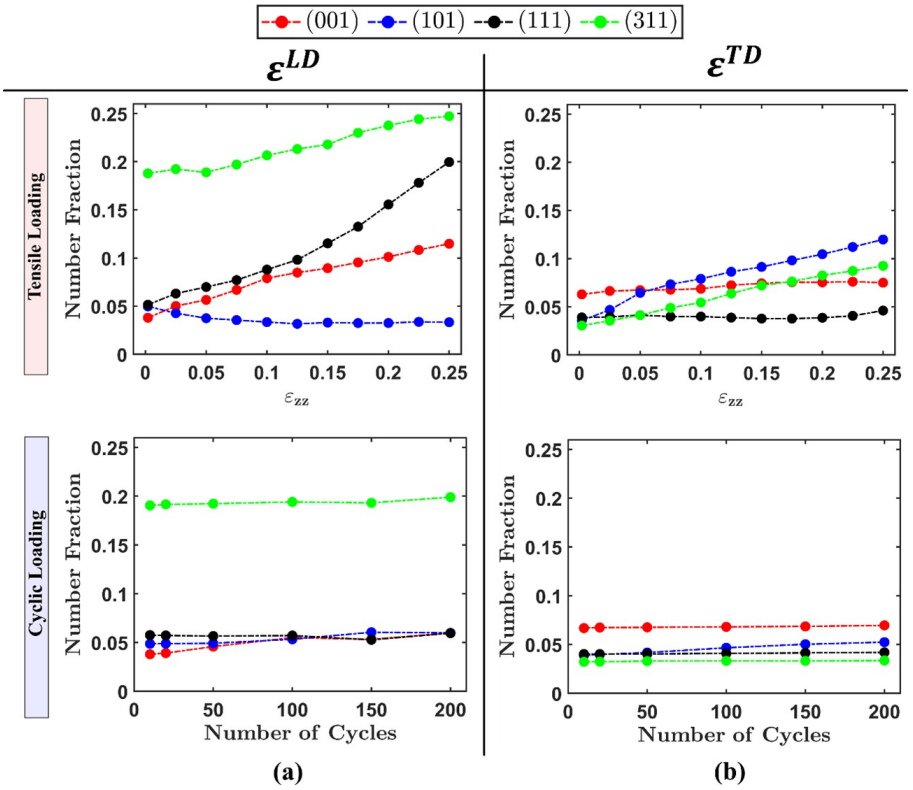

FIGURE 7.9: Evolution of the number fraction of material points contributing to the estimated (a) longitudinal, ε^{LD}, and (b) transverse, ε^{TD}, lattice strains during tensile and cyclic deformation.

A significant relaxation is observed in the longitudinal lattice strains for the (101) family of grains, ε^{LD}_{101} (see red arrow in Figure 7.8(c)). Such a phenomena is observed in both experiments and simulations, and has also been observed in earlier studies (Clausen et al., 1999; Brown et al., 2017). A relaxation in lattice strains is indicative of the fact that these grains have started deforming plastically, and hence, do not contribute further in accommodating the elastic deformation (Brown et al., 2017). The resulting load shed by the (101) family is accommodated by the (001) family of grains, which shows a concurrent increase in the longitudinal lattice strains (see red arrow in Figure 7.8(b)). This load transfer from the (101) to the (001) family can be clearly noted in Figure 7.8(e), which shows the evolution of the simulated bulk lattice strains as a function of the true stress and has also been reported in the literature (Kanjarla et al., 2012). Though Brown et al. (2017) have observed relaxation in the (111) grain family as well, we only observed a saturation in their magnitudes. Similarly, a saturation is observed in the ε^{LD}_{311} up to 0.2 imposed strain, following which a slight decrease in its magnitude can be observed. The transverse lattice strains, on the other hand, mostly indicate a saturation for the (101) and the (311) family.

A small relaxation is observed for the ε_{111}^{TD}, thus resulting in a corresponding hardening, though minimal, for the (001) grain family.

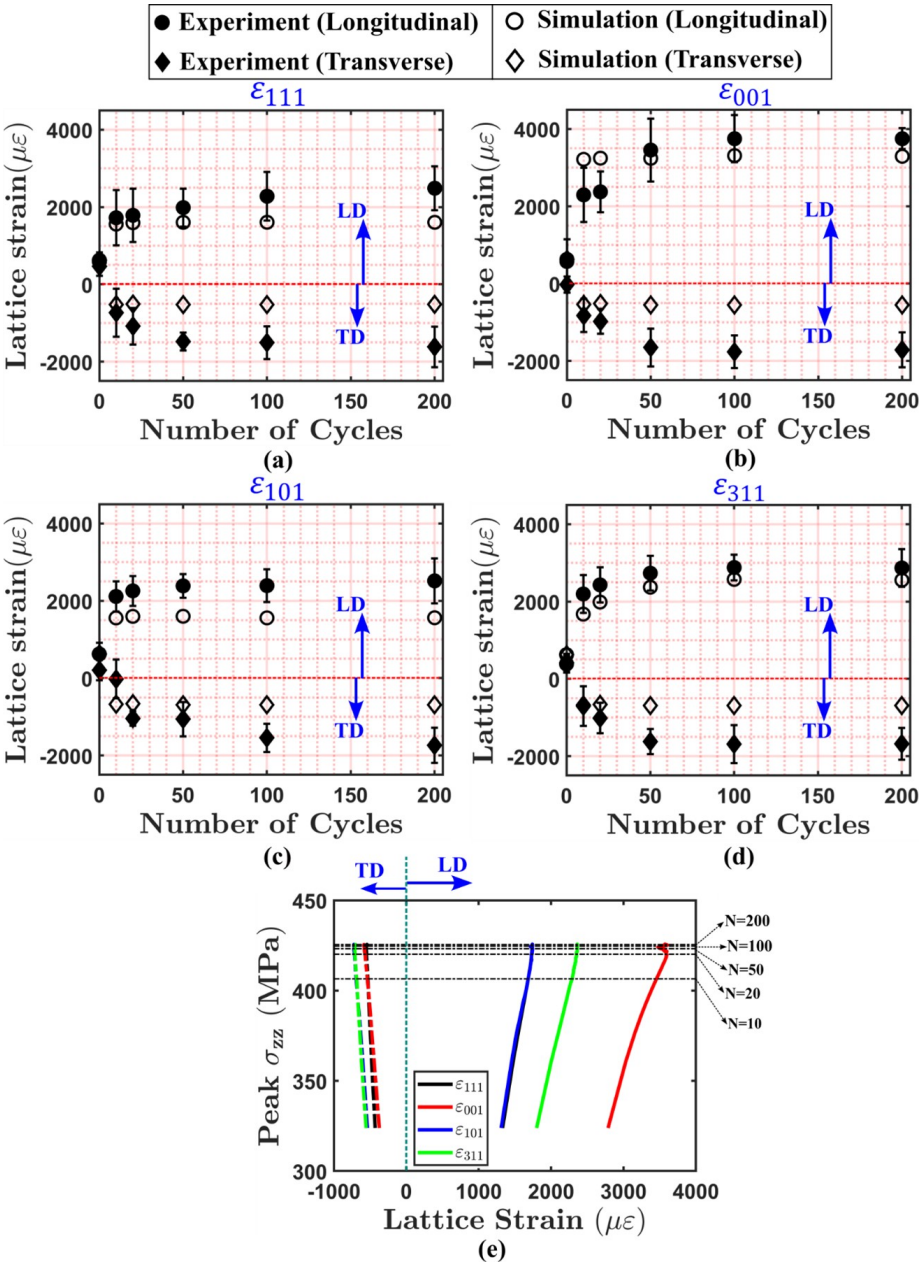

FIGURE 7.10: Evolution of the bulk lattice strains during cyclic loading for the (a) (111), (b) (001), (c) (101) and (d) (311) family of planes as a function of the number of cycles. (e) Evolution of the simulated bulk lattice strains in terms of peak stress as a function of the number of cycles during cyclic deformation.

Figure 7.10 presents a similar comparison of the lattice strain evolution with the number of cycles, N, for cyclic loading. The hierarchy in lattice strain evolution is followed for cyclic loading as well, i.e., $\varepsilon_{001}^{LD} > \varepsilon_{311}^{LD} > \varepsilon_{101}^{LD} > \varepsilon_{111}^{LD}$. Similar to the observations of Saleh et al. (2013) on TWIP steel, a saturation in the longitudinal lattice strains can be observed for all

grain families following the initial 10-20 cycles in both experiments and simulations. The trends in the simulated and experimental lattice strains are qualitatively similar. However, there are some quantitative differences, for example, at lower number of cycles for ε^{LD}_{001} and at higher number of cycles for ε^{LD}_{111}. This disparity is possibly because the shift in XRD-2θ peak profiles for the low angle peaks (43.02° for (111) and 50.01° for (001)) cannot be captured accurately for minute changes in the d-spacing (Cullity, 1956; Noyan and Cohen, 2013); a small variation in lattice strains may result in a pronounced shift in the XRD-2θ peaks at larger 2θ values (Cullity, 1956; Verlinden et al., 2007; Noyan and Cohen, 2013). However, a reasonable match is noted in the lattice strain magnitudes for the higher angle peaks, see ε^{LD}_{101} (Figure 7.10(c)) and ε^{LD}_{311} (Figure 7.10(d)). As with tensile deformation, the transverse strains during cyclic deformation are also under-predicted. Note however that except for ε^{LD}_{101}, the model predictions for LD strains are generally within the scatter bars of the experimental measurements. Further, as can be seen in Figure 7.10, the lattice strains exhibit a saturation for most of the grain families beyond 50 cycles (with the exception of (001) family) from both experiments and simulations. The macroscopic mechanical response presented in Figure 7.3(b) also shows a saturation beyond 50 cycles (cf. Figure 7.3(e) for the evolution of the peak stress as a function of the number of cycles). It may be expected that a saturation in the macroscopic response and the evolution of lattice strains would extend beyond 200 cycles, until the development of strain localizations or microcracks within certain grains/ grain families, which may cause a relaxation or decay in the lattice strains (Wang et al., 2003; Zheng et al., 2013).

There have been similar studies (Wang et al., 2003; Zheng et al., 2013) reporting a decay in the lattice strain magnitudes during cyclic loading of a stainless steel. The decay was further correlated to the cumulative slip and the Taylor factor evolution (Zheng et al., 2013). However, we only observe a saturation in the lattice strains with increasing N. Further, the transverse lattice strains also show a saturation in the magnitudes with increasing number of cycles, for the simulations as well as experiments. A non-negligible relaxation, followed by hardening can be seen around $N = 50 - 100$ cycles for the (001) grain family in Figure 7.10(e). This could possibly arise due to the development of strain localizations in a few (001) grains. The former would result in those grains deforming plastically, and hence not contributing to the bulk lattice strain estimation. Finally, the relatively low number of cycles during cyclic loading did not contribute to large-scale (unimodal) grain rotation (see Figure 7.5). This impeded the rotation of grains to more favourable orientations, inhibiting the activation of additional slip systems and preventing relaxation in certain lattice strains.

Note that the plastic strain amplitude, $\Delta\epsilon^p/2 \approx 0.008$, in our experiments and simulations. It might be difficult to draw an equivalence in the amount of imposed plastic deformation

between cyclic and tensile deformation. However, our objective is to compare qualitative trends between the different loading modes. Cyclic deformation was performed till there is a saturation in the macroscopic response (and presumably the dislocations substructure), which is also expected to reflect in the saturation of the residual strains. On the other hand, tensile deformation was only conducted till a nominal strain of 0.25, which is well below the uniform elongation strain and also does not result in the formation of deformation twins. Further, phase quantification using Rietveld refinement of the XRD-2θ peaks (Rietveld, 1969) showed that the volume fraction of the strain-induced martensite is negligible after $\varepsilon_{zz} = 0.25$ tensile strain and after $N = 200$ cycles.

In this Section, we focused on the evolution of lattice strains on four specific (hkl) families, or, grains with specific hkl plane normals. The subsequent Section attempts to explain the observed trends in lattice strains in terms of the orientation gradients and substructure evolution, which are representative of the plastic deformation exhibited by a given grain family.

7.4.3 Role of Misorientation Developments on the Relaxation of Residual Strains

Different misorientation measures exist in the literature to quantify the orientation gradients/lattice rotations developing during deformation (Schwartz et al., 2009; Wright et al., 2011; Thool et al., 2020). Here, we employ the Grain Reference Orientation Deviation (GROD), which quantifies the deviation of a pixel orientation with respect to that of the grain centroid, and is mathematically written as (Wright et al., 2011):

$$\text{GROD} = \Delta(\boldsymbol{g}_i, \boldsymbol{g}_{centroid}) \tag{7.15}$$

where, $\boldsymbol{g}_i$ and $\boldsymbol{g}_{centroid}$ denote the orientation tensor at the pixel i and the grain centroid, respectively.

Figure 7.11 (a,b) show the average experimental and simulated GROD within the (001), (101) and (111) grain families, i.e., grains with $<001>$, $<101>$ and $<111>$ axis parallel to the Loading Direction (LD), after tensile and cyclic deformation. Although the simulated average GROD values follow a similar trend as in the experiments, their magnitudes are under-predicted as compared to the experimental measurements. This can be attributed to the fact that the cube-shaped simulation domain used a coarser mesh with only 27 elements per grain, as compared to the 0.75 μm step size used during large-area EBSD measurements. However, the (101) grain family displays the highest GROD

magnitude during tensile deformation in both experiments and simulations. These are followed by the (001) and (111) grain families. Similar observations have also been reported by Lebensohn et al. (2008), who noted higher misorientation in the $< 110 >$ grains with increasing tensile deformation. They proposed that the interaction of the $< 110 >$ grains with subdomains of the surrounding (stable) $< 001 >$ and $< 111 >$ grains were responsible for such trends in the deformed microstructures. However, note that the experimental as well as simulated GROD magnitudes are relatively lower in the material subjected to cyclic deformation, as compared to tensile deformation. Similarly, as seen in Figure 7.5, the peak intensity along the α fibre ($\phi_1 \sim 20°$-$30°$) is significantly diffused after tensile deformation, in comparison to its cyclically deformed counterpart. Since the present study uses a strain amplitude of $\Delta\varepsilon/2 = 0.01$ for a relatively low number of cyclic reversals ($N = 200$), the experimental GROD values are generally lower in comparison to the monotonically loaded tensile specimens. Further, Hestroffer et al. (2022) noted that the grains rarely undergo complete reversals (in lattice rotation) during cyclic loading. However, similar to the present study, they did notice a narrower distribution of the grain average lattice rotation on reverse loading.

In summary, the experimental as well as simulated texture predictions show that grains of the (101) family develop large intragranular orientation gradients during tensile deformation as compared to cyclic deformation. Further, Figure 7.11 (c,d) and 7.11 (e,f) show the simulated SSD density, ρ_{SSD}, and the average effective backstress, $\bar{\chi}$, magnitudes in the grains belonging to the (001), (101) and (111) grain family, after tensile and cyclic deformation. These trends in the substructure variables, along with the GROD evolution show that the grains belonging to the (101) family undergo the maximum amount of plastic deformation under tensile deformation. These are followed by the grains of the (001) family, which although lower, do exhibit reasonable developments in the GROD and substructure variables, $\bar{\chi}$ and ρ_{SSD}. For the material subjected to cyclic deformation, the (001) and the (101) grain families exhibit nearly comparable magnitudes of GROD and ρ_{SSD}. The $\bar{\chi}$ however, shows slightly higher magnitude, by about 3 MPa, for the (001) family as compared to the (101) family. Finally, the (111) grain family shows the least amount of average GROD, $\bar{\chi}$ and ρ_{SSD} during tensile and cyclic deformation.

As noted in the literature, increasing (imposed) deformation results in the rotation of the crystal towards "softer" orientations (Dillamore et al., 1979). These lattice rotations generally occur from crystal orientations with less than 5 active slip systems, rotating them to plastically compliant "softer" orientations, with additional active slip systems. This enables the grain to accommodate higher plastic deformation. The large intragranular orientation gradients (GROD), effective backstress and SSD densities noted in the grains belonging to

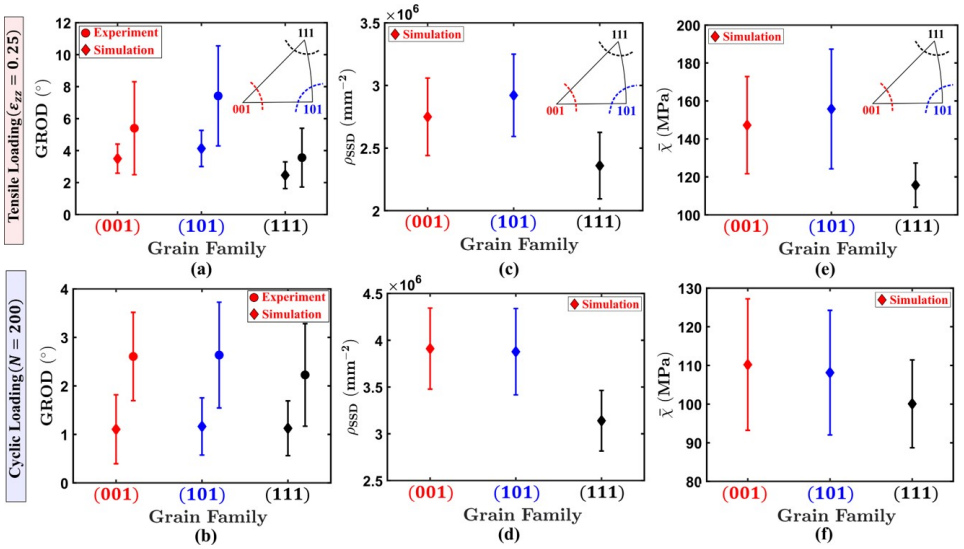

FIGURE 7.11: Average measures of (a,b) experimental and simulated Grain Reference Orientation Deviation (GROD), (c,d) simulated Statistically Stored Dislocation (SSD) density, ρ_{SSD}, and (e,f) simulated effective backstress, $\bar{\chi}$, on the (001), (101) and (111) family of grains, i.e., grains with $< 001 > ||LD$, $< 101 > ||LD$ and $< 111 > ||LD$. The top row represents the material subjected to tensile deformation ($\varepsilon_{zz} = 0.25$), while the bottom row represents the material subjected to cyclic deformation ($N = 200$).

the (101) family are indicative of this fact (cf. Figure 7.11). However, these plastically compliant grains do not contribute towards accommodating the elastic lattice distortion, thus exhibiting relaxations in lattice strains (Brown et al., 2017). The same was also observed in our measurements and predictions of bulk lattice strains. Moreover, the volume fraction of the (101) grain family is relatively high ($\sim 41\%$), which necessitates that these orientations deform plastically in order to accommodate the macroscopic shape change, while also leading to relaxations in the (elastic) lattice strains. For the cyclic deformation, the intragranular orientation gradients (GROD), $\bar{\chi}$ and ρ_{SSD} are not only lower, but nearly equivalent between the (001) and the (101) grain family. Thus no lattice strain relaxations are observed during cyclic deformation for the (101) grain family. The (001) grain family possesses at least 5 active slip systems, even in the undeformed configuration, and is thus plastically compliant. Hence, it does not require significant lattice rotations to accommodate the imposed deformation. Despite the development of intragranular orientation gradients (GROD) or $\bar{\chi}$, no lattice strain relaxations are observed for the (001) grains after tensile and cyclic deformation. Finally, the (111) grain family is less compliant both elastically and plastically (with low Schmid factor). Hence, they are found to have the lowest GROD, $\bar{\chi}$ and ρ_{SSD}, and also do not exhibit any relaxation in the bulk lattice strains.

Local misorientation developments can also be quantified in terms of the Kernel Average Misorientation (KAM) (Kocks et al., 2000; Wright et al., 2011, 2016). Comparison of the

average KAM between experiments and simulations for both tensile and cyclic deformation are presented in Figure 7.12. However, it should be noted that a relatively coarse mesh was used in the simulations (as compared to the pixel size used for experimental measurements) and a one-to-one comparison should be avoided. Nonetheless, the qualitative trends for KAM developments are similar those for the corresponding GROD observations from both experiments and simulations.

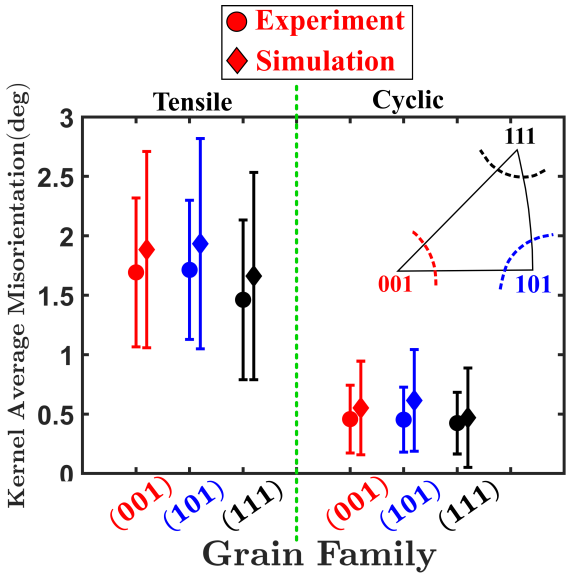

FIGURE 7.12: Average measures of the experimental and simulated Kernel Average Misorientation (KAM) for the (001), (101) and (111) family of grains, i.e., grains with $< 001 > ||LD$, $< 101 > ||LD$ and $< 111 > ||LD$.

Figure 7.13 shows the crystallographic orientation of the simulated material points belonging to the (001), (101) and (111) grain families in an IPF, projected along the loading direction, prior to deformation, and after tensile and cyclic deformation simulations. This crystallographic orientation data is obtained from the material points belonging to the respective grain families in our simulation domain. Analogous to our observations in Figures 7.5 and 7.11(a,b), material points belonging to the (101) family exhibit significantly large lattice rotations, followed by those belonging to the (111) and the (001) family under tensile deformation (see Figure 7.13(b)). Such large lattice rotations are representative of heterogeneous plastic deformation to accommodate the imposed deformation. The lattice rotation also results in a large dispersion in the scattering vector, thus causing a number of material points to violate the tolerance criterion and not contribute to the given $< hkl >$ reflections (cf. Equation 7.11). This also contributes to the observed relaxations in lattice strains in Figure 7.8. As seen in Figure 7.13(c), the lattice rotations were found to be significantly lower subsequent to cyclic deformation. Hence no significant lattice strain relaxations were observed after cyclic deformation.

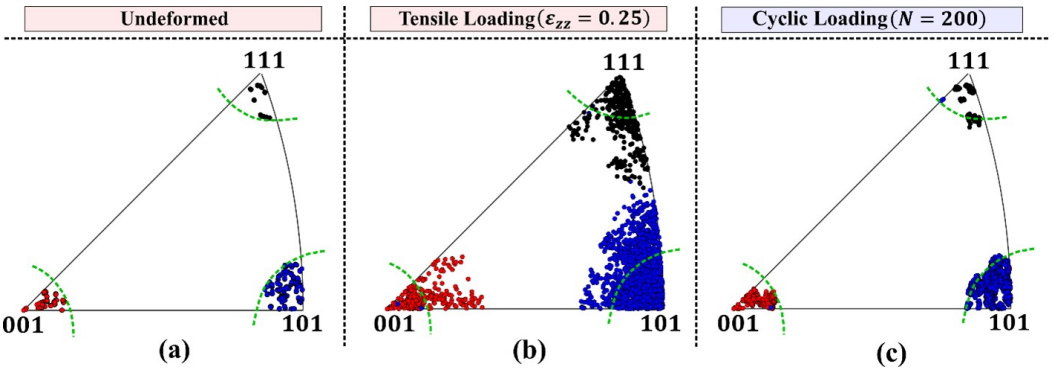

FIGURE 7.13: (a) Crystallographic orientation of material points belonging to the (001), (101) and (111) family in the undeformed simulation domain presented in an Inverse Pole Figure (IPF) projection (along the Loading Direction). Deformed orientations of the material points after (a) tensile deformation ($\varepsilon_{zz} = 0.25$), and (b) cyclic deformation ($N = 200$).

While we have studied the evolution of bulk lattice strains in the present section, the local microstructural features, such as the twin boundaries, neighboring grain orientation, triple junctions etc. may lead to localized plastic deformation and influence the development of local residual strains. To this end, the subsequent section focuses on exploring the role played by these local microstructural features on the evolution of local residual strains.

7.4.4 Local Residual Strains

In this Section, we report the development of local residual strains studied during tensile and cyclic deformation. While X-ray diffraction was used for the measurement of bulk residual strains in the previous sections, the local residual strains are determined using the HR-EBSD technique, which quantifies the shift in zone axes positions to estimate spatially resolved residual strains within a microstructure. This is performed from the measured EBSD patterns using the open source OpenXY tool (Fullwood, 2020) and is described in detail in Fullwood et al. (2015) and Chapter 6.

The microstructures derived from focused/small area EBSD scans were directly used as input for our Crystal Plasticity Finite Element (CPFE) simulations. These are first meshed using 3D hexahedral elements of size 1 μm and linear interpolation. Following Patra et al. (2023a), the simulation domain consists of a single element along the thickness or the out-of-plane direction, while noting that addition of elements along the out-of-plane direction may improve the accuracy of strain field predictions (Lim et al., 2014). The use of such a simulation setup can be justified since the HR-EBSD measurements are also based on the plane stress approximation, as the backscattered electrons get reflected from $\sim 20\, nm$ within the specimen surface (Wilkinson et al., 2006; Fullwood et al., 2015). Note that a much finer

mesh size has been used here as compared to the bulk residual strain simulations, thus allowing us to capture spatial variations in the development of residual strains. Following previous studies (Chaudhary et al., 2023; Patra et al., 2023a), the boundary conditions, as shown in Figure 7.14, were used in the present simulations. Displacements normal to the respective directions were constrained for the left, back and bottom faces, while fully constraining the corner common to these three faces. As shown in Figure 7.14, displacement controlled loading was applied at a nominal strain rate of 10^{-3} s^{-1} along the z-direction for both tensile and cyclic deformation. The front face was kept traction free to simulate a plane stress condition, as is also assumed in the experimental HR-EBSD residual strain calculations. Given the finer mesh, these simulations are more computationally intensive as compared to the bulk simulations. Hence, tensile deformation was only performed till an applied strain of 0.1, while the cyclic deformation was performed for 20 loading cycles at a strain amplitude of 0.01.

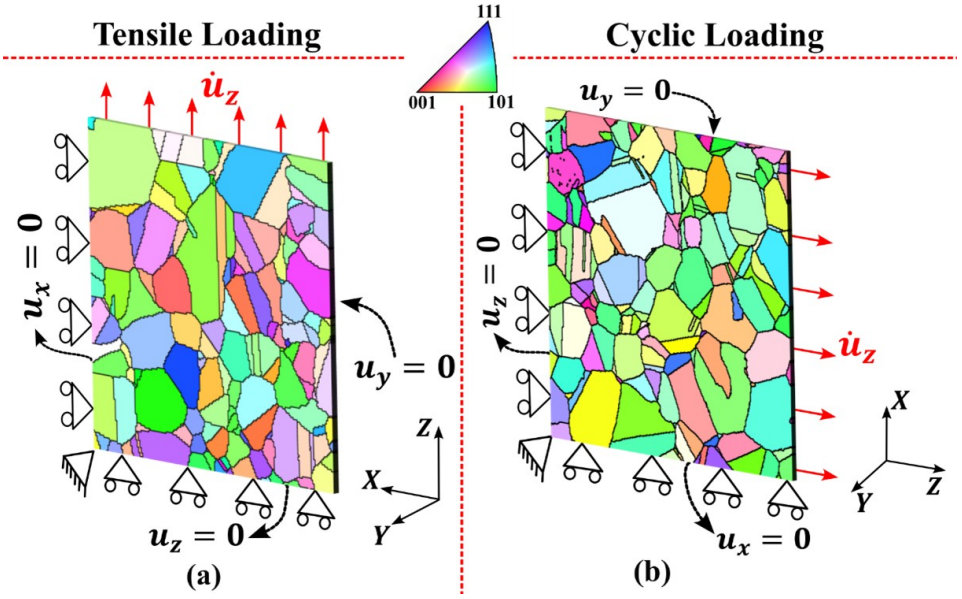

FIGURE 7.14: Schematic of the EBSD simulation setup and boundary conditions employed for studying the development of local residual strains under (a) tensile and (b) cyclic loading. The color scheme is representative of the crystallographic orientations shown in the Inverse Pole Figure (IPF) key.

Figure 7.15 shows the deformed microstructure at an applied tensile strain of 0.1 in terms of the contours of the experimental and simulated local residual strains (Figure 7.15(a,b)), elastic modulus along the LD (Figure 7.15(c)), experimental and simulated GROD (Figure 7.15(d,e)), experimental and simulated IPF maps (Figure 7.15(f,g)), PRIAS map to highlight the surface topography (Figure 7.15(h)), simulated ρ_{SSD} (Figure 7.15(i)) and simulated $\bar{\chi}$ (Figure 7.15(j)). Note that the predicted residual strains were plotted after relaxation for

1000 s as presented in Figure 7.6. These grains are a subset of the microstructure shown in Figure 7.14.

The predicted local strain contours along the LD, ε^{LD}, are qualitatively comparable with the HR-EBSD measurements (for example, see grains marked A, B and C in Figure 7.15). Based on the contour of the elastic modulus along the loading direction, these are also the elastically compliant grains that generally accommodate higher elastic strains. However, there are also elastically stiffer grains, for example, see grains marked D, E and F, which exhibit relatively high residual strains. This is due to the spatial arrangement of the grains, especially with respect to their neighbors, which induce higher residual strains in such grains. Specifically, grains which share boundaries with the annealing twins or other grains with relatively high plastic deformation, have higher residual strains, even if they are elastically stiffer. This indicates that the length-scales over which the local residual strains equilibrate are also governed by the local microstructural features, in addition to the crystallographic texture (or the elastic stiffness).

In order to highlight this, three grains marked 1-3 in Figure 7.15 are chosen such that their initial crystallographic orientations are similar, however with a difference in spatial arrangement with respect to their neighbors. The residual elastic strains obtained from isolated single crystal simulations for these three grains/orientations were compared with the respective grain-averaged local residual strains from the polycrystal simulation. This is shown in Figure 7.16. It can be seen that the evolution of the grain-averaged residual strains (cf. Figure 7.16(a)) are significantly different from the corresponding single crystal predictions (cf. Figure 7.16(b)) and are influenced by their neighbors. While grain 1 shows a relaxation in residual strains during the later stages of deformation (also see strain contours at the different stages of deformation in Figure 7.16(a)), grains 2 and 3 show an increase in residual strains with increasing ε_{zz}. This is primarily due to the development of strain localizations, manifested in the form of higher ρ_{SSD} and $\bar{\chi}$ in grain 1 (see Figure 7.15)) with increasing ε_{zz}. Such heterogeneties, especially near the grain boundaries and triple junctions, result in stress concentrations and necessitate that the grain deforms plastically, while also relaxing the contribution to the concurrent elastic deformation. These observations provide a clear indication that unlike the bulk lattice strains, the crystallographic orientation is not the sole factor governing the local residual strain development in polycrystalline microstructures.

A reasonable similarity can be observed between the CPFE predicted and experimental GROD measurements, see black markers in Figure 7.15 for example. Further, the simulated as well as experimental GROD maps show the development of large intragranular orientation gradients in the deformed microstructure, analogous to the high GROD values noted for the wide/large area EBSD scans in Figure 7.11(a). The regions in the vicinity

of grain boundaries often deform heterogeneously, to maintain the local continuity in the microstructure (Nagarajan et al., 2021). This results in a significant accumulation of GROD near the grain boundaries (Mishra et al., 2009). While there is a qualitative concurrence in GROD and residual strain developments between experiments and simulations, the model under-predicts the GROD hotspots in several regions. These predictions could be improved by using a strain gradient plasticity model, which is better suited for prediction of local orientation gradients (cf. Chapters 3 and 4). However, the computational costs associated with such models limit their use in the present case, where cyclic deformation over several cycles has to be performed. Further, it should also be noted that the model takes as input only the surface EBSD scan and tracks their deformation in comparison to the experiments, under a plane stress assumption. Sub-surface deformation, especially at grain boundaries and triple junctions are expected to influence the development of GROD hotspots in the experiments, which are not considered in the model.

A comparison of the GROD contours in Figure 7.15(d,e) with the IPF maps in Figure 7.15(f,g) shows that the (101) family of grains generally develop large orientation gradients. The localized heterogeneity leads to the activation of additional slip systems in this region, as evident from the secondary slip bands seen in the PRIAS image in Figure 7.15(h). This ultimately results in a large heterogeneity in the distribution of local strains, as seen in Figure 7.15(a,b). The relatively coarser mesh employed for the CPFE simulations fails to capture the development of slip bands within these grains. Nevertheless, our simulated strain contours compare qualitatively with the experimental measurements.

The PRIAS image in Figure 7.15(h), which is used to highlight the formation of slip bands, indicative of strain localizations, show that the grains demonstrating higher residual strains, for simulations as well as experiments, do not generally display significant slip bands. The grains with more slip bands do show higher ρ_{SSD} and $\bar{\chi}$, as expected (for example, see lower half of grain A and grain B). However, simple topography-based 2D observations using PRIAS images might not be a sufficient to comment on slip band formation, and more advanced surface profilometry techniques may be utilized for detailed analysis (Prakash et al., 2021).

Figure 7.17 presents an analysis identical to the one performed in Figure 7.15, for the microstructure subjected to cyclic deformation for $N = 20$ cycles (Figure 7.14(b)). Due to high computational costs, we have performed CPFE simulations to only $N = 20$ loading cycles. Given that a saturation in the macroscopic peak cyclic stress was observed after $\approx$20 loading cycles (cf. Figure 7.3, 7.10), the evolution of the local microstructure is also expected to saturate.

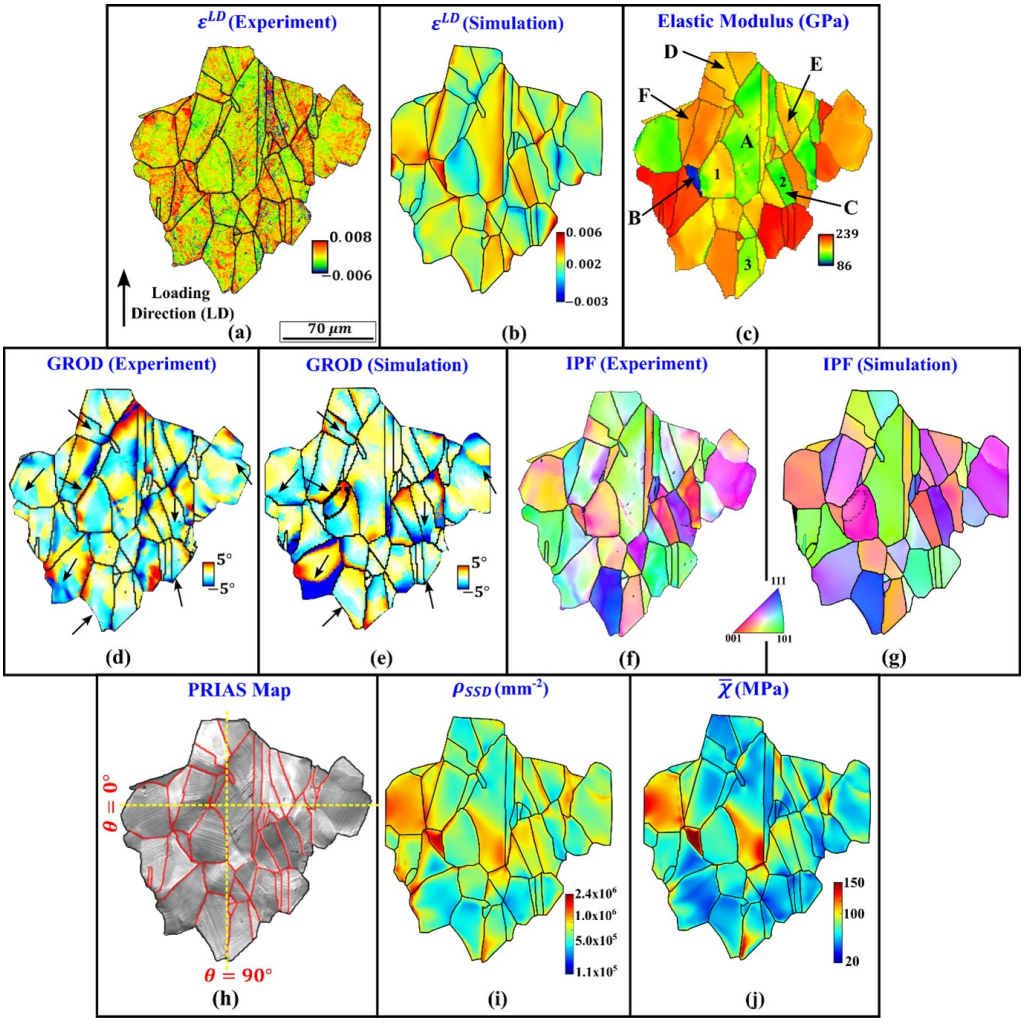

FIGURE 7.15: Deformation contours in the microstructure subjected to tensile deformation ($\varepsilon_{zz} = 0.1$), presented in terms of the (a,b) experimental and simulated local residual strain, ε^{LD} contours, (c) elastic modulus along the Loading Direction (LD), (d,e) experimental and simulated GROD contours, (f,g) experimental and simulated Inverse Pole Figure (IPF) maps, (h) PRIAS image, (i,j) simulated SSD density, ρ_{SSD}, and simulated effective backstress, $\bar{\chi}$, contours. The markers A-F highlight the grains showing higher local residual strains, in both experiments and simulations. The markers 1,2 and 3 denote grains whose (undeformed, at $\varepsilon_{zz} = 0$) orientations are used to study single crystal elastic strain response, see Figure 7.16.

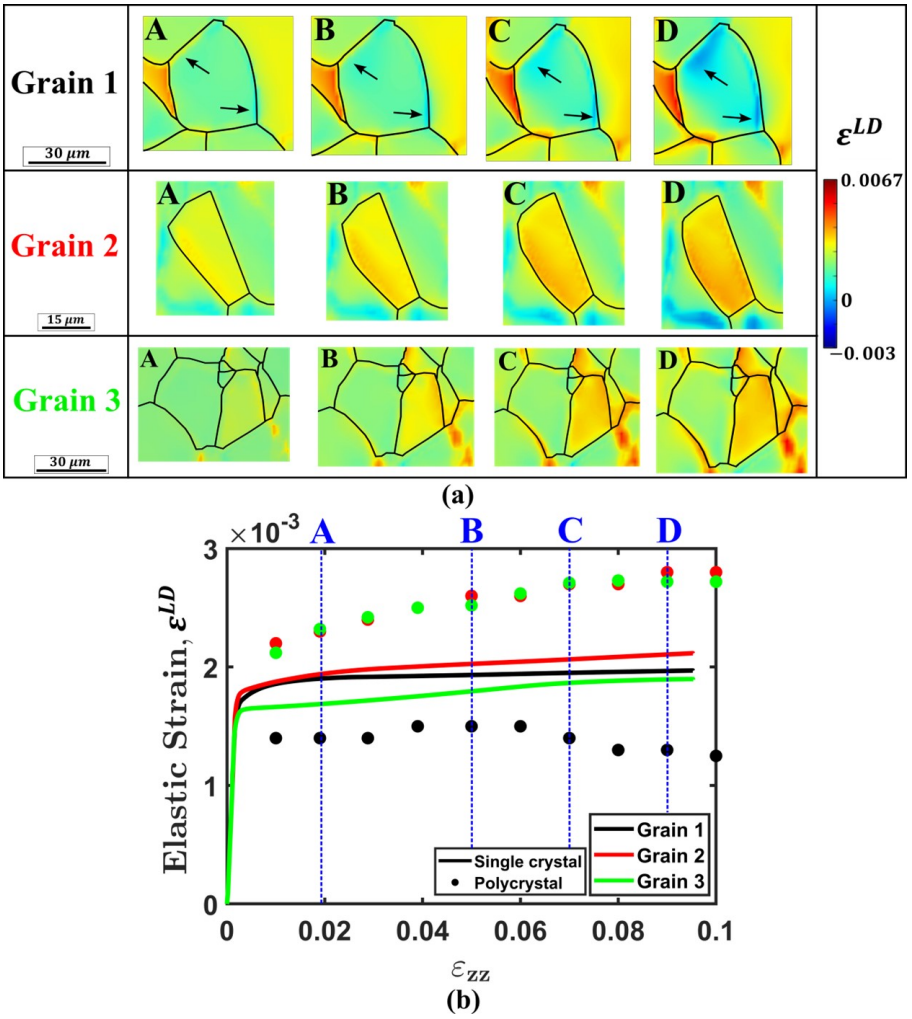

FIGURE 7.16: Contours showing the evolution of local residual strains, ε^{LD}, in the grains marked 1,2 and 3 in Figure 7.15(c). The stages of tensile deformation, A, B, C and D have been marked in (b), which shows the comparison of the residual elastic strains from isolated single crystal simulations (solid lines) with the grain-averaged local residual strains for these three grains from the polycrystal EBSD simulation in Figure 7.15.

Figures 7.17(a,b) show the HR-EBSD measured and CPFE predicted local strain, ε^{LD}, contours after $N = 20$ loading cycles. The grains marked A-F highlight regions showing a qualitative match in ε^{LD} between the simulations and experiments. As observed with the bulk lattice strain studies (cf. Figure 7.8 and 7.10), the elastically compliant grain families accommodate the maximum amount of residual strains (ε^{LD}), for example, see grains marked A,B and E in Figure 7.17(f). However, the spatial arrangement of the grains with respect to local microstructural features such as the twin boundaries (grains marked C and F in Figure 7.17) and triple junctions (grain marked E in Figure 7.17) also influences the development of residual strains.

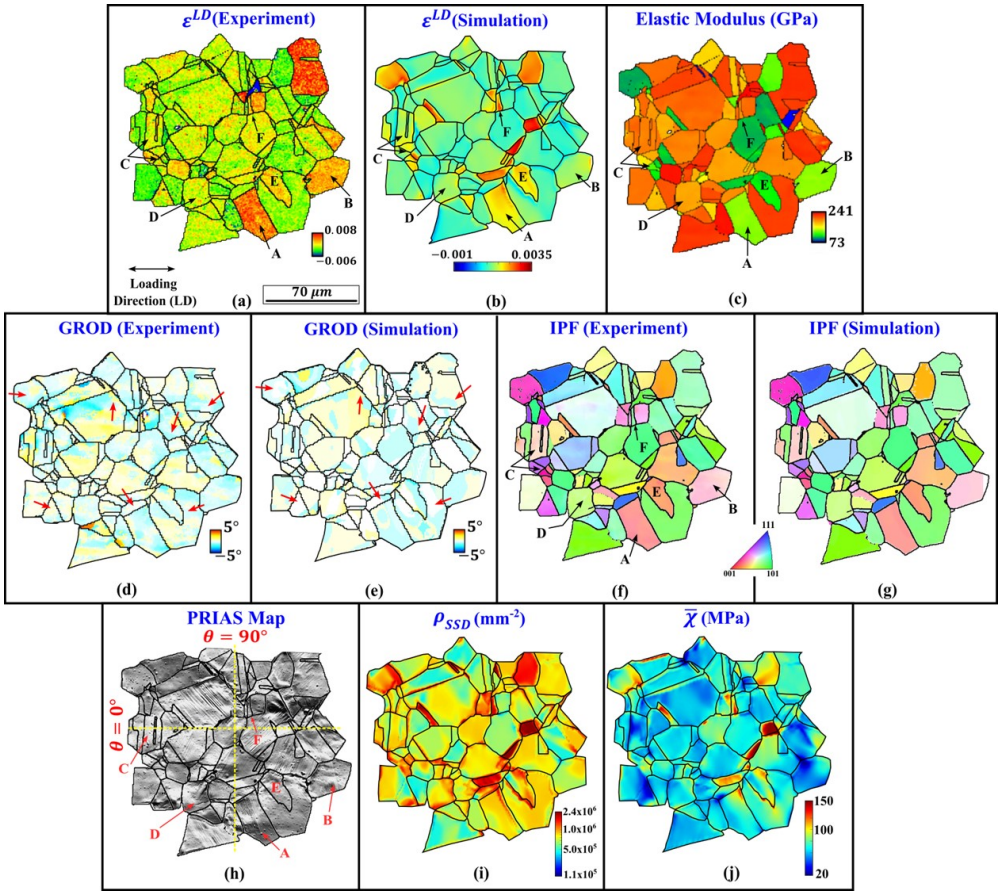

FIGURE 7.17: Deformation contours in the microstructure subjected to cyclic deformation for $N = 20$ cycles, presented in terms of the (a,b) experimental and simulated local residual strain, ε^{LD}, contours, (c) elastic modulus along the Loading Direction (LD), (d,e) experimental and simulated GROD contours, (f,g) experimental and simulated Inverse Pole Figure (IPF) maps, (h) PRIAS image, (i,j) simulated SSD density, ρ_{SSD}, and simulated effective backstress, $\bar{\chi}$, contours. The markers A-F highlight the grains showing higher local residual strains ε^{LD}, in both experiments and simulations.

The experimental and simulated GROD contours are shown in Figures 7.17(d,e). Misorientations develop in the vicinity of the grain and twin boundaries, for example see the red markers shown in Figure 7.17(d,e). However, the magnitude of these misorientations is considerably lower in comparison to the tensile counterparts, as also observed from the bulk measurements in Section 7.4.3. As reported by Hestroffer et al. (2022), the unloading does not result in a full reversal of the grain rotation. The present study also observed that such a non-zero lattice rotation ($\pm 1°$) exists in these microstructures (see GROD maps in Figure 7.17(d,e)) after $N = 20$ loading cycles. This is primarily because the tensile deformation results in a unimodal rotation of the grains, whereas the cyclic loading would lead to partial reversals in the grain rotations. Figure 7.17(f,g) shows the deformed experimental and simulated IPF map of the grain cluster. Unlike our observations in Figure 7.15(f) for the tensile deformation, the IPF map does not show large orientation gradients in the microstructure.

However, these microstructures do exhibit pronounced strain localizations, as seen from the ρ_{SSD} and $\bar{\chi}$ contours in Figures 7.17(i,j). In particular, such concentrations are evident in the regions with annealing twins. In contrast to tensile deformation, accumulation of ρ_{SSD} and $\bar{\chi}$ inside the twins is only observed during cyclic deformation. This could also potentially lead to failure initiation at the annealing twin boundaries as reported extensively in the literature (Chaudhary et al., 2023; Stinville et al., 2017).

Another important difference between the microstructures subjected to tensile and cyclic deformation is in the development of ρ_{SSD} (cf. Figures 7.15 and 7.17). The former shows lower magnitudes of ρ_{SSD} over its cyclic counterpart. This was observed in the bulk simulation predictions reported in Figure 7.11 as well. A similar observation was also noted by Jiang et al. (2015), who reported higher total dislocation density in their cyclically deformed specimens (after 2 cycles) over a monotonically strained specimen (after 10% deformation). Further, they noted that the difference between the two diminished with increasing number of cycles (Jiang et al., 2015). During cyclic deformation, the dislocations often undergo repetitive back-and-forth motion on the same set of slip systems. Since the lattice rotation is primarily limited to the minor under-reversals, large lattice rotations to favorably activate additional slip systems are generally absent in the initial stages of cyclic deformation (Hestroffer et al., 2022). This results in congestion of dislocations on only a few active slip systems and reduces the mean free path for the dislocation movement, thus increasing dislocation pileups (Benzerga et al., 2003). In our crystal plasticity model which has consideration for directional shear, these pileups are reflected in the form of strain localizations and higher dislocation density during cyclic deformation. In addition, the microstructure presented in Figure 7.17 has a relatively higher (annealing) twin fraction (fraction of $\Sigma 3$ boundaries: 0.391) in comparison to its tensile counterpart (fraction of $\Sigma 3$ boundaries: 0.273). The ρ_{SSD} accumulations are often noted in the vicinity of these regions, see Figure 7.17(i). Thus, the higher ρ_{SSD} during cyclic deformation may also be attributed to these local microstructural features

Finally, the results derived from the simulation domain presented in Figure 7.14 show that the elastically compliant grains accommodate the maximum elastic strains and vice-versa. Similarly, grains exhibiting large intragranular orientation gradients, indicative of significant plastic deformation, show relaxations in the local residual strains from essentially plane stress simulations (cf. Figures 7.15(a-e) and 7.16). Qualitatively, these results are similar to those obtained from their bulk, 3D counterparts (cf. Figures 7.8 and 7.10), with quantitative differences attributed to the local deformation characteristics due to neighboring grains, annealing twins, triple junctions, etc.

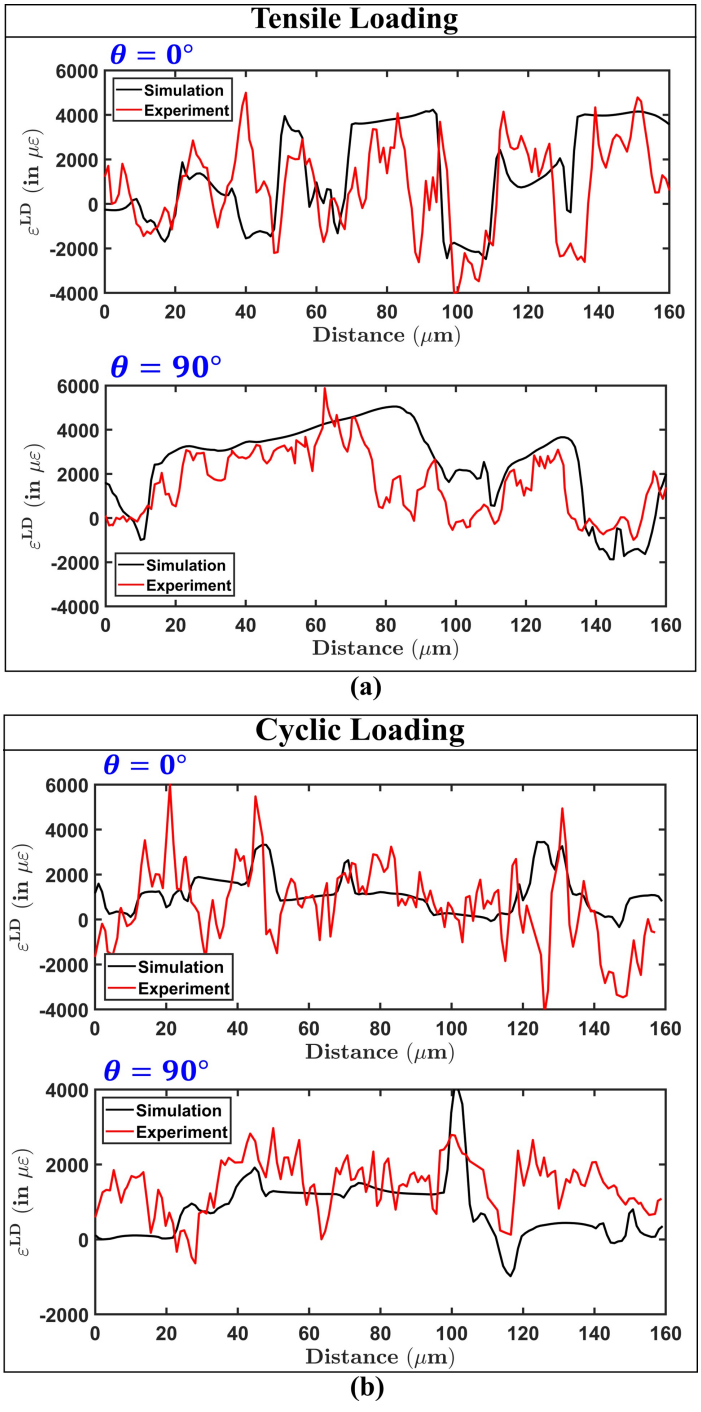

FIGURE 7.18: Comparison between the line profiles of the experimental and simulated residual strains, ε^{LD}, under (a,b) tensile and (c,d) cyclic loading along the different straight lines highlighted on the PRIAS images shown in Figure 7.15 (for tensile loading) and Figure 7.17 (for cyclic loading). For both microstructures, the labels, $\theta = 0°$ and $\theta = 90°$, denote the horizontal and vertical line profiles, respectively.

We have performed a comparison of the line profiles of local residual strains for the microstructures reported in Figures 7.15 and 7.17. Figure 7.18 presents a comparison of the simulated and measured local residual strains (ε^{LD}) for the deformed microstructures after tensile (Figure 7.18(a,b)) and cyclic deformation (Figure 7.18(c,d)). The labels $\theta = 0°$ and $\theta = 90°$ represent the horizontal and vertical lines marked on the PRIAS images shown in Figure 7.15(h) for tensile deformation and Figure 7.17(h) for cyclic deformation. A 3 point moving average was applied for the simulated as well as experimental datasets to smoothen the line profiles.

As can be seen, there is some noise in the experimental HR-EBSD measurements, while the CPFE predictions are relatively smoother. Possible contributions to the experimental noise were discussed in Chapter 6. Additionally, coarsening of the experimental dataset to attain a step size identical to the mesh size employed for our CPFE simulations ($\sim 1\ \mu m$) may have led to inaccurate representation of the strain localizations. Nevertheless, our simulations have reasonably predicted the hills and the valleys observed along the respective line profiles, especially for tensile deformation for both $\theta = 0°$ and $\theta = 90°$. For cyclic deformation, the predicted line profiles are qualitatively similar to the experimental measurements, while not capturing the local pixel-to-pixel variation in residual strains. These predictions could further be improved by using a finer mesh size, along with consideration for the strain gradients (cf. Chapters 3 and 4). Nonetheless, the qualitative comparison of these predictions from the tensile and cyclic deformation simulations, with their experimental counterparts, highlight the predictive capabilities of our modeling framework.

7.4.5 Hierarchy in the Development of Residual Strains

The results presented in Section 7.4.2 showed that the evolution of bulk lattice strains is sensitive to the crystallographic orientation. The development of local residual strains has been studied in Section 7.4.4, which also show a sensitivity to the grain's crystallographic orientation. However, their evolution also appears to be influenced by the local substructure. The statistics of the residual lattice strain data are further analyzed here to establish the orientation-dependent hierarchy (if any) from the bulk simulations for tensile deformation. The crystallographic longitudinal and transverse lattice strains at different stages of the tensile and cyclic deformation are fitted to Gaussian probability distribution functions. The Gaussian distribution plots for the longitudinal (hkl) resolved lattice strains are shown in Figure 7.19. In addition, the mean, μ, and the standard deviation, SD, of the probability distribution functions fitted to the longitudinal and transverse resolved lattice strains have been presented in Table 7.4 (for tensile loading) and Table 7.5 (for cyclic loading). A similar

analysis has also been reported by Kanjarla et al. (2012) from their spatially-resolved crystal plasticity simulations, however only for uniaxial tension.

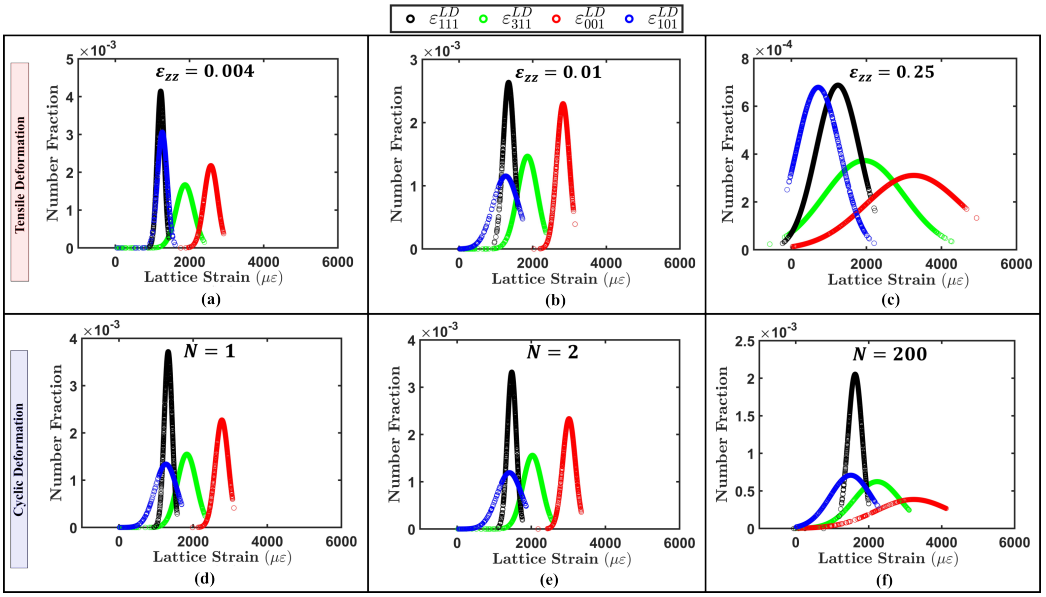

FIGURE 7.19: Statistical analysis of longitudinal lattice strains predicted from the bulk simulations fitted to Gaussian probability distribution functions after (a) $\varepsilon_{zz} = 0.004$, (b) $\varepsilon_{zz} = 0.01$, (c) $\varepsilon_{zz} = 0.25$ during tensile deformation, and (d) $N = 1$, (e) $N = 2$, and (f) $N = 200$ during cyclic deformation. The mean, μ, and the standard deviation, SD, corresponding to the probability distribution functions have been presented in Table 7.4 (for tensile loading) and Table 7.5 (for cyclic loading). The red, green, blue and black dots represent the (001), (311), (101) and (111) grain families, respectively.

TABLE 7.4: The mean, μ, and the standard deviation, SD, of the probability distribution functions fitted to the longitudinal and transverse resolved lattice strains for the specimen deformed under tensile loading.

	(hkl)	$\varepsilon_{zz} = 0.004$			$\varepsilon_{zz} = 0.01$			$\varepsilon_{zz} = 0.25$		
		μ	SD	$\lvert\mu\rvert$/SD	μ	SD	$\lvert\mu\rvert$/SD	μ	SD	$\lvert\mu\rvert$/SD
Longitudinal	**(111)**	1213.2	96.3	12.60	1344.6	151.3	8.88	1395.5	651.8	2.14
	(001)	2575.6	183.4	14.04	2823.8	173.4	16.28	3261.2	1283.6	2.54
	(101)	1284.1	130.2	9.85	1278.9	345.7	3.69	714.6	587.4	1.22
	(311)	1707.1	217.3	7.85	1857.3	271.8	6.83	1786.1	980.4	1.82
Transverse	**(111)**	−372.3	175.2	2.12	−424.7	206.8	2.05	−253.29	295.88	0.85
	(001)	−395.9	381.9	1.03	−353.1	440.2	0.80	−572.95	781.02	0.73
	(101)	−497.5	232.2	2.14	−537.9	270.6	1.98	−467.59	477.34	0.97
	(311)	−530.3	291.8	1.81	−563.3	374.8	1.50	−448.05	635.58	0.70

TABLE 7.5: The mean, μ, and the standard deviation, SD, of the probability distribution functions fitted to the longitudinal and transverse resolved lattice strains for the specimen deformed under cyclic loading.

	(hkl)	$N = 1$			$N = 2$			$N = 200$		
		μ	SD	$\lvert\mu\rvert$/SD	μ	SD	$\lvert\mu\rvert$/SD	μ	SD	$\lvert\mu\rvert$/SD
Longitudinal	**(111)**	1326.7	107.3	12.36	1473.4	120.2	12.25	1627.1	194.3	8.37
	(001)	2774.8	175.5	15.81	3017.3	170.8	17.66	3231.9	1032.1	3.13
	(101)	1265.8	297.7	4.25	1410.6	334.5	4.21	1507.2	563.1	2.67
	(311)	1829.7	257.3	7.11	2030.4	255.7	7.94	2231.1	639.6	3.48
Transverse	**(111)**	−415.8	202.5	2.05	−466.8	216.9	2.15	−534.4	264.2	2.02
	(001)	−342.8	425.5	0.81	−408.3	425.4	0.95	−550.0	509.1	1.08
	(101)	−528.8	264.6	1.99	−592.9	286.9	2.06	−694.4	354.2	1.96
	(311)	−556.3	363.5	1.53	−616.2	355.7	1.73	−679.4	408.6	1.66

At any given stage, both the mean and the standard deviation of the lattice strain in the elastically compliant (001) grain family are higher as compared to the respective quantities for the other grain families during both tensile and cyclic deformation. Although lower in magnitude, the value of the predicted standard deviation of the longitudinal strain, ε_{001}, is qualitatively comparable to those reported from the neutron diffraction experiments during tensile deformation of a mildly-textured stainless steel by Kanjarla et al. (2012). They performed full field crystal plasticity simulations using the Fast Fourier Transform (FFT) method and also found that their simulated standard deviations of longitudinal lattice strains are lower than the experimental measurements (Kanjarla et al., 2012). Presumably, the predicted standard deviation may be higher if more number of elements are considered per grain. Nonetheless, these standard distributions of stresses/strains can be used to inform mean field crystal plasticity models, where the intragranular distribution of stresses are utilized (cf. Wang et al. (2017); Patra and Tomé (2024)).

Further, it can be seen that the ratio of the (absolute) mean to the standard deviation, $|\mu|$/SD, is significantly lower for the transverse lattice strains in comparison to their longitudinal counterparts, especially under large tensile or cyclic deformation (cf. Table 7.4, 7.5). This indicates that there is significant dispersion of the transverse scattering vector (Neil et al., 2010), resulting in poor prediction of the simulated lattice strains along the transverse direction; essentially there are very few material points satisfying the tolerance criterion in Equation 7.14 for the transverse direction.

As can be seen from the mean, μ, and the standard deviation, SD, values of the probability distribution functions presented in Table 7.4, the longitudinal lattice strains follow the hierarchy in the order: (001) $>$ (311) $>$ (101) $>$ (111) grain families immediately after the yield. At larger imposed deformations however, the hierarchy is in the order: (001) $>$ (311) $>$ (111) $>$ (101). This is also evident from the evolution of simulated lattice strains as a function of the true stress, σ_{zz}, shown in Figure 7.8(e). The alterations are a result of the relaxations noted in the (101) family with increasing tensile strains. On the other hand, the μ and SD values presented in Table 7.5 for cyclic loading follows a hierarchy in the order: (001) $>$ (311) $>$ (111) $\sim$ (101) from the end of the first loading cycle itself. The evolution of lattice strains during cyclic deformation presented in Figure 7.10(e) are also indicative that the lattice strain developments do not show any notable relaxation or strain redistribution between the grain families, with the exception of some deviation in the (001) family.

These observations indicate that there are two factors contributing to the development of longitudinal lattice strains: (a) elastic stiffness, and (b) grain rotation (due to plastic deformation). The elastic stiffness of the grain families are in the following order: $E_{(001)} <$

$E_{(311)} < E_{(101)} < E_{(111)}$. Generally, the stiffer grains are expected to accommodate lower residual strains and vice-versa. While this expected hierarchy in the development of the longitudinal strains is observed during the initial stages of tensile deformation, when grain rotation is limited, the (101) grain family has lower residual strains than the (111) grain family during subsequent stages. This is driven by the grain rotation, as is also evident from the crystallographic orientation data reported earlier in Figure 7.13. Since the cyclic deformation was performed for relatively low number of cycles and because of the previously discussed strain reversals, no significant misorientation or textural softening is visible in the microstructure (see GROD contours in Figure 7.17). In the absence of grain rotation, the elastically stiffest (111) family showed similar longitudinal lattice strains as the (101) family of grains.

Statistics of data from the Electron Backscatter Diffraction (EBSD) simulations were also analyzed to study the hierarchy in local residual strain developments. While qualitative trends remain the same as in our bulk simulations (cf. Figure 7.20 and Table 7.6), there are some quantitative differences, which may be attributed to the limited statistics.

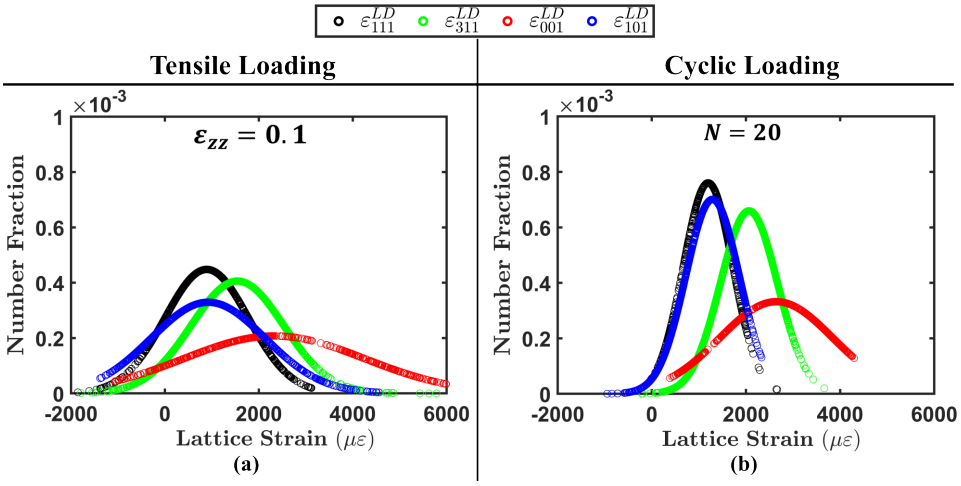

FIGURE 7.20: Statistical analysis of the simulated longitudinal local residual strains, ε^{LD}, predicted from the EBSD mesh simulations in Section 7.4.4, after (a) $\varepsilon_{zz} = 0.1$ during tensile deformation, and (b) $N = 20$ during cyclic deformation.

7.4.6 Effect of Crystallographic Texture on the Hierarchy of Lattice Strains

In order to explore the effect of crystallographic texture on the hierarchy of lattice strain developments, simulations have been performed with two different textures, one with a completely random texture and the other representative of a 90% cold reduction (Chowdhury et al., 2005). Uniaxial tension and cyclic deformation simulations are performed for both these textures. The simulation setup, boundary conditions and model parameters

TABLE 7.6: The mean, μ, and the standard deviation, SD, of the probability distribution functions fitted to the simulated longitudinal local residual strains (ε^{LD}) for the specimen deformed under (a) tensile ($\varepsilon_{zz} = 0.1$) and (b) cyclic loading ($N = 20$).

(a)

(hkl)	μ	SD	$\lvert\mu\rvert$/SD
(111)	890.13	889.13	1.01
(001)	2326.91	1921.88	1.21
(101)	899.44	1211.20	0.74
(311)	1544.40	982.71	1.57

(b)

(hkl)	μ	SD	$\lvert\mu\rvert$/SD
(111)	1196.90	524.66	2.28
(001)	2644.38	1201.13	2.20
(101)	1248.61	569.18	2.19
(311)	2064.74	604.83	3.41

are kept identical to those presented in Section 7.4.1. The input/starting crystallographic textures corresponding to these simulations domains have been represented in terms of the $\phi_2 = 0°$, 45° and 65° ODF sections in Figure 7.21(a).A quantitative description of crystallographic textures is also obtained as the volume fraction of ideal orientations and fibers. The anisotropy or texturing, in particular, is best represented by texture index (TI) (Van Houtte et al., 2005; Raveendra et al., 2011):

$$TI = \int f(g)^2 dg \tag{7.16}$$

where $f(g)$ represents the numerical ODF value in a small Euler space segment of dg. TI approaching 1 represents texture randomization, while $TI > 1$ provides relative texturing or anisotropy (Raveendra et al., 2011). The experimental texture given in Figure 5.1 has a TI of 1.94, while the random texture has a TI of 1.23 and the rolled texture has a TI of 3.04.

The mechanical response under tensile and cyclic deformation for these textures have been presented in Figures 7.21(b, c), along with ones from experimental texture in Figure 7.1(b). Further, the evolution of longitudinal lattice strains on the (001), (311), (101) and (111) grain families corresponding to these simulation domains have been presented in Figures 7.21(d, e). Since the trends in lattice strain developments did not differ qualitatively beyond $\varepsilon_{zz} = 0.2$ under tensile and N=10 in cyclic loading (cf. Figure 7.8(e), 7.10(e)), we have performed simulations only till these respective deformations. As can be seen, the lattice strain predictions for the rolled texture is slightly lower at a given stress in comparison to its randomly textured counterpart, which in turn is similar to the mildly textured material

presented earlier in Figure 7.1(b), during both tensile and cyclic deformation. More importantly, a lattice strain hierarchy similar to the one noted in Tables 7.4 and 7.5 is observed for all textures. This important observation suggests that while their relative magnitudes may differ based on the input volume fractions of idealized orientations, the hierarchy in residual strain developments with respect to different grain families are not influenced by the initial texture of the microstructure. As discussed earlier, the role of neighboring grain orientations on the local residual strains has been studied previously (Abdolvand et al., 2018; Thool et al., 2020; Louca et al., 2024). However, our results indicate that the role of neighboring grain orientations on the overall hierarchy of the bulk lattice strain developments is limited; it may only alter the relative magnitudes, while not affecting their respective order.

7.4.7 Discussion

The present study focused on exploring the residual strains in different grain families within polycrystalline aggregates. Very often, the volume fraction of various texture components can be tailored to suit certain applications. To this end, the texture of a material typically develops or gets altered due to solidification, heat treatment, phase transformation and plastic deformation (Suwas and Ray, 2014). Solidification, for example, is associated with growth selection and texturing (Rappaz and Gandin, 1993; Suwas and Ray, 2014). Directionally solidified cubic metals typically display strong evidence of (001) texture, with grains having their $< 001 >$ axes parallel to the heat extraction direction (Suwas and Ray, 2014). On the other hand, axisymmetric deformation processes such as cold drawing typically display a typical double fiber texture composed of the (001) and (111) grain families (English and Chin, 1965). A range of material as well as deformation parameters (for e.g. Stacking Fault Energy (SFE), drawing speed) influence the intensity ratio between the two components (English and Chin, 1965; Verlinden et al., 2007). Similarly, uniaxially compressed FCC metals often manifest a texture dominated by the (101) grain family (Kumar and Dawson, 2000). Further examples on application of thermomechanical processing for control of crystallographic texture (and properties) range from obtaining strong ND$||< 111 >$ textures in Body Centered Cubic (BCC) car body steel for improved formability to balance between Cube and rolling texture components for earing control in FCC aluminum (Verlinden et al., 2007).

The inferences derived from the present study may be useful in combined tailoring of the texture and residual stress evolution in structural materials for desired anisotropic response. The fraction of the compliant (001) grains may be maximized via processing in applications where a compliant mechanical response is desired, for example, damping. Automotive engine

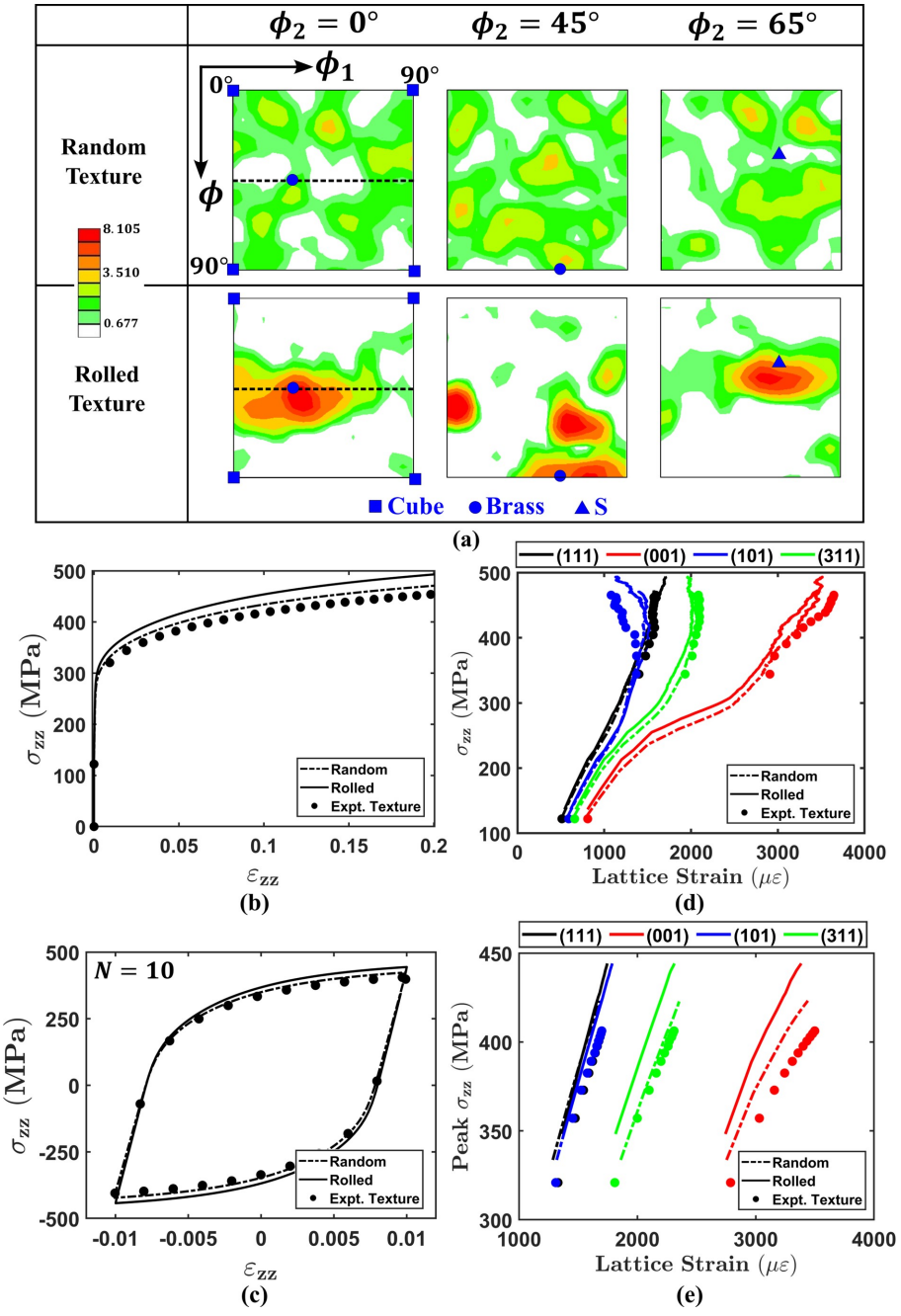

FIGURE 7.21: (a) Representative initial crystallographic texture of randomly oriented and rolled polycrystals presented in terms of the $\phi_2 = 0°$, 45° and 65° Orientation Distribution Function (ODF) sections. The blue markers highlight the typical texture components in Face Centered Cubic (FCC) metals. (b, c) Predicted mechanical response with random and rolled initial textures under tensile and cyclic deformation as compared with the simulated response from our experimental texture presented in Figure 7.1. The hysteresis loop after N=10 cycles is plotted for the latter. Evolution of the simulated longitudinal lattice strains as a function of increasing (d) true stress, σ_{zz}, during tensile loading and (e) peak stress during cyclic loading.

components subjected to thermomechanical loading require materials with high damping coefficients (Fontaine, 1980; Guesser and Martins, 2016; Pierce et al., 2019). While several other microstructural properties may also influence the damping behavior of steels, such as, carbon concentration, stacking faults, martensite fraction, etc. (Förster and Köster, 1939; Talonen and Hänninen, 2004), the damping coefficient is higher for (001) grains as compared to (101) or (111) grains (Manda et al., 2023). This is correlated with the compliant response and higher residual strains of the (001) family of grains observed in our work. There are some limited studies on the effect of pre-existing residual stresses on thermo-elastic damping (Vahdat and Rezazadeh, 2011; Manda et al., 2023). However, the textural dependence and its correlation with residual strains needs to be studied in detail in the future. Further, with regards to cyclic deformation, lower magnitude of axial stresses within the elastically compliant $< 100 >$ orientations have been attributed to be an important factor influencing the fatigue life of SS 316L with higher fraction of (100) grains (Blochwitz et al., 2008). On the other hand, rolling/forging may be used in structural materials to increase the fraction of (101) and (111) grains, where a stiffer material response is desired (Verlinden et al., 2007). It should be noted that rolling/forging may also result in an increase in the dislocation density, the effect of which on the residual strain developments have not been studied in our work.

The novel contribution of our work lies in the use of combined modeling and experiments to establish the factors governing the hierarchy in lattice strain developments. As discussed earlier in Section 7.1, there are several studies in the literature that study the lattice strains during tensile deformation. However, to the best of our knowledge, studies on the hierarchy of lattice/residual strain developments during cyclic deformation and their comparison with the tensile deformation counterparts are rather limited (cf. Jiang et al. (2015)). Moreover, the works that study lattice strain developments only during cyclic deformation, focus only on the initial few cycles (< 10) (Lorentzen et al., 2002; Wollmershauser et al., 2012; Saleh et al., 2013).

The modeling framework itself has several advantages over existing models in the literature. For example, our physically-based model accounts for both isotropic and kinematic hardening due to dislocation densities. Further, it should be noted that the same set of model parameters have been used for predicting tensile and cyclic deformation. Additionally, validation of the model has been performed by predicting the mechanical response under plane strain deformation. Evolution of bulk lattice strains has generally been studied using the mean-field crystal plasticity frameworks. This is primarily due to their computationally efficiency as compared to the full-field counterparts. However, a drawback of these frameworks lies in their inability to account for the local intragranular stresses and orientation

gradients. As presented in Figures 7.8-7.13 and 7.19, the lattice rotations during plastic deformation may alter the local residual strain developments and full field models are better suited for capturing them. To the best of our knowledge, the lattice strain predictions using full-field models have mostly been restricted to tensile deformation and very limited studies exist for cyclic deformation (for example, Zheng et al. (2013)). However, these existing studies have not explored the factors contributing to redistribution of lattice strains among different grain families during deformation, which may influence the hierarchy in the lattice strain developments. Finally, prediction of local residual strains during tensile and cyclic deformation, and their comparison with HR-EBSD counterparts is another novel contribution of our work. Studies correlating the substructural developments with the local residual strain measurements using HR-EBSD itself are fairly limited (Jiang et al., 2015; Kartal et al., 2012; Sedaghat and Abdolvand, 2021), and our modeling framework, which uses EBSD microstructures as input, can be used to predict the same.

In summary, the combined modeling and experimental methodology provides a novel, in-depth analysis on the hierarchy of residual strain developments during tensile and cyclic deformation.

7.5 Conclusions

We have presented a combined experimental and crystal plasticity modeling framework to study the development of bulk lattice (residual) strains and local residual strains during tensile and cyclic deformation. The bulk lattice strains were measured using X-Ray Diffraction, while the local residual strains were measured using HR-EBSD. A dislocation density-based crystal plasticity model, combined with a slip system-level Armstrong-Frederick type back-stress model for directional hardening, was developed and implemented in the ρ-CP crystal plasticity framework for predicting the residual strains during deformation. The model also has consideration for processing-induced residual strains prior to deformation. Based on the detailed analysis of the experimental and simulated results, following are the key conclusions that can be drawn from the present study:

1. The predicted longitudinal lattice strains are qualitatively comparable with the XRD measurements for both tensile and cyclic deformation, while the transverse lattice strains are marginally underpredicted. The predicted local residual strains are also qualitatively comparable with the HR-EBSD measurements, with evidence of localized deformation at annealing twins, especially during cyclic deformation.

2. There is relaxation in the longitudinal lattice strains for the (101) grain family, saturation for the (111) and (311), and increase for the (001) grain family during tensile deformation. In contrast, a saturation in the longitudinal lattice strain magnitudes was noted for all grain families during cyclic deformation.

3. The texturally dominant (101) grain family exhibited the largest intragranular orientation gradients, SSD density and backstress, thus implying that these grains deformed plastically to accommodate the imposed tensile deformation. In contrast, magnitudes of these substructure variables were relatively lower in the cyclically deformed microstructures.

4. The elastically and plastically stiffer (111) family exhibited a much lower magnitude of misorientation, SSD density and backstress, and did not show any relaxation in the lattice strains during tensile and cyclic deformation.

5. Based on the analysis of the predicted mean and standard deviation of the longitudinal residual strains from the bulk simulations, they follow the hierarchy in the following order for the different grain families: $(001) > (311) > (111) > (101)$ for tensile deformation, while $(001) > (311) > (111) \sim (101)$ for cyclic deformation.

6. The factors contributing to the observed hierarchy in the longitudinal residual strains are the elastic stiffness and the grain rotations (or lack thereof) for the respective grain families during tensile and cyclic deformation.

7. The trends in the hierarchy of the residual strain developments are not influenced by the initial texture of the polycrystalline aggregates.

Chapter 8

Summary and Conclusions

8.1 Summary of the Thesis

The thesis focused on developing experimentally informed mesoscale finite element frameworks, in order to understand the correlation between the backstress, solute segregation and residual strains in microstructures subjected to mechanical deformation. To achieve this objective, each of the aspects were systematically introduced in (or coupled to) a finite deformation plasticity framework, followed by its validation with the corresponding experimental or analytical dataset. Following this, the combined experimental and modeling framework was employed to examine various (practical) case studies, the outcomes of which would help researchers in developing microstructures manifesting enhanced mechanical properties.

The novel contributions of the thesis, in terms of model development are:

1. Taylor hardening based Strain Gradient Crystal Plasticity framework (SGCP) (see Chapter 3).
2. Extension of SGCP model to Strain Gradient J_2 Plasticity (SGP) framework, while accounting for the crystal orientation based anisotropy (see Chapter 5).
3. Coupled Phase Field (PF)-SGP framework, accounting for the orientation-based anisotropy, multi-grain interaction, anisotropic temperature-dependent elasticity, dislocation strengthening, solid solution strengthening, along with GND-induced directional backstress (see Chapter 5).

4. Lattice strain estimation module within a crystal plasticity framework, which uses a Kocks-Mecking model for dislocation evolution, a Taylor hardening model for dislocation strengthening and a slip system-level Armstrong-Frederick type backstress (see Chapter 7).

Similarly, the novel contributions of the thesis in terms of modifications to existing experimental methodologies are:

1. Establishing numerical convergence between the two (different) estimates of lattice distortion ($(\Delta\theta/\theta)$-sensitive versus $(\Delta d/d)$-sensitive residual strains) (see Chapter 6).
2. Validation of the experimentally estimated scaling factor through kinematical and dynamical pattern simulations of a virtually deformed cubic lattice (see Chapter 6).

8.2 Conclusions

Based on the work performed, the major conclusions from the different Chapters are summarized as follows:

Chapter 3: Study of Grain Boundary Orientation Gradients

Chapter 3 studied the microstructural factors contributing to the formation of Near Boundary Gradient Zones (NBGZs) in an Aluminum-Magnesium (Al-6 wt.% Mg) alloy using combined experiments and modeling. Following are the main conclusions:

- The normalized width of the NBGZs, $\frac{L_{NBGZ}}{D}$, was found to scale with the grain average Schmid factor, i.e., the (plastically) hard grains display relatively smaller NBGZs in comparison to the soft grains, as the deformation remains localized to a small region in the vicinity of grain boundaries.
- A possibly strong relationship was observed between the L_{NBGZ} and the mean grain size, especially for the (plastically) soft grains.

Chapter 4: Effect of Precipitates on the Development of Near Boundary Gradient Zones

Chapter 4 employed the SGCP framework to study the substructure evolution within the NBGZs at precipitate decorated grain boundaries in an Aluminum-Copper (Al-4 wt.% Cu) alloy subjected to compressive deformation. The hot-forged alloy displayed Al_2Cu precipitates at a majority of the grain boundaries. Following are the main conclusions:

- Our combined modeling and experimental approach showed that the orientation dependence of the NBGZ width is minimal for the (plastically) hard, Schmid factor$\leq$0.35, and intermediate, 0.35<Schmid factor$\leq$0.45, grains in the presence of Al_2Cu precipitates, i.e., the width of the normalized length of the NBGZs did not show a clear dependence on the grain-average Schmid factor. The (plastically) soft grains, Schmid factor$\geq$0.45, however, did exhibit a much wider NBGZ, especially in the presence of Al_2Cu precipitates.
- The Cu segregation however, did not alter or deviate the orientation-dependent behavior of the NBGZ width, for either of the grain types (soft, intermediate and hard).
- The presence of a harder, non-deforming second phase decorating the grain boundaries played a much larger role over the crystallographic orientation, in governing the deformation behavior within the NBGZs.

Chapter 5: Microstructural Factors Influencing the Tension-Compression Asymmetry of Rapidly Solidified Alloys

Chapter 5 focused on the development of a novel coupled PF-SGP framework to study the microstructural and mechanical aspects, in particular, the Tension-Compression (TC) asymmetry, frequently observed in rapidly solidified microstructures. Following are the main conclusions:

- The TC asymmetry, quantified in terms of the Strength Differential (SD) showed that the model predictions were able to sufficiently predict the previously reported experimental SDs (for Fe-Cr alloys).
- This behavior could be attributed to the negative component of backstress along the transverse direction and positive component of backstress along the longitudinal direction.
- The TC asymmetry was largely governed by the thermal distortion induced GND densities, and hence the backstresses, which translate the yield surface.

Chapter 6: Diffraction-Based Multiscale Residual Strain Measurements

A systematic comparison of the residual strains measured using the $\Delta d/d$ sensitive (micro-Laue XRD and Transmission Electron Microscope (TEM)-based Precession Electron Diffraction (PED)) and ($\Delta\theta/\theta$) sensitive (High Resolution-Electron Backscatter Diffraction (HR-EBSD) and Transmission Kikuchi Diffraction (HR-TKD)) was performed during progressive, albeit interrupted tensile tests, on a Body Centered Cubic (BCC) Interstitial Free (IF) steel. Following are the main conclusions:

- The measurements sensitive to changes in interplanar angle ($\Delta\theta/\theta$) provided quantitatively higher residual strain values than those sensitive to changes in interplanar spacing ($\Delta d/d$). Further, it was seen that there appears to be a consistent scaling factor between the two measurement types as residual strain increases.
- A scaling factor by which HR-EBSD underestimates ($\Delta d/d$)-based strain, compared to ($\Delta\theta/\theta$)-based strain, was derived from pattern simulations. Interestingly, this scaling factor was similar in magnitude to the difference between the micro-Laue XRD and HR-EBSD based measurements (~ 1.57).
- The scaling factor was further validated at sub-micron scales, by comparing and analyzing the residual strains measured from identical locations using HR-TKD and TEM-PED.

Chapter 7: Orientation-Dependent Residual Strains during Tensile and Cyclic Deformation

Chapter 7 modified an existing dislocation density based crystal plasticity solver, $\rho - CP$, to predict the evolution of bulk ($\Delta d/d$-sensitive) lattice and local ($\Delta\theta/\theta$-sensitive) residual strains during tensile and cyclic deformation of an austenitic stainless steel. Following are the main conclusions:

- The simulated predictions of longitudinal lattice strains were nearly identical to those obtained from our XRD-based d-sin$^2\psi$ measurements. The transverse lattice strains were marginally underpredicted, albeit, the aggregate trends were similar to their experimental counterparts. Similarly, the predicted trends in local residual strains were qualitatively identical to those of their experimental HR-EBSD based counterparts.
- The lattice strain relaxations in the (101) grain family, with increasing tensile strains, were noted to be a result of the significant misorientation and orientation gradients developing within those grains. These further enhanced with increasing plastic deformation, thus rendering the grain incapable of accommodating any further elastic strains. The load shed was accommodated by the (001) grain family.

- Such orientation gradients, and hence lattice strain relaxations, were not observed for any of the grain families during cyclic deformation.
- Model predictions of bulk lattice strains as well as local residual strains showed the following hierarchy among different grain families: (001) > (311) > (111) > (101) for tensile deformation and (001) > (311) > (111) ∼ (101) for cyclic deformation. The key factors that were found to influence the hierarchy were the elastic stiffness and the grain rotation, during tensile as well as cyclic deformation.

In summary, the thesis made an attempt to explore the possible relationship and interdependency between (mis)orientation and (mis)orientation gradients, segregation and residual strains in metallic systems, using a combination of novel modeling and experimental techniques.

8.3 Future Scope

As can be seen in each of the Chapters, the thesis firstly introduces the proposed mesoscale modeling framework, followed by its validation and application to a practical scenario. The future scope can also be divided on similar lines as follows:

1. Improvements to the existing modeling framework:
    - Chapter 3 introduced a Taylor hardening based SGCP framework to study the grain boundary orientation gradients. Possible future research can be directed towards application of higher order models (cf. Evers et al. (2004a,b)), since they provide a realistic estimation of backstress based on the spatial distribution of GNDs.
    - Iterative algorithms to derive the GND configurations from the Nye tensor, with physically realistic weights (for example, energy minimization) could provide realistic GND density configurations. These can be physically verified using TEM-PED based GND density measurements, since they provide an atomic-level resolution.
    - The dislocation interaction parameter employed in Chapters 3 and 4, which accounts for the hardening associated with interactions of dislocations gliding on different slip systems can be derived from lower length-scale models, such as Discrete Dislocation Dynamics (DDD).

- Chapter 5 focuses on employing a PF-SGP for capturing the microstructural developments during rapid solidification. A more accurate prediction of thermal distortion induced heterogeneties can be obtained by introducing a PF-SGCP type of framework. Alternatively, an entry-wise one norm can be used to estimate GNDs in PF-SGCP, to reduce the computational expenses involved.

2. Model applications:

   - The PF-SGP predicted solidified microstructure in Chapter 5 was cooled immediately to the room temperature. In reality, additively manufactured microstructures undergo significant amount of thermal cycling during their (layer-by-layer) deposition. Possible future research may employ such Boundary Conditions (BCs) and then evaluate their effects on the post-solidification mechanical properties.
   - Employing a SGCP framework to evaluate the orientation-dependent residual strains, in place of the Armstrong-Frederick model currently employed in Chapter 7.
   - Estimating hydrostatic strains from the HR-EBSD based Kikuchi patterns, followed by their validation using SGCP. Such a combined experimental and modeling framework can be used to examine the void propagation and hence the failure behavior of ductile materials.

8.4 Significant Contributions from the Thesis

8.4.1 Journal Publications

8.4.1.1 Published

- Pai, N., Prakash, A., Samajdar, I., Patra, A., "Study of grain boundary orientation gradients through combined experiments and strain gradient crystal plasticity modeling", International Journal of Plasticity, Vol. 156, 2022, 103360.
- Pai, N., Manda, S., Sudhalkar, B., Syphus, B., Fullwood, D., de Kloe, R., Wright, S., Patra, A., and Samajdar, I., "Diffraction-based multiscale residual strain measurements", Microscopy and Microanalysis, Vol. 30, 2024.
- Pai, N., Samajdar, I., and Patra., A., 2024. "Microstructural and mechanistic insights into the tension-compression asymmetry of rapidly solidified Fe-Cr alloys: a phase field

and strain gradient plasticity study", Journal of the Mechanics and Physics of Solids, Vol. 189, 2024, 105695.

- Pai, N., Samajdar, I., Patra., A., "Study of orientation-dependent residual strains during tensile and cyclic deformation of an austenitic stainless steel", International Journal of Plasticity, Vol. 185, 2025, 104228.

8.4.2 Conference Presentations

- Pai, N.*, Prakash, A., Samajdar, I., Patra, A., "Study of near boundary gradient zones in an aluminum alloy using strain gradient crystal plasticity and experiments", Virtual Presentation, MS & T 21, Columbus, USA, October 17-21, 2021.

- Pai, N.*, Samajdar, I., Patra, A., "Study of the effect of gradient plasticity on the deformation of metallic systems via combined modeling and experiments", 24th International Conference on Computer Methods in Mechanics (CMM) & 42nd Solid Mechanics Conference (SolMech), Swinoujscie, Poland, September 5-8, 2022.

- Pai, N.*, Samajdar, I., Patra, A., "Insights into the tension-compression asymmetry of additively manufactured alloys: a combined phase field-strain gradient plasticity study", 29th International Conference on Processing and Fabrication of Advanced Materials, Indian Institute of Technology Tirupati, September 6-8, 2023.

- Pai, N.*, Samajdar, I., Patra, A., "Exploring The relative magnitudes of diffraction-based residual strain measurements", International Conference on Texture of Materials, 2024, Metz, France, June 30-July 6, 2024.

* indicates speaker.

References

Abdolvand, H., Wright, J., Wilkinson, A.J., 2018. Strong grain neighbour effects in polycrystals. Nature communications 9, 171.

Aburakhia, A., Bonakdar, A., Molavi-Zarandi, M., Kelleher, J., Abdolvand, H., 2022. Deformation mechanisms of additively manufactured hastelloy-x: A neutron diffraction experiment and crystal plasticity finite element modeling. Materials & Design 222, 111030.

Acevedo, R., Sedlak, P., Kolman, R., Fredel, M., 2020. Residual stress analysis of additive manufacturing of metallic parts using ultrasonic waves: State of the art review. Journal of Materials Research and Technology 9, 9457–9477.

Acharya, R., Sharon, J.A., Staroselsky, A., 2017. Prediction of microstructure in laser powder bed fusion process. Acta Materialia 124, 360–371.

Adams, B.L., Wright, S.I., Kunze, K., 1993. Orientation imaging: the emergence of a new microscopy. Metallurgical Transactions A 24, 819–831.

Agius, D., Kareer, A., Al Mamun, A., Truman, C., Collins, D.M., Mostafavi, M., Knowles, D., 2022. A crystal plasticity model that accounts for grain size effects and slip system interactions on the deformation of austenitic stainless steels. International Journal of Plasticity 152, 103249.

Agnew, S., Tomé, C., Brown, D., Holden, T., Vogel, S., 2003. Study of slip mechanisms in a magnesium alloy by neutron diffraction and modeling. Scripta materialia 48, 1003–1008.

Agnew, S.R., Singh, A., Calhoun, C.A., Mulay, R.P., Bhattacharyya, J.J., Somekawa, H., Mukai, T., Clausen, B., Wu, P., 2018. In-situ neutron diffraction of a quasicrystal-containing mg alloy interpreted using a new polycrystal plasticity model of hardening due to {10.2} tensile twinning. International Journal of Plasticity 100, 34–51.

Alankar, A., Mastorakos, I.N., Field, D.P., 2009. A dislocation-density-based 3d crystal plasticity model for pure aluminum. Acta materialia 57, 5936–5946.

Allain-Bonasso, N., Wagner, F., Berbenni, S., Field, D.P., 2012. A study of the heterogeneity of plastic deformation in if steel by ebsd. Materials Science and Engineering: A 548, 56–63.

Almen, J.O., Black, P.H., 1963. Residual stresses and fatigue in metals. (No Title) .

An, D., Zhang, X., Zaefferer, S., 2020. The combined and interactive effects of orientation, strain amplitude, cycle number, stacking fault energy and hydrogen doping on microstructure evolution of polycrystalline high-manganese steels under low-cycle fatigue. International Journal of Plasticity 134, 102803.

Armigliato, A., Spessot, A., Balboni, R., Benedetti, A., Carnevale, G., Frabboni, S., Mastracchio, G., Pavia, G., 2006. Convergent beam electron diffraction investigation of strain induced by ti self-aligned silicides in shallow trench si isolation structures. Journal of applied physics 99.

Armstrong, P.J., Frederick, C., et al., 1966. A mathematical representation of the multiaxial Bauschinger effect. volume 731. Central Electricity Generating Board [and] Berkeley Nuclear Laboratories ....

Armstrong, R., Codd, I., Douthwaite, R., Petch, N., 1962. The plastic deformation of polycrystalline aggregates. The Philosophical Magazine: A Journal of Theoretical Experimental and Applied Physics 7, 45–58.

Arsenlis, A., 2001. Modeling dislocation density evolution in continuum crystal plasticity. Ph.D. thesis. Massachusetts Institute of Technology.

Arsenlis, A., Parks, D., 1999. Crystallographic aspects of geometrically-necessary and statistically-stored dislocation density. Acta materialia 47, 1597–1611.

Arsenlis, A., Parks, D.M., Becker, R., Bulatov, V.V., 2004. On the evolution of crystallographic dislocation density in non-homogeneously deforming crystals. Journal of the Mechanics and Physics of Solids 52, 1213–1246.

Asaro, R.J., Rice, J., 1977. Strain localization in ductile single crystals. Journal of the Mechanics and Physics of Solids 25, 309–338.

Ashby, M., 1970. The deformation of plastically non-homogeneous materials. The Philosophical Magazine: A Journal of Theoretical Experimental and Applied Physics 21, 399–424.

Astafurov, S.V., Maier, G.G., Melnikov, E.V., Moskvina, V.A., Panchenko, M.Y., Astafurova, E.G., 2019. The strain-rate dependence of the hall-petch effect in two austenitic stainless steels with different stacking fault energies. Materials Science and Engineering: A 756, 365–372.

ASTM, A., et al., 2012. Standard test method for strain-controlled fatigue testing. ASTM E606/E606M, ASTM International .

Azizi, H., Ebrahimi, A., Ofori-Opoku, N., Greenwood, M., Provatas, N., Mohammadi, M., 2021. Characterizing the microstructural effect of build direction during solidification of laser-powder bed fusion of al-si alloys in the dilute limit: A phase-field study. Acta Materialia 214, 116983.

Bachmann, F., Hielscher, R., Schaeben, H., 2010. Texture analysis with mtex–free and open source software toolbox. Solid state phenomena 160, 63–68.

Baczmanski, A., Wierzbanowski, K., Haije, W., Helmholdt, R., Ekambaranathan, G., Pathiraj, B., et al., 1993. Diffraction elastic constants for textured materials-different methods of calculation. Crystal Research and Technology 28, 229–243.

Bahl, S., Rakhmonov, J.U., Kenel, C., Dunand, D.C., Shyam, A., 2022. Effect of grain-boundary θ-al2cu precipitates on tensile and compressive creep properties of cast al–cu–mn–zr alloys. Materials Science and Engineering: A 840, 142946.

Bandyopadhyay, R., Gustafson, S.E., Kapoor, K., Naragani, D., Pagan, D.C., Sangid, M.D., 2021. Comparative assessment of backstress models using high-energy x-ray diffraction microscopy experiments and crystal plasticity finite element simulations. International journal of plasticity 136, 102887.

Bandyopadhyay, R., Stopka, K.S., Sangid, M.D., 2024. Initializing intragranular residual stresses within statistically equivalent microstructures for crystal plasticity simulations. Journal of the Mechanics and Physics of Solids 184, 105529.

Barker, E.I., Li, D., Zbib, H.M., Sun, X., 2013. Gradient Plasticity Model and its Implementation into MARMOT. Technical Report. Pacific Northwest National Lab.(PNNL), Richland, WA (United States).

Bashir, A., Millar, R.W., Gallacher, K., Paul, D.J., Darbal, A.D., Stroud, R., Ballabio, A., Frigerio, J., Isella, G., MacLaren, I., 2019. Strain analysis of a ge micro disk using precession electron diffraction. Journal of Applied Physics 126.

Basinger, J., Fullwood, D., Kacher, J., Adams, B., 2011. Pattern center determination in electron backscatter diffraction microscopy. Microscopy and Microanalysis 17, 330–340.

Bassani, J., Racherla, V., 2011. From non-planar dislocation cores to non-associated plasticity and strain bursts. Progress in Materials Science 56, 852–863.

Bayley, C., Brekelmans, W., Geers, M., 2006. A comparison of dislocation induced back stress formulations in strain gradient crystal plasticity. International Journal of Solids and Structures 43, 7268–7286.

Bean, C., Wang, F., Charpagne, M., Villechaise, P., Valle, V., Agnew, S., Gianola, D., Pollock, T., Stinville, J., 2022. Heterogeneous slip localization in an additively manufactured 316l stainless steel. International Journal of Plasticity 159, 103436.

Béché, A., Rouvière, J., Barnes, J., Cooper, D., 2013. Strain measurement at the nanoscale: Comparison between convergent beam electron diffraction, nano-beam electron diffraction, high resolution imaging and dark field electron holography. Ultramicroscopy 131, 10–23.

Bell, D.C., Garratt-Reed, A.J., 2003. Energy dispersive X-ray analysis in the electron microscope. Garland Science.

Benzerga, A., Bréchet, Y., Needleman, A., Van der Giessen, E., 2003. Incorporating three-dimensional mechanisms into two-dimensional dislocation dynamics. Modelling and Simulation in Materials Science and Engineering 12, 159.

Berbenni, S., Taupin, V., Lebensohn, R.A., 2020. A fast fourier transform-based mesoscale field dislocation mechanics study of grain size effects and reversible plasticity in polycrystals. Journal of the Mechanics and Physics of Solids 135, 103808.

Beretta, S., Romano, S., 2017. A comparison of fatigue strength sensitivity to defects for materials manufactured by am or traditional processes. International Journal of Fatigue 94, 178–191.

Bertoli, U.S., MacDonald, B.E., Schoenung, J.M., 2019. Stability of cellular microstructure in laser powder bed fusion of 316l stainless steel. Materials Science and Engineering: A 739, 109–117.

Bertsch, K., De Bellefon, G.M., Kuehl, B., Thoma, D., 2020. Origin of dislocation structures in an additively manufactured austenitic stainless steel 316l. Acta Materialia 199, 19–33.

Bhattacharyya, J., Bittmann, B., Agnew, S., 2019. The effect of precipitate-induced back-stresses on plastic anisotropy: Demonstrated by modeling the behavior of aluminum alloy, 7085. International Journal of Plasticity 117, 3–20.

Birnbaum, A.J., Steuben, J.C., Barrick, E.J., Iliopoulos, A.P., Michopoulos, J.G., 2019. Intrinsic strain aging, $\sigma 3$ boundaries, and origins of cellular substructure in additively manufactured 316l. Additive Manufacturing 29, 100784.

Birosca, S., Liu, G., Ding, R., Jiang, J., Simm, T., Deen, C., Whittaker, M., 2019. The dislocation behaviour and gnd development in a nickel based superalloy during creep. International Journal of Plasticity 118, 252–268.

Biswas, S., Liu, D., Aagesen, L.K., Jiang, W., 2022. Solidification and grain formation in alloys: a 2d application of the grand-potential-based phase-field approach. Modelling and Simulation in Materials Science and Engineering 30, 025013.

Black, R., Anjaria, D., Genée, J., Valle, V., Stinville, J., 2024. Micro-strain and cyclic slip accumulation in a polycrystalline nickel-based superalloy. Acta Materialia 266, 119657.

Blochwitz, C., Jacob, S., Tirschler, W., 2008. Grain orientation effects on the growth of short fatigue cracks in austenitic stainless steel. Materials Science and Engineering: A 496, 59–66.

Blum, W., Finkel, A., 1982. New technique for evaluating long range internal back stresses. Acta Metallurgica 30, 1705–1715.

Bönisch, M., Barriobero-Vila, P., Dhekne, P.P., Stark, A., Schell, N., Ungár, T., Requena, G., Seefeldt, M., 2023. Tension-compression asymmetry of metastable austenitic stainless steel studied by in-situ high-energy x-ray diffraction. International journal of plasticity 170, 103767.

Brahme, A.P., Inal, K., Mishra, R.K., Saimoto, S., 2011. The backstress effect of evolving deformation boundaries in fcc polycrystals. International journal of plasticity 27, 1252–1266.

van Bremen, R., Gomes, D.R., de Jeer, L.T., Ocelík, V., De Hosson, J.T.M., 2016. On the optimum resolution of transmission-electron backscattered diffraction (t-ebsd). Ultramicroscopy 160, 256–264.

Brinckmann, S., Siegmund, T., Huang, Y., 2006. A dislocation density based strain gradient model. International journal of plasticity 22, 1784–1797.

Britton, T., Wilkinson, A., 2011. Measurement of residual elastic strain and lattice rotations with high resolution electron backscatter diffraction. Ultramicroscopy 111, 1395–1404.

Britton, T., Wilkinson, A.J., 2012. High resolution electron backscatter diffraction measurements of elastic strain variations in the presence of larger lattice rotations. Ultramicroscopy 114, 82–95.

Brown, D., Adams, D., Balogh, L., Carpenter, J., Clausen, B., King, G., Reedlunn, B., Palmer, T., Maguire, M., Vogel, S., 2017. In situ neutron diffraction study of the influence

of microstructure on the mechanical response of additively manufactured 304l stainless steel. Metallurgical and Materials Transactions A 48, 6055–6069.

Brown, D.W., Adams, D., Balogh, L., Carpenter, J.S., Clausen, B., Livescu, V., Martinez, R.M., Morrow, B.M., Palmer, T., Pokharel, R., et al., 2019. Using in situ neutron diffraction to isolate specific features of additively manufactured microstructures in 304l stainless steel and identify their effects on macroscopic strength. Metallurgical and Materials Transactions A 50, 3399–3413.

Bunge, H.J., 2013. Texture analysis in materials science: mathematical methods. Elsevier.

Burlet, H., Cailletaud, G., 1987. Modeling of cyclic plasticity in finite element codes, in: 2nd Int. Conf. on Constitutive Laws for Engineering Materials: Theory and Applications. Elsevier, Tucson, pp. 1157–1164.

Butt, M., Feltham, P., 1993. Solid-solution hardening. Journal of materials science 28, 2557–2576.

Calcagnotto, M., Ponge, D., Demir, E., Raabe, D., 2010. Orientation gradients and geometrically necessary dislocations in ultrafine grained dual-phase steels studied by 2d and 3d ebsd. Materials Science and Engineering: A 527, 2738–2746.

Callahan, P.G., De Graef, M., 2013. Dynamical electron backscatter diffraction patterns. part i: Pattern simulations. Microscopy and Microanalysis 19, 1255–1265.

Castelluccio, G.M., McDowell, D.L., 2017. Mesoscale cyclic crystal plasticity with dislocation substructures. International Journal of Plasticity 98, 1–26.

Cha, P.R., Kim, S.G., Yeon, D.H., Yoon, J.K., 2002. A phase field model for the solute drag on moving grain boundaries. Acta materialia 50, 3817–3829.

Chaboche, J., Nouailhas, D., 1989. Constitutive modeling of ratchetting effects—part ii: possibilities of some additional kinematic rules. Journal of Engineering Materials and Technology 111, 409–416.

Chaudhary, S., Guruprasad, P., Patra, A., 2022. Crystal plasticity constitutive modeling of tensile, creep and cyclic deformation in single crystal ni-based superalloys. Mechanics of Materials 174, 104474.

Chaudhary, S., Pai, N., Rao, G.A., Alam, Z., Sankarasubramanian, R., Guruprasad, P., Samajdar, I., Patra, A., 2023. Competitive role of primary γ precipitates and annealing twins on the heterogeneous deformation of a polycrystalline ni-based superalloy: Crystal plasticity modeling and experiments. Journal of Alloys and Compounds 967, 171783.

Chaudhary, S., Sudhalkar, B., Pai, N., Palit, M., Alam, Z., Sankarasubramanian, R., Samajdar, I., Patra, A., 2025. A crystal plasticity-based micromechanical model for precipitate shearing: Application to cyclic softening of polycrystalline ni-based superalloys. International Journal of Fatigue 190, 108582.

Chen, C., Li, S., Wen, J., Jia, W., 2000. Finite element analysis about effects of stiffness distribution on stresses and elastic strain energy near the triple junction in a tricrystal. Materials Science and Engineering: A 282, 170–176.

Chen, J., Furushima, T., 2024. Effects of intergranular deformation incompatibility on stress state and fracture initiation at grain boundary: Experiments and crystal plasticity simulations. International Journal of Plasticity 180, 104052.

Chen, J., Wang, Z., Korsunsky, A.M., 2022a. Multiscale stress and strain statistics in the deformation of polycrystalline alloys. International Journal of Plasticity 152, 103260.

Chen, W., Voisin, T., Zhang, Y., Forien, J.B., Spadaccini, C.M., McDowell, D.L., Zhu, T., Wang, Y.M., 2019. Microscale residual stresses in additively manufactured stainless steel. Nature communications 10, 1–12.

Chen, X., Sha, Y., Chen, S., Zhang, F., Zuo, L., 2022b. Neighbor-affected orientation rotation in the grain boundary region. Materials 15, 1059.

Choi, S., Griffin, B.A., 2016. Local residual stress monitoring of aluminum nitride mems using uv micro-raman spectroscopy. Journal of Micromechanics and Microengineering 26, 025009.

Chowdhury, S.G., Das, S., De, P., 2005. Cold rolling behaviour and textural evolution in aisi 316l austenitic stainless steel. Acta Materialia 53, 3951–3959.

Clausen, B., Lorentzen, T., Bourke, M.A., Daymond, M.R., 1999. Lattice strain evolution during uniaxial tensile loading of stainless steel. Materials Science and Engineering: A 259, 17–24.

Collins, D., Stone, H., 2014. A modelling approach to yield strength optimisation in a nickel-base superalloy. International Journal of Plasticity 54, 96–112.

Cordero, Z.C., Knight, B.E., Schuh, C.A., 2016. Six decades of the hall–petch effect–a survey of grain-size strengthening studies on pure metals. International Materials Reviews 61, 495–512.

Cullity, B.D., 1956. Elements of X-ray Diffraction. Addison-Wesley Publishing.

Dafalias, Y.F., 1985. The plastic spin. Journal of Applied Mechanics 52(4), 865–71.

Dai, H., 1997. Geometrically-necessary dislocation density in continuum plasticity theory, FEM implementation and applications. Ph.D. thesis. Massachusetts Institute of Technology.

Das, S., Hofmann, F., Tarleton, E., 2018. Consistent determination of geometrically necessary dislocation density from simulations and experiments. International Journal of Plasticity 109, 18–42.

Das, S., Yu, H., Mizohata, K., Tarleton, E., Hofmann, F., 2020. Modified deformation behaviour of self-ion irradiated tungsten: A combined nano-indentation, hr-ebsd and crystal plasticity study. International Journal of Plasticity 135, 102817.

Dawson, P., Boyce, D., MacEwen, S., Rogge, R., 2001. On the influence of crystal elastic moduli on computed lattice strains in aa-5182 following plastic straining. Materials Science and Engineering: A 313, 123–144.

Deal, A., Spinelli, I., Chuang, A., Gao, Y., Broderick, T., 2021. Measuring residual stress in ti-6al-4v with hr-ebsd, using reference patterns from annealed material. Materials Characterization 175, 111027.

DebRoy, T., Wei, H., Zuback, J., Mukherjee, T., Elmer, J., Milewski, J., Beese, A.M., Wilson-Heid, A.d., De, A., Zhang, W., 2018. Additive manufacturing of metallic components–process, structure and properties. Progress in Materials Science 92, 112–224.

Detor, A.J., Schuh, C.A., 2007. Grain boundary segregation, chemical ordering and stability of nanocrystalline alloys: Atomistic computer simulations in the ni–w system. Acta Materialia 55, 4221–4232.

Devaraj, A., Wang, W., Vemuri, R., Kovarik, L., Jiang, X., Bowden, M., Trelewicz, J., Mathaudhu, S., Rohatgi, A., 2019. Grain boundary segregation and intermetallic precipitation in coarsening resistant nanocrystalline aluminum alloys. Acta Materialia 165, 698–708.

Dieter, G.E., Bacon, D., 1976. Mechanical metallurgy. volume 3. McGraw-hill New York.

Dillamore, I., Roberts, J., Bush, A., 1979. Occurrence of shear bands in heavily rolled cubic metals. Metal Science 13, 73–77.

Ding, J., Colegrove, P., Mehnen, J., Ganguly, S., Almeida, P.S., Wang, F., Williams, S., 2011. Thermo-mechanical analysis of wire and arc additive layer manufacturing process on large multi-layer parts. Computational Materials Science 50, 3315–3322.

Dingley, D., 2004. Progressive steps in the development of electron backscatter diffraction and orientation imaging microscopy. Journal of microscopy 213, 214–224.

Dinsdale, A.T., 1991. Sgte data for pure elements. Calphad 15, 317–425.

Driver, J., Papazian, J., 1985. Microstructural effects of the cyclic and monotonic hardening of al-5mg. Materials Science and Engineering 76, 51–56.

Drury, M., Humphreys, F., 1986. The development of microstructure in al-5% mg during high temperature deformation. Acta Metallurgica 34, 2259–2271.

Du Plessis, A., Yadroitsava, I., Yadroitsev, I., 2020. Effects of defects on mechanical properties in metal additive manufacturing: A review focusing on x-ray tomography insights. Materials & Design 187, 108385.

Dunne, F., Kiwanuka, R., Wilkinson, A., 2012. Crystal plasticity analysis of microdeformation, lattice rotation and geometrically necessary dislocation density. Proceedings of the Royal Society A: Mathematical, Physical and Engineering Sciences 468, 2509–2531.

Echebarria, B., Folch, R., Karma, A., Plapp, M., 2004. Quantitative phase-field model of alloy solidification. Physical review E 70, 061604.

English, A., Chin, G., 1965. On the variation of wire texture with stacking fault energy in fcc metals and alloys. Acta metallurgica 13, 1013–1016.

Erinosho, T., Collins, D., Wilkinson, A., Todd, R., Dunne, F., 2016. Assessment of x-ray diffraction and crystal plasticity lattice strain evolutions under biaxial loading. International Journal of Plasticity 83, 1–18.

Erinosho, T., Dunne, F., 2016. Lattice strains at cracks in single crystal titanium: Elastic distortion and gnd contributions. International Journal of Solids and Structures 80, 237–245.

Esmaeili, S., Lloyd, D., Poole, W., 2003. A yield strength model for the al-mg-si-cu alloy aa6111. Acta Materialia 51, 2243–2257.

Estrin, Y., 1996. Dislocation-density-related constitutive modeling. Unified constitutive laws of plastic deformation 1, 69–106.

Evers, L., Brekelmans, W., Geers, M., 2004a. Non-local crystal plasticity model with intrinsic ssd and gnd effects. Journal of the Mechanics and Physics of Solids 52, 2379–2401.

Evers, L., Brekelmans, W., Geers, M., 2004b. Scale dependent crystal plasticity framework with dislocation density and grain boundary effects. International Journal of solids and structures 41, 5209–5230.

Farooq, M., Villaurrutia, R., MacLaren, I., Burnett, T., Comyn, T., Bell, A., Kungl, H., Hoffmann, M., 2008. Electron backscatter diffraction mapping of herringbone domain structures in tetragonal piezoelectrics. Journal of Applied Physics 104.

Farshidianfar, M.H., Khajepour, A., Gerlich, A.P., 2016. Effect of real-time cooling rate on microstructure in laser additive manufacturing. Journal of Materials Processing Technology 231, 468–478.

Farzadi, A., Do-Quang, M., Serajzadeh, S., Kokabi, A., Amberg, G., 2008. Phase-field simulation of weld solidification microstructure in an al–cu alloy. Modelling and Simulation in Materials Science and Engineering 16, 065005.

Ferreri, N.C., Feng, Z., Savage, D.J., Brown, D.W., Clausen, B., Sisneros, T.A., Knezevic, M., 2022. In-situ high-energy x-ray diffraction and crystal plasticity modeling to predict the evolution of texture, twinning, lattice strains and strength during loading and reloading of beryllium. International Journal of Plasticity 150, 103217.

Field, D., Trivedi, P., Wright, S., Kumar, M., 2005. Analysis of local orientation gradients in deformed single crystals. Ultramicroscopy 103, 33–39.

Fisher, D., Rappaz, M., Kurz, W., 2023. Fundamentals of solidification. Fundamentals of Solidification , 1–353.

Fleck, N., Muller, G., Ashby, M.F., Hutchinson, J.W., 1994. Strain gradient plasticity: theory and experiment. Acta Metallurgica et materialia 42, 475–487.

Fleischer, R.L., 1963. Substitutional solution hardening. Acta metallurgica 11, 203–209.

Fontaine, P., 1980. Ni-resist type d5s—an improved material for turbocharger housings. SAE Transactions , 37–57.

Förster, F., Köster, W., 1939. Modulus of elasticity and damping in relation to the state of the material. Journal of the Institution of Electrical Engineers 84, 558–564.

Fribourg, G., Bréchet, Y., Deschamps, A., Simar, A., 2011. Microstructure-based modelling of isotropic and kinematic strain hardening in a precipitation-hardened aluminium alloy. Acta Materialia 59, 3621–3635.

Fu, W., Li, Y., Hu, S., Sushko, P., Mathaudhu, S., 2022. Effect of loading path on grain misorientation and geometrically necessary dislocation density in polycrystalline aluminum under reciprocating shear. Computational Materials Science 205, 111221.

Fullwood, D., 2020. Openxy. `https://github.com/BYU-MicrostructureOfMaterials/OpenXY`.

Fullwood, D., Vaudin, M., Daniels, C., Ruggles, T., Wright, S.I., 2015. Validation of kinematically simulated pattern hr-ebsd for measuring absolute strains and lattice tetragonality. Materials Characterization 107, 270–277.

Fullwood, D.T., Sanderson, S., Baird, S., Christensen, J., Homer, E.R., Johnson, O.K., 2022. Determining grain boundary position and geometry from ebsd data: Limits of accuracy. Microscopy and Microanalysis 28, 96–108.

Gallet, J., Perez, M., Guillou, R., Ernould, C., Le Bourlot, C., Langlois, C., Beausir, B., Bouzy, E., Chaise, T., Cazottes, S., 2023. Experimental measurement of dislocation density in metallic materials: a quantitative comparison between measurements techniques (xrd, r-ecci, hr-ebsd, tem). Materials Characterization 199, 112842.

Gan, Z., He, Y., Liu, D., Zhang, B., Shen, L., 2014. Hall–petch effect and strain gradient effect in the torsion of thin gold wires. Scripta Materialia 87, 41–44.

Gao, W., Zhang, Y., Ramanujan, D., Ramani, K., Chen, Y., Williams, C.B., Wang, C.C., Shin, Y.C., Zhang, S., Zavattieri, P.D., 2015. The status, challenges, and future of additive manufacturing in engineering. Computer-Aided Design 69, 65–89.

Gault, B., Chiaramonti, A., Cojocaru-Mirédin, O., Stender, P., Dubosq, R., Freysoldt, C., Makineni, S.K., Li, T., Moody, M., Cairney, J.M., 2021. Atom probe tomography. Nature Reviews Methods Primers 1, 51.

Geers, M., Brekelmans, W., Bayley, C., 2006a. Second-order crystal plasticity: internal stress effects and cyclic loading. Modelling and Simulation in Materials Science and Engineering 15, S133.

Geers, M.G., Brekelmans, W., Janssen, P., 2006b. Size effects in miniaturized polycrystalline fcc samples: strengthening versus weakening. International Journal of Solids and Structures 43, 7304–7321.

Geiger, F., Kunze, K., Etter, T., 2016. Tailoring the texture of in738lc processed by selective laser melting (slm) by specific scanning strategies. Materials Science and Engineering A 661, 240–246.

Genée, J., Gey, N., Bonnet, F., Lebensohn, R., Berbenni, S., 2021. Experimental and numerical investigation of key microstructural features influencing the localization of plastic deformation in fe-tib2 metal matrix composite. Journal of Materials Science 56, 11278–11297.

Gerken, J.M., Dawson, P.R., 2008. A crystal plasticity model that incorporates stresses and strains due to slip gradients. Journal of the Mechanics and Physics of Solids 56, 1651–1672.

Ghamarian, I., 2017. Application of ASTAR™/Precession Electron Diffraction Technique to Quantitatively Study Defects in Nanocrystalline Metallic Materials. Ph.D. thesis. Iowa State University.

Ghamarian, I., Liu, Y., Samimi, P., Collins, P.C., 2014. Development and application of a novel precession electron diffraction technique to quantify and map deformation structures in highly deformed materials—as applied to ultrafine-grained titanium. Acta Materialia 79, 203–215.

Ghosh, S., Ma, L., Ofori-Opoku, N., Guyer, J.E., 2017. On the primary spacing and microsegregation of cellular dendrites in laser deposited ni–nb alloys. Modelling and simulation in materials science and engineering 25, 065002.

Godec, M., Zaefferer, S., Podgornik, B., Šinko, M., Tchernychova, E., 2020. Quantitative multiscale correlative microstructure analysis of additive manufacturing of stainless steel 316l processed by selective laser melting. Materials Characterization 160, 110074.

Goodhew, P.J., Humphreys, J., 2000. Electron microscopy and analysis. CRC press.

Guesser, W.L., Martins, L., 2016. Stiffness and vibration damping capacity of high strength cast irons. Technical Report. SAE Technical Paper.

Guo, R., Wu, J., 2018. Dislocation density based model for al-cu-mg alloy during quenching with considering the quench-induced precipitates. Journal of Alloys and Compounds 741, 432–441.

Guo, Y., Abdolvand, H., Britton, T., Wilkinson, A., 2017. Growth of {112 2} twins in titanium: A combined experimental and modelling investigation of the local state of deformation. Acta Materialia 126, 221–235.

Gurtin, M.E., 2002. A gradient theory of single-crystal viscoplasticity that accounts for geometrically necessary dislocations. Journal of the Mechanics and Physics of Solids 50, 5–32.

Hall, E., 1951. The deformation and ageing of mild steel: Iii discussion of results. Proceedings of the Physical Society. Section B 64, 747.

Hansen, L.T., Fullwood, D.T., Homer, E.R., Wagoner, R.H., Lim, H., Carroll, J.D., Zhou, G., Bong, H.J., 2020. An investigation of geometrically necessary dislocations and back

stress in large grained tantalum via ebsd and cpfem. Materials Science and Engineering: A 772, 138704.

Hansen, N., 1977. The effect of grain size and strain on the tensile flow stress of aluminium at room temperature. Acta Metallurgica 25, 863–869.

Haouala, S., Lucarini, S., LLorca, J., Segurado, J., 2020. Simulation of the hall-petch effect in fcc polycrystals by means of strain gradient crystal plasticity and fft homogenization. Journal of the Mechanics and Physics of Solids 134, 103755.

Hardin, T., Ruggles, T., Koch, D., Niezgoda, S., Fullwood, D., Homer, E., 2015. Analysis of traction-free assumption in high-resolution ebsd measurements. Journal of microscopy 260, 73–85.

Hartley, C.S., Kysar, J.W., 2020. Plane strain deformation by slip in fcc crystals. International Journal of Plasticity 133, 102842.

Hashiguchi, K., 2020. Nonlinear continuum mechanics for finite elasticity-plasticity: Multiplicative decomposition with subloading surface model. Elsevier.

He, B.B., 2003. Introduction to two-dimensional x-ray diffraction. Powder diffraction 18, 71–85.

Herzog, D., Seyda, V., Wycisk, E., Emmelmann, C., 2016. Additive manufacturing of metals. Acta Materialia 117, 371–392.

Hestroffer, J.M., Latypov, M.I., Stinville, J.C., Charpagne, M.A., Valle, V., Miller, M.P., Pollock, T.M., Beyerlein, I.J., 2022. Development of grain-scale slip activity and lattice rotation fields in inconel 718. Acta Materialia 226, 117627.

Higham, N., Gentleman, A.V.S., 1963. The major achievements of henry clifton sorby.

Hill, R., 1948. A theory of the yielding and plastic flow of anisotropic metals. Proceedings of the Royal Society of London. Series A. Mathematical and Physical Sciences 193, 281–297.

Hu, D., Grilli, N., Wang, L., Yang, M., Yan, W., 2022. Microscale residual stresses in additively manufactured stainless steel: Computational simulation. Journal of the Mechanics and Physics of Solids 161, 104822.

Hu, D., Grilli, N., Yan, W., 2023. Dislocation structures formation induced by thermal stress in additive manufacturing: Multiscale crystal plasticity modeling of dislocation transport. Journal of the Mechanics and Physics of Solids 173, 105235.

Hüe, F., Hÿtch, M., Bender, H., Houdellier, F., Claverie, A., 2008. Direct mapping of strain in a strained silicon transistor by high-resolution electron microscopy. Physical review letters 100, 156602.

Hughes, D., 1993. Microstructural evolution in a non-cell forming metal: Al-mg. Acta metallurgica et materialia 41, 1421–1430.

Humphreys, F., 2004. Characterisation of fine-scale microstructures by electron backscatter diffraction (ebsd). Scripta materialia 51, 771–776.

Humphreys, F., Huang, Y., Brough, I., Harris, C., 1999. Electron backscatter diffraction of grain and subgrain structures—resolution considerations. Journal of Microscopy 195, 212–216.

Humphreys, F.J., Hatherly, M., 2012. Recrystallization and related annealing phenomena. Elsevier.

Jeon, J.M., Park, J.M., Yu, J.H., Kim, J.G., Seong, Y., Park, S.H., Seop, K.H., 2019. Effects of microstructure and internal defects on mechanical anisotropy and asymmetry of selective laser-melted 316l austenitic stainless steel. Materials Science and Engineering A 763, 138152.

Jeong, Y., Tomé, C.N., 2020. An efficient elasto-visco-plastic self-consistent formulation: Application to steel subjected to loading path changes. International Journal of Plasticity 135, 102812.

Jiang, J., Britton, T., Wilkinson, A., 2013a. Evolution of dislocation density distributions in copper during tensile deformation. Acta Materialia 61, 7227–7239.

Jiang, J., Britton, T., Wilkinson, A., 2013b. Measurement of geometrically necessary dislocation density with high resolution electron backscatter diffraction: effects of detector binning and step size. Ultramicroscopy 125, 1–9.

Jiang, J., Britton, T.B., Wilkinson, A.J., 2015. Evolution of intragranular stresses and dislocation densities during cyclic deformation of polycrystalline copper. Acta Materialia 94, 193–204.

Kalácska, S., Dankházi, Z., Zilahi, G., Maeder, X., Michler, J., Ispánovity, P.D., Groma, I., 2020. Investigation of geometrically necessary dislocation structures in compressed cu micropillars by 3-dimensional hr-ebsd. Materials Science and Engineering: A 770, 138499.

Kalácska, S., Groma, I., Borbély, A., Ispánovity, P.D., 2017. Comparison of the dislocation density obtained by hr-ebsd and x-ray profile analysis. Applied Physics Letters 110.

Kang, J., Wilkinson, D., Jain, M., Embury, J., Beaudoin, A., Kim, S., Mishira, R., Sachdev, A., 2006. On the sequence of inhomogeneous deformation processes occurring during tensile deformation of strip cast aa5754. Acta Materialia 54, 209–218.

Kanjarla, A., Lebensohn, R., Balogh, L., Tomé, C., 2012. Study of internal lattice strain distributions in stainless steel using a full-field elasto-viscoplastic formulation based on fast fourier transforms. Acta Materialia 60, 3094–3106.

Kapoor, K., Sangid, M.D., 2018. Initializing type-2 residual stresses in crystal plasticity finite element simulations utilizing high-energy diffraction microscopy data. Materials Science and Engineering: A 729, 53–63.

Kapoor, K., Yoo, Y.S.J., Book, T.A., Kacher, J.P., Sangid, M.D., 2018. Incorporating grain-level residual stresses and validating a crystal plasticity model of a two-phase ti-6al-4 v alloy produced via additive manufacturing. Journal of the Mechanics and Physics of Solids 121, 447–462.

Kartal, M.E., Dunne, F.P., Wilkinson, A.J., 2012. Determination of the complete microscale residual stress tensor at a subsurface carbide particle in a single-crystal superalloy from free-surface ebsd. Acta materialia 60, 5300–5310.

Kaufman, J.G., Rooy, E.L., 2004. Aluminum alloy castings: properties, processes, and applications. Asm International.

Keskar, N., Mukherjee, S., Krishna, K.M., Srivastava, D., Dey, G., Pant, P., Doherty, R., Samajdar, I., 2014. Quantifying the mesoscopic shear strains in plane strain compressed polycrystalline zirconium. Acta materialia 69, 265–274.

Khan, A.S., Huang, S., 1995. Continuum theory of plasticity. John Wiley & Sons.

Kim, D.C., Ogura, T., Hamada, R., Yamashita, S., Saida, K., 2021. Establishment of a theoretical model based on the phase-field method for predicting the γ phase precipitation in fe–cr–ni ternary alloys. Materials Today Communications 26, 101932.

Kim, E.Y., Woo, W., Heo, Y.U., Seong, B., Choi, J., Choi, S.H., 2016a. Effect of kinematic stability of the austenite phase on phase transformation behavior and deformation heterogeneity in duplex stainless steel using the crystal plasticity finite element method. International Journal of Plasticity 79, 48–67.

Kim, S.G., Lee, J.S., Lee, B.J., 2016b. Thermodynamic properties of phase-field models for grain boundary segregation. Acta Materialia 112, 150–161.

Kobayashi, R., 1993. Modeling and numerical simulations of dendritic crystal growth. Physica D: Nonlinear Phenomena 63, 410–423.

Kocks, U., Argon, A., Ashby, M., 1975. Progress in material science vol. 19: Thermodynamics and kinetics of slip, editors: Chalmers b., christian jw, massalski tb.

Kocks, U., Mecking, H., 2003. Physics and phenomenology of strain hardening: the fcc case. Progress in materials science 48, 171–273.

Kocks, U.F., Tomé, C.N., Wenk, H.R., 1998. Texture and anisotropy: preferred orientations in polycrystals and their effect on materials properties. Cambridge university press.

Kocks, U.F., Tomé, C.N., Wenk, H.R., 2000. Texture and anisotropy: preferred orientations in polycrystals and their effect on materials properties. Cambridge university press.

Korsunsky, A., Daymond, M., James, K., 2002. The correlation between plastic strain and anisotropy strain in aluminium alloy polycrystals. Materials Science and Engineering: A 334, 41–48.

Kothari, M., Anand, L., 1998. Elasto-viscoplastic constitutive equations for polycrystalline metals: application to tantalum. Journal of the Mechanics and Physics of Solids 46, 51–83.

Koyama, T., Onodera, H., 2004. Phase-field simulation of phase decomposition in fe- cr- co alloy under an external magnetic field. Metals and Materials International 10, 321–326.

Kozar, R., Suzuki, A., Milligan, W., Schirra, J., Savage, M., Pollock, T., 2009. Strengthening mechanisms in polycrystalline multimodal nickel-base superalloys. Metallurgical and materials transactions A 40, 1588–1603.

Krakow, R., Bennett, R.J., Johnstone, D.N., Vukmanovic, Z., Solano-Alvarez, W., Lainé, S.J., Einsle, J.F., Midgley, P.A., Rae, C.M., Hielscher, R., 2017. On three-dimensional misorientation spaces. Proceedings of the Royal Society A: Mathematical, Physical and Engineering Sciences 473, 20170274.

Krawitz, A.D., Holden, T.M., 1990. The measurement of residual stresses using neutron diffraction. MRS Bulletin 15, 57–64.

Kröner, E., 1962. Dislocations and continuum mechanics. Appl. Mech. Rev 15, 599–606.

Krost, A., Bläsing, J., 2009. Fast, micrometer scale characterization of group-iii nitrides with laboratory x-ray diffraction. Materials Science and Engineering: A 524, 82–88.

Kubushiro, K., Sakakibara, Y., Ohtani, T., 2015. Creep strain analysis of austenitic stainless steel by sem/ebsd. Journal of the Society of Materials Science, Japan 64, 106–112.

Kumar, A., Dawson, P., 2000. Computational modeling of fcc deformation textures over rodrigues' space. Acta Materialia 48, 2719–2736.

Kumar, B., Nagamani Jaya, B., 2023. Thermal stability and residual stresses in additively manufactured single and multi-material systems. Metallurgical and Materials Transactions A 54, 1808–1824.

Kumar, G., Kanjarla, A., Lodh, A., Singh, J., Singh, R., Srivastava, D., Dey, G., Saibaba, N., Doherty, R., Samajdar, I., 2016. Burst ductility of zirconium clads: The defining role of residual stress. Metallurgical and Materials Transactions A 47, 3882–3896.

Kumar, S., Pai, N.N., Manda, S., Tewary, U., Fullwood, D.T., Giri, S., Kundu, S., Murty, S., Anoop, C., Samajdar, I., 2025. Austenite residual stress and lath martensite variant selection in low carbon steels. Acta Materialia , 120885.

Kuna, L., Birnbaum, A.J., Teferra, K., 2023. A framework for predicting residual mechanical response fields for laser powder bed fusion at the polycrystalline length scale. Additive Manufacturing 78, 103830.

Kundu, A., Field, D.P., 2016. Influence of plastic deformation heterogeneity on development of geometrically necessary dislocation density in dual phase steel. Materials Science and Engineering: A 667, 435–443.

Kundu, A., Field, D.P., 2020. Influence of microstructural heterogeneity and plastic strain on geometrically necessary dislocation structure evolution in single-phase and two-phase alloys. Materials Characterization 170, 110690.

Kuroda, M., Tvergaard, V., 2006. Studies of scale dependent crystal viscoplasticity models. Journal of the Mechanics and Physics of Solids 54, 1789–1810.

Kuroda, M., Tvergaard, V., 2008. On the formulations of higher-order strain gradient crystal plasticity models. Journal of the Mechanics and Physics of Solids 56, 1591–1608.

Kysar, J., Saito, Y., Oztop, M., Lee, D., Huh, W., 2010. Experimental lower bounds on geometrically necessary dislocation density. International Journal of Plasticity 26, 1097–1123.

Kysar, J.W., Gan, Y.X., Morse, T.L., Chen, X., Jones, M.E., 2007. High strain gradient plasticity associated with wedge indentation into face-centered cubic single crystals: geometrically necessary dislocation densities. Journal of the Mechanics and Physics of Solids 55, 1554–1573.

Labusch, R., 1972. Statistische theorien der mischkristallhärtung. Acta metallurgica 20, 917–927.

Laird, C., Charsley, P., Mughrabi, H., 1986. Low energy dislocation structures produced by cyclic deformation. Materials science and engineering 81, 433–450.

Lebensohn, R.A., Brenner, R., Castelnau, O., Rollett, A.D., 2008. Orientation image-based micromechanical modelling of subgrain texture evolution in polycrystalline copper. Acta Materialia 56, 3914–3926.

Lee, D.N., Kim, K.h., Lee, Y.g., Choi, C.H., 1997. Factors determining crystal orientation of dendritic growth during solidification. Materials chemistry and physics 47, 154–158.

Li, D.F., O'Dowd, N.P., 2011. On the evolution of lattice deformation in austenitic stainless steels—the role of work hardening at finite strains. Journal of the Mechanics and Physics of Solids 59, 2421–2441.

Li, J., Zhang, Q., Huang, R., Li, X., Gao, H., 2020a. Towards understanding the structure–property relationships of heterogeneous-structured materials. Scripta Materialia 186, 304–311.

Li, S., Lim, S.H., 2005. Variational principles for generalized plane strain problems and their applications. Composites Part A: Applied Science and Manufacturing 36, 353–365.

Li, Y., Zou, D., Chen, W., Zhang, Y., Zhang, W., Xu, F., 2022. Effect of cooling rate on solidification and segregation characteristics of 904l super austenitic stainless steel. Metals and Materials International 28, 1907–1918.

Li, Y.L., Kohar, C.P., Mishra, R.K., Inal, K., 2020b. A new crystal plasticity constitutive model for simulating precipitation-hardenable aluminum alloys. International Journal of Plasticity 132, 102759.

Liang, H., Dunne, F., 2009. Gnd accumulation in bi-crystal deformation: Crystal plasticity analysis and comparison with experiments. International Journal of Mechanical Sciences 51, 326–333.

Lim, H., Carroll, J., Battaile, C.C., Buchheit, T., Boyce, B., Weinberger, C., 2014. Grain-scale experimental validation of crystal plasticity finite element simulations of tantalum oligocrystals. International Journal of Plasticity 60, 1–18.

Lindgren, L.E., Hao, Q., Wedberg, D., 2017. Improved and simplified dislocation density based plasticity model for aisi 316 l. Mechanics of Materials 108, 68–76.

Lindroos, M., Pinomaa, T., Ammar, K., Laukkanen, A., Provatas, N., Forest, S., 2022. Dislocation density in cellular rapid solidification using phase field modeling and crystal plasticity. International Journal of Plasticity 148, 103139.

Lingda, X., Guoli, Z., Gaoyang, M., Chunming, W., Ping, J., 2021. A phase-field simulation of columnar-to-equiaxed transition in the entire laser welding molten pool. Journal of Alloys and Compounds 858, 157669.

Liu, F., Kirchheim, R., 2004. Grain boundary saturation and grain growth. Scripta materialia 51, 521–525.

Liu, L., Ding, Q., Zhong, Y., Zou, J., Wu, J., Chiu, Y.L., Li, J., Zhang, Z., Yu, Q., Shen, Z., 2018a. Dislocation network in additive manufactured steel breaks strength–ductility trade-off. Materials Today 21, 354–361.

Liu, P., Ji, Y., Wang, Z., Qiu, C., Antonysamy, A., Chen, L.Q., Cui, X., Chen, L., 2018b. Investigation on evolution mechanisms of site-specific grain structures during metal additive manufacturing. Journal of Materials Processing Technology 257, 191–202.

Liu, P., Wang, Z., Xiao, Y., Lebensohn, R.A., Liu, Y., Horstemeyer, M.F., Cui, X., Chen, L., 2020a. Integration of phase-field model and crystal plasticity for the prediction of process-structure-property relation of additively manufactured metallic materials. International Journal of Plasticity 128, 102670.

Liu, Y., Zheng, B., Jian, Y., Zhang, L., Yi, Y., Li, W., 2020b. Anisotropic in elasticity, sound velocity and minimum thermal conductivity of al–cu intermetallic compounds. Intermetallics 124, 106880.

Liu, Z., Lin, B., Liang, X., Du, A., 2021. Numerical simulation of laser-generated rayleigh wave pulses propagation in the machined surface with residual stress using finite-difference method. Optik 248, 168072.

Lodh, A., Tak, T.N., Prakash, A., Guruprasad, P., Hutchinson, C., Samajdar, I., 2017. Relating residual stress and substructural evolution during tensile deformation of an aluminum-manganese alloy. Metallurgical and Materials Transactions A 48, 5317–5331.

Lodh, A., Tak, T.N., Prakash, A., Guruprasad, P., Keralavarma, S.M., Benzerga, A.A., Hutchinson, C., Samajdar, I., 2019. Microstructural origin of residual stress relief in aluminum. Metallurgical and Materials Transactions A 50, 5038–5055.

Lodh, A., Tewary, U., Singh, R.P., Tak, T.N., Prakash, A., Alankar, A., Guruprasad, P., Samajdar, I., 2018. Orientation-dependent developments in misorientation and residual

stress in rolled aluminum: the defining role of dislocation interactions. Metallurgical and Materials Transactions A 49, 5946–5952.

Lodh, A., Thool, K., Samajdar, I., 2022. X-ray diffraction for the determination of residual stress of crystalline material: An overview. Transactions of the Indian Institute of Metals 75, 983–995.

Lorentzen, T., Daymond, M., Clausen, B., Tomé, C., 2002. Lattice strain evolution during cyclic loading of stainless steel. Acta materialia 50, 1627–1638.

Louca, K., Shanks, K.S., Das, A., Abdolvand, H., 2024. The asymmetric evolution of grain-scale stresses in notched specimens under cyclic loads. Acta Materialia 264, 119567.

Lu, X., Dunne, F.P., Xu, Y., 2020. A crystal plasticity investigation of slip system interaction, gnd density and stored energy in non-proportional fatigue in nickel-based superalloy. International Journal of Fatigue 139, 105782.

Magagnosc, D., Lloyd, J., Meredith, C., Pilchak, A., Schuster, B., 2021. Incipient dynamic recrystallization and adiabatic shear bands in ti–7al studied via in situ x-ray diffraction. International Journal of Plasticity 141, 102992.

Manda, S., Kumar, S., Pai, N.N., Soni, L., Tewary, U., Rastogi, P., Asif, S., Panwar, A.S., Samajdar, I., 2024. Plasticity induced anelasticity: The atomistic origin. International Journal of Plasticity , 103901.

Manda, S., Kumar, S., Pal, K., Bhattacharyya, A.R., Panwar, A.S., Samajdar, I., 2023. Snoek-dominated internal friction response in bcc steel: Relating experiments with a multi-scale atomistic computational framework. Metallurgical and Materials Transactions A 54, 562–576.

Margulies, L., Lorentzen, T., Poulsen, H., Leffers, T., 2002. Strain tensor development in a single grain in the bulk of a polycrystal under loading. Acta Materialia 50, 1771–1779.

Maurice, C., Driver, J.H., Fortunier, R., 2012. On solving the orientation gradient dependency of high angular resolution ebsd. Ultramicroscopy 113, 171–181.

Mayeur, J., McDowell, D., 2014. A comparison of gurtin type and micropolar theories of generalized single crystal plasticity. International Journal of Plasticity 57, 29–51.

Mayeur, J.R., 2011. Generalized continuum modeling of scale-dependent crystalline plasticity. Ph.D. thesis. Georgia Institute of Technology.

Mayeur, J.R., McDowell, D.L., 2011. Bending of single crystal thin films modeled with micropolar crystal plasticity. International journal of engineering science 49, 1357–1366.

McGuire, M.F., 2008. Stainless steels for design engineers. ASM International, Materials Park, Ohio 44073-0002.

Mehtani, H., Khan, M., Durgaprasad, A., Deb, S., Parida, S., Prasad, M., Fullwood, D., Doherty, R., Samajdar, I., 2020. Oxidation behavior of interstitial free steel: The defining role of substrate crystallographic texture. Acta Materialia 190, 43–57.

Miettinen, J., 1999. Thermodynamic reassessment of fe-cr-ni system with emphasis on the iron-rich corner. Calphad 23, 231–248.

Militzer, M., 2011. Phase field modeling of microstructure evolution in steels. Current Opinion in Solid State and Materials Science 15, 106–115.

Mishra, S., Pant, P., Narasimhan, K., Rollett, A., Samajdar, I., 2009. On the widths of orientation gradient zones adjacent to grain boundaries. Scripta materialia 61, 273–276.

Moelans, N., Blanpain, B., Wollants, P., 2008. An introduction to phase-field modeling of microstructure evolution. Calphad 32, 268–294.

Mun, D.J., Shin, E.J., Choi, Y.W., Lee, J.S., Koo, Y.M., 2012. Effects of cooling rate, austenitizing temperature and austenite deformation on the transformation behavior of high-strength boron steel. Materials science and engineering: A 545, 214–224.

Murr, L.E., Gaytan, S.M., Ramirez, D.A., Martinez, E., Hernandez, J., Amato, K.N., Shindo, P.W., Medina, F.R., Wicker, R.B., 2012. Metal fabrication by additive manufacturing using laser and electron beam melting technologies. Journal of Materials Science & Technology 28, 1–14.

Musinski, W.D., McDowell, D.L., 2015. On the eigenstrain application of shot-peened residual stresses within a crystal plasticity framework: Application to ni-base superalloy specimens. International Journal of Mechanical Sciences 100, 195–208.

Nabarro, F., 1977. The theory of solution hardening. Philosophical magazine 35, 613–622.

Nagarajan, S., Jain, R., Gurao, N., 2021. Microstructural characteristics governing the lattice rotation in al-mg alloy using in-situ ebsd. Materials Characterization 180, 111405.

Nave, M., Barnett, M., 2004. Texture change near grain boundaries and triple points in cold-rolled interstitial-free steel. Materials Science and Engineering: A 386, 244–253.

Neil, C., Wollmershauser, J., Clausen, B., Tomé, C., Agnew, S., 2010. Modeling lattice strain evolution at finite strains and experimental verification for copper and stainless steel using in situ neutron diffraction. International Journal of Plasticity 26, 1772–1791.

Neog, S.P., Pai, N., Yadav, D., Curry, N., Joshi, S., Jaya, B.N., Samajdar, I., 2024. Growth selection induced residual stresses and fracture behavior of as-deposited thermal barrier coatings. Journal of the American Ceramic Society .

Neuhaus, J., Leitner, M., Nicolaus, K., Petry, W., Hennion, B., Hiess, A., 2014. Role of vibrational entropy in the stabilization of the high-temperature phases of iron. Physical Review B 89, 184302.

Newbury, D.E., Ritchie, N.W., 2013. Elemental mapping of microstructures by scanning electron microscopy-energy dispersive x-ray spectrometry (sem-eds): extraordinary advances with the silicon drift detector (sdd). Journal of Analytical Atomic Spectrometry 28, 973–988.

Niessen, F., Burrows, A., da Silva Fanta, A.B., 2018. A systematic comparison of on-axis and off-axis transmission kikuchi diffraction. Ultramicroscopy 186, 158–170.

Nikulin, I., Kaibyshev, R., Skorobogatykh, V., 2010. High temperature properties of an austenitic stainless steel, in: Journal of Physics: Conference Series, IOP Publishing. p. 012071.

Noyan, I.C., Cohen, J.B., 2013. Residual stress: measurement by diffraction and interpretation. Springer.

Nuttall, R.H., 1981. The first microscope of henry clifton sorby. Technology and culture 22, 275–280.

Nye, J.F., 1953. Some geometrical relations in dislocated crystals. Acta metallurgica 1, 153–162.

Ohashi, T., Barabash, R.I., Pang, J., Ice, G.E., Barabash, O.M., 2009. X-ray microdiffraction and strain gradient crystal plasticity studies of geometrically necessary dislocations near a ni bicrystal grain boundary. International Journal of Plasticity 25, 920–941.

Ohashi, T., Kawamukai, M., Zbib, H., 2007. A multiscale approach for modeling scale-dependent yield stress in polycrystalline metals. International Journal of Plasticity 23, 897–914.

Ohno, N., Okumura, D., 2007. Higher-order stress and grain size effects due to self-energy of geometrically necessary dislocations. Journal of the Mechanics and Physics of Solids 55, 1879–1898.

Ohno, N., Wang, J.D., 1993. Kinematic hardening rules with critical state of dynamic recovery, part i: formulation and basic features for ratchetting behavior. International journal of plasticity 9, 375–390.

Olson, M., DeWald, A., Hill, M., 2021. Precision of hole-drilling residual stress depth profile measurements and an updated uncertainty estimator. Experimental Mechanics 61, 549–564.

Osgood, W., 1954. Residual stresses in metals & metal construction, reinhold publishing corp.

Ozdol, V., Gammer, C., Jin, X., Ercius, P., Ophus, C., Ciston, J., Minor, A., 2015. Strain mapping at nanometer resolution using advanced nano-beam electron diffraction. Applied Physics Letters 106.

Pai, N., Manda, S., Sudhalkar, B., Syphus, B., Fullwood, D., de Kloe, R., Wright, S., Patra, A., Samajdar, I., 2024a. Diffraction-based multiscale residual strain measurements. Microscopy and Microanalysis 30, 236–252.

Pai, N., Prakash, A., Samajdar, I., Patra, A., 2022. Study of grain boundary orientation gradients through combined experiments and strain gradient crystal plasticity modeling. International Journal of Plasticity 156, 103360.

Pai, N., Samajdar, I., Patra, A., 2024b. Microstructural and mechanistic insights into the tension-compression asymmetry of rapidly solidified fe-cr alloys: A phase field and strain gradient plasticity study. Journal of the Mechanics and Physics of Solids , 105695.

Pai, N., Samajdar, I., Patra, A., 2025. Study of orientation-dependent residual strains during tensile and cyclic deformation of an austenitic stainless steel. International Journal of Plasticity , 104228.

Pantleon, W., 2008. Resolving the geometrically necessary dislocation content by conventional electron backscattering diffraction. Scripta Materialia 58, 994–997.

Patra, A., Chaudhary, S., Pai, N., Ramgopal, T., Khandelwal, S., Rao, A., McDowell, D.L., 2023a. ρ-cp: Open source dislocation density based crystal plasticity framework for simulating temperature-and strain rate-dependent deformation. Computational Materials Science 224, 112182.

Patra, A., McDowell, D.L., 2012. Crystal plasticity-based constitutive modelling of irradiated bcc structures. Philosophical Magazine 92, 861–887.

Patra, A., Pai, N., Sharma, P., 2023b. Modeling intrinsic size effects using dislocation density-based strain gradient plasticity. Mechanics Research Communications 127, 104038.

Patra, A., Tomé, C.N., 2024. A dislocation density-based crystal plasticity constitutive model: comparison of vpsc effective medium predictions with ρ-cp finite element predictions. Modelling and Simulation in Materials Science and Engineering 32, 045014.

Patra, A., Zhu, T., McDowell, D.L., 2014. Constitutive equations for modeling non-schmid effects in single crystal bcc-fe at low and ambient temperatures. International Journal of Plasticity 59, 1–14.

Paul, S.K., Raj, A., Biswas, P., Manikandan, G., Verma, R., 2014. Tensile flow behavior of ultra low carbon, low carbon and micro alloyed steel sheets for auto application under low to intermediate strain rate. Materials & Design 57, 211–217.

Pekin, T.C., Gammer, C., Ciston, J., Minor, A.M., Ophus, C., 2017. Optimizing disk registration algorithms for nanobeam electron diffraction strain mapping. Ultramicroscopy 176, 170–176.

Permann, C.J., Gaston, D.R., Andrš, D., Carlsen, R.W., Kong, F., Lindsay, A.D., Miller, J.M., Peterson, J.W., Slaughter, A.E., Stogner, R.H., et al., 2020. Moose: Enabling massively parallel multiphysics simulation. SoftwareX 11, 100430.

Permann, C.J., Tonks, M.R., Fromm, B., Gaston, D.R., 2016. Order parameter re-mapping algorithm for 3d phase field model of grain growth using fem. Computational Materials Science 115, 18–25.

Pierce, D., Haynes, A., Hughes, J., Graves, R., Maziasz, P., Muralidharan, G., Shyam, A., Wang, B., England, R., Daniel, C., 2019. High temperature materials for heavy duty diesel engines: Historical and future trends. Progress in Materials Science 103, 109–179.

Pinomaa, T., Lindroos, M., Jreidini, P., Haapalehto, M., Ammar, K., Wang, L., Forest, S., Provatas, N., Laukkanen, A., 2022. Multiscale analysis of crystalline defect formation in rapid solidification of pure aluminium and aluminium–copper alloys. Philosophical Transactions of the Royal Society A 380, 20200319.

Pinomaa, T., Lindroos, M., Walbrühl, M., Provatas, N., Laukkanen, A., 2020a. The significance of spatial length scales and solute segregation in strengthening rapid solidification microstructures of 316l stainless steel. Acta Materialia 184, 1–16.

Pinomaa, T., McKeown, J.M., Wiezorek, J.M., Provatas, N., Laukkanen, A., Suhonen, T., 2020b. Phase field modeling of rapid resolidification of al-cu thin films. Journal of Crystal Growth 532, 125418.

Plapp, M., 2011. Unified derivation of phase-field models for alloy solidification from a grand-potential functional. Physical Review E 84, 031601.

Plotkowski, A., Saleeby, K., Fancher, C.M., Haley, J., Madireddy, G., An, K., Kannan, R., Feldhausen, T., Lee, Y., Yu, D., et al., 2023. Operando neutron diffraction reveals mechanisms for controlled strain evolution in 3d printing. Nature Communications 14, 4950.

Pokharel, R., Lind, J., Li, S.F., Kenesei, P., Lebensohn, R.A., Suter, R.M., Rollett, A.D., 2015. In-situ observation of bulk 3d grain evolution during plastic deformation in polycrystalline cu. International Journal of Plasticity 67, 217–234.

Pokharel, R., Patra, A., Brown, D.W., Clausen, B., Vogel, S.C., Gray III, G.T., 2019. An analysis of phase stresses in additively manufactured 304l stainless steel using neutron diffraction measurements and crystal plasticity finite element simulations. International Journal of Plasticity 121, 201–217.

Portillo, J., Rauch, E.F., Nicolopoulos, S., Gemmi, M., Bultreys, D., 2010. Precession electron diffraction assisted orientation mapping in the transmission electron microscope, in: Materials science forum, Trans Tech Publ. pp. 1–7.

Prager, W., 1955. The theory of plasticity: a survey of recent achievements. Proceedings of the Institution of Mechanical Engineers 169, 41–57.

Prakash, A., Tak, T.N., Lodh, A., Nayan, N., Narayana Murty, S., Guruprasad, P., Samajdar, I., 2019. Composition gradient and particle deformed zone: an emerging correlation. Metallurgical and Materials Transactions A 50, 1250–1260.

Prakash, A., Tak, T.N., Pai, N.N., Murty, S.N., Guruprasad, P., Doherty, R., Samajdar, I., 2021. Slip band formation in low and high solute aluminum: a combined experimental and modeling study. Modelling and Simulation in Materials Science and Engineering 29, 085016.

Prakash, A., Tak, T.N., Pai, N.N., Seekala, H., Murty, S.N., Phani, P., Mahesh, S., Guruprasad, P., Samajdar, I., 2023. Inception of macroscopic shear bands during hot working of aluminum alloys. International Journal of Plasticity 166, 103632.

Prasad, A., Yuan, L., Lee, P., Patel, M., Qiu, D., Easton, M., StJohn, D., 2020. Towards understanding grain nucleation under additive manufacturing solidification conditions. Acta Materialia 195, 392–403.

Prevéy, P.S., 1986. X-ray diffraction residual stress techniques. volume 10. American Society for Metals, Metals Park, OH.

Quey, R., Dawson, P., Barbe, F., 2011. Large-scale 3d random polycrystals for the finite element method: Generation, meshing and remeshing. Computer Methods in Applied Mechanics and Engineering 200, 1729–1745.

Ramirez, D., Murr, L., Martinez, E., Hernandez, D., Martinez, J., Machado, B.I., Medina, F., Frigola, P., Wicker, R., 2011. Novel precipitate–microstructural architecture developed in the fabrication of solid copper components by additive manufacturing using electron beam melting. Acta Materialia 59, 4088–4099.

Randle, V., Engler, O., 2000. Introduction to texture analysis: macrotexture, microtexture and orientation mapping. CRC press.

Randle, V., Hansen, N., Jensen, D.J., 1996. The deformation behaviour of grain boundary regions in polycrystalline aluminium. Philosophical Magazine A 73, 265–282.

Rappaz, M., Gandin, C.A., 1993. Probabilistic modelling of microstructure formation in solidification processes. Acta metallurgica et materialia 41, 345–360.

Rauch, E., Veron, M., 2005. Coupled microstructural observations and local texture measurements with an automated crystallographic orientation mapping tool attached to a tem. Materialwissenschaft und Werkstofftechnik: Entwicklung, Fertigung, Prüfung, Eigenschaften und Anwendungen technischer Werkstoffe 36, 552–556.

Rauch, E.F., Portillo, J., Nicolopoulos, S., Bultreys, D., Rouvimov, S., Moeck, P., 2010. Automated nanocrystal orientation and phase mapping in the transmission electron microscope on the basis of precession electron diffraction. Zeitschrift für Kristallographie 225, 103–109.

Raveendra, S., Kanjarla, A., Paranjape, H., Mishra, S., Mishra, S., Delannay, L., Samajdar, I., Van Houtte, P., 2011. Strain mode dependence of deformation texture developments: microstructural origin. Metallurgical and Materials Transactions A 42, 2113–2124.

Revelly, A., Becker, H., Vishwanadh, B., Mani Krishna, K., Tewari, R., Srivastava, D., Dey, G., Samajdar, I., Panwar, A., 2015. High-purity zirconium under niobium ion implantation: possibility of a dynamic precipitation? Philosophical Magazine 95, 3727–3744.

Rietveld, H.M., 1969. A profile refinement method for nuclear and magnetic structures. Journal of applied Crystallography 2, 65–71.

Rollett, A.D., Wagner, F., Allain-Bonasso, N., Field, D.P., Lebensohn, R.A., 2012. Comparison of gradients in orientation and stress between experiment and simulation, in: Materials Science Forum, Trans Tech Publ. pp. 463–468.

Rout, M., Pal, S.K., Singh, S.B., 2015. Cross rolling: a metal forming process. Modern manufacturing engineering , 41–64.

Ruggles, T., Fullwood, D., 2013. Estimations of bulk geometrically necessary dislocation density using high resolution ebsd. Ultramicroscopy 133, 8–15.

Ruggles, T., Rampton, T., Khosravani, A., Fullwood, D., 2016. The effect of length scale on the determination of geometrically necessary dislocations via ebsd continuum dislocation microscopy. Ultramicroscopy 164, 1–10.

Ruggles, T., Yoo, Y., Dunlap, B., Crimp, M., Kacher, J., 2020. Correlating results from high resolution ebsd with tem-and ecci-based dislocation microscopy: Approaching single dislocation sensitivity via noise reduction. Ultramicroscopy 210, 112927.

Rui, S.S., Niu, L.S., Shi, H.J., Wei, S., Tasan, C.C., 2019. Diffraction-based misorientation mapping: A continuum mechanics description. Journal of the Mechanics and Physics of Solids 133, 103709.

Saeidi, K., Gao, X., Zhong, Y., Shen, Z.J., 2015. Hardened austenite steel with columnar sub-grain structure formed by laser melting. Materials Science and Engineering: A 625, 221–229.

Saleh, A.A., Pereloma, E.V., Clausen, B., Brown, D.W., Tomé, C.N., Gazder, A.A., 2013. On the evolution and modelling of lattice strains during the cyclic loading of twip steel. Acta materialia 61, 5247–5262.

Sanaei, N., Fatemi, A., 2021. Defects in additive manufactured metals and their effect on fatigue performance: A state-of-the-art review. Progress in Materials Science 117, 100724.

Santus, C., Grossi, T., Romanelli, L., Pedranz, M., Benedetti, M., 2023. A computationally fast and accurate procedure for the identification of the chaboche isotropic-kinematic hardening model parameters based on strain-controlled cycles and asymptotic ratcheting rate. International Journal of Plasticity 160, 103503.

Sarkar, A., Kumar, S., Sudhalkar, B.R., Mondal, R., Khan, M.I., Ghosal, A.M., Chandra, K., Kain, V., Samajdar, I., 2022. Relating microstructures of hierarchical tertiary phases with corrosion performance in a super duplex stainless steel. Materials Characterization 194, 112426.

Sauvage, X., Enikeev, N., Valiev, R., Nasedkina, Y., Murashkin, M., 2014. Atomic-scale analysis of the segregation and precipitation mechanisms in a severely deformed al–mg alloy. Acta Materialia 72, 125–136.

Saylor, D.M., El-Dasher, B.S., Adams, B.L., Rohrer, G.S., 2004. Measuring the five-parameter grain-boundary distribution from observations of planar sections. Metallurgical and Materials Transactions A 35, 1981–1989.

Schmitt, P., Zorn, S., Gericke, K., 2021. Additive manufacturing research landscape: a literature review. Proceedings of the Design Society 1, 333–344.

Schröder, J., Evans, A., Polatidis, E., Čapek, J., Mohr, G., Serrano-Munoz, I., Bruno, G., 2022. Understanding the impact of texture on the micromechanical anisotropy of laser powder bed fused inconel 718. Journal of materials science 57, 15036–15058.

Schwartz, A.J., Kumar, M., Adams, B.L., Field, D.P., 2009. Electron backscatter diffraction in materials science. volume 2. Springer.

Schwarzer, R.A., Field, D.P., Adams, B.L., Kumar, M., Schwartz, A.J., 2009. Present state of electron backscatter diffraction and prospective developments. Electron backscatter diffraction in materials science , 1–20.

Sedaghat, O., Abdolvand, H., 2021. A non-local crystal plasticity constitutive model for hexagonal close-packed polycrystals. International Journal of Plasticity 136, 102883.

Senez, V., Armigliato, A., De Wolf, I., Carnevale, G., Balboni, R., Frabboni, S., Benedetti, A., 2003. Strain determination in silicon microstructures by combined convergent beam electron diffraction, process simulation, and micro-raman spectroscopy. Journal of Applied Physics 94, 5574–5583.

Shade, P.A., Musinski, W.D., Obstalecki, M., Pagan, D.C., Beaudoin, A.J., Bernier, J.V., Turner, T.J., 2019. Exploring new links between crystal plasticity models and high-energy x-ray diffraction microscopy. Current Opinion in Solid State and Materials Science 23, 100763.

Shamsujjoha, M., Agnew, S.R., Fitz-Gerald, J.M., Moore, W.R., Newman, T.A., 2018. High strength and ductility of additively manufactured 316l stainless steel explained. Metallurgical and Materials Transactions A 49, 3011–3027.

Sharma, R., Marki, R., Webb, A., Knezevic, M., Miles, M.P., Fullwood, D.T., 2024. Strain-gradient crystal plasticity model with slip-system level gnd tracking: Simulation vs experiment for sequential strain path change in aa6016-t4. Materialia 38, 102304.

Sharma, R.C., 2003. Principles of heat treatment of steels. New Age International.

Shenoy, M., Tjiptowidjojo, Y., McDowell, D., 2008. Microstructure-sensitive modeling of polycrystalline in 100. International Journal of Plasticity 24, 1694–1730.

Shishvan, S.S., Mohammadi, S., Rahimian, M., Van der Giessen, E., 2011. Plane-strain discrete dislocation plasticity incorporating anisotropic elasticity. International Journal of Solids and Structures 48, 374–387.

Sieurin, H., Zander, J., Sandström, R., 2006. Modelling solid solution hardening in stainless steels. Materials Science and Engineering: A 415, 66–71.

Singh, J., Mahesh, S., Kumar, G., Pant, P., Srivastava, D., Dey, G., Saibaba, N., Samajdar, I., 2015. Deformation twinning in zirconium: direct experimental observations and polycrystal plasticity predictions. Metallurgical and Materials Transactions A 46, 5058–5071.

Singh, J., Mahesh, S., Roy, S., Kumar, G., Srivastava, D., Dey, G., Saibaba, N., Samajdar, I., 2017. Temperature dependence of work hardening in sparsely twinning zirconium. Acta Materialia 123, 337–349.

Słowik, J., Zieba, A., 2005. Silicon strip detector applied to x-ray diffractometer: Angular resolution and counting rate. Nuclear Instruments and Methods in Physics Research Section A: Accelerators, Spectrometers, Detectors and Associated Equipment 551, 73–77.

Small, K.A., Clayburn, Z., DeMott, R., Primig, S., Fullwood, D., Taheri, M.L., 2020. Interplay of dislocation substructure and elastic strain evolution in additively manufactured inconel 625. Materials Science and Engineering: A 785, 139380.

Small, K.A., Taheri, M.L., 2021. Role of processing in microstructural evolution in inconel 625: a comparison of three additive manufacturing techniques. Metallurgical and Materials Transactions A 52, 2811–2820.

Sneddon, G.C., Trimby, P.W., Cairney, J.M., 2016. Transmission kikuchi diffraction in a scanning electron microscope: A review. Materials Science and Engineering: R: Reports 110, 1–12.

Soper, A.K., 2011. GudrunN and GudrunX: programs for correcting raw neutron and X-ray diffraction data to differential scattering cross section. Science & Technology Facilities Council Swindon, UK.

Spittle, J., Brown, S., 1989. Computer simulation of the effects of alloy variables on the grain structures of castings. Acta Metallurgica 37, 1803–1810.

Srinivasan, N., Bhaskar, L.K., Kumar, R., Baragetti, S., 2018. Residual stress gradient and relaxation upon fatigue deformation of diamond-like carbon coated aluminum alloy in air and methanol environments. Materials & Design 160, 303–312.

Srinivasan, N., Kain, V., Birbilis, N., Krishna, K.M., Shekhawat, S., Samajdar, I., 2015. Near boundary gradient zone and sensitization control in austenitic stainless steel. Corrosion Science 100, 544–555.

Stinville, J.C., Lenthe, W.C., Echlin, M.P., Callahan, P.G., Texier, D., Pollock, T.M., 2017. Microstructural statistics for fatigue crack initiation in polycrystalline nickel-base superalloys. International Journal of Fracture 208, 221–240.

Stölken, J.S., Evans, A., 1998. A microbend test method for measuring the plasticity length scale. Acta Materialia 46, 5109–5115.

Subedi, S., Pokharel, R., Rollett, A.D., 2015. Orientation gradients in relation to grain boundaries at varying strain level and spatial resolution. Materials Science and Engineering: A 638, 348–356.

Sudhalkar, B.R., Pai, N., Patra, A., Kapoor, K., Kapoor, R., Agarwal, A., Samajdar, I., 2024. Grain boundary localized damage in hexagonal titanium. Materials Science and Engineering: A 902, 146608.

Sun, F., Wang, S., Xie, Q., 2022. Role of particles and lattice rotation in tension–compression asymmetry of aluminium alloys. International Journal of Plasticity 159, 103464.

Sun, S., Adams, B., King, W., 2000. Observations of lattice curvature near the interface of a deformed aluminium bicrystal. Philosophical Magazine A 80, 9–25.

Sun, Z., Tan, X., Tor, S.B., Chua, C.K., 2018. Simultaneously enhanced strength and ductility for 3d-printed stainless steel 316l by selective laser melting. NPG Asia Materials 10, 127–136.

Suwas, S., Ray, R.K., 2014. Crystallographic texture of materials. Springer.

Takajo, S., Tomé, C.N., Vogel, S.C., Beyerlein, I.J., 2018. Texture simulation of a severely cold rolled low carbon steel using polycrystal modeling. International Journal of Plasticity 109, 137–152.

Taleb, L., Cailletaud, G., Blaj, L., 2006. Numerical simulation of complex ratcheting tests with a multi-mechanism model type. International Journal of Plasticity 22, 724–753.

Talonen, J., Hänninen, H., 2004. Damping properties of austenitic stainless steels containing strain-induced martensite. Metallurgical and Materials Transactions A 35, 2401–2406.

Taylor, G.I., 1934. The mechanism of plastic deformation of crystals. part i.—theoretical. Proceedings of the Royal Society of London. Series A, Containing Papers of a Mathematical and Physical Character 145, 362–387.

Taylor, G.I., 1938. Plastic strain in metals. J. Inst. Metals 62, 307–324.

Tayon, W.A., Pagan, D.C., Yeratapally, S.R., Phan, T.Q., Hochhalter, J.D., 2024. Exploring the role of type-ii residual stresses in a laser powder bed fusion nickel-based superalloy using measurement and modeling. International Journal of Fatigue 181, 108153.

Thool, K., Patra, A., Fullwood, D., Krishna, K.M., Srivastava, D., Samajdar, I., 2020. The role of crystallographic orientations on heterogeneous deformation in a zirconium alloy: A combined experimental and modeling study. International Journal of Plasticity 133, 102785.

Tome, C.N., Lebensohn, R.A., 2023. Material modeling with the visco-plastic self-consistent (VPSC) approach: theory and practical applications. Elsevier.

Tóth, L.S., Estrin, Y., Lapovok, R., Gu, C., 2010. A model of grain fragmentation based on lattice curvature. Acta Materialia 58, 1782–1794.

Tran, M.T., Nguyen, X.M., Kim, H., Chae, H., Woo, W., Lee, H.W., Kim, D.K., 2023. Micromechanical properties and deformation behavior of the constituent phases in 3rd generation complex phase ahss: In-situ neutron experiment and crystal plasticity simulation. International Journal of Plasticity 171, 103812.

Trimby, P.W., 2012. Orientation mapping of nanostructured materials using transmission kikuchi diffraction in the scanning electron microscope. Ultramicroscopy 120, 16–24.

Ungár, T., Gubicza, J., Hanák, P., Alexandrov, I., 2001. Densities and character of dislocations and size-distribution of subgrains in deformed metals by x-ray diffraction profile analysis. Materials Science and Engineering: A 319, 274–278.

Upadhyay, M.V., Capek, J., Panzner, T., Van Swygenhoven, H., 2019. Microstructure evolution of stainless steel subjected to biaxial load path changes: In-situ neutron diffraction and multi-scale modeling. International Journal of Plasticity 122, 49–72.

Vahdat, A.S., Rezazadeh, G., 2011. Effects of axial and residual stresses on thermoelastic damping in capacitive micro-beam resonators. Journal of the Franklin Institute 348, 622–639.

Valentini, E., Bertelli, L., Benincasa, A., Gulisano, S., 2019. Recent advancements in the hole-drilling strain-gage method for determining residual stresses. New Challenges in Residual Stress Measurements and Evaluation , 9–15.

Van Houtte, P., De Buyser, L., 1993. The influence of crystallographic texture on diffraction measurements of residual stress. Acta metallurgica et materialia 41, 323–336.

Van Houtte, P., Li, S., Seefeldt, M., Delannay, L., 2005. Deformation texture prediction: from the taylor model to the advanced lamel model. International journal of plasticity 21, 589–624.

Vaudin, M.D., Osborn, W.A., Friedman, L.H., Gorham, J.M., Vartanian, V., Cook, R., 2015. Designing a standard for strain mapping: Hr-ebsd analysis of sige thin film structures on si. Ultramicroscopy 148, 94–104.

Verlinden, B., Driver, J., Samajdar, I., Doherty, R.D., 2007. Thermo-mechanical processing of metallic materials. Elsevier.

Viladot, D., Véron, M., Gemmi, M., Peiró, F., Portillo, J., Estradé, S., Mendoza, J., LLORCA-ISERN, N., Nicolopoulos, S., 2013. Orientation and phase mapping in the transmission electron microscope using precession-assisted diffraction spot recognition: state-of-the-art results. Journal of microscopy 252, 23–34.

Vincent, R., Midgley, P., 1994. Double conical beam-rocking system for measurement of integrated electron diffraction intensities. Ultramicroscopy 53, 271–282.

Voisin, T., Forien, J.B., Perron, A., Aubry, S., Bertin, N., Samanta, A., Baker, A., Wang, Y.M., 2021. New insights on cellular structures strengthening mechanisms and thermal stability of an austenitic stainless steel fabricated by laser powder-bed-fusion. Acta Materialia 203, 116476.

Voyiadjis, G.Z., Song, Y., 2019. Strain gradient continuum plasticity theories: theoretical, numerical and experimental investigations. International Journal of Plasticity 121, 21–75.

Wang, H., Capolungo, L., Clausen, B., Tomé, C., 2017. A crystal plasticity model based on transition state theory. International Journal of Plasticity 93, 251–268.

Wang, H., Clausen, B., Capolungo, L., Beyerlein, I.J., Wang, J., Tome, C.N., 2016. Stress and strain relaxation in magnesium az31 rolled plate: In-situ neutron measurement and elastic viscoplastic polycrystal modeling. International Journal of Plasticity 79, 275–292.

Wang, H., Clausen, B., Tomé, C., Wu, P., 2013. Studying the effect of stress relaxation and creep on lattice strain evolution of stainless steel under tension. Acta Materialia 61, 1179–1188.

Wang, M., Wu, J., Yang, S., Knezevic, M., Huang, Z., Zhao, Y., Liu, T., Shen, B., Wang, J., 2024. Outstanding thermal stability of cold-rolled al–y alloy revealed using in-situ

synchrotron x-ray diffraction and ex-situ microscopy. Journal of Materials Research and Technology 28, 2898–2908.

Wang, Y.D., Tian, H., Stoica, A.D., Wang, X.L., Liaw, P.K., Richardson, J.W., 2003. The development of grain-orientation-dependent residual stressess in a cyclically deformed alloy. Nature Materials 2, 101–106.

Wang, Y.M., Voisin, T., McKeown, J.T., Ye, J., Calta, N.P., Li, Z., Zeng, Z., Zhang, Y., Chen, W., Roehling, T.T., et al., 2018. Additively manufactured hierarchical stainless steels with high strength and ductility. Nature materials 17, 63–71.

Wang, Z., Gong, B., 2002. Residual stress in the forming of materials. Handbook of residual stress and deformation of steel , 141–49.

Wang, Z., Jiang, B., Wu, S., Liu, W., 2023. Anisotropic tension-compression asymmetry in slm 316l stainless steel. International Journal of Mechanical Sciences 246, 108139.

Wasnik, D., Kain, V., Samajdar, I., Verlinden, B., De, P., 2002. Resistance to sensitization and intergranular corrosion through extreme randomization of grain boundaries. Acta Materialia 50, 4587–4601.

Weber, G., Anand, L., 1990. Finite deformation constitutive equations and a time integration procedure for isotropic, hyperelastic-viscoplastic solids. Computer Methods in Applied Mechanics and Engineering 79, 173–202.

Wilkinson, A.J., Dingley, D.J., Meaden, G., 2009. Strain mapping using electron backscatter diffraction. Electron Backscatter Diffraction in Materials Science , 231–249.

Wilkinson, A.J., Meaden, G., Dingley, D.J., 2006. High-resolution elastic strain measurement from electron backscatter diffraction patterns: New levels of sensitivity. Ultramicroscopy 106, 307–313.

Winkelmann, A., 2010. Principles of depth-resolved kikuchi pattern simulation for electron backscatter diffraction. Journal of microscopy 239, 32–45.

Winkelmann, A., Trager-Cowan, C., Sweeney, F., Day, A.P., Parbrook, P., 2007. Many-beam dynamical simulation of electron backscatter diffraction patterns. Ultramicroscopy 107, 414–421.

Withers, P.J., Bhadeshia, H., 2001. Residual stress. part 1–measurement techniques. Materials science and Technology 17, 355–365.

Wollmershauser, J., Clausen, B., Agnew, S., 2012. A slip system-based kinematic hardening model application to in situ neutron diffraction of cyclic deformation of austenitic stainless steel. International Journal of Fatigue 36, 181–193.

Wright, S.I., Adams, B.L., 1992. Automatic analysis of electron backscatter diffraction patterns. Metallurgical Transactions A 23, 759–767.

Wright, S.I., Nowell, M.M., Field, D.P., 2011. A review of strain analysis using electron backscatter diffraction. Microscopy and microanalysis 17, 316–329.

Wright, S.I., Suzuki, S., Nowell, M.M., 2016. In situ ebsd observations of the evolution in crystallographic orientation with deformation. JOM 68, 2730–2736.

Wu, A.S., Brown, D.W., Kumar, M., Gallegos, G.F., King, W.E., 2014. An experimental investigation into additive manufacturing-induced residual stresses in 316l stainless steel. Metallurgical and Materials Transactions A 45, 6260–6270.

Xiao, L., Chen, X., Cao, Y., Zhou, H., Ma, X., Yin, D., Ye, B., Han, X., Zhu, Y., 2020. Solute segregation assisted nanocrystallization of a cold-rolled mg–ag alloy during annealing. Scripta Materialia 177, 69–73.

Yeon, D.H., Cha, P.R., Yoon, J.K., 2001. A phase field study for ferrite–austenite transitions under para-equilibrium. Scripta materialia 45, 661–668.

Yoo, Y.S.J., Book, T.A., Sangid, M.D., Kacher, J., 2018. Identifying strain localization and dislocation processes in fatigued inconel 718 manufactured from selective laser melting. Materials Science and Engineering: A 724, 444–451.

Yu, F., Wei, Y., Ji, Y., Chen, L.Q., 2018. Phase field modeling of solidification microstructure evolution during welding. Journal of Materials Processing Technology 255, 285–293.

Yu, H., Karamched, P., Das, S., Liu, J., Mizohata, K., Hofmann, F., 2021. New perspectives on collision cascade damage in self-ion irradiated tungsten from hr-ebsd and ecci. Journal of Nuclear Materials 554, 153074.

Yu, H., Liu, J., Karamched, P., Wilkinson, A.J., Hofmann, F., 2019. Mapping the full lattice strain tensor of a single dislocation by high angular resolution transmission kikuchi diffraction (hr-tkd). Scripta Materialia 164, 36–41.

Yuan, H., Brodu, E., Chen, C., Bouzy, E., FUNDENBERGER, J.J., Toth, L., 2017. On-axis versus off-axis transmission kikuchi diffraction technique: application to the characterisation of severe plastic deformation-induced ultrafine-grained microstructures. Journal of Microscopy 267, 70–80.

Zaefferer, S., 2007. On the formation mechanisms, spatial resolution and intensity of backscatter kikuchi patterns. Ultramicroscopy 107, 254–266.

Zander, J., Sandström, R., Vitos, L., 2007. Modelling mechanical properties for non-hardenable aluminium alloys. Computational materials science 41, 86–95.

Zecevic, M., Knezevic, M., 2015. A dislocation density based elasto-plastic self-consistent model for the prediction of cyclic deformation: Application to aa6022-t4. International Journal of Plasticity 72, 200–217.

Zecevic, M., Knezevic, M., Beyerlein, I.J., Tomé, C.N., 2015. An elasto-plastic self-consistent model with hardening based on dislocation density, twinning and de-twinning: Application to strain path changes in hcp metals. Materials Science and Engineering: A 638, 262–274.

Zhang, K., Holmedal, B., Manik, T., Saai, A., 2019. Assessment of advanced taylor models, the taylor factor and yield-surface exponent for fcc metals. International Journal of Plasticity 114, 144–160.

Zhang, T., Collins, D.M., Dunne, F.P., Shollock, B.A., 2014. Crystal plasticity and high-resolution electron backscatter diffraction analysis of full-field polycrystal ni superalloy strains and rotations under thermal loading. Acta materialia 80, 25–38.

Zhang, T., Jiang, J., Britton, B., Shollock, B., Dunne, F., 2016. Crack nucleation using combined crystal plasticity modelling, high-resolution digital image correlation and high-resolution electron backscatter diffraction in a superalloy containing non-metallic inclusions under fatigue. Proceedings of the Royal Society A: Mathematical, Physical and Engineering Sciences 472, 20150792.

Zhang, X., Aifantis, K., 2015. Interpreting the internal length scale in strain gradient plasticity. Rev. Adv. Mater. Sci 41, 72–83.

Zhang, X., Lutz, A., Andrä, H., Lahres, M., Gan, W., Maawad, E., Emmelmann, C., 2021a. Evolution of microscopic strains, stresses, and dislocation density during in-situ tensile loading of additively manufactured alsi10mg alloy. International journal of plasticity 139, 102946.

Zhang, X., Lutz, A., Andrä, H., Lahres, M., Sittig, D., Maawad, E., Gan, W., Knoop, D., 2021b. An additively manufactured and direct-aged alsi3. 5mg2. 5 alloy with superior strength and ductility: Micromechanical mechanisms. International Journal of Plasticity 146, 103083.

Zhang, X., Zhao, J., Kang, G., Zaiser, M., 2023. Geometrically necessary dislocations and related kinematic hardening in gradient grained materials: A nonlocal crystal plasticity study. International Journal of Plasticity 163, 103553.

Zhang, Y., Ding, K., Gu, Y., Chen, W., Wang, Y.M., El-Awady, J., McDowell, D.L., Zhu, T., 2022. Modeling of microscale internal stresses in additively manufactured stainless steel. Modelling and Simulation in Materials Science and Engineering 30, 074001.

Zhao, C., Li, X., 2021. Quantitative study of residual strain and geometrically necessary dislocation density using hr-ebsd method. Experimental Mechanics 61, 1281–1290.

Zhao, D., Patel, A., Barbosa, A., Hansen, M.H., Wang, A.L., Dong, J., Zhang, Y., Umale, T., Karaman, I., Shamberger, P., et al., 2023. A reference-area-free strain mapping method using precession electron diffraction data. Ultramicroscopy 247, 113700.

Zhao, J., Zaiser, M., Lu, X., Zhang, B., Huang, C., Kang, G., Zhang, X., 2021. Size-dependent plasticity of hetero-structured laminates: A constitutive model considering deformation heterogeneities. International Journal of Plasticity 145, 103063.

Zheng, L., Gao, Y., Wang, Y., Stoica, A.D., An, K., Wang, X.L., 2013. Grain orientation dependence of lattice strains and intergranular damage rates in polycrystals under cyclic loading. Scripta Materialia 68, 265–268.

Zhong, H., Shi, Q., Dan, C., You, X., Zong, S., Zhong, S., Zhang, Y., Wang, H., Chen, Z., 2024. Resolving localized geometrically necessary dislocation densities in al-mg polycrystal via in situ ebsd. Acta Materialia 279, 120290.

Zhou, G., Jeong, W., Homer, E., Fullwood, D., Lee, M., Kim, J., Lim, H., Zbib, H., Wagoner, R., 2020. A predictive strain-gradient model with no undetermined constants or length scales. Journal of the Mechanics and Physics of Solids 145, 104178.

Zhou, X., 2020. Numerical Simulation of Dendrites Growth in Continuous Casting by Using Open Source Software. Ph.D. thesis. Purdue University Graduate School.

Zhu, C., Harrington, T., Gray III, G.T., Vecchio, K.S., 2018. Dislocation-type evolution in quasi-statically compressed polycrystalline nickel. Acta Materialia 155, 104–116.

Zhu, G., Wang, L., Sun, Y., Shang, X., Wang, J., Wang, H., Zeng, X., 2021a. Grain-size effect on the deformation of mg–3al–3sn alloy: Experiments and elastic-viscoplastic self-consistent modeling. International Journal of Plasticity 143, 103018.

Zhu, Z., Ma, X., Jiang, P., Mi, G., Wang, C., 2021b. Planar-cellular-dendritic transformation in the fusion zone of a gh909 superalloy weldment. Journal of Materials Research and Technology 10, 960–975.

Ziegler, H., 1959. A modification of prager's hardening rule. Quarterly of Applied mathematics 17, 55–65.

Zirkle, T., Zhu, T., McDowell, D.L., 2021. Micromechanical crystal plasticity back stress evolution within fcc dislocation substructure. International Journal of Plasticity 146, 103082.

Acknowledgments

First and foremost, I am deeply indebted to my supervisor Prof. Anirban Patra for his contributions in my thesis. While providing me sufficient freedom to explore/tackle the problem statement as I deemed fit, he also guided me whenever I faced any challenges in my thesis. I would always try to implement his professionalism, dedication and discipline in my career further as a researcher. I am also extremely grateful to my co-supervisor, Prof. Indradev Samajdar, whose experimental expertise was crucial in completing my thesis. His precise understanding on various technical aspects of X-ray/electron diffraction helped me navigate through some important roadblocks. Looking back at my 4.5 years in IITB, I can surely state that both my supervisors played a crucial role in me not only maturing as a researcher, but also as a good human being.

I would like to thank Prof. David Fullwood (and his group), whose expertise and technical inputs on HR-EBSD were crucial at different stages of my thesis. I am also grateful to my Research Progress Committee (RPC) members, Prof. P.J. Guruprasad, Prof. Nagamani Jaya Balila and Prof. M.J.N.V. Prasad, and my PMRF review committee members, for their technical inputs and counsel during the course of my PhD. Their inputs played a key role in shaping up my thesis. Additionally, I would like to thank Dr. Stuart Wright, Dr. Rene de Kloe, Dr. Carlos Tome and Prof. Sivasambu Mahesh, with whom I have collaborated/discussed my work during the course of my thesis.

As with any other research, my thesis too involved contributions from various colleagues. To begin with, I would like thank Suketa Chaudhary, Saurabh Kumar, Sanjay Manda, Subhas Bhunia, Bhargav Sudhalkar, Vikram Chavan, Junaid Akhter and Mahesh Alanka for their significant assistance at various stages of my PhD. The numerous technical as well as social interactions we had would always be cherished. I am also grateful to Dr. Aditya Prakash, Dr. Tawqeer Tak, Dr. Hitesh Mehtani, Dr. Irshad Khan and Mr. Parvej Raut, who

patiently trained me in various tools during the early years of my PhD. I would also like to thank all members from Prof. Nagamani Jaya Balila's and Prof. Sushil Mishra's group, who routinely helped me in performing my deformation experiments. I am also thankful to the lab/department technicians, mainly Mr. Sopan Satre, Mr. Prashant Patil and Mr. Abhishek Pawar for their timely assistance.

I am also grateful for the financial assistance received from the PMRF as well as the DST-SERB project (under Prof. Anirban Patra) during the course of my PhD.

Finally, I would like thank my parents who inculcated the discipline, values and work ethics in me right from my childhood. Though they may only be partly familiar with this field, they have always supported me at every stage of the journey.